Universidade de Aveiro Departamento de Física
2005

Sérgio Manuel de Sousa Pereira

Estudo de propriedades estruturais e ópticas de multicamadas epitaxiais emissoras de luz baseadas em InGaN/GaN.

Universidade de Aveiro Departamento de Física
2005

Sérgio Manuel de Sousa Pereira

Structural and optical characterization of light emitting InGaN/GaN epitaxial layers

dissertação apresentada à Universidade de Aveiro para cumprimento dos requisitos necessários à obtenção do grau de Doutor em Física, realizada sob a orientação científica da Professora Estela Pereira, Professora Catedrática do Departamento de Física da Universidade de Aveiro e do Professor Kevin O'Donnell Professor Catedrático do Department of Physics and Applied Physics da Universidade de Strathclyde (Glasgow, RU).

o júri

presidente Prof. Drª. Estela Pereira

Prof. Dr. Kevin O'Donnell

Prof. Dr. Eduardo Alves

Prof. Dr. Luís Rebouta

Prof. Dr. Nikolai Sobolev

agradecimentos

Não posso deixar de exprimir os meus sinceros agradecimentos a todas as pessoas e instituições que, de forma directa ou indirecta, contribuíram para este trabalho de investigação. Nomeadamente, quero deixar uma palavra de gratidão aos meus supervisores, a Professora Doutora Estela Pereira do Departamento de Física da Universidade de Aveiro (UA) e o Professor Kevin O'Donnell do *Department of Physics and Applied Physics* da *University of Strathclyde* no RU, que me acolheram e orientaram. Agradeço a sua disponibilidade pessoal, confiança, entusiasmo transmitido e as oportunidades oferecidas durante este trabalho. A nível institucional gostaria de agradecer à Fundação para a Ciência e Tecnologia pela bolsa de doutoramento concedida (SFRH/BD/859/2000).

O trabalho subjacente a esta tese de doutoramento contém contribuições de vários investigadores que demostraram interesse genuíno em colaborar, trocar conhecimentos e contribuir para o desenvolvimento cientifico nesta área. Dessas pessoas destaco algumas, sem ordem de preferência, cujo contributo considero essencial; A colega de doutoramento Drª Rosário Correia da UA, com quem as discussões acerca dos temas tratados neste trabalho foram estimulantes e extremamente proveitosas. O Dr. Eduardo Alves, do Instituto Tecnológico Nuclear (ITN), pelas medidas de RBS efectuadas, mas acima de tudo pela enorme motivação e entusiasmo demostrado acerca do meu trabalho. O Dr. Nuno Barradas (ITN) pelo contributo importante na interpretação e simulação dos resultados de RBS. O Dr. Nuno Franco e o Dr. António Sequeira (ITN) que contribuíram na área de difracção de raios-X. Das pessoas com quem trabalhei em Glasgow, quero agradecer à Drª Carol Trager-Cowan ao Dr. Robert Martin do grupo de investigação *Semiconductor Spectroscopy and Devices* e ao Dr. Ian Watson do *Institute of Photonics*, que cresceu parte as amostras estudadas nesta tese.

A nível pessoal não posso deixar de agradecer aos meu pais, Camilo Pereira e Belmira Pereira, que desde sempre prestaram um apoio incondicional e motivação para a realização deste trabalho. Por último, dedico este trabalho à minha outra metade Sílvia Marçal, que me apoiou com carinho e entusiasmo. O meu obrigado também para todas as pessoas que me acompanharam de várias formas e cujo contributo não é aqui destacado.

resumo

Esta tese apresenta os resultados de uma investigação experimental em filmes epitaxiais emissores de luz baseados em $In_xGa_{1-x}N$. O $In_xGa_{1-x}N$ é uma liga semicondutora ternária do grupo III-N muito utilizada como camada activa numa gama de dispositivos optoelectrónicos em desenvolvimento, incluindo díodos emissores de luz (LEDs) e díodos laser (LDs), para operação na região do visível e ultravioleta do espectro electromagnético.

Neste estudo, caracterizam-se as propriedade ópticas e estruturais de camadas simples e poços quânticos múltiplos (Multiple Quantum Wells, MQWs) de $In_xGa_{1-x}N/GaN$, com ênfase nas suas propriedades físicas fundamentais. O objectivo central do trabalho prende-se com a compreensão mais profunda dos processos físicos que estão por trás das suas propriedades ópticas, preenchendo o fosso existente entre aplicações tecnológicas e o conhecimento científico. Nomeadamente, a tese aborda os problemas da medição da fracção de InN (x) em multicamadas ultrafinas sujeitas a tensões, a influência da composição e das tensões microscópicas nas propriedades ópticas e estruturais. A questão relativa à segregação de fases em multicamadas de $In_xGa_{1-x}N/GaN$ é também discutida à luz dos resultados obtidos.

A metodologia seguida assenta na integração de resultados obtidos por técnicas complementares através de uma análise sistemática e multidisciplinar. Esta abordagem passa pela combinação de: 1) Crescimento de amostras por deposição epitaxial em fase de vapor organometálico (MOVPE) com características específicas de forma a tentar isolar parâmetros estruturais, tais como espessura e composição; 2) Caracterização nanoestrutural por microscopia de força atómica (AFM), microscópica electrónica de varrimento (SEM), difracção de raios-X e retro-dispersão de Rutherford (RBS); 3) Caracterização óptica a escalas complementares por: espectroscopia de absorção óptica (OA), fotoluminescência (PL), catodoluminescência (CL) e microscopia confocal (CM) com análise espectral.

Com base nos resultados obtidos, a tese propõe modelos de interpretação para as propriedades estruturais e ópticas, dando ênfase às suas correlações. Em particular, estabelece-se a necessidade de considerar fenómenos relacionados com tensões microscópicas na interpretação dos resultados experimentais.

Com este trabalho fica clara a necessidade de um conhecimento detalhado das características nanoestruturais para interpretar as propriedades ópticas das ligas de $In_xGa_{1-x}N$.

abstract

This thesis presents an experimental investigation of light emitting epitaxial layers based on indium gallium nitride ($In_xGa_{1-x}N$). This group III-nitride ternary semiconductor alloy is used as the active layer in a novel class of optoelectronic devices, including light emitting diodes (LEDs) and laser diodes (LDs), under development to operate in the visible and ultraviolet regions of the electromagnetic spectrum. The structural and optical properties of $In_xGa_{1-x}N$/GaN single layers and multiple quantum wells (MQWs) are characterized with an emphasis on their fundamental physical properties.

The fundamental purpose of this work is to provide grounds for better understanding of the yet unclear physics of this important material system, and help to fill the gap between basic scientific knowledge and technological applications. Namely, this work addresses the issues of accurate measurement of the InN mole fraction (x), the influence of composition and strain in the structural and optical properties and the topic of phase segregation in $In_xGa_{1-x}N$.

The approach taken in this thesis is to integrate information provided by several complementary structural and optical characterization techniques through a systematic and multidisciplinary analysis. Specifically we combine: 1) sample growth by metal organic chemical vapour deposition (MOCVD) with specific features in an attempt to isolate the influence of structural parameters, such as layer thickness and composition; 2) Structural characterization by atomic force microscopy (AFM), scanning electron microscopy (SEM), X-ray diffraction (XRD) and Rutherford Backscattering spectrometry (RBS); 3) Optical characterisation at complementary length scales by: optical absorption (OA), photoluminescence (PL), and cathodoluminescence (CL) spectroscopy and confocal microscopy (CM) spectroscopy.

Based on the results obtained, interpretation models to describe the structural and optical features are proposed, with a particular emphasis on the establishment of direct correlations between both. It is concluded that strain-related phenomena must be taken into account to interpret the experimental results. Moreover it is also deduced that a detailed knowledge on the nanostructure is essential to explain $In_xGa_{1-x}N$ optical properties.

List of Publications

Publications directly discussed in the thesis:

[1] S. Pereira, M. R. Correia, T. Monteiro, E. Pereira, M. R. Soares e E. Alves *"Indium content determination related with structural and optical properties of InGaN layers"*, J. Cryst. Growth **230**, 448 (2001).

[2] S. Pereira, M. R. Correia, E. Pereira, K. P. O'Donnell, C. Trager-Cowan, F. Sweeney, E. Alves, A. D. Sequeira and I. M. Watson *"Depth resolved studies of indium content and strain in InGaN layers",* phys. stat. sol.(b) **228** , No.1, 59 (2001)

[3] S. Pereira, M. R. Correia, E. Pereira E. Alves L. C. Alves C. Trager-Cowan and K. P. O'Donnell" *Strain and compositional analysis of InGaN/GaN layers*" Mat. Res. Soc. Proc. **639**, G3.52 (2001).

[4] K. P. O'Donnell, J. F. Mosselmans, R.W. Martin, S. Pereira and M.E. White *"Structural analysis of InGaN Epilayers"* J. Phys. Condens. Matter, **13** 6977 (2001).

[5] S. Pereira M. R. Correia, E. Pereira K. P. O'Donnell E. Alves, A. D. Sequeira, and N. Franco "*Interpretation of double X-ray diffraction peaks from InGaN layers"* Appl. Phys. Lett. **79**, 1432 (2001).

[6] S. Pereira, M. R. Correia, T. Monteiro, E. Pereira, E. Alves, A. D. Sequeira, N. Franco "*Compositional dependence of the strain-free optical bandgap in $In_xGa_{1-x}N$ layers"* Appl. Phys. Lett. **78**, 2137 (2001).

[7] S. Pereira, M. R. Correia, E. Pereira E. Alves C. Trager-Cowan and K. P. O'Donnell "*Compositional pulling effects in $In_xGa_{1-x}N$ layers: A combined Rutherford backscattering and depth resolved Cathodoluminescence study.*" Phys. Rev. B **64**, 205311 (2001).

[8] S. Pereira, M.R. Correia, E. Pereira, K.P. O'Donnell, R.W. Martin, M.E. White, E. Alves, A. D. Sequeira and N. *Franco "Splitting of X-ray diffraction and photoluminescence peaks in InGaN/GaN layers"* Mat. Sci. Eng. B **93**, 163 (2002).

[9] S. Pereira, M. R. Correia, E. Pereira, K. P. O'Donnell, E. Alves, A. D. Sequeira, N. Franco, I. M. Watson and C. Deatcher *"Strain and composition distributions in wurtzite InGaN/GaN layers studied by reciprocal space mapping by high-resolution X-ray diffraction"* Appl. Phys. Lett. **80**, 3913, (2002); Appl. Phys. Lett. **81,** 3500 (2002).

[10] S. Pereira M. R. Correia, E. Pereira C. Trager-Cowan, F. Sweeney and K. P. O'Donnell A. Sequeira, E. Alves, N. Franco *"Structural and optical properties of InGaN/GaN layers close to the critical layer thickness."* Appl. Phys. Lett. **81**, 1207 (2002).

[11] S. Pereira, E. Pereira, E. Alves, N. P. Barradas, K. P. O'Donnell, C. Liu, C. J. Deatcher and I. M. Watson *"Depth profiling InGaN/GaN multiple quantum wells by Rutherford backscattering: The role of intermixing."* Appl. Phys. Lett. **81**, 2950 (2002).

[12] S. Pereira, M. R. Correia, E. Pereira, K. P. O'Donnell, E. Alves, N. P. Barradas, A. D. Sequeira, N. Franco, I. M. Watson, and C. Liu "*Degradation of Structural and Optical Properties of InGaN/GaN Multiple Quantum Wells with Increasing Number of Wells.*" Phys. Stat. Solidi (c) **0**, 302, (2002).

[13] S. Pereira, M. R. Correia, E. Pereira, K. P. O'Donnell, E. Alves, A D. Sequeira, N. Franco "*Interpretation of double x-ray diffraction peaks from InGaN layers (vol 79, pg 1432, 2001)"* Appl. Phys. Lett. **80** (2), 337 (2002).

[14] N. P. Barradas, E. Alves, S. Pereira, V. V. Shvartsman, A. L. Kholkin, E. Pereira, K. P. O'Donnell, C. Liu, C. J. Deatcher, I. M. Watson and M. Mayer *"Roughness in GaN/InGaN films and multilayers determined with Rutherford backscattering"* Nucl. Instr. and Meth. B **217**, 479 (2004).

[15] N. Franco, S. Pereira and A. D. Sequeira *"Absolute Scale Reciprocal Space Mapping on X-ray Diffractometers Incorporating a Position Sensitive Detector: Application to III-Nitride Alloys"* Mater. Sci. Forum **455**,132 (2004).

[16] K. P. O'Donnell, R.W. Martin S. Pereira "*Comment on Low Stokes shift in thick and homogeneous InGaN epilayers [Appl. Phys. Lett. 80, 550 (2002)*]" Appl. Phys. Lett. 81, 1353 (2002)

[17] K. P. O'Donnell, S. Pereira R. W. Martin, P. R. Edwards, M. J. Tobin and J. F. W. Mosselmans *"Wishful physics: some common misconceptions about InGaN" Phys. Stat. Sol. (a)* **195**, 532 (2003).

[18] C. J. Deatcher, C. Liu, S. Pereira, M. Lada, A. G. Cullis, O. Brandt and I. M.Watson *"In Situ Optical Reflectometry Applied to Growth of Indium Gallium Nitride Epilayers and Multi Quantum Well Structures"* Semicond. Sci. Technol. **18** 212 (2003).

Publications related to work presented in this thesis:

[19] M. R. Correia, S. Pereira, N. Pinho, T. Monteiro, E. Pereira and E. Alves "*Raman spectroscopy studies in InGaN/GaN wurtzite epitaxial films*" Mat. Res. Soc. Proc. **639**, G6.10 (2001).

[20] R. Correia, S. Pereira, E. Pereira E. Alves J. Gleize, J. Frandon and M. A. Renucci *"Indium distribution within In(x)Ga(1-x)N epitaxial layers: A combined resonant Raman scattering and Rutherford backscattering study"* Phys. Stat. Sol. (b) **228** No.1, 173 (2001).

[21] M. R. Correia, S. Pereira, A. Cavaco, E. Pereira, and E. Alves "*Preliminary investigations of infrared Er-related photoluminescence in ion-implanted* $In_{0.07}Ga_{0.93}N$" Appl. Phys. Lett. **80**, 4504 (2002).

[22] M. E. White, K.P. O'Donnell, R.W. Martin, S. Pereira, C. J. Deatcher and I. M. Watson *"Photoluminescence excitation spectroscopy of InGaN epilayers"* Mat. Sci. Eng. B **93**, 147 (2002).

[23] K. P. O'Donnell, M.E. White, S. Pereira, J.F.W. Mosselmans, N. Grandjean, B. Damilano and J. Massies "*In K-edge extended X-ray absorption fine structure of InGaN epilayers and quantum boxes*" Mat. Sci. Eng. B **93**, 150 (2002).

[24] E. Alves, S. Pereira, M. R. Correia, E. Pereira, A. D. Sequeira, N. Franco, K. P. O'Donnell, C. Trager-Cowan "*Strain relaxation and composition analysis of InGaN/GaN layers*", Nucl. Instr. and Meth. B **l90**, 560 (2002).

[25] K. P. O'Donnell, R.W. Martin, M.E. White, S. Pereira, J.F.W. Mosselmans, M.J. Tobin, N. Grandjean and B. Damilano *"Occurrence of 'accidental' InN quantum dots in Indium Gallium Nitrude/Gallium nitride heterostructures"* Mat. Res. Soc. Proc. E2.3 (2002).

[26] M. R. Correia, S. Pereira, E. Pereira, J. Frandon, M. A. Renucci, E. Alves, A. D. Sequeira and N. Franco *"Analysis of strain inhomogeneities in an $In_{0.19}Ga_{0.81}N$ layer by Raman spectroscopy"* Phys. Stat. Solidi (c) 0, **563** (2002).

[27] E. Alves, U. Wahl, M.R. Correia, S. Pereira, B. De Vries, A. Vantomme *"Annealing behaviour and lattice site location of Er Implanted InGaN"* Nucl. Instr. and Meth. B, **206**, 1042 (2003).

[28] M. R. Correia, S. Pereira, E. Pereira, J. Frandon, M. A. Renucci and E. Alves *"Raman studies of A_1 (LO) phonon mode on relaxed and pseudomorphic InGaN epilayers"* Appl. Phys. Lett. **83**, 4761 (2003).

[29] A. Kasic, M. Schubert , J. Off, B. Kuhn, F. Scholz, S. Einfeldt, T. Böttcher, D. Hommel, D. J. As, U. Köhler, A. Dadgar, A. Krost, Y. Saito, Y. Nanishi, M. R. Correia, S. Pereira, V. Darakchieva, B. Monemar, H. Amano, I. Akasaki, G. Wagner *"Phonons and Free-carrier Properties of Binary, Ternary, and Quaternary Group-III Nitride Layers Measured by Infrared Spectroscopic Ellipsometry"* Phys. Stat. Sol. **0**, 1750 (2003).

[30] M. R. Correia, S. Pereira, E. Pereira, J. Frandon, I. M. Watson, E. Alves, A. D. Sequeira, N.Franco, *"Direct Evidence for strain inhomogeneity in $In_xGa_{1-x}N$ epilayers by Raman spectroscopy"* Appl. Phys. Lett. **85**, 2235 (2004).

List of symbols

a	In-plane lattice constant of the hexagonal lattice
AFM	Atomic Force Microscopy
c	Out-of-plane lattice constant of the hexagonal lattice
CD	Compact Disk
CL	Cathodoluminescence
CLT	Critical Layer Thickness
CM	Confocal Microscopy
CW	Continuous Wave
DLP	Double Luminescence Peaks
DSR	Discontinuous Strain Relaxation
DVD	Digital Versatile Disks
DCD	Double Crystal Diffractometer
LD	Laser Diode
LED	Light Emitting Diode
ELOG	Epitaxial Lateral Overgrowth
EPMA	Elecron Probe Micro Analysis
E_g	Bandgap Energy
HDTV	High-Definition Television
HVPE	Hydride Vapour Phase Epitaxy
IR	Infrared
LCD	Liquid Crystal Display
MBE	Molecular Beam Epitaxy
MQW	Multiple Quantum Well
MOCVD	Metal Organic Chemical Vapour Deposition
MOVPE	Metal Organic Vapour Phase Epitaxy
OA	Optical Absorption
PC	Personal Computer
PL	Photoluminescence
PSD	Position Sensitive Detector
QD	Quantum Dot
RBS	Rutherford Backscattering Spectrometry
RT	Room Temperature
RLP	Reciprocal Lattice Point

RSM	Reciprocal Space Map
SEM	Scanning Electron Microscopy
SQW	Single Quantum Well
TEM	Transmission Electron Microscopy
UV	Ultraviolet
x	InN molar fraction in $In_xGa_{1-x}N$
XRD	X-ray Diffraction
3D	Two Dimensional
2D	Three Dimensional

Table of Contents

CHAPTER 3: XRD CHARACTERIZATION OF INGAN LAYERS

CHAPTER 4: RBS CHARACTERIZATION OF INGAN/GAN LAYERS

CHAPTER 5: OPTICAL CHARACTERIZATION OF INGAN/GAN HETEROSTRUCTURES

CHAPTER 6: STRAIN STATE AND COMPOSITION OF INGAN EPILAYERS

CHAPTER 8: CONCLUSIONS AND SUGGESTIONS FOR FUTURE WORK

Chapter 1: Introduction

Overview

The purpose of this introductory chapter is to establish the context and provide the necessary background to the work undertaken within the framework of this PhD thesis. The ternary semiconductor alloy, indium gallium nitride ($In_xGa_{1-x}N$) is introduced, in terms of commercial application of the nitrides. The technological significance of the development of efficient solid-state-based light emitting devices covering the visible region, and reaching into the ultraviolet (UV), of the electromagnetic spectra is highlighted. Some of the main applications opened up by the novel InGaN-based light emitting diodes (LEDs) and laser diodes (LD) are enumerated. A brief historical overview of the key breakthroughs regarding nitride semiconductor research, which have brought the nitrides from near obscurity to the headlines, is given. Moreover, some basic material physics issues that remained after commercialisation and which will be addressed throughout this research work, are introduced. Finally, the layout and objectives of this thesis are presented.

1.1 General introduction

This thesis concerns a group III-V semiconductor alloy, indium gallium nitride ($In_xGa_{1-x}N$). $In_xGa_{1-x}N$ is the active layer, i.e. the light emitting medium, in a novel class of optoelectronic devices under development, which operate in the visible and UV regions of the electromagnetic spectrum. The constituents of $In_xGa_{1-x}N$, are the binary semiconductors gallium nitride (GaN) and indium nitride (InN). x refers to the InN fraction in the alloy. Throughout this thesis $In_xGa_{1-x}N$ is usually abbreviated to InGaN, when not referring to a specific InN fraction.

The high degree of fascination about this group III-N semiconductor alloy and the motivations to study it are twofold. First, the marketability of this material system is high. InN, GaN and AlN represent a technologically important trio of semiconductors, because their direct band gaps span the range ~0.7-6.2 eV, including the visible region and extending well out into the infrared (IR) and ultraviolet (UV) range. After all, researchers are as aware as anyone else of the commercial realities embedded in scientific activity. On the other hand, beyond the interest in this group of materials for high-performance optoelectronic and electronic device applications, there is also a great fundamental scientific interest because of their unique structural and optical properties. In particular InGaN alloys represent a rather fascinating material system from the solid state physics point of view as we will have the opportunity to verify during this thesis.

This work presents a multidisciplinary experimental investigation of the structural and optical properties of InGaN/GaN epitaxial heterostructures. The emphasis will be on fundamental science, and the purpose is to provide grounds for better understanding of yet unclear physical properties. The great scientific interest of the group III-nitride semiconductors is well illustrated in a number of books [1-4], and review papers [5-11] already written on this topic. This introductory chapter provides only a brief summary.

1.2 The impact of group III-N semiconductors

Researchers fortunate enough to be currently studying group III nitrides (InN, GaN, AlN) and their alloys are directly involved in one of the more stimulating and satisfying periods of semiconductor materials research. Not only have some challenges regarding growth, characterisation and device production been overcome in a remarkably short amount of time, but commercially viable applications of nitrides are immediately clear for all to see.

In the early 1990's GaN and related compounds were obscure semiconductor materials studied by a restricted group of scientists. Today, in late 2004, GaN-based devices are prominent in our immediate environment and applications of III-nitride optoelectronics range from light emitters for full colour displays to laser diodes in high-density information storage systems. Put simply, the related applications represent a huge market. If the current upward trend in revenues continues the III-nitride market is predicted to reach about 4 billion € in 2009 according to the prediction of the authors of Ref. [12].

What a tremendous change in a period of about 14 years! Such a big bang could not have been driven by pure scientific interest alone. Applications such as blue light emitting diodes and the prospect of large revenue associated with emerging markets (the blue El Dorado!) have been the main driving force.

1.3 Why is InGaN interesting?

The basic interest in InGaN is for the development of efficient solid-state-based blue and green light emitting devices. However, to understand the technological significance of this accomplishment, we need to step back to the second part of the twentieth century and the advent of light emitting semiconductors.

The achievement of high efficiency electroluminescence from semiconductor devices in early 1962 led to the light emitting diode (LED) technology [13]. Subsequently, light amplification by stimulated emission (laser action) in a semiconductor was demonstrated [14]. Initially restricted to red light and later extended to yellow and green, LEDs were first used in wrist watches and instrument panel indicators. The development of semiconductor diode lasers in the near infra-

red allowed the production of highly coherent bright light emitters that soon found applications in telecommunications (optical fibre networks), data storage (compact disk technology), and document production (laser printers).

However, it proved initially to be very difficult to extend such light sources into the short-wavelength region of the spectrum, from blue to violet. This extension is a very important step from the technological point of view since red, green, and blue constitute the set of primary colours from which any desired emission colour can be obtained by colour-mixing, as in the *RGB* phosphor matrix of a colour-TV screen. *RGB* is an additive colour model, because it describes what amount of primary colours needs to be mixed additively to produce a given colour, as illustrated in Fig. 1.1 a).

RGB stores individual values for *R*ed, *G*reen and *B*lue. Thus, there has been a need for efficient blue and green light emitters to combine the three primary colours to obtain multicolour displays, or "white light", for a variety of applications.

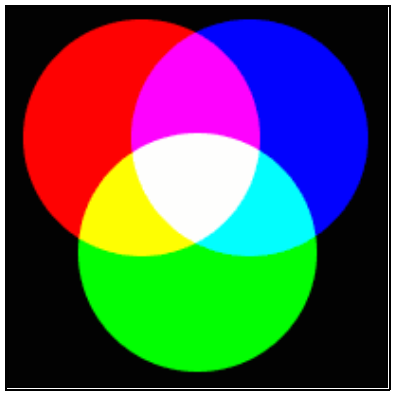

Figure 1.1: The principles of additive colour mixing.

Although successful attempts to make blue LEDs and LDs with SiC and II-VI materials (e.g., ZnSe) have been made, the utility of such devices has been small. The very low efficiency in SiC diodes, orders of magnitude less efficient than their red and yellow counterparts, and the short device lifetimes in the II-VI materials due to the relative ease of defect formation jeopardized their potential use in commercial applications. As a result, the III-V nitride materials have come to dominate the market.

In the last decade research on nitride semiconductors has allowed the commercial introduction of extremely bright LEDs and LDs. LEDs operating in the green to violet range, with efficiencies superior to those of incandescent lamps and comparable to red and yellow LEDs, and LDs emitting light in the blue-violet range were commercially introduced by Nichia

Chemical in 1994 and 1999, respectively. Both types of light emitting devices use InGaN, the material system studied in this thesis, as the active layer.

In a very short time interval, the nitrides caught up, and surpassed the competing wide band gap II-VI compounds (ZnCdSSe) as materials for short wavelength optoelectronic devices. The level of activity generated by such technological developments in the scientific community is well illustrated by the number of publications in related fields. In Fig. 1.2 the evolution of the number of GaN-related publications in the last 24 years is plotted. For comparison, a similar analysis for the II-VI semiconductors is also shown in the Figure.

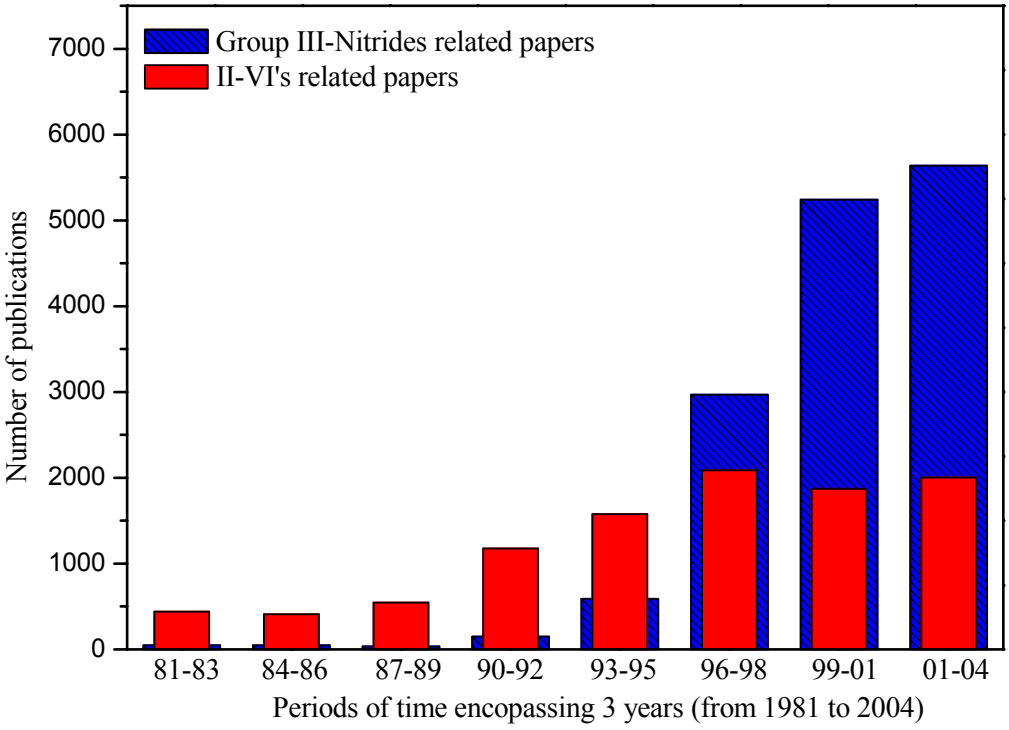

Figure 1.2: The increase in group III nitride-related publications. The data source used was ISI Web of Knowledge[1] and the results were obtained by means of topic search using the following key works; (GaN or InGaN or Gallium Nitride) for nitrides and (CdSe or ZnSe or Zinc Selenide) for II-VI materials, respectively.

In Fig. 1.2, the first notable feature is the remarkable increase of InGaN and GaN related publications, over the last 10 years. Before 1992 less than 100 publications could be found over three year periods. A sudden increase is observed from 1993 to 1995 with over 590 publications. This number increases by nearly a factor of 5 from 1996 to 1998 to about 2967 papers. The increase is smaller, but still astonishing, in the 6 last years with an increase of a factor of ~2 from 1999 to 2001 to 5241 papers and an increase that should be about 10% in the

[1] Website of ISI Web of Knowledge [SM] at: http://isi4.isiknowledge.com/

last 3 years, where over 5638 papers were published so far. The second aspect one can infer from Fig. 1.2 is the relative increase of the scientific interest compared to the most direct "competing" material system, the II-VI semiconductors, which indicates a drift of the research efforts towards nitrides.

An additional piece of information that can be obtained from the publication record is the delay between the increasing scientific interest and the technological developments. As seen in Fig. 1.2, the amount of research papers about nitrides only surpassed that related to II-VI's in 1996-1998. At that time nitride light emitting technology development was already well ahead of the II-VI based technology. This means that commercial developments were achieved without a well established scientific knowledge, leaving behind a lot of scope for fundamental physics.

Finally, Fig. 1.2 points to the difficulty of researchers to keep abreast of the scientific developments in the last few years. Along the period of this PhD, over 5600 papers have been published, just in nitride semiconductors. This represents over 35 papers/week to be read!

Let us now look at the history behind the numbers, and identify the key breakthroughs that brought nitrides from near obscurity to a position of pre-eminence.

1.4 Brief historical outlook

Clearly it was Shuji Nakamura, a relatively unknown Japanese company scientist at that time, who brought nitride semiconductors to the front pages of major scientific journals in recent years. However, III nitride research can be traced back to 1938, when the first attempts to synthesize GaN were made by Juza and Hahn by passing ammonia over gallium at high temperature (>800°C) [15,16]. That study was part of a wider effort to determine the lattice constants of families of compounds. Micron-sized GaN needles and platelets were grown by this method. In 1959 Grimmeiss *et al* used the same method to obtain small crystals of GaN on which the first photoluminescence (PL) spectroscopy measurements were taken [17].

In 1969, Maruska and Tietjen, assistants to Professor Jacques Pankove at RCA Laboratories, became the first researchers to grow epitaxial GaN on sapphire substrates using hydride vapour phase epitaxy (HVPE) [18]. The material thus produced enabled the first reliable electrical and optical evaluation of the compound. The direct optical bandgap energy of GaN was determined to be ~3.39eV at room temperature and the epitaxial material was n-type with electron concentrations typically above ~10^{19}/cm^3. Finally, Pankove *et al*. produced the first GaN-based LED at RCA labs in 1971 [19]. Unfortunately good HVPE material proved difficult to reproduce. These problems, together with difficulties in obtaining p-type material, lead to a fallow period in nitride history.

It was not until the mid-1980s that the material problems began to be overcome, due in large part to the efforts of Isamu Akasaki at Nagoya and Meijo Universities and a group led by Shuji

Nakamura at Nichia Chemical Company. The use of thin, low-temperature AlN [20] and, later, GaN buffer layers [21] facilitated the growth of high-quality GaN films, specular and free of cracks, on sapphire substrates by metal organic chemical vapor deposition (MOCVD). Simultaneously, remarkable improvements in the electrical and optical properties were demonstrated. Another important breakthrough was the successful production of p-type GaN by low-energy electron-beam irradiation (LEEBI) of magnesium-doped GaN, which in the as-grown state exhibits high resistivity [22]. As a result, the first GaN electroluminescent device based on a p-n junction was demonstrated. Subsequently, Nakamura showed that magnesium-doped GaN could be made conductive by thermal annealing in a N_2 ambient at a temperature of about 600°C [23].

On November 29th 1993, Nichia Chemical Industries announced the world's first high brightness InGaN blue LED and that it was proceeding to mass production. Nakamura produced his first blue light emitter in March 1991. Two and a half years and many improvements later, when Nichia went public with is announcement, the diodes were rated at 1 cd. At that time the LED structure was a double MQW heterostructure with InGaN wells and AlGaN cladding layers. Six months later the company announced a 2 cd. All the colours from the UV, blue, green yellow and red were eventually produced and even the generation of white light has since proven to be possible. The control of the emitted wavelength was achieved by changing the ternary alloy composition of the $In_xGa_{1-x}N$ active layer [25-28]. A selection of commercially available InGaN-based LEDs, emitting in the three primary colours, is shown in Fig. 1.3.

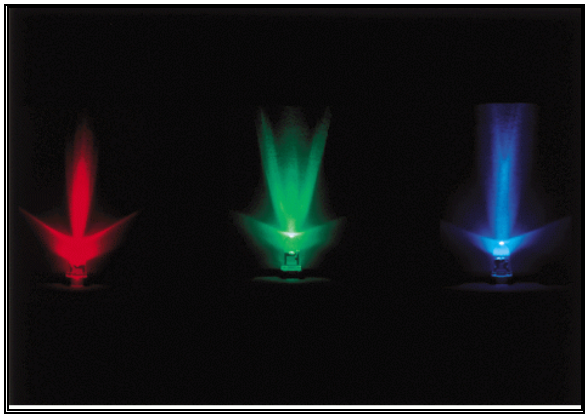

Figure 1.3: Commercial InGaN-based LEDs in the three primary colours [34].

The brightness of the luminescence was astonishing since microscopic characterization of the material revealed that the InGaN layers contained an enormous concentration of line defects ($\sim 10^{11}/cm^2$) and impurities. From these findings it might be concluded that the prospects for realizing a nitride based laser diode (LD) were not good. However, as events unfolded it was shown that this would have represented a pessimistic view.

The stimulated emission was observed from a GaN needle crystal in 1971 at 2K under optical excitation, with promisingly low threshold excitation densities [29]. The first room temperature laser emission from an epitaxial film was observed by Amano *et al.* in 1990 using optical excitation [30]. Following this, the first stimulated surface emission was produced by Khan *et al.* in 1991 [31]. Akasaki also achieved carrier and optical confinement in double heterostructure LEDs and low threshold, optically pumped stimulated emission. Both achievements, high efficiency LEDs and stimulated emission, are necessary for the realization of nitride based laser diodes.

This epochal event came to pass in early 1996 when Shuji Nakamura demostrated the first nitride based LD using an InGaN-based multiple quantum well (MQW) structure [32]. The lasing wavelength of 417 nm was the shortest yet achieved with a semiconductor laser. The first diode had a short lifetime, even under pulsed operation at low temperature, but progress was made very quickly and laser diode lifetimes soon reached 10000 hours under continuous wave (CW) operation at room temperature (RT) [33]. The drastic increase in lifetime was accomplished by introducing epitaxially laterally overgrown (ELOG) GaN which allowed the number of defects in the active region to be substantially reduced. A commercial blue LD produced by Nichia operating in CW at RT is shown in Fig. 1.4.

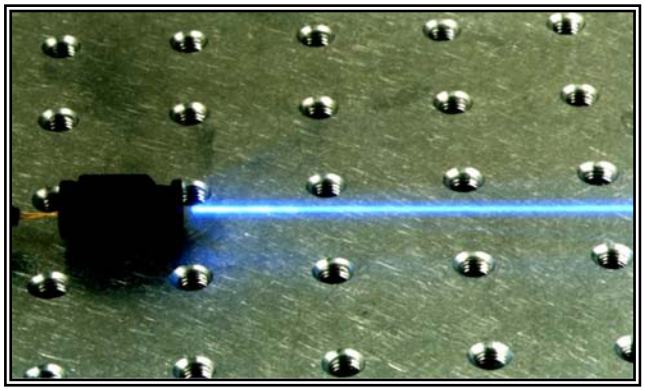

Figure 1.4: An InGaN based laser diode emitting in the blue [35].

In 1999 Nichia became the world's only commercial supplier of InGaN LDs. Presently many research groups and commercial companies including: Sony, Lumileds, AXT, Cree, United Epitaxy Lite-On, GELcore, Vishay Intertechnology, Matsushita, Stanley Electric, Epistar, OptoTech, Arima, VPEC, Nitronex, Osram Optoelectronics, Agilent, Toyoda Gosei, Uniroyal, Rohm Electronics, produce and sell InGaN-based LEDs and LDs for an increasing range of applications. In the next section we highlight some of these applications.

1.5 Some InGaN-related applications

Several areas of application for InGaN-based LEDs are already in widespread use. These include landscape lightning, outdoor displays, portable lightning, camera phone flash, entertainment televisions, full colour, high resolution, high intensity graphic displays and back-lightning of liquid crystal displays (LCD). The automotive and aircraft industries have been beneficiaries of InGaN based LEDs. Lumileds Lighting has developed the exterior lighting for luxury cars using III nitride LEDS, as well as dashboard lighting [34]. Some examples of InGaN-based LEDs in use in our immediate environment are shown in Fig 1.5.

The use of LEDs in traffic signs has been quite successful. Their reliability, robustness, and long lifetime make LEDs more convenient than conventional light sources. Another advantage is the low power consumption: an array of 120 Nichia LEDs consumes only 8.6 W compared to 70 W by an incandescent bulb typically used in traffic lights of the same visibility [36]. Companies, such as Traffic Technologies Inc., are so confident about the cost efficiency of LEDs that they have offered free LED traffic lights to every city in the USA [37]. The only condition on the offer is that the money saved in power costs is paid back for the next five years.

Figure 1.5: Several lighting applications using InGaN-based LEDs developed by Nichia Chemical [35] and Lumileds Lighting [34] companies. From upper left; landscape lightning, outdoor giant screens, solar energy powered traffic signal lights, general illumination purposes, automotive lighting, calculator and notepad backlighting.

III-nitride LEDs are also used in dentistry as a UV curing source [38], as a true blue source in colour scanners, colour facsimile machines, laser printers and computer video games, as well as multiple use display backlighting, such as in mobile phones [34].

Beyond the application of coloured LEDs, "white" lightning is probably the most significant future market of the InGaN-based LEDs industry. There are many useful applications for a compact efficient and reliable solid state white light: applications for harsh working environments, safety flash lights, bright white light sources for emergency workers and vehicles, mining operations and underwater work among may others.

Besides these applications in niche markets, the largest potential market may be that of domestic space lightning. Switching from light bulbs to LEDs reduces the energy consumption by more that 85% and brings important energy savings. Some white LEDs have already developed as night lights, flashlights, and sources of ambient lighting and for toys. But the true replacement for the ordinary white light bulb remains in the future. Considerable global development work is now underway to perfect the most practical and manufacturable ways of combining colours to create the desired hues of white LEDs, the packaging of the lamps, and producing the long-lived light sources required. When perfected, truly pure white LEDs will, indeed, replace power-hungry sources upon which we are currently dependent. When perfected and prolific, the global environment will ultimately be the real winner.

Regarding the application of InGaN based blue and UV LDs, the largest potential market is that of new optical data storage systems. In 1996 the Digital Versatile Disk (DVD) entered production. In the current technology the optical writing and reading process relies on red aluminium indium gallium phosphide (AlInGaP) semiconductor lasers, which emitt at around 650 nm. Single layer DVD has a capacity of about 4.7 gigabytes, compared with 0.65 gigabytes for Compact Disks (CDs), which use infrared aluminium gallium arsenide (AlGaAs) laser diodes, emitting at 785 nm. By moving to violet wavelengths through the use of InGaN-based compound semiconductors, the capacity can be increased to more than 27 gigabytes using a 405 nm blue-violet laser [39]. Sources with shorter wavelengths for optical recording and reading allow sharper focusing of the light, allowing an increasing storage capacity of optical disks since optical storage area densities scale as $1/\lambda^2$. Therefore, InGaN-based LDs are indispensable for next-generation DVDs known as Blu-Ray Disc (BD) [39]. This new-generation optical disc format is being jointly developed by thirteen leading consumer electronics and personal computer (pc) companies (Dell, Hitachi, HP, LG, Mitsubishi, Panasonic, Pioneer, Philips, Samsung, Sharp, Sony, TDK and Thomson). The format is being developed to enable recording, rewriting and playback of high-definition television (HDTV). Blu-ray makes it possible to record over 2 hours of HDTV, or more than 13 hours of SDTV on a 25GB disc. There are also plans for higher capacity discs that are expected to hold up to 200GB of data. As HDTV

becomes more widespread, the consumer demand for recording HDTV programming will rise. Blu-ray was designed with this application in mind and enables direct recording of the MPEG-2 TS (Transport Stream) used by digital broadcasts, which makes it highly compatible with global standards for digital television. This means that HDTV broadcasts can be recorded directly to disc without any extra processing or quality loss. Blu-ray is expected to replace VCRs and current DVD technology within a few years. The format is also likely to become a standard for PC data storage and high-definition movies in the future [39].

Besides mass-market application of InGaN based LDs, many other areas will also benefit from a compact and cheap short wavelength solid state laser diode. These include emitters to employ in integrated, ultra lightweight portable system for bio-agent warning and detection and undersea optical communication systems [24].

1.6 Some fundamental physical properties of InGaN

In this section the key InGaN physical properties, particularly those which make it useful for optoelectronic applications, are highlighted.

1.6.1 Optical bandgap

What primarily determines the photon energy (and the colour) of light emitting devices is the semiconductor bandgap (E_g) of the active region. Therefore $In_xGa_{1-x}N$ alloys are ideally suited for use in optoelectronic devices in the visible region due to their wide and tuneable bandgap, $E_g(x)$. By varying the indium/gallium ratio, determined in the alloy formula by x where $0 \leq x \leq 1$, the optical bandgap of the material can be controlled between that of GaN and InN, allowing coverage of the entire visible spectrum, from UV (GaN) to infrared (InN).

The optical bandgap of GaN is found to be ~3.39eV at RT [18,41], while the optical bandgap of InN has proved more difficult to define. A standard value of ~1.89eV has been generally accepted to be the bandgap of InN for many years [42]. However, in 2001 Inushima *et al.* determined the bandgap to be ~1.1eV from transmission measurements of MBE material [43]. This observation reopened the discussion regarding the InN bandgap. Subsequently, Davydov *et al.* calculated the bandgap to be as low as ~0.7eV, from PL measurements on single crystalline InN material [45]. More recent results, in material of better crystalline quality obtained by Wu *et al.* [47] and Nanishi *et al.* [48] indicate that the bandgap of InN should fall within the 0.6-1eV range. However, there is still some discussion regarding the exact value.

It is an important requirement for a semiconductor to be used in light emitting devices to have a direct bandgap. In a direct bandgap semiconductor, the minimum energy level in the conduction

band and the maximum energy level in the valence band occur at the same value of pseudomomentum, ***k***.

An electron in the conduction band relaxes non-radiatively to the minimum energy level of the band at ***k***=0. This electron may have been promoted either optically, by a photon with sufficient energy to bridge the gap between the valence and the conduction band, or electrically by current injection. The electron can then recombine with a hole, which relaxes to the top of the valence band, as shown in Fig. 1.6 a). Energy released during this recombination is predominantly radiative.

If the semiconductor has an indirect bandgap, such as SiC, the electrons and holes relax to energy minima at different values of ***k***. As momentum has to be conserved in band-to-band transitions, recombination is less likely to occur; phonon assisted recombination may take place whereby a phonon can provide enough momentum to allow recombination, as shown in Fig. 1.6 b). However, this recombination process relies on a suitable passing phonon (a three particle process is therefore less probable); meanwhile the electron may encounter a defect or become trapped, so that radiative emission does not occur. For this reason direct bandgap semiconductors are much more desirable for use in light emitting optoelectronic devices.

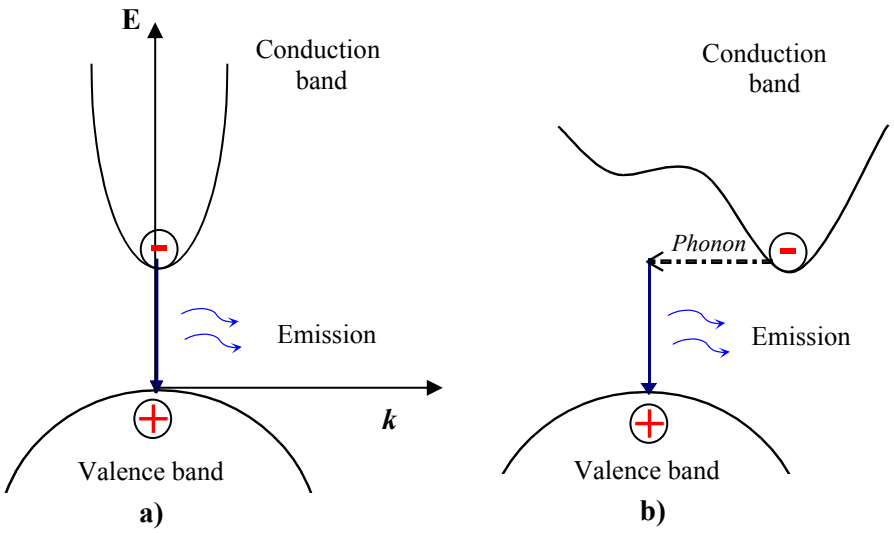

Figure 1.6: Simplified band diagram of recombination in a direct a) and indirect b) bandgap semiconductor [2].

1.6.2 Crystal structure of III-nitrides

The group III nitrides crystallise in one of three crystal structures, wurtzite (hexagonal), zinc-blende (cubic) or rock-salt. Under ambient conditions the thermodynamically stable phase is wurtzite. A phase transition to the rock salt structure takes place at high temperature. The zinc-blend structure is metastable, and may be stabilised only by heteroepitaxial growth on substrates

with topological compatibility. The wurtzite structure is the most common; it is easier to grow, and has given the better results to date in optoelectronic applications [1]. It is the crystalline structure of the samples studied in this work.

Crystallographically, the wurtzite and zincblende structures are very similar, with tetrahedral bonding to the next nearest neighbours, as shown in Fig. 1.7. The wurtzite structure has a hexagonal unit cell with two lattice parameters *a* and *c*, depicted in Fig 1.7 a). This structure is composed by two hexagonal close packed (hcp) sublattices, which are shifted with respect to each other by the amount of u=3/8 in fractional coordinates along the c-axis. Both sublattices are occupied either by group III or N atoms, resulting in four atoms per unit cell. Locally every atom is surrounded by four atoms of the other kind, which are arranged at the vertices of a tetrahedron. The symmetry of the wurtzite structure is given by the $P6_3mc$ (C^4_{6v}) space group, and the two inequivalent atom positions are (1/3, 2/3, 0) and (1/3, 2/3,u) [4]. The structure can be thought of as a sequence of layers of atoms of the same group element built up from regular hexagons [1]. The axis perpendicular to the hexagons, the c-axis, is usually the growth axis.

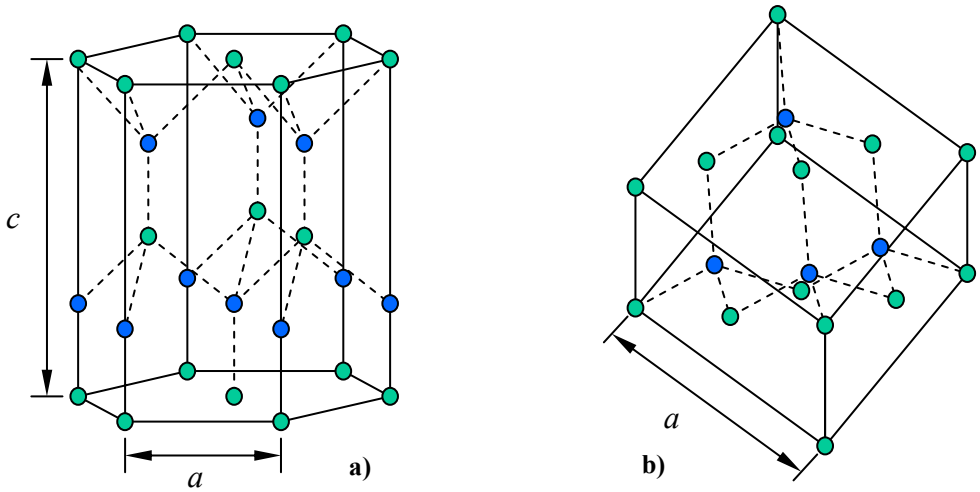

Figure 1.7: a) Wurtzite and b) Zincblende crystal structure of III-nitrides [4].

The zincblende structure consists of two interpenetrating face-centred cubic lattices (fcc) with one of the lattices displaced by 1/4 of a lattice parameter in each direction from the other sublattice. Because of the tetrahedral co-ordination of both the wurtzite and zinc-blende structures, the short range order of these structures is virtually identical. The main difference between the two structures is in the stacking sequence of the closest packed diatomic planes. For the wurtzite structure the stacking sequence of the (0001) planes is ABABAB in the <0001> direction whereas for the zinc-blende structure the stacking sequence of the (111) planes is ABCABC in the <111> direction [3]. None of the above mentioned structures has a centre of inversion. As a result of the lack of inversion symmetry, the crystal exhibits crystallographic polarity. Wurtzite nitride layers epitaxialy grown on hexagonal (0001) substrates such as

sapphire are potentially piezoelectric, and indeed become piezoelectrically active if they are under strain.

In the specific case of $In_xGa_{1-x}N$, and considering a random alloy model, the probability to find a given group III atom, say In for instance, in the respective sublattice is proportional to *x*, the InN fraction. In addition, in ternary alloys the constituent binary compounds influence the distance between the atoms. Experimental values of the lattice constants *a* and *c* in GaN are 3.189 Å and 5.185 Å [49] and in InN are 3.538 Å and 5.703 Å [50]. $In_xGa_{1-x}N$ is also expected to obey Vegard's law, whereby the lattice constant scales linearly with the composition between the two binaries [51]. However, the behaviour of the lattice constants with composition is not as simple as described, mainly due to the fact that InGaN films are usually grown in lattice mismatched GaN pseudo substrates. This issue will be discussed in detail in Chapter 6.

1.7 Scope and layout of the thesis

A literature survey reveals that much fundamental physics remains to be done on this material system, while devices can be produced following a semi-empirical approach, and without a solid knowledge on basic material science. In a very fast growing area such as nitrides the research rush to find solutions, which offer new functionality and commercial opportunities, and leaves behind several interesting opened questions and some poor understanding of InGaN nanostructure. The lack of a well established bandgap value for the InN binary, or the bandgap scaling with the InN mole fraction, are illustrative of the uncertainties and confusion regarding basic $In_xGa_{1-x}N$ material properties.

This thesis intends to clarify some of these uncertain materials physics issues through a systematic and multidisciplinary fundamental study. Let us now introduce some of the issues which were not clear at the time of starting this PhD, and whose explanation falls within the remit of this work.

1.7.1 Some key issues in InGaN research

The first essential step to understand $In_xGa_{1-x}N$ physics is the *accurate measurement of x, the alloy composition*. It should be noted that the errors involved in measuring *x* are perhaps the biggest source of confusion in the literature, since this hampers consensual establishment of the composition dependence of *any* physical property. For example, early measurements, based upon X-ray diffraction (XRD) determination of the *c* lattice constant by Nakamura, appear to overestimate the indium nitride fraction for any given emission energy [1].

Indeed it is hard to measure the InN fraction accurately. The difficulty arises from the reduced thickness of the films (as thin as a few nanometers) and the fact that InGaN films may be under

biaxial strain. We will attempt to overcome these problems, and develop methods to correctly determine the composition in InGaN/GaN heterostructures.

Provided this first obstacle is overcome the second major objective is to ascertain *the influence of composition on the structural and optical properties of InGaN.* This is a vast problem, and various open questions fall within this topic: Do InGaN alloys follow Vegards's law valid for the lattice constants? How does the InN content affect crystalline quality, surface morphology and lateral and depth uniformity of the epitaxial layers? Is there any critical composition for phase separation in InGaN?

The question of phase separation in InGaN has been highly debated in the literature. In 1996 Stringfellow *et al.* predicted theoretically that the solubility limit of InN in GaN is only about 6% [52]. Thus InGaN alloys were believed to have a tendency to phase segregate above a certain value of x. Following this theoretical prediction many works have claimed to find experimental evidence of such phase separation [53-59]. In general InGaN films above a certain composition (say, $x > 0.1$) appeared to show peculiar structural and optical features, such as double XRD or double luminescence peaks (DLP), which have been invariably ascribed to phase decomposition. Subsequently, the subject of self formed InN-rich quantum dots (QDs) in InGaN has been proposed by various authors as a possible explanation the observed light emission efficiency despite the large concentration of defects [60-62]. The issue of phase separation will be addressed in great detail throughout this thesis, and the experimental evidence available up to date critically discussed.

Another uncertainty regarding InGaN is how the optical properties, such as optical absorption and luminescence vary with the alloy composition. The establishment of a consensual value for the bowing parameter, i.e. the bandgap energy dependence on the InN mole fraction, for $In_xGa_{1-x}N$ has not been possible, and a wide range of reported values can be found in the literature [63-69]. We will investigate the reasons for disagreement and attempt to establish a reliable bowing parameter for InGaN alloys.

The last central matter to be addressed is the *understanding of the strain phenomena in InGaN/GaN epitaxial layers*. How do we define the amount of strain? What is the interrelation between strain and composition? How does the amount of strain influence the structural and optical properties? How does strain affect the XRD determined values of composition? Does strain relaxation occur continuously? Are there depth variations of strain? How does strain correlate to the overall structural and optical properties? What is the critical layer thickness (CLT) for strain relaxation in an InGaN/GaN layers? These are some of the open questions related to strain phenomena in InGaN.

1.7.2 Thesis structure

In the course of this thesis we will attempt to clarify many of the topics presented here, and others which will arise along the way to the understanding of these unclear issues. The material presented is divided into eight chapters. The present chapter has covered the motivation to study InGaN, through a historical perspective on the applications and the basic material properties.

In Chapter 2, the necessary background regarding epitaxial growth of InGaN/GaN heterostructures is provided. The principles of the MOCVD growth technique, which is the main procedure used to grow InGaN/GaN nano-structured epilayers are presented. We will also highlight some difficulties in growing high quality InGaN/GaN layers with controlled parameters. The issues of lattice mismatch between the nitride layer and the sapphire substrate, 3D islanding growth and metallic In droplet formation during growth, are discussed in this context. The basic multilayer structure of the two types of samples used: InGaN/GaN single layers and InGaN/GaN multiple quantum wells (MQWs), is described and a list of samples studied in this work is provided.

The aim of Chapter 3 is to introduce the XRD technique and illustrate its contribution to the microstructural analysis of nitride semiconductors. A brief introduction to the concepts involved in XRD is given. The emphasis is on concepts related to the application of XRD to the InGaN/GaN system. The effectiveness of the technique is illustrated directly with reference to experimental results obtained for a number of InGaN/GaN samples of increasing complexity.

Chapter 4 describes the basic principles of the Rutherford backscattering spectrometry (RBS) analytical technique, to provide necessary background for a better understanding of the structural characterisation results obtained by RBS. Some illustrative examples of the utility of RBS for structural characterization of InGaN/GaN heterostructures are given.

In Chapter 5 the basic optical properties of InGaN/GaN heterostructures are introduced. The fundamental physical principles and experimental setups of the characterization techniques used; optical absorption (OA) spectroscopy, photoluminescence (PL) spectroscopy, confocal microscopy/spectroscopy (CM) and cathodoluminescence (CL) spectroscopy with depth profiling, are described. The main characteristics of optical absorption and PL spectra for InGaN layers with different composition are discussed. It is illustrated how to obtain a systematic measurement of the alloy bandgap energy (E_g) by fitting the absorption curves to a sigmoidal expression. The CM technique is shown to be useful to study the light emitting properties, and correlate luminescence with surface morphology, at a μm length scale. The potential of CL spectroscopy with variable electron beam energy to depth profile luminescence properties in InGaN layers is illustrated.

In Chapter 6, the issues of strain and chemical composition of InGaN/GaN heterostructures are discussed in detail. These two fundamental structural properties are experimentally

characterized using XRD and RBS, introduced in the two previous chapters. We introduce the components of the strain tensor, show the interrelation between composition and strain, and critically address the methods to precisely determine these parameters in thin $In_xGa_{1-x}N$/GaN heterostructures. Also the fact that the different levels of approximation regarding the interpretation of XRD data may critically affect the result obtained for x is discussed. The importance of characterizing the layer relaxation state, by measuring the in-plane and out-of-plane lattice constants, is evidenced. A method based on the elastic theory of solids that takes into account the lattice distortion due to the effect of strain in the composition determination is presented. The important concept of critical layer thickness (CLT) of and InGaN/GaN layer is also introduced.

In Chapter 7 the information about InGaN/GaN heterostructures provided by the structural and optical characterization techniques is integrated. The optical properties are interpreted and discussed with reference to structural features, and the influence of the samples' nanostructure on measurements of the alloy optical properties is clearly evidenced.

By using RBS measured values of x, and bandgap energies extracted from optical absorption spectroscopy, the composition dependence of the alloy bandgap ($0<x<0.25$), free from the state of strain, is established. The biaxial strain effects, quantified in all samples by XRD, are taken into account to correct the bandgap of strained layers. The bandgap variation as a function of composition is discussed and compared with other results found in the literature. The optical properties of samples with particular structural properties are investigated. Given the interest in the issue of InGaN samples showing double XRD peaks, and the misinterpretations found in literature of this peculiar structural feature, the optical properties of these samples are analysed great in detail.

Finally, in Chapter 8 conclusions and some suggestions for future work are presented.

1.8 Summary

In summary, this chapter attempts to provide the basic background needed to understand the motivation to study InGaN semiconductors in the context of this PhD work.

The technological importance of the development of efficient solid state light emitting devices covering the visible spectral region was pointed out as the strongest driving force to investigate this material system. In addition, the secondary reason to study InGaN concerns its unique and rather interesting physical properties. The major breakthroughs that brought nitride semiconductors to the headlines, and triggered a dramatic increase in scientific activity were described, and a brief historical perspective was given. Some applications of InGaN based LEDs and LD's in areas such as lightning and optical storage data systems, respectively, were underlined. The fundamental physical properties of InGaN that make it an ideal semiconductor for light emitting devices in the visible region, and some of the open questions regarding basic material science, were briefly discussed. Finally, the objectives and the general layout of this thesis have been presented.

1.9 References:

[1] S. Nakamura and G. Fasol, *"The blue laser diode"*, Springer, Berlin (1997).

[2] B. Gil, ed. *"Group III nitride semiconductor compounds, physics and applications"*. Series on Semiconductor Science and Technology 6, Oxford Science Publications, Oxford (1998).

[3] B. Gil, ed. "*Low-dimensional nitride semiconductors"* Oxford University Press, Oxford (2002).

[4] J. H. Edgar, *"Gallium nitride and related semiconductors"*, No. 23 EMIS Datareview, INSPEC, London (1998).

[5] H. Morkoç, S. Strite, G. Gao, M. Lin, B. Sverdlov, and M. Burns, J. Appl. Phys. **76**, 1363 (1994).

[6] D. Steigerwald, S. Rudaz, H. Liu, R. S. Kern, W. Götz and R. Fletcher, J. of Minerals **49**, 18 (1997): http://www.tms.org/pubs/journals/JOM/9709/Steigerwald-9709.html#Steigerwald

[7] J. W. Orton and C. T. Foxon, Rep. Prog. Phys. **61**, 1 (1998).

[8] S. C. Jain, M. Willander, J. Narayan, and R. V. Overstraeten, J. Appl. Phys. **87**, 965 (2000).

[9] S. Nakamura, Science, **281** (1998).

[10] F. A. Ponce and D. P. Bour, Nature **386**, 351 (1997).

[11] T. Mukai, S. Nagahama, M. Sano, T. Yanamoto, D. Morita , T. Mitani, Y. Narukawa, S. Yamamoto, I. Niki, M. Yamada, S. Sonobe, S Shioji, K. Deguchi , T. Naitou, H. Tamaki, Y. Murazaki, M. Kameshima Phys. Stat. Sol. A **200**, 52 (2003).

[12] Robert V. Steele, Compound Semiconductor, **6**, 5 (2000).

[13] J. Black H. Lowckwood and S. Mayburg, J. Appl. Phys. **34**, 178 (1963).

[14] N. Holonyak, Jr. and S. F. Bevacqua, Appl. Phys. Lett. **1**, 82 (1962).

[15] R. Juza and H. Hahn. Z. Anorg. Allg. Chem. **239**, 282 (1938).

[16] R. Juza and H. Hahn. Z. Anorg. Allg. Chem. **244**, 133 (1940).

[17] H. Grimmesiss and Z. H-Koelmans. Z. Naturforsch Nature **14a**, 264. (1959).

[18] H. P. Maruska and J. J. Tietjen. Appl. Phys. Lett. **15**, 327 (1969).

[19] J. L. Pankove, E. A. Miller and J. E. Berkeyheiser. RCA Review **32**, 383.
(1971).

[20] H. Amano, N. Sawaki, I. Akasaki and Y. Toyoda. Appl. Phys. Lett. **48**, 353 (1986).

[21] S. Nakamura, Jpn. J. Appl. Phys. **30**, L1705 (1991).

[22] H. Amano, M. Kito, K. Hiramatsu, and I. Akasaki, Jpn. J. Appl. Phys., Part 2 **28**, L2112 (1989).

[23] S. Nakamura, M. Senoh, and T. Mukai, Jpn. J. Appl. Phys. **31**, L139 (1992).

[24] S. Nakamura, M. Senoh and T. Mukai. Jpn. J. Appl. Phys. **32**, L8 (1993).

[25] Shuji Nakamura, Masayuki Senoh, and Takashi Mukai, Appl. Phys. Lett. **62**, 2390 (1993)

[26] Shuji Nakamura, Takashi Mukai, and Masayuki Senoh, Appl. Phys. Lett. **64**, 1687 (1994)

[27] S. Nakamura, M. Senoh, N. Iwasa, S.-I. Nagahama, T. Yamada and T. Mukai. Jpn. J. Appl. Phys. **34**, L1332. (1995).

[28] Shuji Nakamura, Masayuki Senoh, Naruhito Iwasa, and Shin-ichi Nagahama, Appl. Phys. Lett. **67**, 1868 (1995)

[29] R. Dingle Appl. Phys. Lett. **19**, 5 (1971).

[30] H. Amano J. Appl. Phys. **29**, 205 (1990).

[31] M. A. Khan Appl. Phys. Lett. **58**, 1515 (1991).

[32] S. Nakamura, M. Senoh, S.-I. Nagahama, N. Iwasa, T. Yamada, T. Matsushita, H. Kiyoku and Y. Sugimoto. Jpn. J. Appl. Phys. **35**, L74. (1996).

[33] S Nakamura. Proceedings of the 2nd International conference on Nitride semiconductors, Tokushima 444 (1997).

[34] Lumileds Lighting website: http://www.lumileds.com/

[35] Nichia Corporation website: http://www.nichia.co.jp/

[36] S. J. Matthews *"Back to basics, III-V light emitting diodes, new light from old sources."* Laser Focus World, April (2001).

[37] Compound Semiconductor Press Release, *"Arizona Trafficlight Technologies Inc. offers free traffic signals to every US city"*, July (2000).
http://compoundsemiconductor.net/articles/news/4/7/41/1.

[38] R. W. Mills and K. D. Jandt. *"Blue LEDs for curing polymer-based dental filling materials."* IEEE, LEOS Newsletter, June (1998).

[39] Blu-ray Disc website : http://www.blu-ray.com/

[40] S. Nakamura. Semicond. Sci. Technol. 14, R27. (1999).

[41] H. Amano, M. Kito, K. Hiramatsu and I. Akasaki, Jpn. J. Appl. Phys. **28**, L2112 (1989).

[42] B. Gil and M. Leroux, *Properties of Indium Nitride*, EMIS Datareview 23 (1999).

[43] T. Inushima, V. V. Mamutin, V. A. Vekshin, S. V. Ivanov, T. Sakon, M. Motokawa and S. Ohoya, J. Cryst. Growth **227-228**, 481 (2001).

[44] T. Inushima, T. Yaguchi, A. Nagase, A. Iso and T. Shiraishi, Inst. Phys. Conf. Ser. No. **142**: Chapter 5, 971 (1995).

[45] V. Yu. Davydov, A. A. Klochikhin, V. V. Emtsev, S. V. Ivanov, V. V. Vekshin, F. Bechstedt, J. Furthmüller, H. Harima, A. V. Mudryi, A. Hashimoto, A. Yamamoto, J. Aderhold, J. Graul and E. E. Haller, phys. stat. sol. (b) **230**, R4 (2002).

[46] V. Yu. Davydov, A. A. Klochikhin, R. P. Seisyan, V. V. Emtsev, S. V. Ivanov, F. Bechstedt, J. Furthmüller, H. Harima, A. V. Mudryi, J. Aderhold, O. Semchinova and J. Graul, phys. stat. sol. (b) **229**, R1 (2002).

[47] J. Wu, W. Walukiewicz, K. M. Yu, J. W. Ager III, E. E. Hailer, H. Lu, and W. J. Schaff, Appl. Phys. Lett. **80**, 4741 (2002).

[48] Y. Nanishi *et al.,* Invited communication at the EMRS spring meeting, **LII.6**, (2004).

[49] T. Detchprohm, K. Hiramatsu, K. Itoh and I Akasaki, Jpn. J. Appl. Phys. **31**, L1454 (1992).

[50] W. Paszkowicz, Powder Diffraction **14**, 258 (1999).

[51] L. Vegard, Z. Phys. 5, **17** (1921).

[52] I. Ho and G. B. Stringfellow, Appl. Phys. Lett. **68**, 2701 (1996).

[53] R. Singh, D. Doppalapudi, T. D. Moustakas, and L. T. Romano, Appl. Phys. Lett. **70**, 1089 (1997).

[54] D. Doppalapudi, S. N. Basu, K. F. Ludwig , and T. D. Moustakas, J. Appl. Phys. **84**, 1389 (1998).

[55]N. A. El-Masry, E. L. Piner, S. X. Liu and S. M. Bedair, Appl. Phys. Lett. **72**, 40 (1998).

[56] Yong-Tae Moon, Dong-Joon Kim, Keun-Man Song, In-Hwan Lee, Min-Su Yi, Do-Young Noh, Chel-Jong Choi, Tae-Yeon Seong, and Seong-Ju Park, Phys. Stat. Sol. (b) **216**, 167 (1999).

[57] D. Rudolff, Phys. Stat. Sol. (b) **216**, 315 (1999).

[58] Z. Liliental-Weber, M. Benamara, J. Washburn, J. Z. Domagala, J. Bak-Misiuk, E. L. Piner, J. C. Roberts, S. M. Bedair, J. Electr. Mat, **30** (4), 439 (2001).

[59] E. Zielinska-Rohozinska, J. Gronkowski, M. Regulska, M. Majer, K. Pakula, Cryst. Res. Technol., **36** (8-10), 903 (2001).

[60] S. Chichibu, T. Azuhata, T. Sota and S. Nakamura, Appl. Phys. Lett. 69, 4188 (1996).

[61] Y. Narukawa, Y. Kawakami, M. Funato, S. Fujita, S. Fujita and S. Nakamura, Appl. Phys. Lett. 70, 981 (1997).

[62] K. P. O'Donnell, R. W. Martin and P. G. Middleton, Phys. Rev. Lett. 82, 237 (1999).

[63] L. T. Romano, B. S. Krusor, M. D. McCluskey and D. P. Bour, K. Nauka, Appl. Phys. Lett. 73, 1757 (1998).

[64] C. Wetzel, T. Takeuchi, S. Yamaguchi, H. Katoh, H. Amano and I. Akasaki, Appl. Phys. Lett. **73**, 1994 (1998).

[65] C. A. Parker, J. C. Roberts S. M. Bedair, M. J. Reed, S. X. Liu, N. A. El-Masry and L. H. Robins, Appl. Phys. Lett. **75**, 2566 (1999).

[66] F. B. Naranjo, M. A. Sanchez-Garcia, F. Calle, E. Calleja, B. Jenichen, and K. H. Ploog, Appl. Phys. Lett. **80**, 231 (2002).

[67] S. F. Chichibu, M. Sugiyama, T. Kuroda, A. Tackeuchi, T. Kitamura, H. Nakanishi, T. Sota, S. P. DenBaars, S. Nakamura, Y. Ishida, and H. Okumura, Appl. Phys. Lett. **79**, 3600 (2001).

[68] L. Bellaiche, T. Mattila, L.-W. Wang, S.-H. Wei, and A. Zunger, Appl. Phys. Lett. **74**, 1842 (1999).

[69] M. Ferhat, J. Furthmuller, and F. Bechstedt, Appl. Phys. Lett. **80**, 1394 (2002).

Chapter 2: Growth, sample structure and morphology of InGaN/GaN layers

Overview

This chapter provides the basic background regarding epitaxial growth of the InGaN/GaN heterostructures studied in this thesis. The principles of the MOCVD growth technique, and the main procedures used to grow the InGaN/GaN nano-structured epilayers are presented. A brief description of Molecular Beam Epitaxy (MBE), which is an alternative method to grow InGaN/GaN heterostructures, is also given.

We highlight some difficulties in the growth of high quality InGaN/GaN layers with controlled parameters. The issues of lattice mismatch between the nitride layer and the sapphire substrate, three-dimensional (3D) islanding growth and metallic In droplet formation during growth, are discussed in this context.

The importance of growing a GaN buffer layer in order to accommodate strain, obtain a planar two-dimensional (2D) growth and reduce the dislocation density is evidenced. The main steps performed during the MOCVD growth of InGaN/GaN heterostructures, and the *in situ* optical reflectometry monitoring technique used to control the structural parameters during growth are presented. Finally, the basic multilayer structure of the two types of samples used: InGaN/GaN single layers and InGaN/GaN multiple quantum wells (MQWs), is described and a list of the samples studied in this work is given.

2.1 Introduction

Growth of InGaN/GaN heterostructures of good uniformity and high crystalline quality is essential for device production and for basic characterisation purposes. This task has proven to be very challenging, particularly when high indium concentrations are required. High melting temperatures and dissociation pressures are the main obstacles to the production of large single crystals of III-N compounds which could serve as substrates for *homoepitaxial* growth. Consequently crystalline films have to be grown *heteroepitaxially* onto substrates that do not match in terms of lattice constants and thermal expansion coefficients.

In this chapter, the very basic principles related to growth of InGaN/GaN heterostructures are presented. Growth of nitrides is a rather complex issue and a detailed description is beyond the scope of this work. Further details on the growth techniques, procedures, alternative methods

and recent advances on the field, can be found in some of the books and review works published in the literature [1-7].

2.2 InGaN growth techniques

The two growth techniques typically used to produce InGaN are MOCVD and MBE. However, MOCVD is more suitable for high-volume production for III-N semiconductors for two reasons: higher throughput (lower cost) and demonstrated superior material quality [8]. The structure of the InGaN samples can take a variety of different forms. The InGaN active layer may be grown as a single film on GaN (epilayer), sandwiched between GaN barriers (QW) or on the form of self-assembled quantum dots (QD).
A general description of the MOCVD growth technique used to produce the samples investigated in this work and a brief reference to MBE, which is an alternative method to grow InGaN layers, is outlined in the following sections.

2.2.1 Metal Organic Chemical Vapour Deposition

The use of metal organic vapour phase epitaxy (MOVPE), and in particular MOCVD, underwent great advances during the 1980's for the preparation of high purity epitaxial layers of a wide range of semiconductor materials. The pioneering work of Manasevit *et al.* [9,10] gave rise to the remarkable interest subsequently shown in processes that use metal-organic compounds for the production of semiconductor materials. MOCVD is an accepted production technique yielding novel electronic and optoelectronic devices [11-15], and has been the most commonly used method for the epitaxial growth of device quality III-Nitride materials [3].
The elements required for MOCVD growth are produced by the thermal decomposition of source gases on a heated substrate. This process requires organometallic source materials (precursors) of high purity, whose decomposition leads to the production of the desired III-nitride material, such as InGaN. Typically, the precursors for the InGaN production are:

1) Trimethylgallium, TMGa ($Ga(CH_3)_3$), that provides gallium and is stored as a liquid.

2) Trimethylindium, TMIn ($In(CH_3)_3$), that provides indium and is stored as a solid or as a liquid suspension.

3) Ammonia, (NH_3), that provides nitrogen.

The TMGa and TMIn are taken from the bubbler by means of a carrier gas, such as hydrogen (H_2) or nitrogen (N_2), to the substrate, which is held in a reaction chamber. Ammonia is introduced directly into the chamber from a separate gas cylinder. The reagents are then dissociated in the reaction chamber and deposited onto the substrate. The susceptor is used to transfer heat to the substrate through conduction or radiation. A diagram of a typical MOCVD growth reactor system is shown in Fig. 2.1.

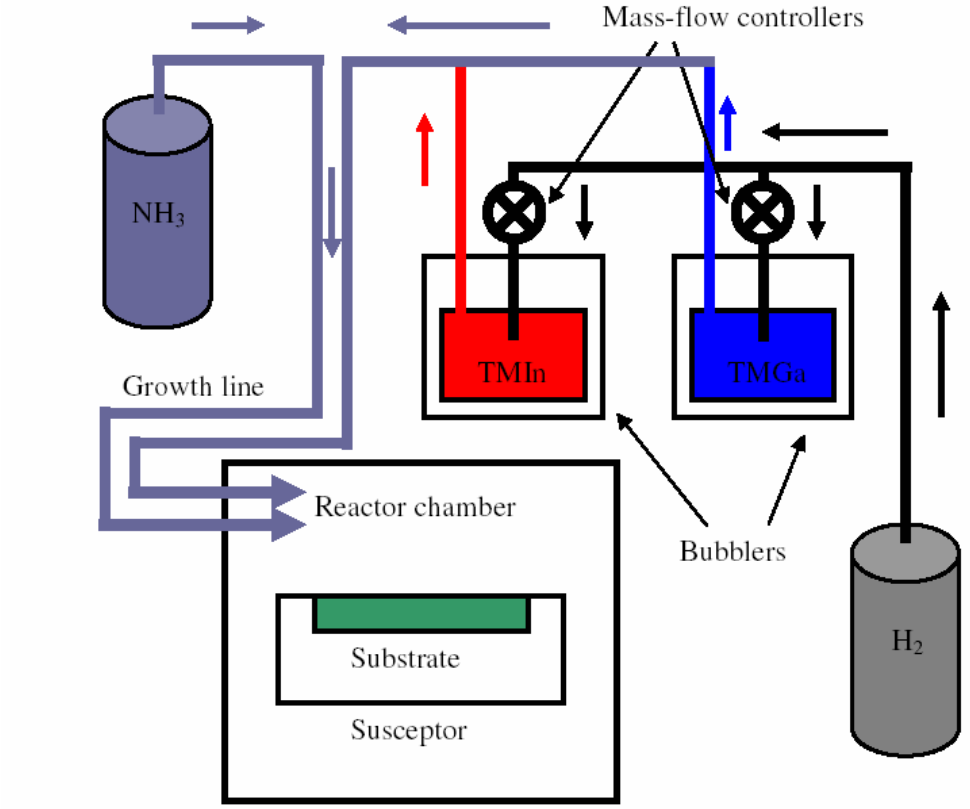

Figure 2.1: Schematic diagram of a MOVCD growth reactor used to grow InGaN/GaN heterostructures.

A number of modifications have been applied to the MOCVD process to improve the quality of the InGaN material produced. Two of the most successful techniques that have been applied are the use of showerheads [20] and the two-flow growth process [1]. Showerheads are used to prevent pre-reaction of the reagents in the reaction chamber, and the two flow growth process has, in addition to the main gas flow parallel to the substrate, another subflow perpendicular to the substrate.

The stoichiometric expression describing GaN growth is as follows [3]:

$$Ga(CH_3)_3 + NH_3 \rightarrow GaN + 3\ CH_4 \qquad \text{(Eq. 2.1)}$$

In the case of InGaN growth, the stoichiometric expression is:

$$x*In(CH_3)_3 + (1-x)*Ga(CH_3)_3 + NH_3 \rightarrow In_xGa_{(1-x)}N + 3\ CH_4 \qquad \text{(Eq. 2.2)}$$

However, the concentration of the growing species required in the reactor to grow $In_xGa_{1-x}N$ does not correspond to the stoichiometric expression (Eq. 2.2).

One of the problems found in the growth of device quality nitride layers is that the ammonia is a very stable molecule and its dissociation efficiency is low. In order to maintain the solid stoichiometry in the grown film, very high ammonia partial pressure in the growth ambient is required, to avoid the formation of nitrogen vacancies [16]. Keller *et al.* in Ref. [17], reported that an extremely high V/III ratio is required to prevent the formation of In droplets in the surface of the epilayers, obtaining values of NH_3/TMIn ratios around 20000 for InGaN films grown at approximately 770 ^{0}C.

The substrate temperature, V/III ratio, gas flow rate and even the type of carrier gas have been found to influence the material growth [2,3]. Problems encountered in producing MOCVD InGaN include the difficulty of incorporating indium and nitrogen into the material. The volatility of indium above ~1000ºC limits the upper growth temperature that can be used [19], while the temperature must also be low enough to stop indium droplets forming on the surface. The difficulty of controlling In incorporation is illustrated in Fig. 2.2 where the appearance of metallic In droplets on the surface of an InGaN/GaN heterostructre (S225E) is shown.

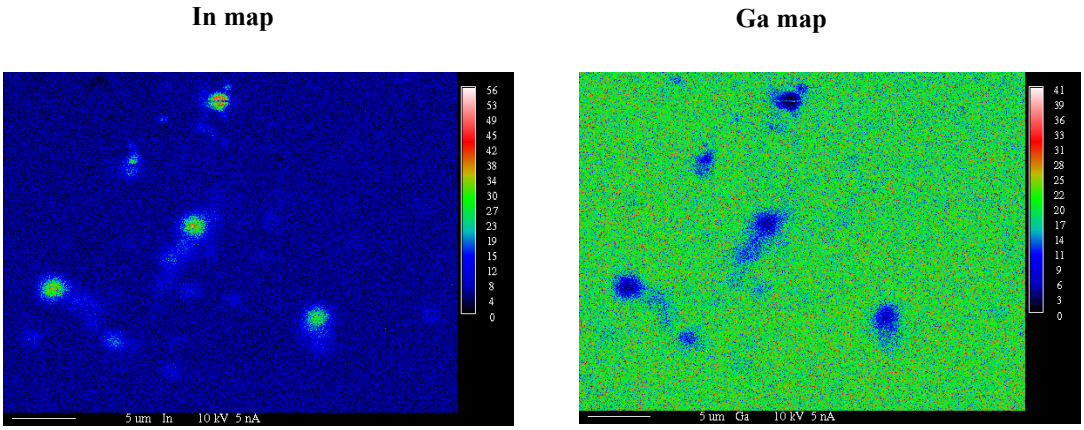

Figure 2.2: Chemical map of an InGaN/GaN single layer (S225E) showing metallic In droplets.

The Ga and In maps obtained by electron probe microanalysis (EPMA)[1] show complementary between In-rich/In-poor regions which appear on the sample surface over a μm length scale, evidencing the presence of metallic In at the surface.

[1] EPMA is a non-destructive analysis technique that can be used to determine compositional information, with a spatial resolution on order of 1μm. The EPMA works by bombarding materials with a focused electron probe beam and analysing the X-ray photons emitted by the various elements in the material, as the wavelengths of X-ray lines are characteristic of the emitting species; the material composition can be identified.

Using nitrogen, as opposed to hydrogen, as the carrier gas has also been found to reduce In droplet formation [3]. The issue of In droplets on InGaN will be further discussed concerning interpretation of X-ray diffraction from InGaN layers in Section 3.9.1.2

2.2.2 Molecular Beam Epitaxy

MBE growth is, at its simplest, a refined form of ultrahigh vacuum (UHV) evaporation [1]. Although well established for the growth of semiconductors since its invention in 1958 [22], the development of MBE for the III-nitrides has been slow. This is mainly because the low growth temperatures involved make it difficult to incorporate nitrogen into the growing layer.
The source elements are evaporated in Knudsen cells. The atoms or molecules are then directed onto a heated substrate where they react to form the layers. Figure 2.3 shows a schematic diagram of a MBE growth system [20], where some typical features of MBE are also sketched: the Beam Equivalent Pressure (BEP) gauge, to measure the growth rate of the layers, the Reflection High-Energy Electron Diffraction (RHEED), that is a growth control technique and the Continual Azimuthal Rotation (CAR), a rotational magnetic holder where the samples are mounted.

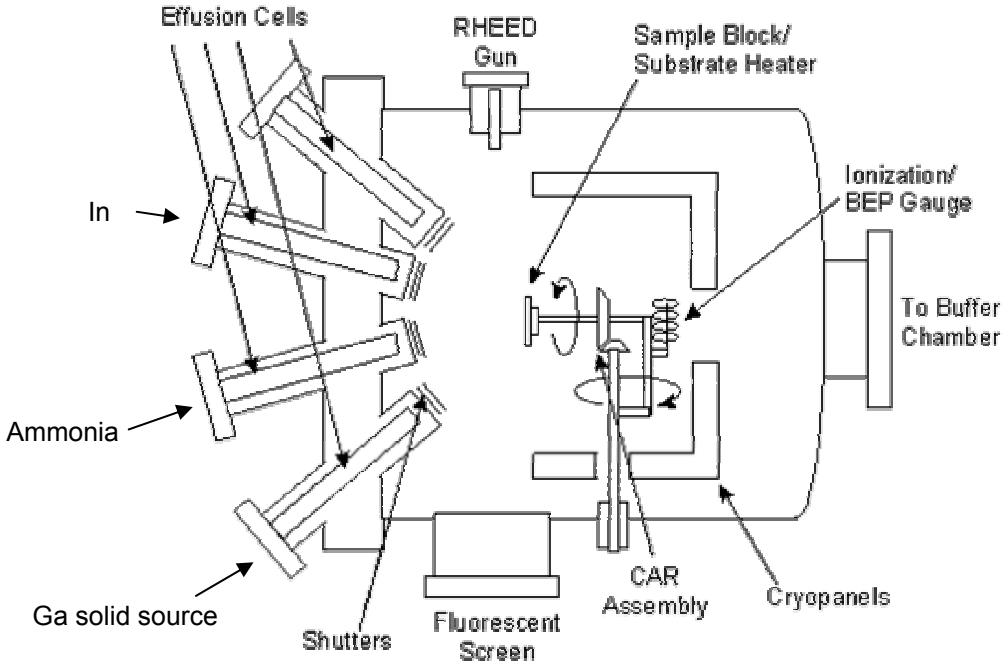

Figure 2.3: A typical III-nitride MBE growth reactor system [21].

For InGaN growth, solid sources are often used for the Ga and In supply. However, due to the extremely high binding energy of the N_2 molecule, nitrogen cannot be supplied directly and is provided in the form of ammonia. InGaN MBE growth can be performed at much lower

temperatures than MOCVD, typically ~600°C. This suits the conditions required to incorporate indium into the material. Furthermore, the UHV environment reduces the level of background contamination in the growth chamber. The UHV also makes possible the use of in-situ electron-beam characterisation. Techniques such as RHEED can be used to monitor the evolving surface structure of the material and to determine its composition [23].
In summary, when applied to InGaN, MOVPE makes high quality material with low In content, while MBE is more suitable for high-In alloys, which may however be defective.

2.3 Substrate and lattice mismatch issues

Considering that bulk GaN is not widely available, the main problem for growing nitride semiconductor films in general, is the lack of a suitable substrate that matches their lattice constants and thermal-expansion coefficients. Several substrates have been tried: Sapphire (Al_2O_3), SiC, Si, ZnO MgO, GaAs, and GaP, among others. Sapphire and SiC are the most commonly used. Sapphire is an insulator with obvious disadvantages in terms of carrier injection. SiC is better in terms of lattice parameters and expansion coefficients difference and it is conductive, meaning less steps in device processing. Major disadvantages of SiC are, lack of an appropriate chemical etch for the surface, and high cost.
Despite the several alternative substrates proposed [2-6], sapphire remains favoured because of its low price, transparency, availability in large area crystals of good quality, stability at high temperatures and a mature growth technology. However, sapphire has very large lattice and thermal expansion coefficient mismatches. Note that although different substrate orientations have been tried, the most commonly used is the (*0001*). The epitaxial relation in this case is such that:

(0001) GaN // (0001) Sapphire and (01-10) GaN // (-2110) Sapphire

corresponding to a 30º rotation of the crystal axis of GaN relatively to those of sapphire in the basal plane. In this case, the apparent lattice mismatch is ~14%, which is still huge[2]. The lattice mismatch and the relative orientation between the GaN and sapphire lattices are illustrated in Fig. 2.4. The lattice mismatch results in large strain between the substrate-layer interface with an inevitable propagation of dislocations and 3D growth. Figure 2.5 illustrates the growth of a rough 3D GaN layer directly on sapphire.

[2] Note that the in-plane lattice parameter of GaN (a_{GaN}=3.189 Å) is approximately 33% smaller than sapphire ($a_{sapphire}$=4.758 Å). However, since there is a 30º rotation of the GaN lattice, which is grown into the oxygen sublattice, there is a reduction of the in-plane lattice mismatch to about 14%.

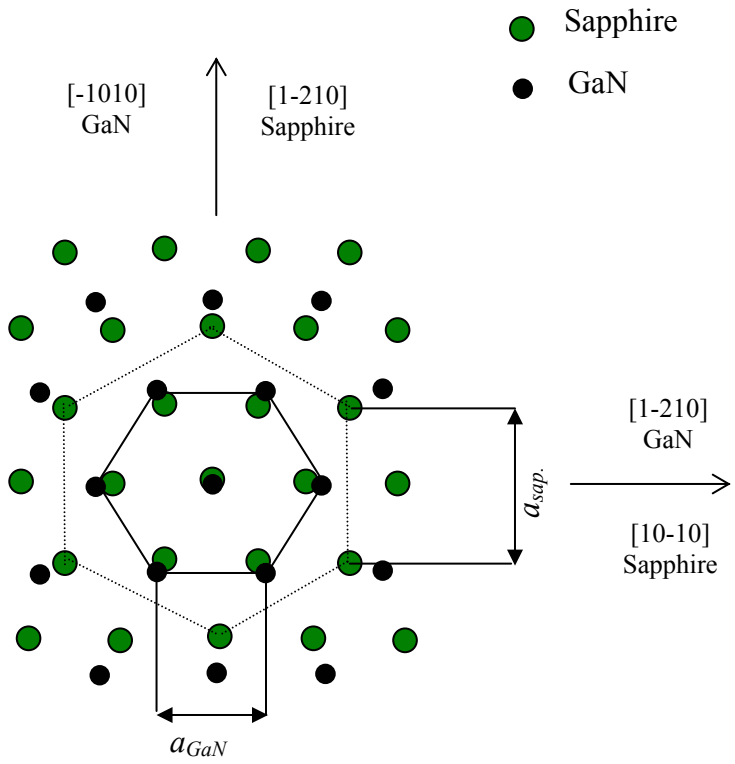

Figure 2.4: Schematic representation of GaN grown onto sapphire (0001) surface showing the lattice mismatch and relative orientation between the layer and the substrate lattices.

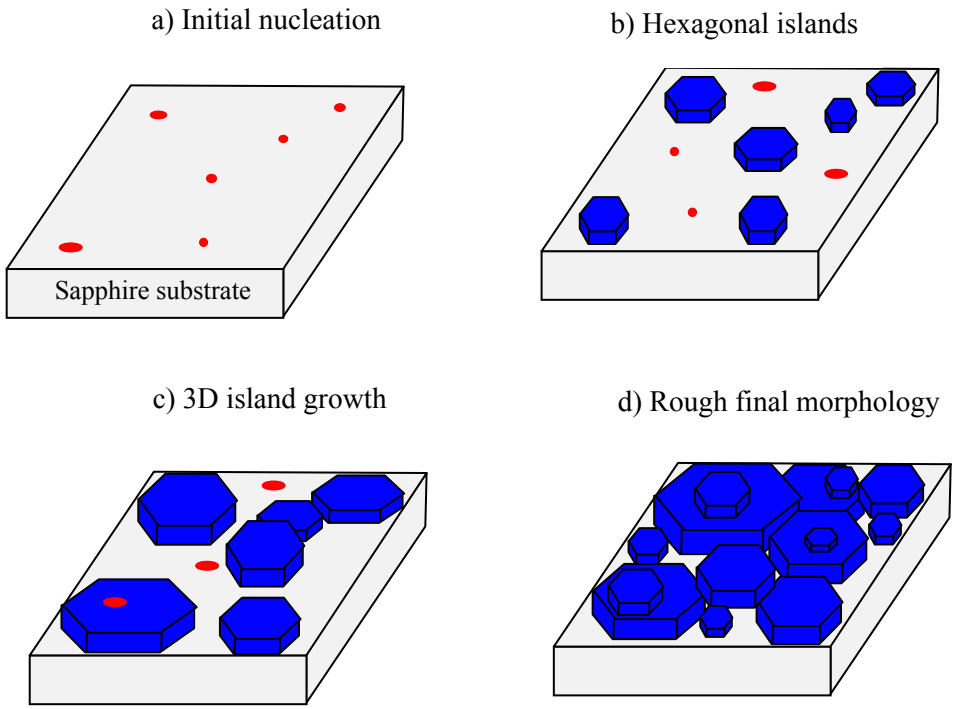

Figure 2.5: Mechanism of hexagonal island growth leading to a rough 3D surface. The GaN layer is grown directly on a sapphire substrate [2].

2.3.1 Buffer layer

Trying to overcome the problems of lattice mismatch and 3D growth, in the mid 1980's the Japanese research group led by I. Akasaki introduced the *two-step* MOCVD process on a *c*-plane sapphire substrate. They grew a thin (~200Å) AlN buffer layer at low temperature followed by a high-temperature thick layer of GaN. Mirror-like GaN films with improved optical and electrical properties were thus obtained [25]. The use of a thin buffer layer was found to enhance the two-dimensional nucleation and a layer by layer growth mechanism could be achieved. In early 1990, Nakamura and co-workers at Nichia Chemical Company[3] used a similar approach in which a GaN buffer layer was grown at low temperature as an accommodation layer [26].

The principle of the buffer layer is illustrated in Fig. 2.6. When the main GaN layer is grown onto a buffer, due to the reduced interfacial energy between GaN and its buffer (compared to GaN/Al_2O_3) a high density of nucleation is obtained, as shown in Fig. 2.7 a). Then the nuclei grow to small hexagonal islands, as in the case of GaN grown directly on sapphire, Fig. 2.5 b) and Fig. 2.7 b).

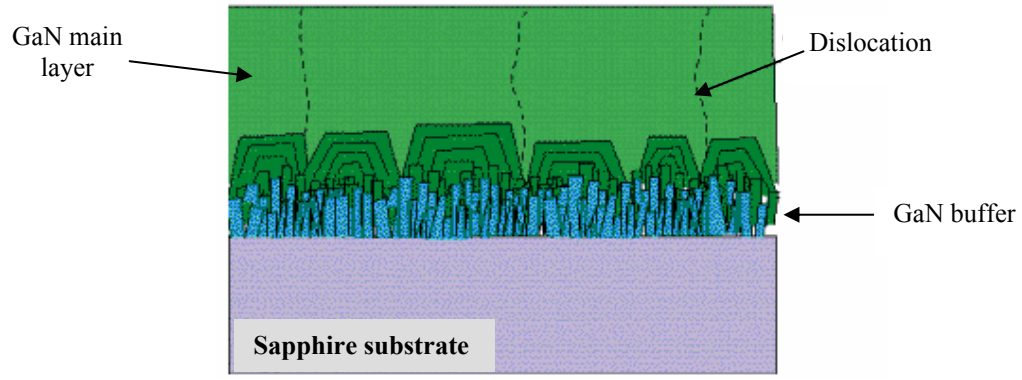

Figure 2.6: This figure shows the principle of a buffer layer, initially proposed by Akasaki *et al.* [25] and used by Nakamura *et al.* [26], to grow GaN with good quality on a sapphire substrate despite the very large lattice mismatch. The buffer layer is normally grown at lower temperatures than the main layer.

However, at an early stage of the island growth the lateral growth mode is enhanced. The islands expand laterally, and coalescence occurs rapidly Fig 2.7c). The final result is a 2D smooth film, as depicted in Fig. 2.7 d), as opposed to the rough 3D like film obtained in the case of GaN grown directly on sapphire as seen in Fig. 2.6 d).

[3] Visit Nichia website at: http://www.nichia.com/

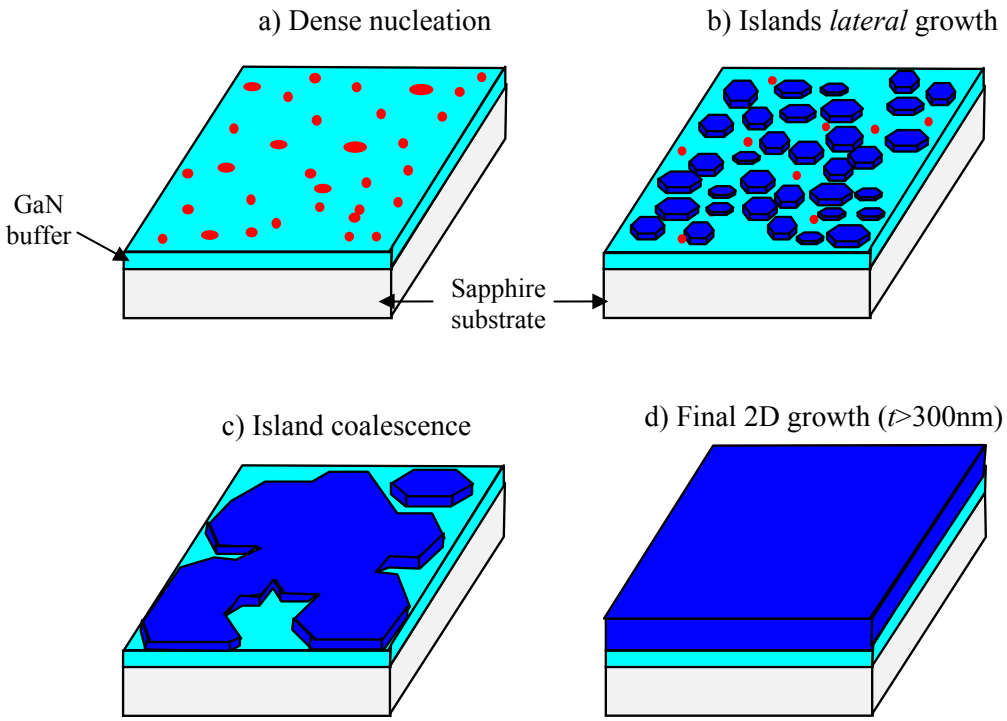

Figure 2.7: Mechanism of hexagonal islands coalescence, leading to a 2D growth for GaN grown on a buffer layer.

The improvement of the GaN quality when using a buffer layer in terms of optical properties, crystalline quality, electrical properties is notorious [6]. However, despite these improvements, the nitride layers are still of relatively poor quality.

As mentioned, a GaN layer grown on sapphire experiences a compressive biaxial strain upon cooling down leading to an in-plane lattice parameter reduction of the GaN films grown onto sapphire and a tensile stress along the crystal *c*-axis. The strain depends on the substrate used. For instance, if SiC is used as substrate, GaN grown onto SiC undergoes tensile strain, due to the difference in thermal expansion coefficients of GaN and SiC. The strain due to the lattice mismatch is typically relieved by the generation of dislocations.

The GaN films grown by MBE show dislocation densities in the range between ~$1x10^9$ and $1x10^{10}$ cm^{-2} [1]. This number is lower if the growth mechanism is MOCVD, with values around ~$1x10^8$-$1x10^9$ cm^{-2}[2]. The number of dislocations is more reduced using techniques such as lateral epitaxial overgrowth (LEO). This technique consists in the growth of GaN horizontally over silica stripes previously deposited onto GaN layer. A subsequent growth of GaN on such structure leads to a lateral GaN overgrowth over the silica stripes. This material presents a lower dislocation density in the order of $2x10^7$ cm^{-2}, and superior optical properties [27,28].

2.4 Growth procedures

The MOCVD reactor specifically used to carry out the growth of most of the samples characterized in this thesis is an Aixtron[4] AIX 200/4 RF-S reactor [17], installed at the Institute of Photonics (IOP), University of Strathclyde[5]. It is a single-wafer, horizontal-flow reactor. Some features of this reactor include a pyrometer for temperature control, and a reagent separation plate at the inlet of the reactor. The purpose of the separation plate is to prevent pre-reaction of the group III sources and ammonia, which could otherwise cause particle formation in the gas phase. Other features incorporated in this reactor are RF induction heating and *in-situ* monitoring using optical methods, to obtain information on the structures growing structure in real time [29].

2.4.1 Description of the growth steps

Since the quality of the epilayers has been shown to be greatly improved, the two step procedure has now become a standard method for the III–nitride growth by MOVPE. Here we describe the growth process and identify the main growth steps in the MOVCD growth of an InGaN/GaN/Al_2O_3 heterostructure.

a) *Substrate pre-treatment*: the Al_2O_3 substrate is heated at elevated temperatures (above 1000ºC) to reorganise and improve its surface.

b) *Buffer layer deposition:* after the pre-treatment, the substrate is cooled to a temperature between 500 and 800 ºC at which point deposition of a GaN buffer occurs. In this work a GaN buffer ~20nm thick was grown at 540 ºC.

c) *Buffer layer heat treatment:* since the crystalline quality of the as-grown buffer layer is very poor, a "recrystallization" heat treatment is performed at around 1000 ºC.

d) *Growth of the high quality GaN layer.* Note that this GaN layer acts as the InGaN pseudo-substrate. The typical thickness of this layer is about 1μm the growth temperature around 1150 ºC and the growth rate is of the order of 1μm/h. This layer is grown under a hydrogen ambient.

[4] See more details at: http://www.aixtron.com/
[5] Visit the IOP webpage at: http://www.photonics.ac.uk/research/nitrides.html

e) InGaN Growth.

-*Epilayers.* InGaN layers were grown in nitrogen ambient at temperatures between 760 and 832ºC, with thickness of 50-400nm, depending on the growth conditions. InGaN layers growth rates are about 100 nm per hour.

-*MQWs.* In MQW structures growth was interrupted during temperature ramps between the nucleation and buffer layers and the first InGaN well. The InGaN well and GaN barrier were subsequently grown at a constant temperature, without any further interruptions.

In Fig. 2.8 the main growth steps and the correspondent temperature variation are depicted. The pressure for all growth steps was $2x10^4$ Pa.

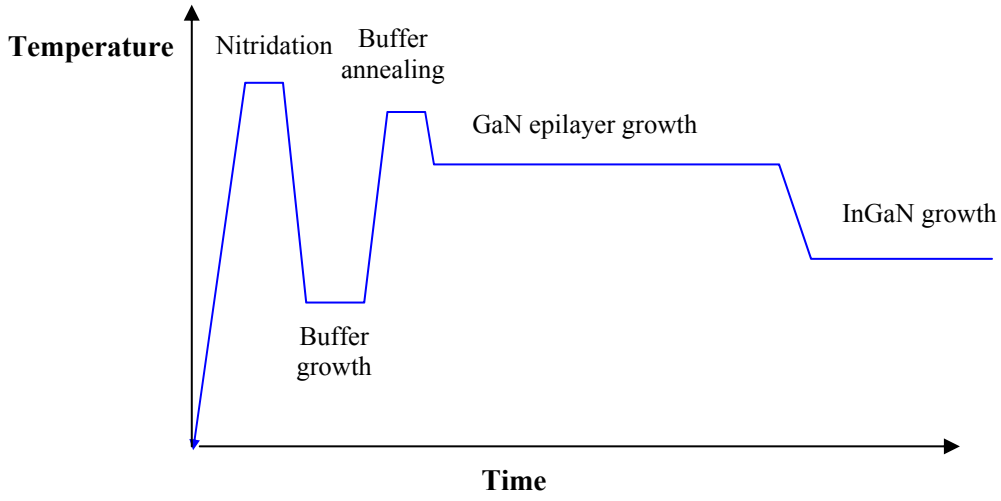

Figure 2.8: Sketch of the double-step process and the various steps of the growth sequence.

All MOCVD III-N layers are non-intentionally doped and InGaN layers grown under these conditions have colours ranging from light yellow to brown, depending on their indium content and thickness. The InN content of InGaN structures usually ranges from around 0.05 to 0.30. We have attempted to grow MOCVD epilayers with InN content higher than approximately 0.40, which resulted in samples with gross lack of homogeneity, with variations of InN content visible on a macroscopic scale. This work has been published in [28,30].

2.5 Typical sample structures

Concerning the samples grown, two types of sample structures feature prominently in this thesis; single InGaN layers and samples containing multiple quantum wells, where thin InGaN layers are sandwiched between GaN layers. In the case of one quantum well, the structure is called a single quantum well (SQW) in the case of more than one well it is called multiple quantum well (MQW). A diagram depicting the general multilayer structure of single InGaN layers and a InGaN/GaN 4-well MQW structure is show in Fig. 2.9.

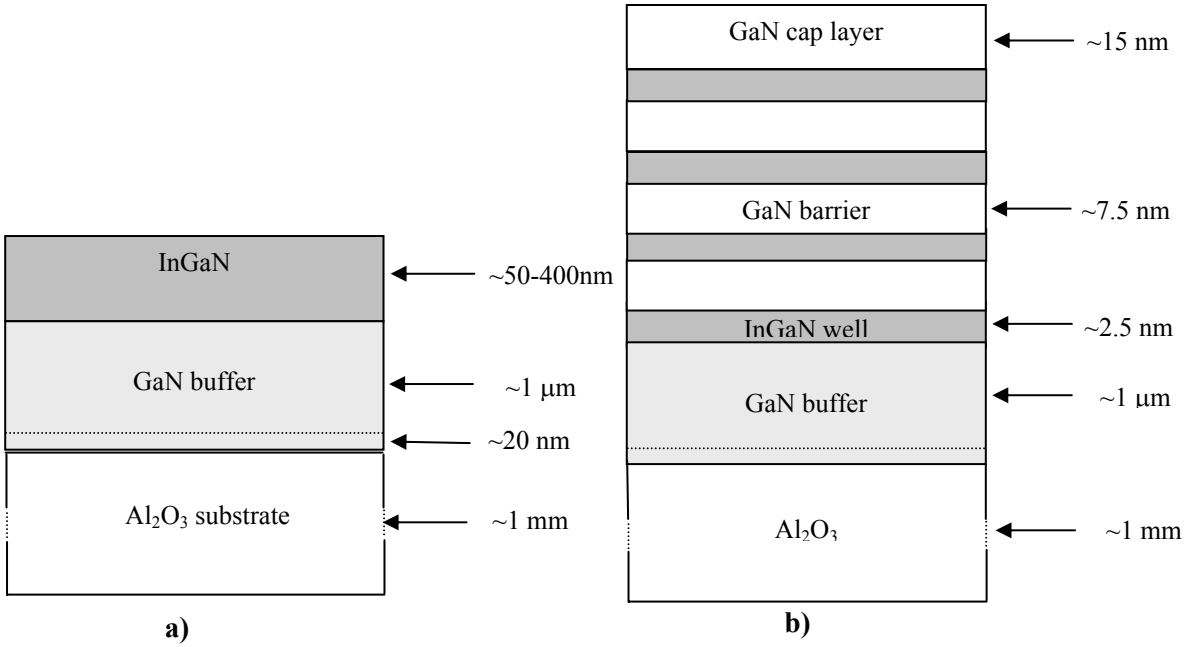

Figure 2.9: Diagram of the two types of structures grown and characterized in this work; a) represents a typical InGaN single layer, and b) represents a InGaN/GaN MQW structure with 4 wells and a 15nm thick GaN cap layer on the top of the heterostructure.

2.5.1 InGaN/GaN single epilayers

In an ideal material, epilayer growth is where a thin single-crystal layer of material is grown on the surface of a single-crystal substrate. However, InGaN epilayer growth is more complicated than such an idealised system. InGaN films grown on top of a GaN buffer layer which is deposited onto a sapphire substrate frequently show a columnar habit, being composed of hexagonal columns with approximately the same orientation, i.e. the so-called mosaic structure [31,32]. In Fig. 2.10 a cross-sectional scanning electron microscope (SEM) micrograph of sample AIX1025 illustrates this mosaic structure rather characteristic of nitrides.

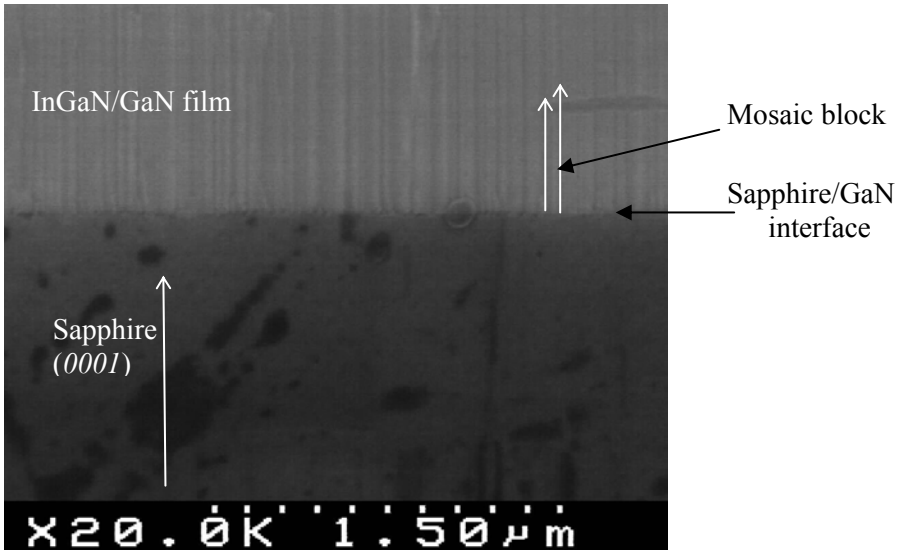

Figure 2.10: Cross section scanning electron microscope (SEM) micrograph illustrating the columnar habit of nitride layers. The mosaic block lateral size is of the order of 150 nm.

Defects and dislocations in the epilayer are mainly generated at the boundaries between grains. The mosaic structure of InGaN/GaN layers, and its influence on the XRD widths, is discussed in Section 3.9.2.1.

Since the GaN layer is the "virtual substrate" to the InGaN films, the prime determinant for the lattice mismatch is the InN fraction. The in-plane lattice mismatch, $l(x)$, in the case of an $In_xGa_{1-x}N$ film grown on GaN is given by:

$$l(x) = \frac{a^{In_xGa_{1-x}N} - a^{GaN}}{a^{GaN}} \qquad \text{(Eq. 2.3)}$$

Assuming a linear scaling of the in-plane lattice constant, a^{InGaN}, with the InN fraction, x, (Vegard's law [33]), Eq. 2.3 can be rewritten as:

$$l(x) = \frac{x \cdot (a^{InN} - a^{GaN})}{a^{GaN}} \qquad \text{(Eq. 2.4)}$$

Therefore, the lattice mismatch $In_xGa_{1-x}N$ with respect to GaN may vary from nearly zero for very low InN content up to the limit of ~10 % for InN/GaN (a^{InN}=3.537 Å and a^{GaN} =3.189 Å).

The lattice mismatch and the layer thickness appear to influence the surface morphology of InGaN/GaN layers. As a general trend, $In_xGa_{1-x}N$ layers with higher x, and thicker films show a rough 3D like surface, as revealed by SEM in Fig 2.11 for sample AIX1025 (t_{InGaN}=355nm and

x=0.14). On the other hand, thin low composition InGaN films feature an essentially flat surface interspersed with hexagonal pits, as demonstrated in Fig. 2.12 where the SEM and AFM surface micrographs of sample AEC51 (t_{InGaN}=50nm and x=0.10) are shown.

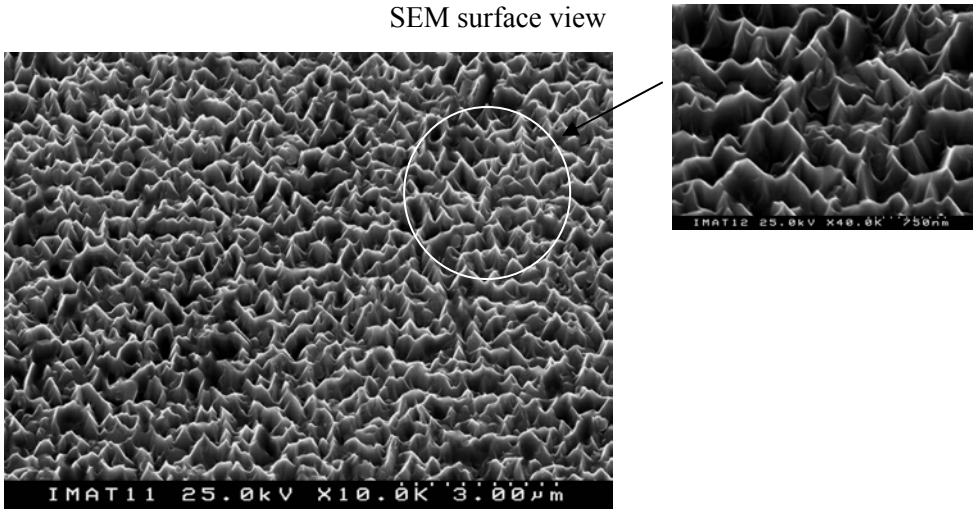

Figure 2.11: Scanning electron microscope (SEM) surface micrographs of sample AIX1025 a 355nm thick $In_{0.14}Ga_{0.86}N$/GaN layer.

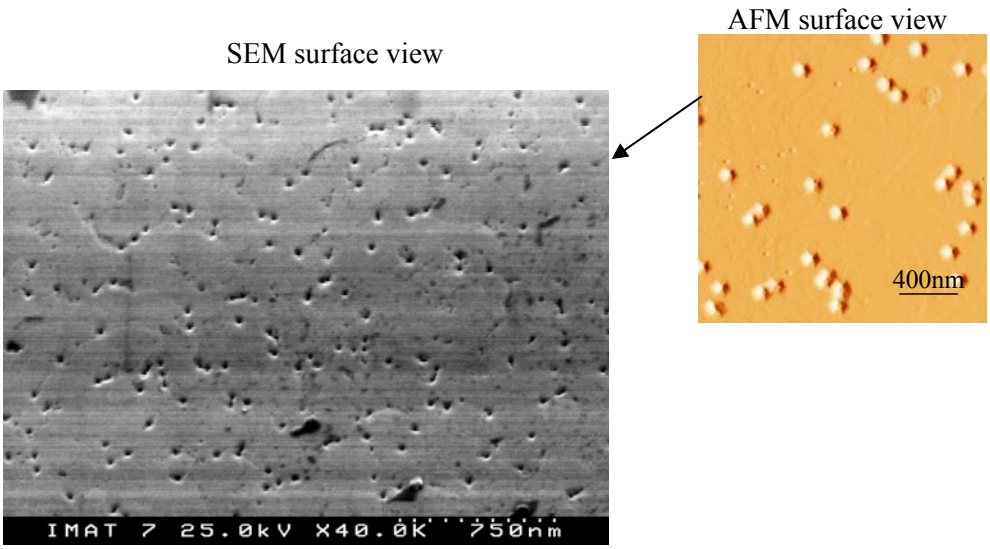

Figure 2.12: SEM and atomic force microscopy (AFM) surface micrographs of sample AEC51 a 50nm thick $In_{0.1}Ga_{0.9}N$/GaN layer.

The surface morphology of sample AIX1025 is typical of relaxed layers, as shall be discussed in Chapter 6. In addition, the rough surface resembles the growth diagram in Fig. 2.5.

Regarding the surface morphology of sample AEC51, the surface is essentially smooth, but interspersed with the so-called V-defects (hexagonal pinholes) characteristic of coherent InGaN/GaN layers which appear at the termination of threading dislocations [36]. The pit

density in this sample is ~5×10^8/cm^2, typical of high quality MOCVD-grown InGaN/GaN layers. The influence of layer thickness and InN fraction, on the evolution of surface morphology is discussed in detail in Chapter 6. We shall demonstrate that the surface morphology is ruled by the amount of strain in the InGaN epilayer, and is related to the critical layer thickness (CLT) for strain relaxation.

2.5.2 GaN/InGaN/GaN quantum wells

In a quantum well (QW) structure, the sample can be thought of as a sandwich (ABA) composed of two different semiconductor materials, A and B. In the case of MQW, this structure is periodically repeated, as shown in Fig. 2.9 b). If the two semiconductors have different optical bandgap values, then discontinuities in the conduction and valence band form at the interfaces. When the material placed in the middle of the sandwich has a lower optical bandgap value than those surrounding it then a "potential well" is formed, as shown in Figure 2.13. In this case, known as a type I QW, the electrons and holes are both confined in the same layer. The material with the smaller bandgap is termed the "well", while the larger bandgap material is the "barrier"[6]. In InGaN/GaN QWs, the InGaN layer is the well and the GaN the barrier. This structure confines the electron motion to two dimensions, and this quantum confinement of the excited electron and hole produces series of discrete energy levels in the well. The width and depth of the well determines the values of these energy levels.

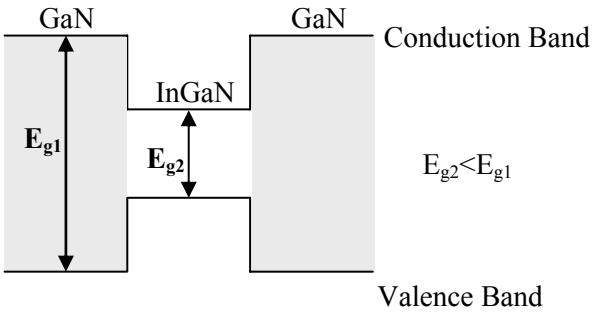

Figure 2.13: Energy diagram of a type I quantum well structure.

For a sample with a number of active layers, each separated by a barrier layer as shown in Fig. 2.9 b), the structure is termed a multiple quantum well (MQW). In a MQW, assuming the barrier layer is thick enough to prevent coupling of the electrons between wells, then each well will act independently. This effectively amplifies the optical properties of the structure while

[6] Note that even in type II band alignment, at least one QW is formed either for electrons or holes. In type I both wells form.

maintaining the original confinement conditions of a SQW. Typical thickness of the InGaN active layer is of the order of 2.5 nm. The optical properties of the material are dependent on the well dimensions through the quantum confinement effect.

The reduced thickness of the InGaN well region suggest that for a typical InGaN/GaN QW, the InGaN layer is grown coherent (i.e. with the same in-plane lattice constant) to the GaN barrier. In addition, the surface morphology of MQW samples is typical of coherent growth, i.e. identical to the case of sample AEC51, as shown in Fig. 2.12.

2.6 In-situ monitoring of InGaN/GaN MOCVD growth using optical interference

A real time *in situ* monitoring technique for MOCVD is very useful to identify the growth steps and to control the growth rate of the multilayer structure. *In situ* optical reflectometry has been widely adopted for monitoring growth of GaN-based structures using MOVPE [1]. When 2D growth is established, the transparency of GaN to visible light means that reflectometry can be used to obtain real time growth rates for layers many microns in thickness. From the optical interference fringes one can obtain useful information regarding the growing layer.

In the Strathclyde MOCVD setup, *in situ* reflectance data were collected at 600 and 800 nm in every run. The reflectance curves were collected with a Filmetrics F30 normal-incidence spectroscopic reflectometer, similar to the prototype described by Breiland and Killeen [34], using a tungsten lamp as a source of white incident light. The instrument allows simultaneous collection of reflectance data at up to three wavelengths in the range 400-900 nm, and interrogates a ~6-mm diameter area at the centre of the rotating substrate. Wavelength calibration at 600 nm was checked by recording a spectrum from an interference filter with a 10-nm pass band.

Typical results of real time monitoring during growth of sample STR58 at 820°C are shown in Fig. 2.14 where a 600-nm reflectance *versus* time plot from a growth is shown.

Derivation of the thickness of InGaN epilayers from reflectance data requires an estimate of the InGaN refractive index appropriate to the normal-incidence geometry. To our knowledge, no empirical refractive index values have been published for an extended range of InGaN compositions. We therefore used Peng and Piprek's interpolation scheme [23] to calculate room temperature refractive index values appropriate to the targeted indium nitride fraction.

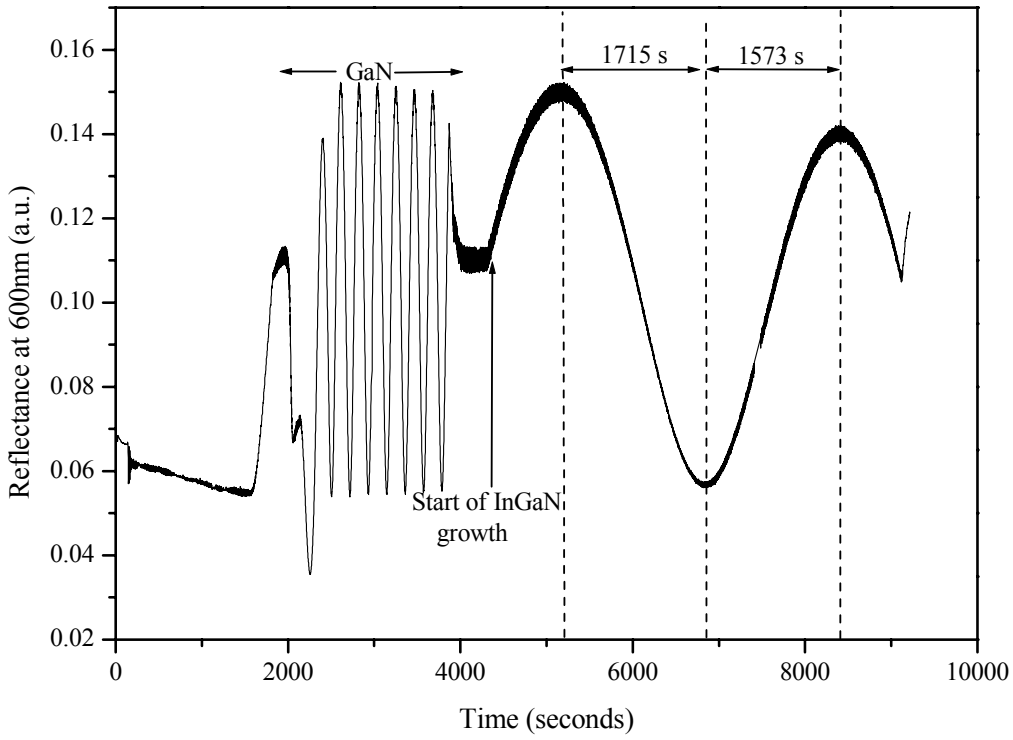

Figure 2.14: A 600-nm reflectance *versus* time plot corresponding to growth of an InGaN epilayer ~180 nm thick at 820°C (STR58), plus the underlying GaN buffer and nucleation layers.

For optically smooth films growing at a constant rate and exhibiting minimal absorption, it is well known that Fabry-Perot interference causes time-periodic variations in the intensity of reflected light. The relation between the growth rate, *G*, film refractive index at the wavelength used, *n*, period of reflectance oscillations, *P*, and monitoring wavelength, λ, is [29]:

$$G = \lambda/2nP \qquad \text{(Eq. 2.5)}$$

As it can be observed in Fig. 2.14 , InGaN growth commenced after an elapsed time of ~4320 s. Earlier events correspond to GaN nucleation on the sapphire substrate, and growth of a GaN buffer layer ~1μm thick.

The "growth thickness" of one oscillation period corresponds to $\lambda/2n$. Considering that 8 complete oscillations are observed for the GaN buffer growth we obtain a total thickness of ~8*600/2*2.5=960 nm. The thickness derived from reflectometry for the InGaN layer is ~179 nm. The values obtained from Rutherford Backscattering (RBS) analysis are a GaN buffer layer thickness of 976±10 nm and an InGaN layer thickness of 180±5 nm. In addition, the total nitride layer thickness (GaN+InGaN) obtained by analysis of the Fabry-Perot interference fringes in the optical absorption spectra is t=1.152±0.001 μm. RBS analysis in InGaN/GaN layers is detailed

in Chapter 4, whereas the process to obtain the total nitride layer thickness by optical absorption is explained in Section 5.1.3.1.

A notable feature of the 600 nm reflectance data is that the intervals between successive reflectance extrema can vary significantly within a single InGaN epilayer growth. For example, in Fig. 2.14 the time between the first maximum and the minimum is 1715 s, while the interval between the minimum and the second maximum is 1573 s. This indicates that for the InGaN layer the growth rate increases with the layer thickness.

In addition, it should be noted that as a general trend the interference fringes tend to become attenuated, and in some cases disappear, as the InGaN layer thickness increases. This indicates that the surface morphology is affected by the layer thickness: thicker InGaN layers tend to be rougher, as discussed in Section 2.5.1. The roughness corresponds to a thickness fluctuation, and when it reaches values of the order of half the growth thickness of one oscillation period ($\lambda/4n$, ~60 nm for the case of reflectance curves measured at 600 nm), the interference fringes disappear.

A full account of the results that we obtained by *in situ* reflectometry and comparisons between *in situ* and *ex situ* analysis in InGaN single layers and MQWs is published in Ref. [29].

2.7 Growth details and list of InGaN/GaN samples studied

All samples studied in this work which includes single layers and MQWs were grown by MOCVD and obtained from different sources, namely: University of Strathclyde, Aixtron AG, Thomson-CSF and University of Ghent.

The growth details, which were made available, are given in the following sections. It should be noted that given the difficulties to control/monitor the growth of InGaN, nominal parameters, such as InN mole fraction or layer thickness, can not be used confidently, since they fail to be close to the measured values. In fact, part of the objective of this research work, is to develop methods to accurately measure such parameters.

2.7.1 MOCVD InGaN from the University of Strathclyde

These InGaN samples were grown at the Institute of Photonics (IOP) in the University of Strathclyde by Dr. Ian Watson using an Aixtron 200/4 RF-S reactor [29]. The samples investigated are nominally undoped wurtzite InGaN epilayers and MQWs deposited on a GaN buffer layer with a GaN nucleation layer grown onto (0001) sapphire substrates.

2.7.1.1 InGaN single layers

The growth temperatures for the nucleation, buffer and InGaN layers were 540°C, 1140°C and 760°C respectively. The thickness of each layer was estimated by *in situ* optical reflectometry measurements. In particular, for the series of samples STR11#, the fluxes of trimethylgallium and trimethylindium were 22.1 and 14.3 μmol/min respectively, and the total V/III ratio was ~6100. The three layers were prepared in consecutive runs, with successive growth periods of 25, 50 and 100 minutes. Details regarding the structure of Strathclyde single layers are outlined in Table 2.I.

Table 2.I: Details of the single layer samples from the IOP at the University of Strathclyde.

Sample	GaN nucleation layer thickness (nm)	GaN buffer layer thickness (nm)	InGaN layer thickness (nm)	InGaN layer composition (*x*)
STR58	20	1000	180	0.12
STR59	20	1000	193	0.24
STR99	20	1000	207	0.11
STR116	20	1100	60	0.25
STR117	20	1100	120	0.25
STR115	20	1000	240	0.25

2.7.1.2 InGaN/GaN MQWs

Following deposition of ~1.2-μm GaN buffer layers on c-sapphire substrates at 1140°C, growth was interrupted for cooling to the MQW growth temperature. The InGaN wells, GaN barriers and cap layers were grown at a constant temperature, without any further interruptions.

The 10-period MQW designated STR94 was grown at 832°C and the growth periods for wells and barriers were respectively 90 and 270 s, chosen to give nominal thicknesses of 2.5 and 7.5 nm. The other two structures, STR121 and STR120, were grown at 760° C, and contained 18 and 8 wells, respectively. The barrier growth period was also 270 s, but for the well was 78 s. Growth periods for the GaN cap layers of STR94 and STR121 last 540 s. However, growth of STR121 cap was interrupt ~15 s after the 8th well, before reaching the pre-set value. The nominal parameters of the three MQW samples are summarised in Table 2.II

Table 2.II: Details of the MQWs samples from the IOP at the University of Strathclyde

Sample Reference Number	GaN buffer layer thickness (nm)	GaN barrier thickness (nm)	InGaN well thickness (nm)	InGaN well composition (*x*)
STR121 (18-wells)	1200	7.5	2.75	0.20
STR120 (8-wells)	1200	7.5	2.75	0.20
STR94 (10-wells)	1200	7.5	2.75	0.10

2.7.2 MOCVD InGaN from the University of Ghent

The InGaN samples from the University of Ghent were grown in a Thomas Swan and Co., Ltd rotating-disc reactor. A description of the growth reactor and modifications made to the system can be found in reference [37]. The samples investigated were all InGaN/GaN bilayers grown onto a sapphire substrate. The nominal growth temperature and layer thickness for each sample are presented in Table 2.III.

Table 2.III: Details of the MOCVD samples from the University of Ghent

Sample Reference Number	GaN growth temperature (°C)	GaN layer thickness (nm)	InGaN growth temperature (°C)	InGaN layer thickness (nm)
85	1050	2000	850	250-300
331	1080	2200	780	270
336	1080	2200	780	230

2.7.3 MOCVD InGaN from Aixtron AG and Thomson-CSF LCR

These InGaN/GaN samples were grown at Aixtron AG, Germany and Thomson-CSF LCR, France as part of the Brite-Euram project, Rainbow. The samples listed in Table 2.IV with a reference number pre-fixed by an 'S' and "AIX" were grown by Aixtron AG, in a AIX2000/2400HT reactor; the other samples (AEC51 and AEC53) were grown by Thomson-CSF LCR in a home-made MOCVD reactor. All samples were InGaN epilayers grown at temperatures of approximately 800°C.

Table 2.IV: Details of the MOCVD samples grown as part of the Brite-Euram Project, Rainbow

Sample Reference Number	GaN buffer layer thickness (nm)	InGaN layer thickness (nm)	InGaN layer composition (*x*)
AEC51	675	50	0.10
AEC53	500	75	0.16
AIX1027	1800	750	0.19
AIX1025	2100	355	0.14
S101	>1000	120	0.19
S102	>1000	180	0.12
S103	>1000	157	0.061
S104	>1000	191	0.02
S201	>1000	325	0.23
S202	>1000	225	0.099
S204	>1000	200	0.070

2.8 Summary

In this chapter, the basic principles of the techniques used to grow InGaN/GaN heterostructures, with particular emphasis on MOVCD growth, were presented. Some of the difficulties encountered during the growth of high quality InGaN/GaN heterostructures with controlled parameters were discussed. Namely, the issues of lattice mismatch between the sapphire substrate and the GaN layer and the consequent 3D growth, were described. Furthermore, it was shown that difficulties in the growth process may lead to an undesired rough surface morphology, In droplet formation, and heterogeneous growth rates and In incorporation. We presented the main growth steps which included the growth of a GaN buffer layer to improve the overall crystalline quality of the subsequent nitride heterostructure. The usefulness of the *in situ* optical reflectivity technique to monitor the films growth process was demonstrated. The types of structures grown, InGaN single layers and InGaN/GaN MQWs, were described. Finally, a list of the samples provided by the various crystal growers was presented.

2.9 References:

[1] S. Nakamura and G. Fasol, *"The blue laser diode"*, Springer, Berlin (1997).

[2] B. Gil, ed. *"Group III nitride semiconductor compounds, physics and applications".* Series on Semiconductor Science and Technology 6*,* Oxford Science Publications, Oxford (1998).

[3] J. H. Edgar, *"Gallium nitride and related semiconductors"*, No. 23 EMIS Datareview, INSPEC, London (1998).

[4] H. Morkoç, S. Strite, G. Gao, M. Lin, B. Sverdlov, and M. Burns, J. Appl. Phys. **76**, 1363 (1994).

[5] J. W. Orton and C. T. Foxon, Rep. Prog. Phys. **61**, 1 (1998).

[6] S. C. Jain, M. Willander, J. Narayan, and R. V. Overstraeten, J. Appl. Phys. **87**, 965 (2000).

[7] N. Grandjean, B. Damilano, and J. Massies, J. Phys.: Condens. Matter **13**, 6945 (2001).

[8] S. Nakamura and T. Mukai, Jpn. J. Appl. Phys., **31** L1457(1992).

[9] H. M. Manasevit. Appl. Phys. Lett. **12**, 136 (1968).

[10] H. M. Manasevit and W. I. Simpson. Journal of Electrochemical Society, **116**, 1725 (1969).

[11] P. D. Dapkus, Journal of Crystal Growth, **68**, 345 (1984).

[12] P. H. Manuel, M. Defour, C. Grattepain, F. Omnes, O. Archer, G. Timms and M. Razeghi, Chemtronics, **4**, 40 (1989).

[13] M. Razeghi and Adam Hilger, *"The MOVCD challenge"*, **1**, Bristol (1989).

14] H. Sasaki, M. Tanaka and J. Yoshino, Japanese Applied Physics, **24**, 417 (1985).

[15] T. Fukui and H. Saito, Japanese Applied Physics, **24**, L774 (1985).

[16] D. Steigerwald, S. Rudaz, H. Liu, R. S. Kern, W. Götz and R. Fletcher, J. of Minerals **49** 18 (1997). http://www.tms.org/pubs/journals/JOM/9709/Steigerwald-9709.html#Steigerwald

[17] S. Keller, B. P. Keller, D. Kapolnek, U. K. Mishra, S. P. DanBaars, I. K. Shmagin, R. M. Kolbas and S. Krishnankutty. Journal of Crystal Growth, **170**, 349 (1997).

[18] A. Sohmer, J. Off, H. Bolay, V. Härle, V. Syganow, J. S. Im, V. Wagner, F. dler, A. Hangleiter, A. Dörnen, F. Scholz, D. Brunner, O. Ambacher and H. Lakner, MRS Int. J. Semiconductors. Res. 2, **14** (1997).

[19] P. Li, S. J.Chua, M. Hao, W. Wang, X. Zhang, T. Sugahara and S. Sakai. MRS Internet J. Nitride Semicond. Res. **5S1**, W11.31 (2000).

[20] Thomas Swan Scientific Equipment Ltd. http://www.thomasswan.co.uk/mocvd.html

[21] Electrical and Computer Engineering. The University of Texas at Austin, USA. Website: http://www.ece.utexas.edu/projects/ece/mrc/groups/street_mbe/mbechapter.html

[22] K. G. Günther, Z. Nat. Forsch. A, **13**, 1081 (1958).

[23] N. Grandjean and J. Massies, Appl. Phys. Lett. **72**, 1078 (1998).

[24] D. Neaman, *"Semiconductor Physics and Devices Basic Principles"*, IRWIN, USA (1992).

[25] H. Amano, N. Sawaki, I. Akasaki, and Y. Toyoda, Appl. Phys. Lett. **48**, 353 (1986).

[26] S. Nakamura, Jpn. J. Appl. Phys., **30** p. L1705 (1991).

[27] Tsvetanka S. Zheleva, Ok-Hyun Nam, Michael D. Bremser, and Robert F. Davis, Appl. Phys. Lett. **71**, 2472 (1997)

[28] S. Nakamura, M. Senoh, S. Nagahama, N. Iwasa, T. Yamada, T. Matsushita, H. Kiyoku, Y. Sugimoto, T. Kozaki, H. Umemoto, M. Sano and K. Chocho. Jpn. J. Appl. Appl. Phys. **37**, L309. (1998).

[29] C. J. Deatcher, C. Liu, S. Pereira, M. Lada, A. G. Cullis, O. Brandt and I. M.Watson Semicond. Sci. Technol. **18** 212 (2003).

[30] K. P. O'Donnell, C. Trager-Cowan, S. Pereira, A. Bangura, C. Young, M.E. White and M.J. Tobin, Phys. Stat. Sol. (b) **216**, 157 (1999).

[31] P. F. Fewster "*X-Ray scattering from semiconductors*" Imperial College Press, London, UK (2001).

[32] A. Krost in *"Nano-optoelectronics: concepts, physics and devices"*, M. Grundmann Ed., Springer, Berlin (2002).

[33] L. Vegard, Z. Phys. 5, **17** (1921).

[34] W. G. Breiland and K. P. Killeen *J. Appl. Phys.* **78**, 6726 (1995)

[35] T. Peng and J. Piprek *Electron. Lett.* **32** 2285 (1996); [*Equation (1) is incorrect as published, and the first exponent should be –2*].

[36] Y. Chen, T. Takeuchi, H. Amano, I. Akasaki, N. Yamada, Y. Kaneko, and S. Y. Wang, Appl. Phys. Lett. **72**, 710 (1998).

[37] Wim Van der Stricht, PhD Thesis, *"Development of group III nitride technology for the realisation of light emitting diodes"*, University of Ghent, (1999).

Chapter 3: XRD characterization of InGaN layers

Overview

The aim of this chapter is to introduce the X-ray diffraction (XRD) technique and illustrate its potential contribution to the microstructural analysis of nitride semiconductors. A brief introduction to the concepts involved in XRD is given. The emphasis is on concepts related to the application of XRD to the InGaN/GaN system. Therefore, the fundamental geometrical relations for an XRD experiment, the general expressions for inter-planar spacing, the angular relations between planes and the general expression for the structure factor are provided for the case of hexagonal structure[1]. The concept of reciprocal space (RS) is introduced and the conversion of the XRD maps from angular coordinates to RS units is explained. The different types of scans, the way the scattering vector moves in the RS and the information that can be obtained, are briefly described. In addition, the experimental setup used for the XRD experiments performed in this thesis is depicted.

Finally, the effectiveness of the technique is illustrated directly with reference to experimental results obtained for various InGaN/GaN samples of increasing complexity. Starting from the simplest experiment, a θ-2θ symmetric scan, up to more complex analysis of reciprocal space maps and in-plane diffraction reveals the richness of the microstructural information that can be obtained by the different types of XRD experiments.

3.1 Introduction

X-ray diffraction (XRD) is sensitive to thin films of thicknesses from atomic dimensions to a few microns, by virtue of X-ray wavelengths employed and the very high reciprocal space resolutions attainable. X-ray methods are non destructive, no sample preparation is required and they provide a very appropriate route to obtain structural information on thin films and multilayers. Conventional high resolution XRD has been developed into a powerful tool for the non-destructive ex-situ investigation of epitaxial layers, heterostructures and superllatice systems. The information which is obtained from diffraction patterns concerns the composition and uniformity of epitaxial layers, their thickness, the built in strain and strain relaxation, and the crystalline perfection related to their dislocation density. Furthermore, information on interface effects like interdiffusion can also be obtained under favourable circumstances. The XRD instrumentation has been continuously improved and simple powder diffractometers using a focusing path for the X-rays have been replaced by double and triple-axis spectrometers

[1] This is unusual since most semiconductors are cubic.

equipped with multiple crystals or channel cut monochromators and analysers. Apart from the investigations under normal Bragg conditions, grazing angle techniques for determination of layer thickness as well as for precise information on the lattice constants of thin films have been developed.

In addition to the fundamental books treating the basics of the XRD technique and the historical developments [1-9], there are a number of good reviews on the analysis of epitaxial layers [10-14], and a few works that deal with application of XRD to nitrides [15-18].

3.2 X-ray radiation

In 1895, Wilhelm Röntgen discovered X-rays while working at the University of Wurzburg, Germany on cathode ray tubes. For the X-ray discovery he was awarded the first Nobel prize for Physics in 1901. X-rays are electromagnetic waves whose wavelengths are in the neighborhood of 0.1-10Å. The wavelength of an X-ray radiation is thus of the same order of magnitude as the lattice constants of crystals, and it is this which makes X-rays useful in the analysis of crystal structures.

X-ray radiation is produced when rapidly moving electrons strike a solid target and their kinetic energy is converted into radiation. The electron deceleration gives rise to electromagnetic radiation. For historical reasons, this X-ray component is referred to as *"bremsstrahlung"* after the German word for the deceleration process by which it occurs. If the energy of the electrons exceeds a critical value, the characteristic X-radiation is generated, which appears in the spectrum as individual lines superimposed on the continuous *bremsstrahlung* spectrum. These lines are generated when high-energy electrons penetrate deep into the atomic shells of the anode material and eject electrons from the innermost orbitals by collision. These spectrally sharp spikes are called *characteristic lines* and the X-radiation is termed characteristic radiation. Particular lines are caused by electrons being knocked out of the *K* (n=1) shell of an atom and then the electrons from the *L* (n=2) shell cascading down into the vacancies in this *K* shell. The energy emitted in this process corresponds to the so-called K_α line[2]. Therefore the resulting X-radiation is characteristic the anode material, mainly a function of the atomic number of the target atoms.

In most XRD work, a single well-defined wavelength of radiation is necessary and therefore the X-rays must be filtered. The way to obtain approximately monochromatic X-ray radiation is by using a monochromator crystal. Throughout this work, the Cu radiation is used, and most of the results if not otherwise mentioned, are obtained using only the Cu $K_{\alpha 1}$ line. The parameters for the relevant cooper lines are*:* $\lambda(CuK_{\alpha 1})=1.54056$ *Å* and $\lambda(CuK_{\alpha 2})=1.54439$ *Å* with $I(K_{\alpha 2})/(IK_{\alpha 1})=0.5$.

[2] Note that the spin-orbit coupling splits the L shell and we will observe a doublet; the $K\alpha_1$ and $K\alpha_2$ lines.

3.3 Bragg's law

In 1913 W.H. and W.L. Bragg found that crystalline substances gave remarkable characteristic patterns of reflected X-radiation, quite unlike those produced by liquids [19]: for certain sharply defined incidence directions, intense peaks of scattered radiation (now know as Bragg peaks) were observed. W.L. Bragg accounted for this by regarding a crystal as made out of parallel planes, spaced a distance apart *d*. The conditions for a sharp peak in the intensity of the scattered radiation were: (1) that the X-rays would be specularly "reflected" from any plane (2) that the reflected X-rays from successive planes would interfere constructively. Rays specularly reflected from adjoining planes are shown in Fig. 3.1.

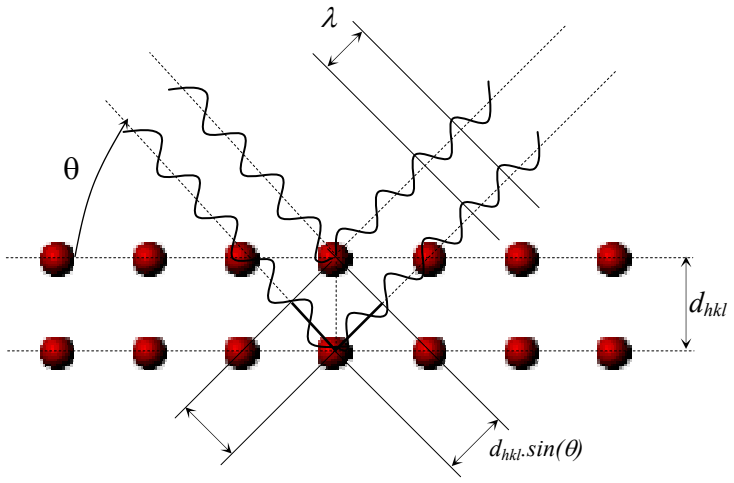

Figure 3.1 : A Bragg "reflection" from a particular family of lattice planes (*hkl*), separated by a distance d_{hkl}. Incident and reflected rays are shown for two neighboring planes. The path difference is $2dsin\theta$.

The path difference between the two rays is just $2dsin\theta$, where θ is the angle of incidence[3]. For the rays to interfere constructively, this path difference must be an integral number of wavelengths, leading to the celebrated Bragg condition:

$$2dsin\theta = n\lambda \qquad \text{(Eq. 3.1)}$$

The integer *n* is known as the order of the corresponding Bragg reflection.

The discovery of X-rays, and Braggs' law, was not only the turning point in crystallography, but was also the landmark in modern science. For from this time forth, matter of molecular

[3] The angle of incidence in X-ray diffraction is conventionally measured from the plane of "reflection" rather than from the normal to the plane (as in classical optics). Note that θ is just half the angle of detection of the incident beam (Fig. 3.1).

dimensions could be probed by studying the way it scattered X-rays. The discovery gave the Braggs the Nobel Prize in Physics in 1915. An interesting historic account of XRD can be found in Ref. [1]

3.4 Basic geometrical relations for wurtzite structures

The planes in a crystal are characterized by the miller indices *h*, *k*, and *l*. A Miller index for a plane is expressed as (*hkl*), where *h*, *k* and *l* are integers such that the shortest distance between Bragg planes is inversely proportional to the index. A family of crystallographically equivalent planes is expressed as {*hkl*} and the directions [normal to a given (*hkl*) plane] are expressed as <*hkl*>. The additional index typically used in the hexagonal notation (*hkil*) can be derived from *i*=-(*h*+*k*). Therefore, (*hkil*), (*hk.l*) or simply (*hkl*) are equivalent notations for the same plane. In Fig. 3.2, the fundamental geometrical parameters and the scattering geometry for XRD are depicted.

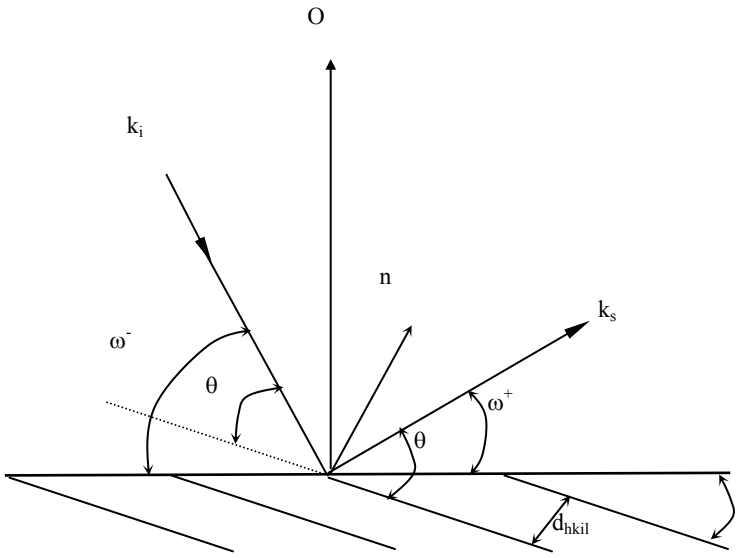

Figure 3.2: Geometry of the typical diffraction experiment

In the diagram, k_i and k_s are the incident and scattered wavevectors, respectively, *O* is the surface normal, *n* is the normal of the reflecting planes, φ is the angle between the <*hk.l*> plane and the surface normal <*000.1*>, d_{hkil} is the interplanar distance of the (*hk.l*) plane, 2θ is the Bragg angle, ω^- and ω^+ are the incidence and emergence angles of the X-ray beam relatively to the surface, respectively.

The interplanar spacing for the (*hk.l*) plane can be related to the hexagonal lattice constants *c* and *a* by [5]:

$$d_{hkl} = \frac{1}{\sqrt{\frac{4}{3a^2}(h^2 + k^2 + hk) + \frac{l^2}{c^2}}} \quad \text{(Eq. 3.2)}$$

also, in the hexagonal structures, the angle between a given plane (*hk.l*) and the surface normal is defined by [5]:

$$\tan\varphi = \frac{c}{a}\sqrt{\frac{4}{3}\left(\frac{h^2 + hk + k^2}{l^2}\right)} \; . \quad \text{(Eq. 3.3)}$$

Note that in the case of the hexagonal structures, contrary to the cubic case, the angles between different planes varies with the *c/a* ratio. Therefore, to represent the stereographic projections and calculate the geometrical parameters for each *c/a* ratio the software Carine Crystalography [4] was used. In practice, and since the angles do not vary much with the *c/a* ratio, values calculated for GaN are a good guide to find the reflections associated to the InGaN layers of moderate InN content. Some fundamental geometrical parameters for the typical reflections used along this thesis are summarized in Table 3.I.

Table 3.I: Geometrical parameters of reflections used in the thesis, calculated for GaN.

h	*k*	*l*	φ (º)	2θ (º)	ω^-(º)	ω^+(º)	*Geometry*
0	0	2	0	34.57	17.28	17.28	Symmetric
0	0	4	0	72.92	36.46	36.46	Symmetric
0	0	6	0	126.09	63.05	63.05	Symmetric
1	0	5	20.58	105.02	31.93	73.09	Asymmetric
1	1	4	39.11	99.96	10.87	89.09	Asymmetric
0	2	5	36.91	136.54	31.37	105.18	Asymmetric
1	0	0	90	32.39	(~0)	(~0)	In-plane

The Bragg diffraction is called symmetric if φ=0, i.e. the reflecting lattice planes are parallel to the surface. For $\varphi \neq 0$ the Bragg diffraction is defined as asymmetric. Note that the *(10.0)* plane is perpendicular to the growth direction and the way to measure its diffraction is to perform "in-plane" diffraction.

[4] Find more details about the software on: http://pro.wanadoo.fr/carine.crystallography/

3.5 In-plane diffraction

Most of the X-Ray diffraction experiments to be described here were carried out using the standard "Bragg" or "reflection" geometry. Scattering occurs such that the incident and reflected beams enter and emerge from the same surface of the sample as shown in Fig. 3.3.

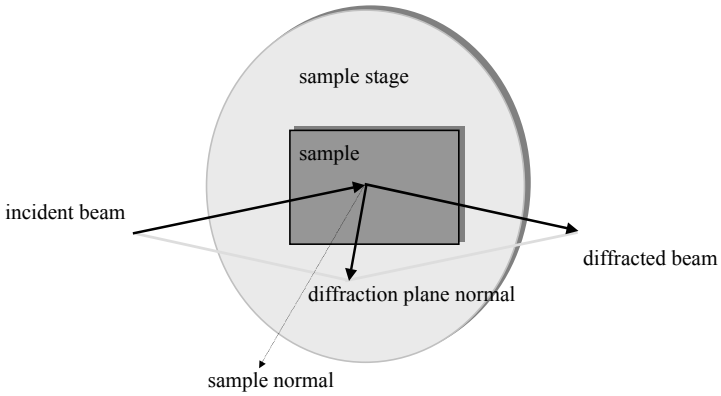

Figure 3.3: The experimental setup used for the "Bragg" or "reflections"

"In-plane scattering" refers to the situation when incident and scattered beam directions are both parallel to this surface plane. For diffraction planes that are oriented such that their normals are in the plane parallel to the surface, the usual experimental set-up (Fig 3.3) cannot be used and so the in-plane scattering geometry is required (see Fig. 3.4).

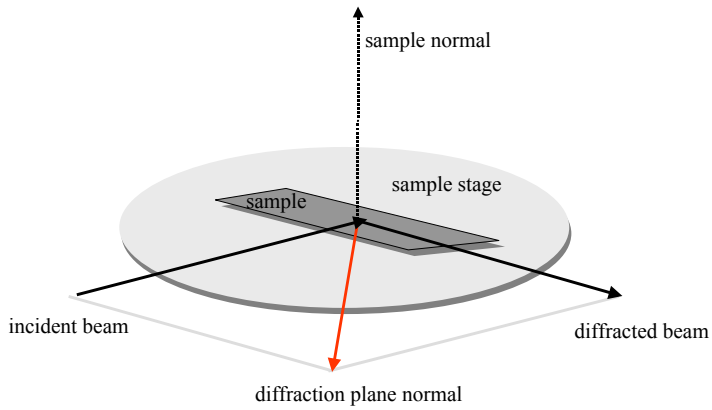

Figure 3.4: The "in-plane" scattering geometry.

To make better use of the volume of material available in thin films, the in-plane scattering geometry can take place through the top surface of the sample. When the incident angle is close to the critical angle for reflectivity, α_c, there is a small penetration of the beam into the surface layers of the sample. Bragg scattering can then occur from planes within this very shallow

region. Typical penetration depths for in-plane scattering are typically within the range 1-50nm [5].

3.6 The structure factor of wurtzite structures

In order to know which Bragg peaks are allowed and to have an idea of their relative intensities it is necessary to introduce the concept of structure factor. This parameter corresponds to the sum of the phases of scattering for all relevant atoms, and so determines the scattering "strength" of a given (*hk.l*) plane. The general expression for the structure factor of a crystallographic plane (*hk.l*) is given by:

$$F_{hkl} = \sum_j f_j e^{2\pi i(hu_n + kv_n + lw_n)} \qquad \text{(Eq. 3.4)}$$

where the summation extends over the n lattice points (u_n, v_n,w_n) and where f_j is the atomic form factor, which is a measure of the scattering strength of the j^{th} atom in the unit cell.
The unit cell of the wurtzite structure has two lattice points with the group III (Ga/In) atoms at (*0,0,0*) and (*1/3, 2/3,1/2*) and two with nitrogen at (*0,0,3/8*) and (*1/3,1/3,7/8*). For this structure, the geometrical structure factor F_{hkl} for a (*hk.l*) plane is given by:

$$F_{hkl} = f_1 + f_2 e^{2\pi i\left(\frac{h+2k}{3}+\frac{l}{2}\right)} + f_N\left[e^{2\pi i\frac{3l}{8}} + e^{2\pi i\left(\frac{h}{3}+\frac{2k}{3}+\frac{7l}{8}\right)}\right] \qquad \text{(Eq.3.5)}$$

where f_N is the scattering factor of the nitrogen atom and f_1 and f_2 are different scattering factors for atoms occupying the (*0,0,0*) and (*1/3, 2/3,1/2*) lattice sites, respectively. From the above equation, $F_{hkl}= f_1-f_2$, if n is odd and $h+2k=3n$, for any integer n. In a random alloy, indium and gallium atoms occupy the two lattice sites (*0,0,0*) and (*1/3, 2/3,1/2*) with the same probability, resulting in equal values for f_1 and f_2. Therefore, in particular, the structure factor of (*00.l*) planes is zero if l is odd.

3.7 Diffraction in reciprocal space

In order to simplify the crystallographic analysis one should introduce the concept of reciprocal lattice (RL), which is related with the Bravais lattice in a simple way. The reciprocal lattice

points (RLP) represent all the possible X-ray reflections and are represented by the miller indexes (*hk.l*) of the respective planes.

Starting with a lattice whose basis vectors are *a,b,c* we can define a new set of basis vectors *a*, b*, c** according to the relations:

$$a^*=K/(b\times c)/V \quad \text{a)} \qquad b^*=K/(a\times c)/V \quad \text{b)} \qquad c^*=K/(a\times b)/V \quad \text{c)} \quad \text{(Eqs. 3.6a, b and c)}$$

where K is the RL constant given by $K=q_{hkl}\bullet d_{hkl}$, V is the unit cell volume given by $V=a\bullet b\times c$. As already mentioned, the reflections for the crystallographic planes are only possible for certain incidence angles, at a given X-ray wavelength.

With a triple axis diffractometer different directions in the reciprocal space can be scanned. The RL diagram for a wurtzite structure is represented in Fig. 3.5.

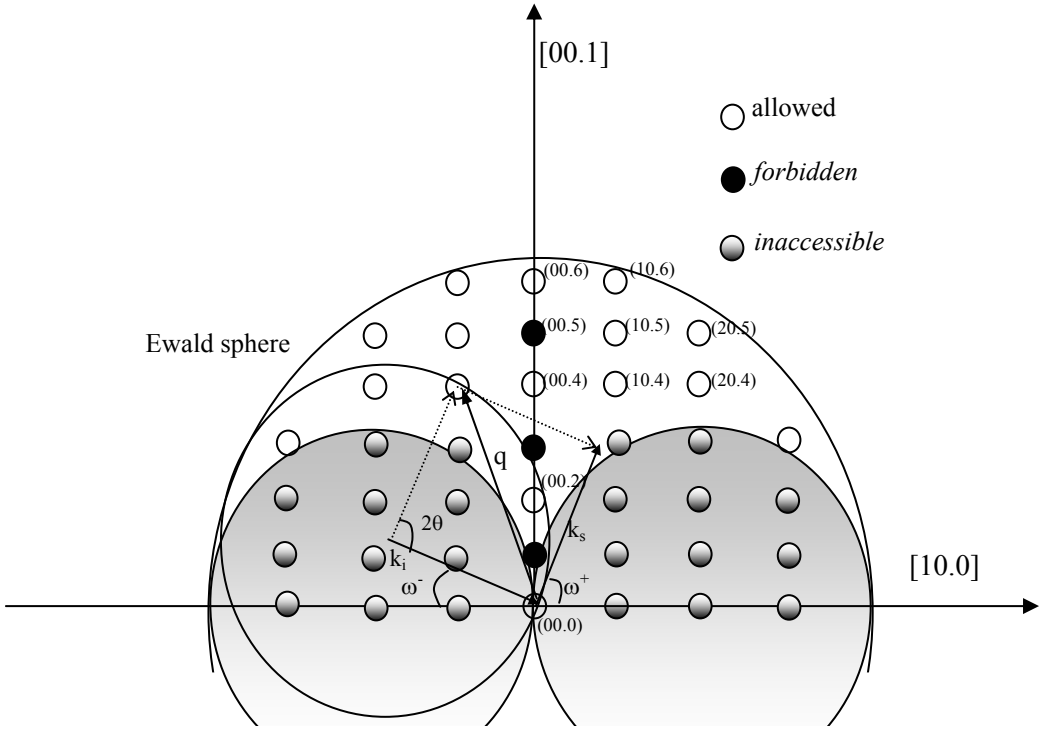

Figure 3.5: Diagram of a wurtzite reciprocal space showing the accessible range for reflection XRD measurements in coplanar geometry. The radius of the outer circle is limited by the maximum diffractometer angle. The shadowed inner circles define the regions that are not accessible in Bragg geometry.

Allowed and forbidden reflections are represented together with the regions that are accessible in the Bragg geometry. The angle ω^- is the incoming angle of the primary X-ray beam $\vec{k}_i$ with respect to the sample surface and 2θ the scattering angle included by the $\vec{k}_i$ and the scattered

beam $\overrightarrow{k_s}$. The scattering vector $\vec{q} = \vec{k}_s - \vec{k}_i$ ends up on the Ewald sphere. The point (*00.0*) represents the crystal surface. The Ewald sphere[5] of radius $1/\lambda$ passes trough the (*00.0*) point.
One can easily determine which diffractions are possible to measure by rotating the Ewald sphere around (*00.0*) for all possible values of θ. For each interception of the Ewald sphere with a RLP we have diffraction corresponding to that set of planes. The bigger sphere, the so-called limiting sphere, *limits* the range of possible reflections reachable for a certain wavelength. The shadowed inner circles are not accessible in the Bragg geometry.

3.7 XRD scans in reciprocal space

Conventional powder diffractometers use a θ-2θ scan for measuring symmetric Bragg reflections (φ=0, ω-=ω+=ω=θ). For such a scan, the detector is rotated twice as fast and in the same direction around the diffractometer axis as the sample. Only planes parallel to the growth direction can be measured. In the reciprocal space (RS), this conventional motion of the sample and detector corresponds to a change of $\vec{q}$ along the [*00.1*] direction and therefore only planes along this direction can be measured.
In a $\omega/2\theta$ scan, the sample is rotated at a fixed 2θ position. Therefore, in coplanar geometry, i.e when $\overrightarrow{k_i}$ and $\overrightarrow{k_s}$ have a common scattering plane, the scattering vector $\vec{q} = \overrightarrow{k_s} - \overrightarrow{k_i}$ moves azimuthally with a constant value around the origin of the reciprocal space. For a symmetric geometry, i.e. with the same angle between the surface and incoming and outcoming X-ray beams, the scan runs parallel to the surface normal.
This type of scan requires a coupled movement of the sample (ω) and the detector in the ratio $\omega/2\theta$=*1/2* in a conventional triple axis diffractometer with a point detector. However, this can be avoided by the use of a double crystal spectrometer equipped with a position sensitive detector (PSD) placed on the 2θ arm of that diffractometer. Despite the fact that the sample is rotated in the conventional ω-direction, the PSD collects the X-rays simultaneously over a 2θ range of about 10º. However, it does not integrate over that range but resolves the scattered intensities with a resolution of ~50 arcsec.
In Fig. 3.6 we illustrate schematically the construction of a RSM in this system.

[5] Note that the RL is 3D and we are only seeing a projection in a plane.

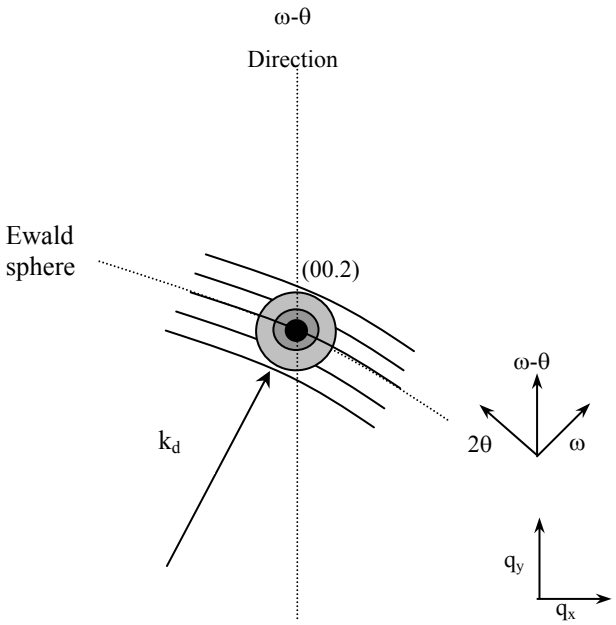

Figure 3.6: The construction of a reciprocal space map.

The successive arcs of circles (projection of the Ewald sphere) correspond to the detector positioning relatively to the sample surface, and are centred in the origin of the RS. The angular amplitude corresponds to the detectors' solid angle. A combination of $\omega/2\theta$ scans with different settings of ω and steps of $\Delta\omega$ yields a map of peak intensity as function of position (ω,2θ). The transformation from angular to reciprocal space coordinates is easily understood with reference to Figure 3.7

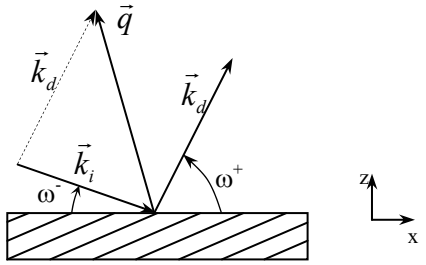

Figure 3.7: Vectorial diagram of the scattering process

The projections of the scattering vector along *x* and *z* directions are given by:

$$q_x = k.[cos(\omega+) - cos(\omega-)] \quad \text{(Eq. 3.7 a)}$$

$$q_z = k.[sin(\omega+) - sin(\omega-)] \quad \text{(Eq. 3.7 b)}$$

q_x and q_z being the components of the scattering vector parallel and perpendicular to the surface, respectively and $k_i=k_d=k=2\pi/\lambda$. The q_x component has a direction parallel to the crystal surface (*hk.0*) and q_z has a direction perpendicular to the surface (*00.l*), both have units of nm^{-1}. Using the above relation the modulus of $\vec{q}$ can be readily calculated as:

$$|\vec{q}| = \frac{2\pi}{\lambda}\sqrt{q_x^2 + {}_z^2} = \frac{2\pi}{\lambda}\sqrt{\left(cos\omega^+ - \cos\omega^-\right)^2 + \left(\sin\omega^+ + \sin\omega^-\right)^2} \quad \text{(Eq. 3.8)}$$

thus,

$$|\vec{q}| = \frac{2\pi}{\lambda}\sqrt{2 - 2\cos\left(\omega^+ + \omega^-\right)} \quad \text{(Eq. 3.9)}$$

since $(\omega^+ + \omega\text{-}) = 2\theta$ and substituting in the previous equation one obtain:

$$|\vec{q}| = \frac{2\pi}{\lambda}\sqrt{\sin\theta} \qquad \text{(Eq. 3.10)}$$

and using Bragg's law

$$|\vec{q}| = \frac{2\pi}{d_{hkl}}. \qquad \text{(Eq. 3.11)}$$

3.7.1 Symmetrical scans

For a symmetrical scan, only planes with $h=0$ and $k=0$ can be scanned; therefore Eq. 3.2 is reduced to:

$$d_{00l}=c/l \qquad \text{(Eq. 3.12)}$$

thus, the relation between the *c* lattice constant and the scattering vector is given by:

$$c = \frac{2\pi l}{q_z}. \qquad \text{(Eq. 3.13)}$$

With a symmetrical scan one can directly determine the tilting between different layers in an epitaxial structure. Since in such scans $\omega\text{+}=\omega\text{-}$, q_x is identically zero. Thus, one concludes that RLPs with the same q_x represent layers that are parallel to each other. If there is a tilt the respective RLP will be measured in $\omega^-+\Delta\omega$ or $\omega^+\text{-}\Delta\omega$ resulting in a different value for q_x.

3.7.2 Asymmetrical reciprocal space mapps

The asymmetrical RSM contains more information than a symmetrical scan since asymmetric planes contain information about the 3 components of the unit cell. There are two ways of

performing an asymmetrical RSM; grazing incident beam, or grazing exit beam. The two configurations used are represented in Fig. 3.8.

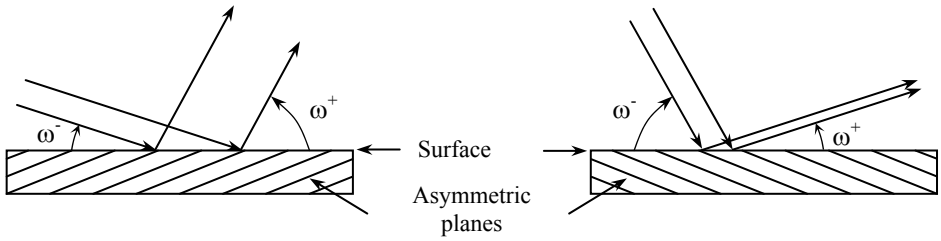

Figure 3.8: Grazing incidence (left) and grazing exit asymmetric scattering geometry.

The first type of scan is more suited to very thin layers maximizing the intensity but losing angular resolution. The equations relating the lattice constants with the scattering components are similar to the symmetric case, however this type of measurement is sensitive to both the in-plane and out-of-plane lattice parameters.

Therefore, in this case using Eq. 3.2 and Eq. 3.11 one can relate the lattice parameter a of the hexagonal structure to the in plane component of the scattering vector by:

$$a = \frac{2\pi}{q_x}\sqrt{\frac{4}{3}(h^2 + k^2 + hk)}\,. \qquad \text{(Eq. 3.14)}$$

With an asymmetric map, information about the coherency of InGaN films relative to the GaN pseudo buffer can be directly obtained by comparing the positions of the InGaN and GaN RLP along q_x.

3.8 Instrumental description

3.8.1 The *Hotbird*

Most XRD results presented in this thesis were obtained in the high-resolution X-ray diffractometer designed and built at the Instituto Tecnológico e Nuclear (ITN) named *Hotbird*[6]. This system can be set as a double-crystal diffractometer (DCD) or triple-axes diffractometer (TAD) allowing to cover a wide range of angular resolutions filling in the gap between the multiple-bounce TAD and the open detector DCD.

An 18 kW rotating anode generator with a fine line focus is the X-ray source of the *Hotbird*. As described in section 3.2, the radiation emitted by the anode comprises the *Bremsstrahlung* and

[6] To know more about the *Hotbird* visit: http://ma3t.itn.mces.pt/Main_Hotbird_2k.html

the copper characteristic lines. Note that the K_α line has the $K_{\alpha1}$ and $K_{\alpha2}$ components. In order to monochromatize the X-ray beam, a flat Ge (444) monochromator and two motorized divergence slits select Cu $K_{\alpha1}$ radiation and allow to adjust the angular resolution according to the type of experiment to be performed, up to a resolution limit of 30 arcsec. In the DCD configuration, the radiation emitted by the source is diffracted twice before being detected; the first in the monochromator crystal, and the second in the sample under consideration. The X-ray beam path is schematically represented in Fig. 3.9.

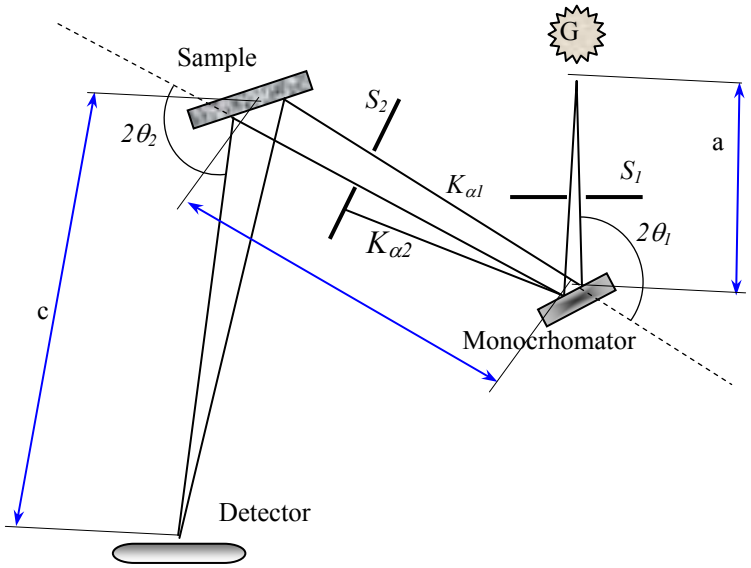

Figure 3.9: The X-ray beam path from the source to the detector.

The diffractometer uses the achromatic geometry. In this configuration, it is possible to eliminate the chromatic aberration as far as the distances *a*, *b* and *c* respect the following relation:

$$c = (a+b)\cdot\frac{\tan\theta_1}{\tan\theta_1 + 2\tan\theta_2} \qquad \text{(Eq. 3.15)}$$

The beam diffracted in the monochromator crystal is selected according to Bragg's law[7]. Then the $K_{\alpha1}$ line is selected in the slit S_2 and only this line will reach the sample and after being diffracted again will hit the detector.

The sample movement is performed by a high precision 4 axis Huber goniometer with a 0.001º reproducibility and a Huber XYZ 5102 position controller. The diffractometer axis that controls

[7] Note that the higher the diffraction angle the larger the angular spread between the different beam components; that is the reason we use the high order (444) reflection from Ge.

the sample angular movement (ω, ϕ and φ) and the x,y,z stage for sample positioning are schematically represented in Fig. 3.10

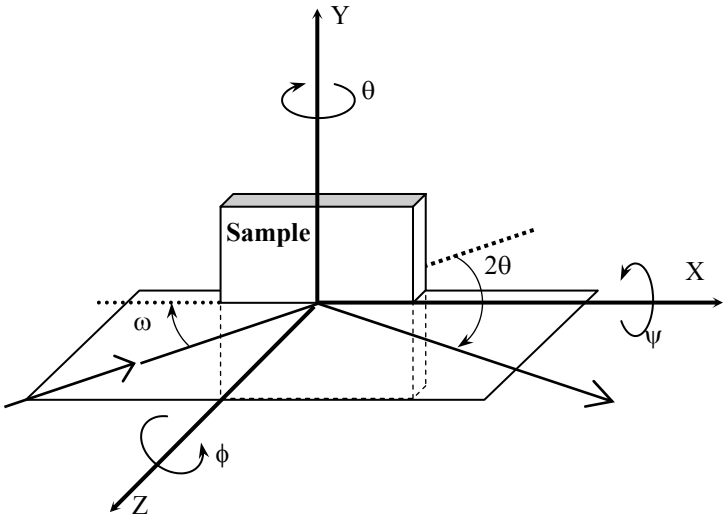

Figure 10: Schematic representation of the diffractometer axes

The forth axis of the goniometer (2θ) scans a position sensitive detector (PSD) Mbraun with 80μm resolution. A general view of the diffractometer is shown in Fig. 3.11.

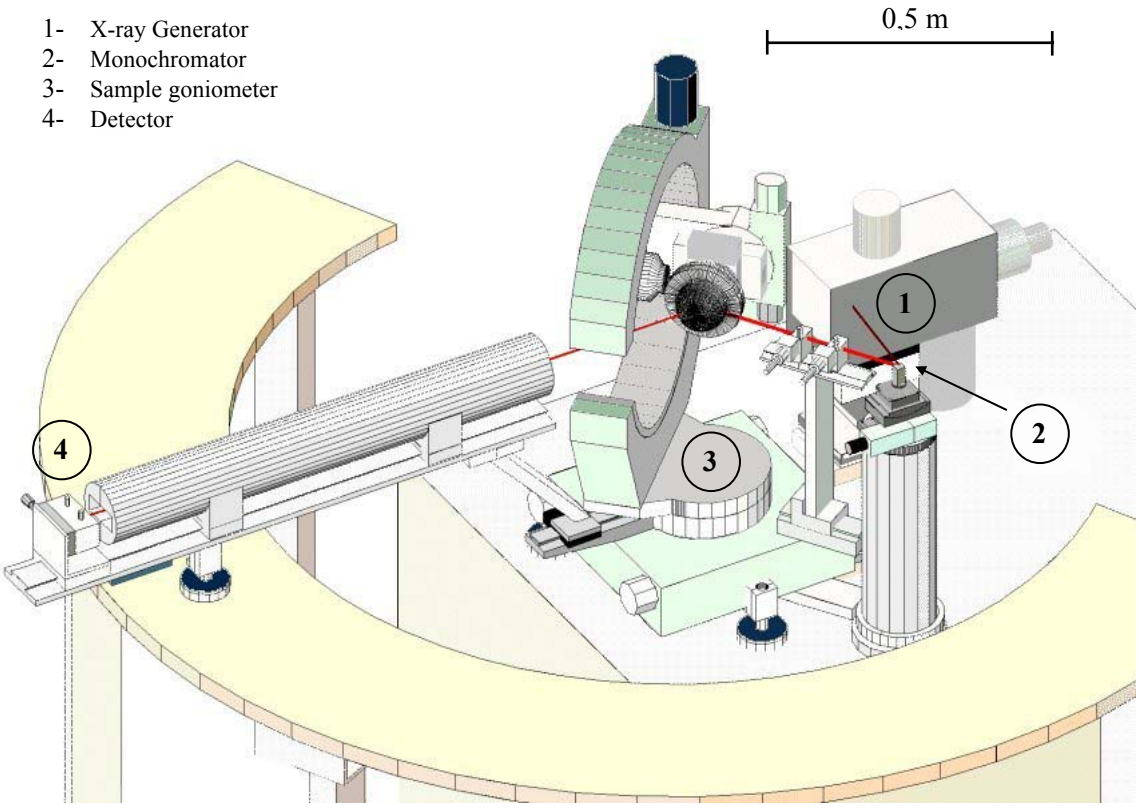

Figure 3.11: Schematic representation of the general view of the *Hotbird* diffractometer showing the positioning of the four main components of the experimental system.

This experimental setup has several advantages for the study of nitrides over more conventional X-ray systems. First, contrary to a conventional DCD incorporating a "point" detector, where X-ray counts diffracted from crystal planes are integrated over a range of 2θ subtended by the detector, the PSD spatially separates the X-ray counts in the 2θ direction. In a traditional DCD system, collection of a RSM adds a great expense in measurement time since 2θ is scanned each time ω is incremented. Consequently, collection times increase proportionally to the number of 2θ points required for the analysis. Therefore, by utilizing the PSD, RSMs can be more readily performed allowing the operator to extract more crystallographic information without an increase in measurement time.

The RSM measurement procedure in this setup consists in a sequence of a full 2θ acquisition for each ω step in the desired ω range. Then a two-dimensional map is constructed by overlapping all the one-dimensional measurements. Subsequently, the matrix of points (ω,2θ,I) covering the desired Bragg peak can be converted to reciprocal lattice units using a computer program. Another major advantage of the PSD for the case of the material system studied here is the ability to locate (and distinguish) very easily both GaN and InGaN related diffraction peaks over the 2θ range. A disadvantage results from the reduced dynamic range of the PSD, which is smaller that that of a conventional X-ray counting system by about two orders of magnitude. Angular resolution is also relatively poor compared with what can be obtained with a conventional system. This disadvantage is not relevant for nitrides, since the width of the diffraction peaks is much broader than the resolution limit. All measurements presented, if not otherwise indicated where performed in this experimental system.

3.8.2 Powder diffractometer

Some XRD measurements were performed on a Phillips X'Pert MPD diffractometer system, equipped with a curved graphite monochromator using Cu K_α radiation. This is a commercial powder diffractometer equipped with a proportional X-ray counter and it uses both the Cu $K_{\alpha1}$ and $K_{\alpha2}$ lines. This system provides a simple and fast way to perform θ-2θ symmetrical scan, and is therefore convenient for a routine analysis.

3.9 A survey of experimental results

3.9.1 Symmetric θ-2θ scans

A θ-2θ symmetric scan is the simplest XRD experiment that can be performed. It can be performed in a powder diffractometer or in a triple axis double crystal system. Here we show what information can be obtained from this experiment.

3.9.1.1 Results obtained with a powder diffractometer

In Fig. 3.12 a θ-2θ symmetric XRD scan from a relatively thick InGaN layer (AIX1025, t=355nm) grown on a GaN/Al_2O_3 substrate is presented.

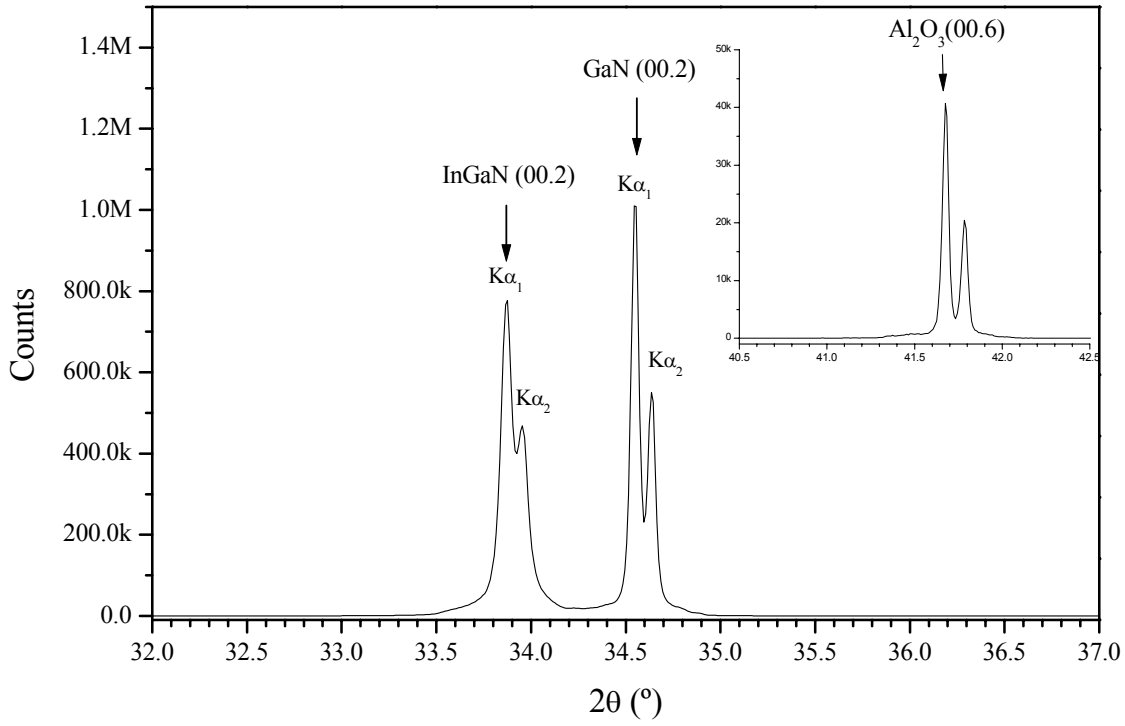

Figure 3.12: θ-2θ symmetric XRD scan from an InGaN/GaN/Al_2O_3 structure showing the nitrides (*00.2*) and the sapphire (*00.6*) diffraction peaks.

This spectrum was obtained in the Philips MPD powder diffractometer described earlier. Two peaks in the 2θ range from 32 to 36º compose the XRD profile. The peak at lower angle and of lower intensity, at 2θ=33.870º, corresponds to the InGaN film whereas the other peak, at higher angle 2θ=34.545º, corresponds to diffraction from the GaN buffer layer. The relative intensities of InGaN and GaN related peaks provide a rough indication of the InGaN layer thickness. In the inset to Fig. 3.12 the sapphire (*00.6*) peak is also shown at 2θ=41.675º. Note that diffraction peaks acquired in this diffractometer are all split into two components because both $CuK_{\alpha 1}$ and $CuK_{\alpha 2}$ are used for diffraction. As expected, the splitting between the two components and hence the apparent resolution, increases with the diffraction angle.

To obtain the InGaN, GaN and sapphire out-of-plane lattice constants, c, one needs only to combine Braggs equation (Eq. 3.1) and the interplanar spacing expression (Eq. 3.2) to obtain:

$$c = l * \lambda_{CuK\alpha 1,2} / (2 \sin \theta_{K\alpha 1,2}) \qquad \text{(Eq. 3.16)}$$

with l=2 in this case. For this sample, c_{InGaN}=5.289 Å, c_{GaN}=5.189 Å and c_{Al2O3}=12.993Å. The lattice constant obtained for sapphire is within 0.001 Å of the generally accepted value, confirming the good precision that can be obtained for the lattice constant measurement in this system.

From this simple XRD experiment one can obtain the GaN and InGaN lattice constants with a good precision, check if there are other InGaN or GaN polytypes (for instance a cubic phase), if there are phase separation effects, ordering effects, or metallic Indium droplet formation at the surface. Additionally, using the measured value of c_{InGaN} one can obtain an estimation of the film composition using Vegards' law [20].

In order to calculate the In content x from XRD results, using *only* the measured lattice constant c_{InGaN} one can use $x = (c_{InGaN}-c_{GaN})/(c_{InN}-c_{GaN})$: the value composition obtained for the sample is x=0.202. It is important to stress that this approach to estimate the composition is *only valid for fully relaxed layers*, this issue will be investigated in great detail in Chapter 6.

3.9.1.2 Double crystal diffractometer

In Fig. 3.13, we compare two θ-2θ XRD scans, obtained in the *Hotbird*.

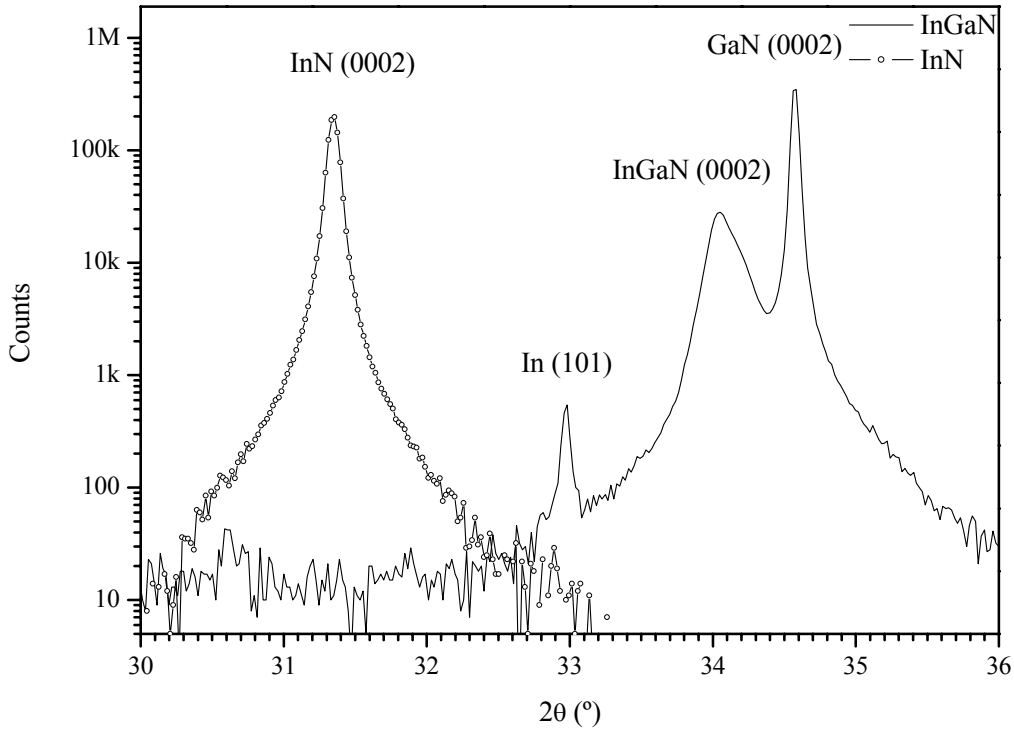

Figure 3.13: θ-2θ symmetric XRD scans from an InGaN/GaN/Al_2O_3 heterostructure (AIX1027) and a pure InN film showing the InGaN, GaN and InN (*00.2*) diffraction peaks. This InGaN film also features a peak, near 33º, due to the metallic In (*101*) diffraction.

As already mentioned, this diffractometer only uses the $CuK_{\alpha 1}$ line at *1.54056 Å*, and therefore for each diffraction plane we obtain a single XRD peak. The InGaN layer whose XRD spectrum is presented (S225E) is of poor surface quality and shows signs of metallic In droplet formation. The XRD pattern of pure InN[8] is also presented in Fig. 3.13. This comparison is useful to delimit the range of diffraction peaks belonging to the alloy that may appear between those of the two binary compounds according to Vegard's law. In particular, this would indicate the angular position expected if the InGaN layers show signs of macroscopic bimodal (InN+InGaN) phase separation, as theoretically expected according to the calculations of Ho and Stringfellow in Ref. [21].

The lattice constant obtained for c_{InN}=5.702 Å, is in excellent agreement with the expected value for relaxed InN. It should be noted that in none of the InGaN samples studied during this thesis, was an InN related peak fond for an InGaN film.

The weak diffraction peak at 2θ=32.97º corresponds to the *(101)* plane of metallic In stemming from droplets found at the surface of this film (see Section 2.2.1). It should be noted that it is relatively rare to find the metallic In peak in InGaN layers and this is only observed in poor quality samples, intended to be grown with high In content. There has been some confusion in the literature between the pure InN and metallic In diffraction peaks: the metallic In *(101)* peak has been misinterpreted as being the (*0002*) InN peak, and the appearance of this feature was reported as evidence for phase separation in the alloy [24,25].

3.9.1.3 Determination of layer thickness

Let us now consider the XRD spectra of InGaN layer (AEC51, *t*=55 nm), which is thin compared to the samples previously presented, and whose surface quality is found to be superior to that of the two last samples, as discussed in Section 2.5.1.

In this case we see in Fig. 3.14 the InGaN and GaN diffraction peaks, but clearly the relative intensitiy of InGaN relative to GaN related peak is smaller than in previous examples, as might be expected for a thinner InGaN film. A modulation of the InGaN related diffraction peak (c_{InGaN}=5.252 Å) is also evident in the spectrum. Satellite (SL_i) peaks up to the 3rd order indicate a uniform thin film with good surface quality as would be expected from the SEM and AFM results on this sample. Note that in previously considered InGaN layers with poorer surface quality no interference fringes were observed.

The subsidiary maxima of the diffraction curve of a layer, also called *thickness fringes*, can be explained as a result of interference.

[8] The MBE grown InN layer was kindly provided by Professor Y. Nanishi of Ritsumeikan University (Japan), details can be found in Ref. [23].

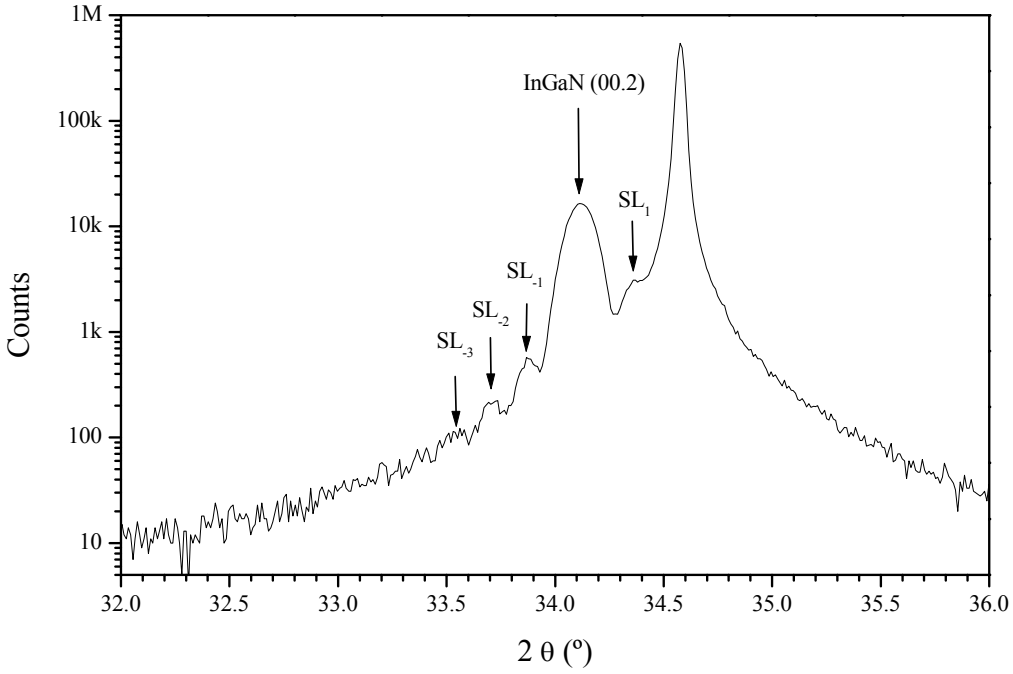

Figure 3.14: *θ-2θ* symmetric XRD scan from an InGaN/GaN/Al_2O_3 heterostructure (AEC51) showing the thickness fringes subsidiary to the main InGaN (*00.2*) peak.

From the angular separation of adjacent maxima one can readily obtain the layer thickness. Using Braggs' equation, which gives the simplest transform from scattering to real space, we write for scattering from planes parallel to the surface:

$$2t\sin\theta_i = n_i\lambda \qquad \text{(Eq. 3.17a)}$$

$$2t\sin\theta_{i+1} = n_{i+1}\lambda \qquad \text{(Eq. 3.17b)}$$

hence,

$$t = \frac{(n_i - n_{(i+1)})\lambda}{2(\sin\theta_{ni} - \sin\theta_{n(i+1)})} \qquad \text{(Eq. 3.18)}$$

where n_i is the order of the fringe, λ the radiation wavelength and θ_{ni} the angular position of the adjacent maxima [5]. For this sample a thickness of 50±5 nm is estimated.

3.9.2 *w-2θ* diffraction maps

As previously mentioned, in the *Hotbird* diffractometer, the PSD collects the X-rays simultaneously over a *2θ* range. Therefore one can obtain, at the same time and in the same measurement, a combination of *θ-2θ* scans and rocking curves, i.e. *ω* scans for set values of *2θ*.

In Fig. 3.15 we present the full ω-2θ contour map obtained for the same sample shown in Fig 3.14. All contour or 3D XRD maps shown in this thesis are on a logarithmic scale of intensity.

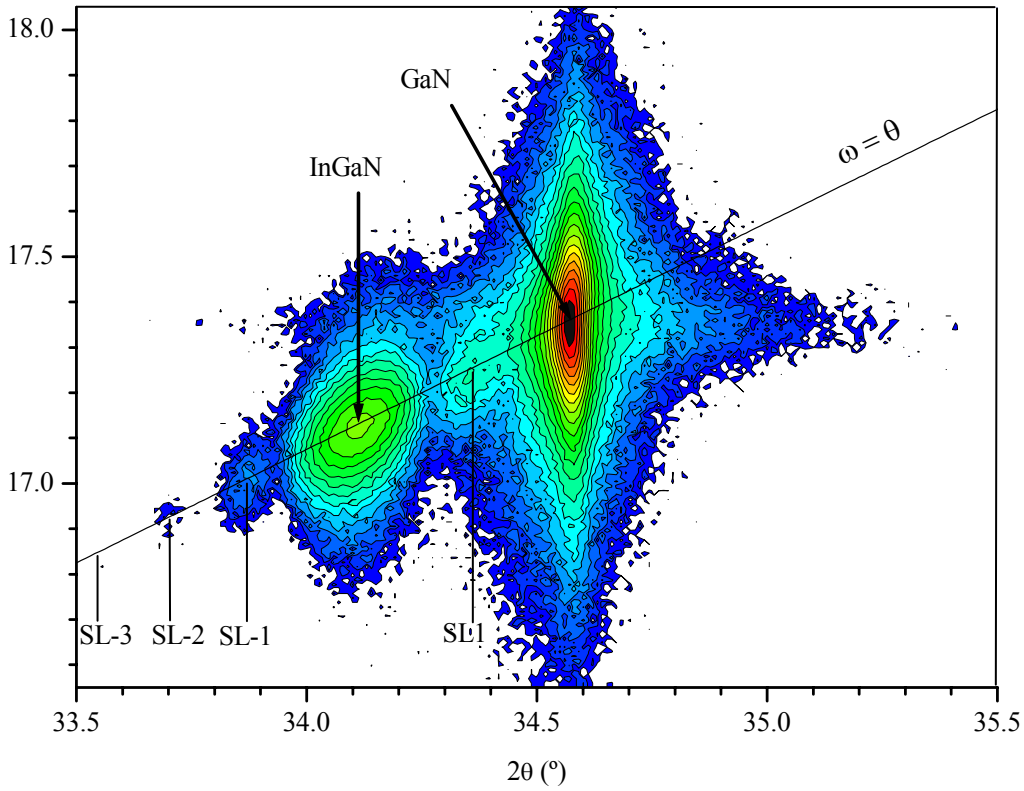

Figure 3.15: ω-2θ map of the InGaN and GaN (*00.2*) reflections for sample AEC51.

The θ-2θ spectrum in Fig. 3.14 was obtained by integrating all the counts obtained in the ω range considered. In a typical DCD the collection would only be along the line ω=θ indicated in the Fig. 3.15. Consequently, there is no information along ω. One of the advantages of collecting the full map is that we can immediately identify tilts between the different layers. In addition, analysing the XRD profile along the ω directly provides information about the degree of *mosaic spread* in the different layers. The spectral broadening along the ω direction is due to tilting between the mosaic blocks that compose the nitride heterostructure. We describe these below.

3.9.2.1 Mosaic structure

All III-nitrides grown so far on sapphire or SiC substrates show some columnar hexagonal habit typically designated as *mosaic structure*. This means they consist of a large number of small nearly perfect hexagonal prisms with their basal (*00.1*) plane approximately parallel to the substrate surface. The diameter of the individual columns ranges from some nm to about 1μm. The basal planes of the individual crystallites can be slightly tilted with respect to each other

and the individual column axes tilted with respect to each other. The degree of tilting and twisting determines the macroscopic crystal quality. Microscopically, the tilting is correlated with the mixed threading dislocation and twisting to the edge threading dislocation density [26]. A schematic diagram of the mosaic structure found in nitrides is shown in Fig. 3.16.

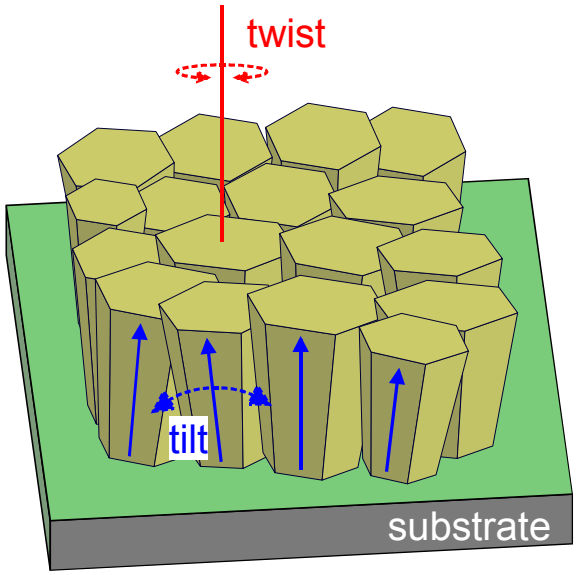

Figure 3.16: Schematic representation of the mosaic structure of nitride layers.

Typically, GaN mosaic blocks on sapphire have a tilting distribution over an angular range between 0.05º and 0.2º. Information on the mosaic tilt distribution can be directly obtained by analysing the map along the ω direction for a specific 2θ, equivalent to a rocking curve. The width along 2θ reflects the lattice constant distribution, whereas the broadening along ω in a symmetrical scan reflects the angular spread of the scattering planes. The 2θ range over which the ω scan is performed defines what part of the film we are analysing through its lattice constant.

3.9.2.2 Conversion to reciprocal space representation

The physical properties of the epitaxial layers under study are better evidenced if the maps are shown in the reciprocal space. For example, the map shown in Fig. 3.15 can be converted to the reciprocal space by using equations (Eq. 3.7). The ω-2θ map in RS coordinates q_x and q_z is shown in Fig. 3.17.

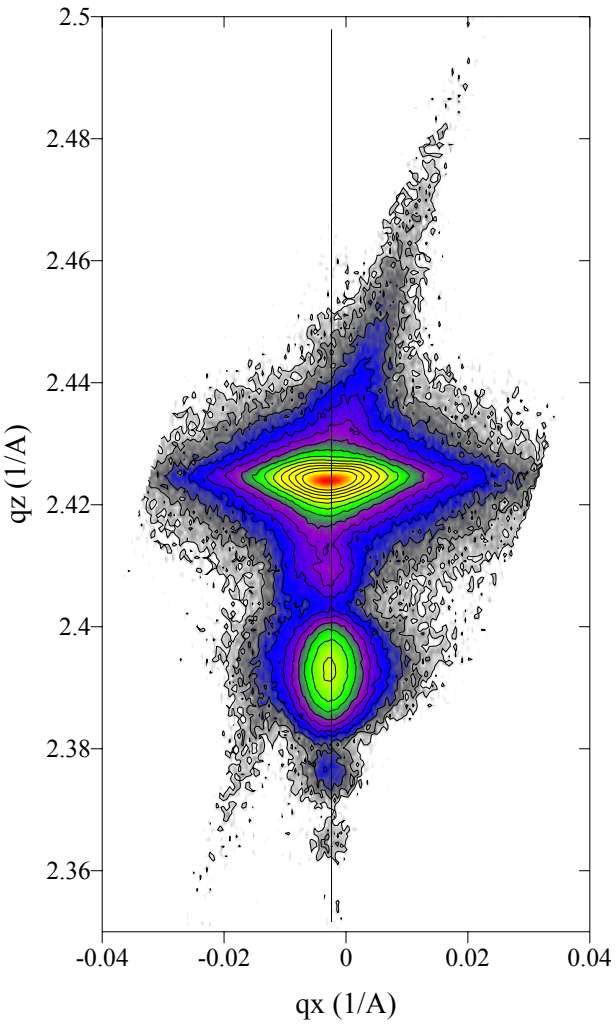

Figure 3.17: Asymmetric reciprocal space map of the InGaN and GaN (*10.5*) reflections for sample AEC51

The InGaN and GaN related RLP alignment along q_x reveals a perfect alignment with (no macroscopic tilts) between the two layers. In the map one can also identify some broadening along q_x, a mosaic spread due to tilting of the mosaic blocks. The diagonal streak along the former 2θ direction is the detector streak; its appearance is due to the very high intensity of the GaN related diffraction and is not relevant for the analysis. A signal spreading of the RLPs along q_z would indicate gradients of the *c* lattice constants.

3.9.3 Asymmetrical reciprocal space mapping

As previously mentioned, symmetrical maps contain information only about the *c* lattice constants of the hexagonal structure. Therefore to obtain information on the in-plane lattice constants *a* an asymmetrical RSM is required. In Fig. 3.18, we present such a map, in this case performed on the (*10.5*) planes.

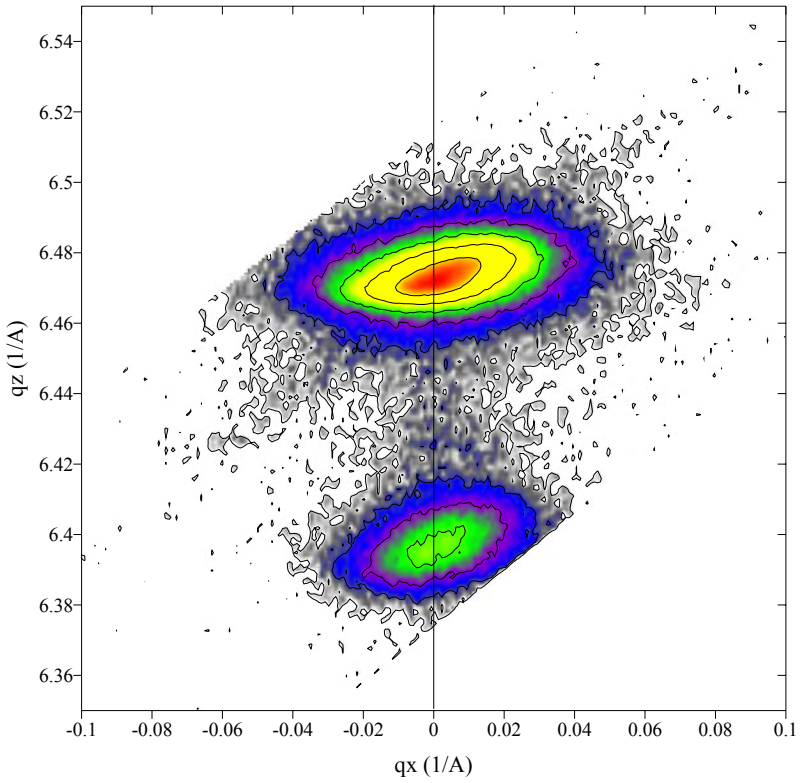

Fig 3.18: Asymmetric reciprocal space map of the InGaN and GaN (*10.5*) reflections

The first important aspect to mention is that experimentally it is much more difficult to obtain an asymmetrical RSM. The peak intensity is very much lower, and it is difficult to find the planes of interest. One should take into account that the *c/a* ratio variation in InGaN for different values of *x* and strain, means that the angles between InGaN crystal planes vary from sample to sample. Also, the sample alignment and detector positioning is critical in this case [27].

In this map it is easy to identify that the ω range would have been larger if the full RLP had been collected. This gives us a feeling on how the RSM is collected in sections as described in Section 3.7, and shows the broad nature of nitride related RLPs.

Again two diffraction peaks are observed in the range collected. The stronger RLP at larger q_z belongs to the GaN buffer. Note that the positioning along q_x and q_z are inversely proportional to the *a* and *c* lattice constants, respectively. Therefore, and since the GaN and InGaN RLP are aligned along q_x, one can immediately conclude that this InGaN film has grown pseudomorphically, i.e. has the same *a* lattice constant as the GaN buffer layer.

3.9.4 Analysis of InGaN layers featuring double XRD peaks

So far we have discussed XRD patterns where there is only one InGaN related peak. Quite interestingly some InGaN layers feature a double XRD peak. Double XRD peaks were found

for InGaN layers of intermediate thickness (100-200nm) for the typical composition range ($0.1<x<0.2$) studied. The common feature in these samples is a rough 3D-like surface. The conditions under which this phenomenon is verified are clarified and discussed in detail in Chapters 6 and 7. Figure 3.19 presents a ω-2θ XRD map of sample S102 (t_{InGaN}=180 nm).

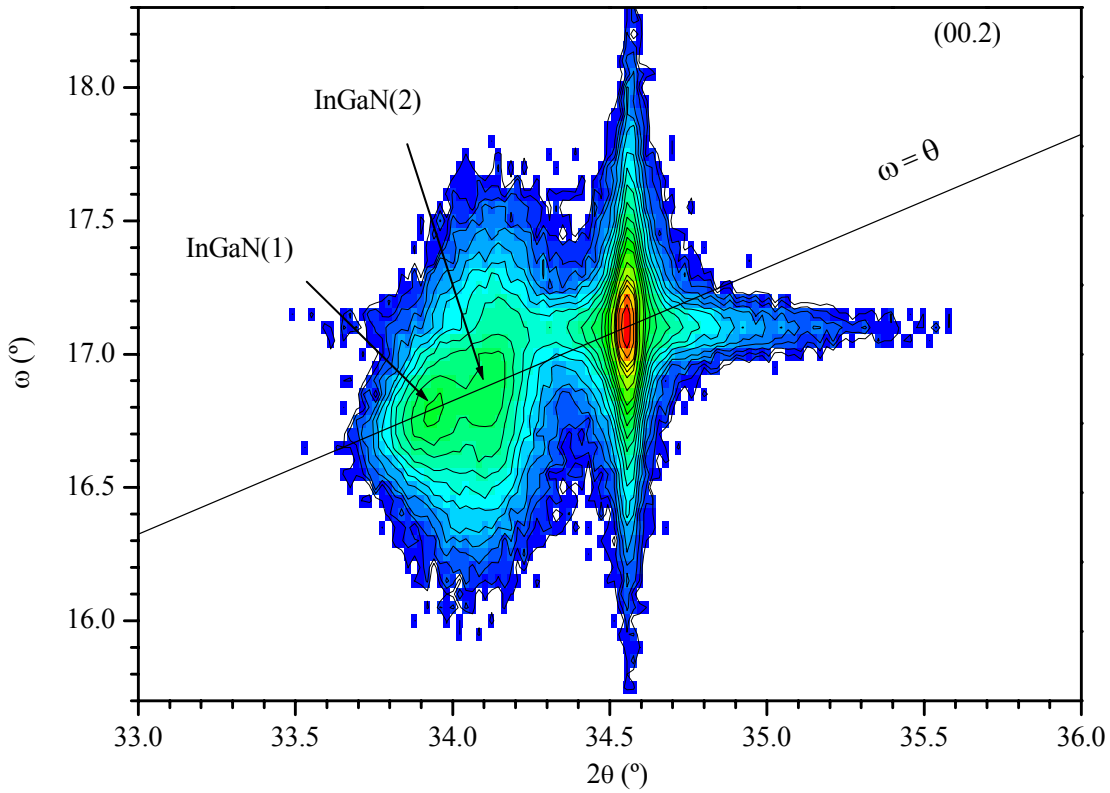

Figure 3.19: ω-2θ map around the GaN and InGaN (*00.2*) diffraction peaks for the layer under study, S102. The $\omega=\theta$ line corresponds to a θ-2θ scan. Labels (1) and (2) refer to the InGaN regions discussed in the text

Two diffraction peaks corresponding to the InGaN layer, labelled InGaN(1) and InGaN(2), can be clearly observed in addition to the much stronger GaN peak at 2θ=34.55º. Note that the width of the InGaN(2) peak, at higher 2θ and therefore lower *c* lattice constant, along ω is larger. This indicates a lower crystalline quality in this InGaN sub-region.

To improve the angular resolution of the doublet a θ-2θ scan on the (*00.6*) reflection is shown in Fig. 3.20. To help to disentangle the two components, and extract the peak positions precisely, a fit to two voigt functions is also shown. Note that InGaN (2) is also broader along 2θ, meaning that this region is also more heterogeneous in terms of spreading of *c* lattice constants.

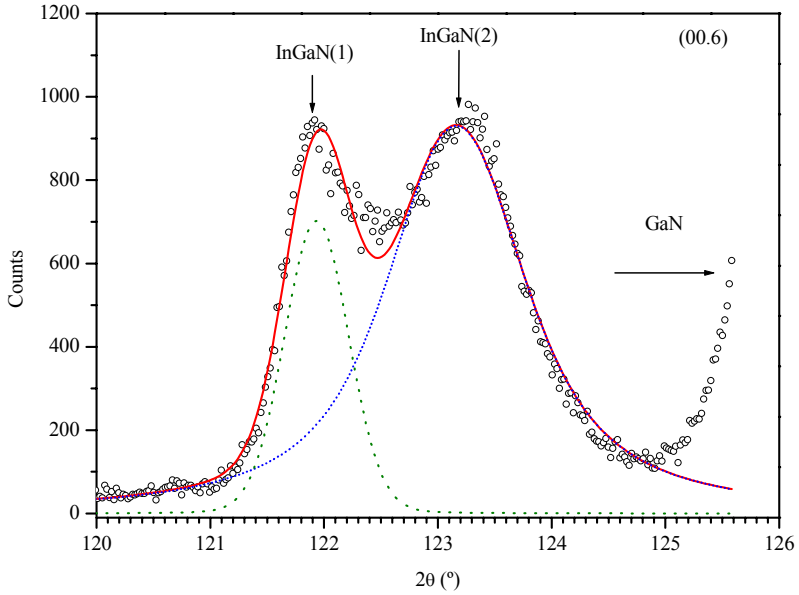

Figure 3.20: *θ-2θ* scan on the InGaN (*00.6*) reflections fitted to two Voigt functions. Labels (1) and (2) refer to the InGaN regions discussed in the text.

For this layer, two values for the InGaN lattice parameters $c_{InGaN}(1)$= 5.286 Å and $c_{InGaN}(2)$= 5.255 Å, are calculated directly from the peak positions in Fig. 3.20.

To get a better insight on this issue, an asymmetrical RSM of the InGaN/GaN structure under study, measured around the (*10.5*) reflection, shown in Fig. 3.21, was performed.

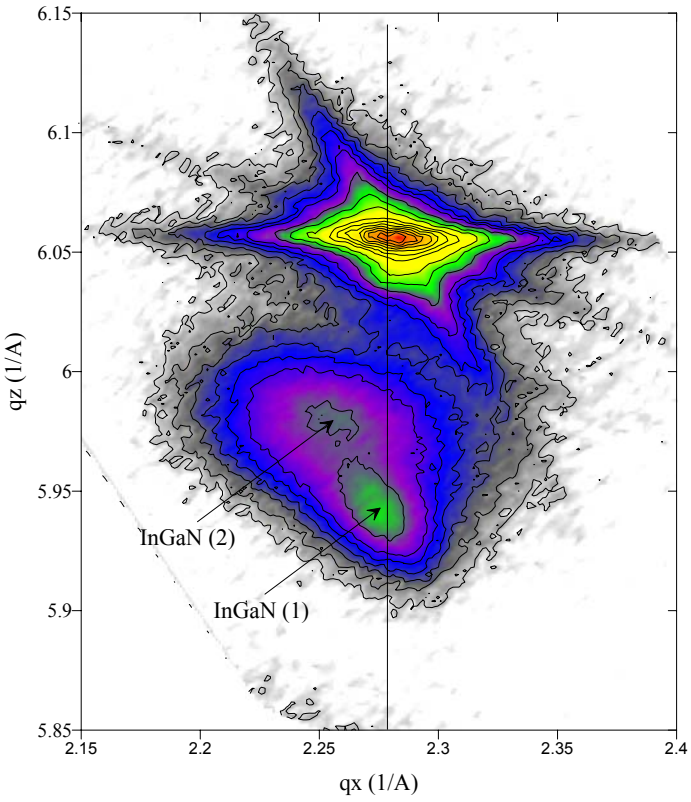

Figure 3.21: Asymmetric reciprocal space map of the InGaN and GaN (*10.5*) reflections of sample S102.

The RSM confirms that two peaks compose the diffraction profile of the InGaN film. Additionally, we can note that one of them is nearly aligned with the GaN diffraction maximum along q_x, the reciprocal space vector in the plane of the layers. From this, it is apparent that one of the sub-regions, InGaN(1), has practically the same in-plane lattice constant as the underlying GaN buffer layer. This InGaN region has a *higher* out-of-plane lattice constant $c_{InGaN}(1)$, as seen by the peak position relative to q_z. On the other hand, the second diffraction peak corresponds to a larger value of $a=a_{InGaN}(2)$ and a smaller value of $c=c_{InGaN}(2)$. From the asymmetric scan, the lattice constants $a_{InGaN}(1)=3.186$ Å and $a_{InGaN}(2)=3.220$ Å, are determined.

These results show that the InGaN(1) component is fully strained to the underlying GaN buffer. Therefore it does not make sense to apply Vegards' law to this component. The details on the errors that can be made using this approach, and a more correct method to determine composition in biaxial strained InGaN samples using both *c* and *a* lattice constants, will be discussed in Chapter 6 of this thesis.

3.9.4.2 In-Plane Diffraction

In plane XRD can depth-locate the regions contributing to the double XRD peak in this layer [36]. This variant of the XRD technique was used to measure the InGaN lattice constants only for the first few tens of nanometers (~50nm) of film near the surface. This can be accomplished by making use of the small penetration of the beam when its incident angle is close to the critical angle (~0.3º) for reflectivity. The X-rays penetrating into the surface region of the sample can be used to scatter from planes approximately normal to the surface plane. The depth penetration limit for this type of geometry is governed by the path X-rays have to take [5]. The (*10.0*) diffraction peak acquired under these conditions is shown in Fig. 3.22.

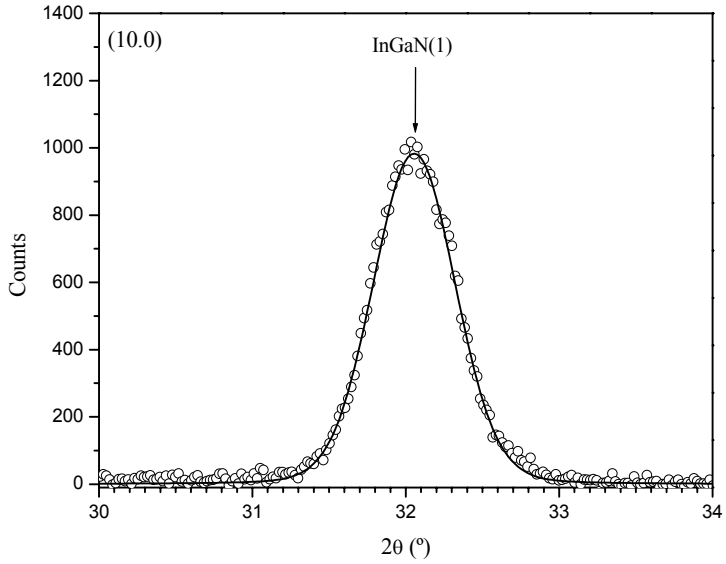

Figure 3.22: In plane X-ray diffraction peak from the (*10.0*) InGaN planes near the surface fitted to a Voigt function.

Only one XRD peak is found under shallow penetration conditions. From the 2θ position one can calculate the lattice constant a_{InGaN} (at the surface) directly. A value of a_{InGaN} (surface)=3.220 Å, identical to $a_{InGaN}(1)$, is determined. This result demonstrates that the two diffraction components, observed in Figs 3.19-3.21, originate from different depths of the InGaN film. With this example we show that the second component InGaN(1), the relaxed part of the film, originates from the surface region illustrating the usefulness of in-plane diffraction to investigate structural features in InGaN layers.

3.9.5 XRD analysis of MQWs

XRD can also provide rich structural information on InGaN MQWs. In these more complex structures the interpretation of X-ray scattering has usually to be based on a careful and systematic analysis, since scattered waves interfere because of the multiplicity of layers, and may produce rather complicated patterns. The added X-ray diffraction peaks that result from the artificially introduced periodicity of the MQW are called *satellites*. And we will refer to the added points in reciprocal space as satellites also. The (*00.2*) symmetrical RSM of a InGaN/GaN 8-period MQW sample (STR120) is shown in Fig. 3.23

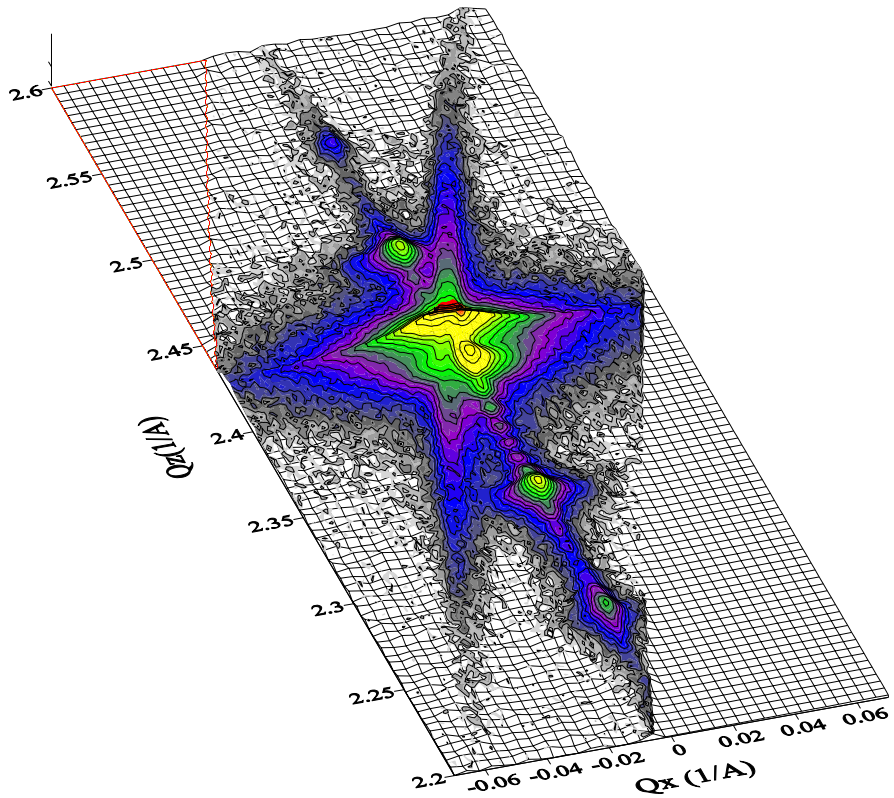

Figure 3.23: 3D contour plot of a symmetrical XRD RSM on the (*00.2*) reflection a 8-period InGaN/GaN MQW STR120.

The XRD spectrum is notably more complex than those corresponding to single InGaN films. The observation of various satellite orders indicates a good interface quality of the MQW structure, and their perfect alignment along q_x demonstrates that the MQW has grown aligned with the GaN buffer, i.e. no macroscopic tilts exist between the different layers in the stack. This has been systematically observed for all InGaN/GaN structures studied.

The (*10.5*) asymmetrical RSM of the same structure is shown in Fig. 3.24

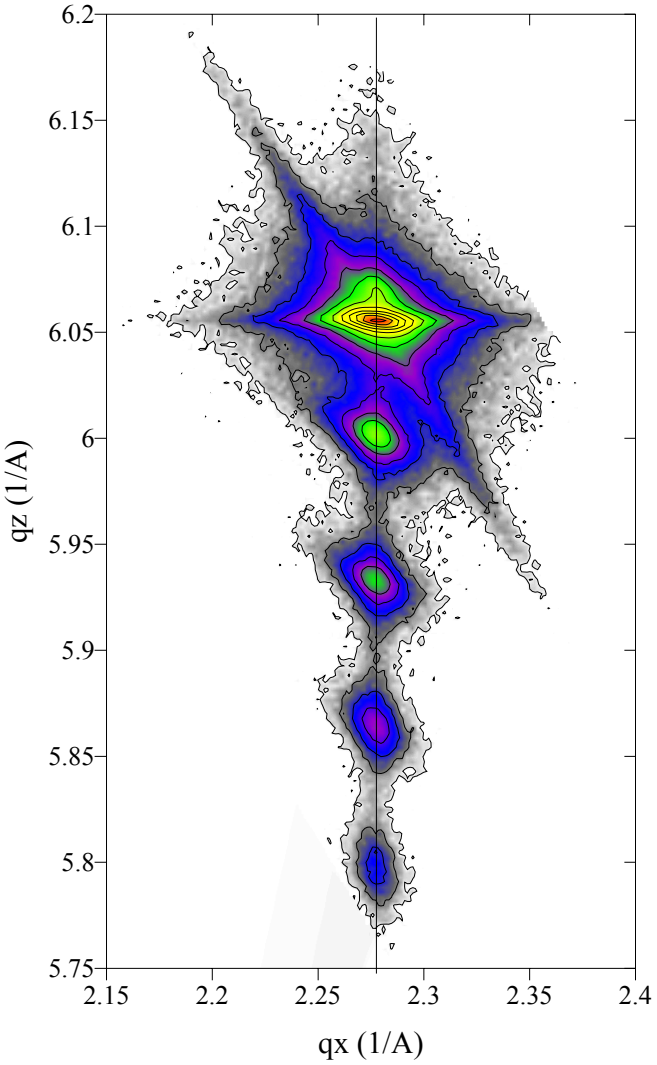

Figure 3.24 Contour plot of a asymmetrical (*10.5*) XRD RSM reflection on the MQW sample STR120.

The asymmetrical map allows the MQW's relaxation state to be explicitly determined. As can be seen the MQW RLPs, or satellites, are in both cases aligned along Q_x. This shows that the MQWs grew coherently on the GaN buffer, and no strain relaxation can be detected within the sensitivity limits of the measurement [29].

3.9.5.2 Simulation of XRD θ-2θ profiles

Knowing only the multilayer relaxation state, one can simulate the XRD profile using the dynamical diffraction theory[9] to obtain more structural information about the MQW under consideration.

The parameters required for the simulation, which are normally well defined, are the X-ray line used, the plane under consideration, the instrumental broadening, the substrate material and orientation, and the degree of relaxation of the structure. Normally the parameters to determine, and which fitted by refinement, are the thickness and composition of InGaN well and GaN barrier. In Fig. 3.25 the experimental and simulated XRD spectra are compared for the MQW sample STR120.

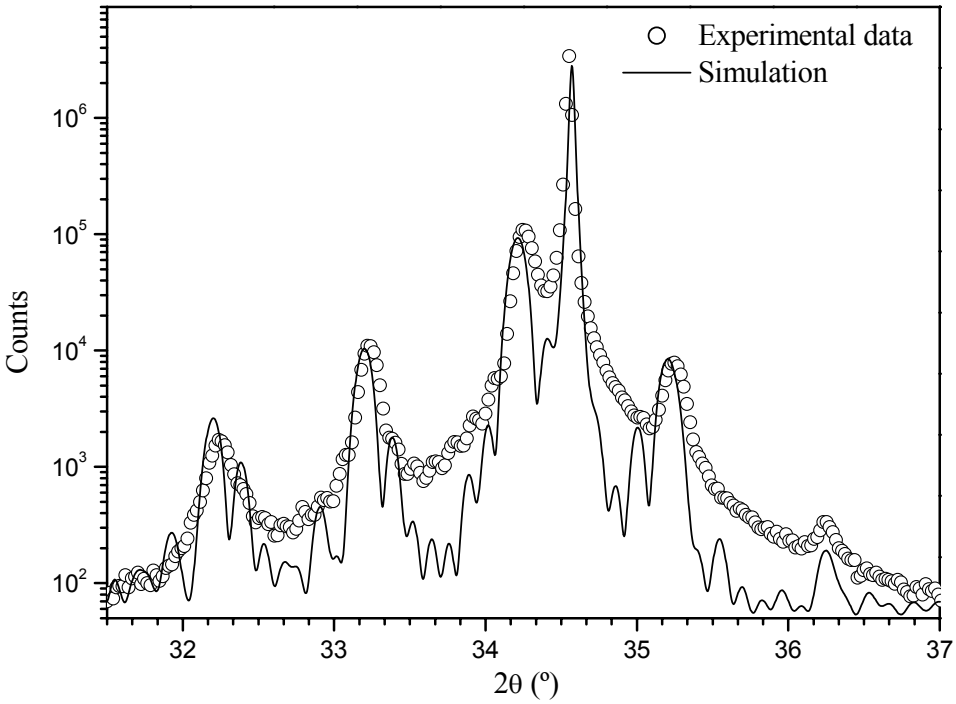

Figure 3.25 Simulated and experimental θ-2θ symmetric XRD scan from a 8-period InGaN/GaN MQW sample STR120, around the (*00.2*) reflections.

The simulation program used was MADMAX[10]. The simulations are based on the dynamical diffraction theory, and the model used in MADMAX is valid for highly mismatched group-III nitride heterostructures [37]. The simulations are done for perfect interfaces and are convoluted

[9] In simple terms, the *dynamical scattering theory* takes into account multiple scattering processes, and therefore represents a more rigorous physical description than that obtained under the *Kinematical approximation*.

[10] The MADMAX software was kindly loaned by Dr. Olivier Brandt from Paul Drude institute in Germany.

with the instrumental resolution only. A model consisting of an 8 period MQW with an average GaN barrier thickness (t_B=6.75nm) and InGaN well thickness (t_w=2.74nm) with an average well composition x_{well}=0.197, provides a reasonable fit to the XRD data. The model structure deduced is fairly close to the nominal values and in good agreement with TEM, and RBS determined values, as discussed in Ref. [38].

3.10 Summary

In this chapter it was shown that XRD provides rich microstructural information about InGaN/GaN heterostructures. Besides the introduction to the technique itself, and the fundamental background to understand the experimental results, we have learned what type of information is obtained by the different variants of the XRD technique.

Starting from the simplest XRD experiment which can be performed in a powder diffractometer, i.e. a symmetric θ-2θ scan around the GaN and InGaN and the Al_2O_3 diffraction peaks, it was shown how to determine the *c* lattice constants of the different layers composing the heterostructure. It was also illustrated how XRD allows the different phases that might exist in the film to be identified. In particular, XRD readily confirmed the existence of metallic In droplets in a poor quality InGaN film. However, in the InGaN films studied in this thesis, no signs of an InN-related XRD component were detected.

It was also shown how the modulation of the XRD spectra can determine the layer thickness for layers with good surface and interface quality. We have also learned how a reciprocal space map can yield further information about microstructural details of the InGaN/GaN films. In particular, it was shown how macroscopic tilts between the different layers can be immediately detected by interpretation of a symmetrical RSM. Again, none of the InGaN/GaN films studied here showed any tilt between the various layers.

The methodology for simultaneous measurement of *c* and *a* lattice constants via asymmetric RSM was introduced. It was shown how direct comparison of the InGaN and GaN RLP allows determination of the coherency of the InGaN film relative to the GaN pseudo substrate. The particular case of InGaN/GaN films showing two InGaN related diffraction peaks was treated. It was found that the component with a lower *c* lattice constant is broader, in the ω and 2θ directions, indicating a poorer crystal quality. A detailed asymmetrical RSM showed that the component with larger *c* is almost perfectly aligned along q_x indicating that this InGaN component has the same lattice constant as the GaN substrate. By using in plane diffraction, it was shown that the relaxed part of the InGaN layer originates from the surface region.

Finally, we have shown how MQWs feature a rather complex XRD structure and illustrated how simulation of the XRD profiles allows fundamental structural parameters, such as well/barrier thickness and composition, to be extracted.

3.11 References:

[1] M. J. Buerger *"Crystal-structure analysis"* John Wiley, New York (1967).

[2] B. E. Warren *"X-ray diffraction"* Addison-Wesley, Massachusetts (1969).

[3] B. D. Cullity *"Elements of X-ray diffraction"* 2nd ed. Addison-Wesley, Reading (1978).

[4] C. Kittel *"Introduction to solid state physics"* 7th ed. John Willey, New York (1996).

[5] P. F. Fewster "*X-ray scattering from semiconductors*" Imperial College Press, London, UK (2001).

[6] Günter Bauer and Wolfgang Richter (Eds.) *"Optical characterization of epitaxial semiconductor layers"* Springer-Verlag, Berlin (1996).

[7] B. K. Tanner Advances in X-ray analysis **33**, 1 (1990).

[8] P. F. Fewster J. Appl. Cryst. **24**, 178 (1991).

[9] P. F. Fewster Appl. Surf. Sci. **50**, 9 (1991).

[10] P. F. Fewster Semicnd. Sci. Technol. **8**, 1915 (1993).

[11] T. Picraux, B. L. Doyle, J. Y. Tsao in "*Semiconductors and semi Metals*", T. P. Pearsall Ed., Academic Press, New York (1991).

[12] C. R. Wie Mater Sci. and Eng. **R13**, 1 (1994).

[13] V. Holý, U. Pietsch and T. Baumbach *"High resolution X-ray scattering from thin films and multilayers"* Springer-Verlag, Berlin (1999).

[14] P. F. Fewster Crit. Rev. Sol. State and Mater. Sci. **22(**2), 69 (1997).

[15] H. Amano and I. Akasaki *"Properties, processing and applications of gallium nitride and related alloys"*, J. H. Edgar, S. Strite, I. Akasaki, H. Amano, C. Wetzel, Eds., INSPEC, London, (1999).

[16] P. F. Fewster, N. L. Andrew, C. T. Foxon J. Cryst. Growth **230**, 398 (2001).

[17] M. Schuster, P. O. Gervais, B. Jobst, W Hösler, R. Averbeck, H. Riechert, A. Iberl and R. Stömmer, J. Phys. D: Appl. Phys. **32**, A56 (1999).

[18] A. Krost in *"Nano-optoelectronics: concepts, physics and devices"*, M. Grundmann Ed., Springer, Berlin (2002).

[19] W. H. Bragg and W. L. Bragg Proc. Roy. Soc London (A) **88** 428 (1913).

[20] L. Vegard, Z. Phys. **5**, 17 (1921).

[21] I. Ho and G. B. Stringfellow, Appl. Phys. Lett. **68**, 2701 (1996).

[22] W. Paszkowicz, Powder Diffraction **14**, 258 (1999).

[23] Y. Nanishi, Y. Saito, T. Yamaguchi, M. Hori, F. Matsuda, T Araki, A. Suzuki, T. Miyajima, phys. stat. sol. (a) **200**, 202 (2003).

[24] R. Singh, D. Doppalapudi, T. D. Moustakas, and L. T. Romano, Appl. Phys. Lett. **70**, 1089 (1997).

[25] D. Doppalapudi, S. N. Basu, K. F. Ludwig , and T. D. Moustakas, J. Appl. Phys. **84**, 1389 (1998)

[26] T. Metzger, R. Hopler, E. Born, O. Ambacher, M. Stutzmann, R. Stommer, M. Schuster, H. Gobel, S. Christiansen, M. Albrecht, H. P. Strunk, Philos. Mag. **A77**, 1013 (1998).

[27] N. Franco, S. Pereira and A. D. Sequeira, Mater. Sci. Forum **455**,132 (2004).

[28] C. J. Deatcher, C. Liu, S. Pereira, M. Lada, A. G. Cullis, O. Brandt and I. M.Watson, Semicond. Sci. Technol. **18** 212 (2003).

[29] S. Pereira, M. R. Correia, E. Pereira, K. P. O'Donnell, C. Trager-Cowan, F. Sweeney, E. Alves, A. D. Sequeira and I. M. Watson*,* phys. stat. sol. (b) **228** , No.1, 59 (2001).

[30] S. Pereira, M. R. Correia, E. Pereira, K. P. O'Donnell, E. Alves, N. P. Barradas, A. D. Sequeira, N. Franco, I. M. Watson, and C. Liu, Phys. Stat. Solidi (c) **0**, 302, (2002).

[31] N. A. El-Masry, E. L. Piner, S. X. Liu and S. M. Bedair, Appl. Phys. Lett. **72**, 40 (1998).

[32] Yong-Tae Moon, Dong-Joon Kim, Keun-Man Song, In-Hwan Lee, Min-Su Yi, Do-Young Noh, Chel-Jong Choi, Tae-Yeon Seong, and Seong-Ju Park *,* Phys. Stat. Sol. (b) **216** 167 (1999).

[33] D. Rudolff, Phys. Stat. Sol. (b) **216**, 315 (1999).

[34] M. Katsikini, E. C. Paloura, F. Boscherini, F. D'Acapito, C. B. Lioutas and D. Doppalapudi, Nucl. Inst. Meth. B, **200**, 114 (2003).

[35] Z. C. Feng, T. R. Yang, R. Liu, T. S. A. Wee, International Journal of Modern Physics B, **16**, 268, (2002).

[36] S. Pereira, M. R. Correia, E. Pereira, K. P. O'Donnell, C. Trager-Cowan, F. Sweeney, E. Alves, A. D. Sequeira and I. M. Watson*,* phys. stat. sol.(b) **228** , No.1, 59 (2001).

[37] O. Brandt, P. Waltereit, and K. H. Ploog, J. Phys. D **35**, 577 (2002).

[38] C. J. Deatcher, C. Liu, S. Pereira, M. Lada, A. G. Cullis, O. Brandt and I. M. Watson Semicond. Sci. Technol. **18** 212 (2003).

Chapter 4: RBS characterization of InGaN/GaN layers

Overview

This chapter describes the basic principles of the Rutherford backscattering spectrometry (RBS) analytical technique. It provides the necessary background for a better understanding of the structural characterisation results obtained by RBS in InGaN/GaN heterostructures. First, we discuss the application of RBS to the determination of layer thickness and composition in InGaN/GaN/Al_2O_3 single layers through simulation of the random experimental spectra. We then consider the use of RBS/C for the assessment of strain and crystalline quality in these structures. The results obtained by grazing incidence RBS experiments, allowed thickness and composition of *individual wells* to be measured directly for the first time in InGaN/GaN MQWs. Finally, we will briefly discuss a novel method developed to estimate surface roughness by RBS, valid for any film, but with particular emphasis on the material system studied in this thesis.

4.1 Introduction

The principle of Rutherford Backscattering spectrometry (RBS) dates back to the classic Rutherford experiments of the early 1900s [1,2]. The major steps required to develop a widely used analytical technique came together with rapid developments in the field of nuclear technology. The radioactive isotopes used as α-particle sources by Rutherford, Geiger and Marsden were substituted by more convenient (in terms of particle energy and flux) and increasingly common, particle accelerators. Additionally, the developments of nuclear electronics combined with solid state detectors and application of personal computers for data reduction contributed to mature the technique, and make it relatively simple and more user-friendly.

Nowadays RBS is a well-established technique to identify and depth-profile, on a nanometer depth scale, the elemental composition of thin films [3-7]. Composition can be determined non-destructively, and free from the effects of strain, with precisions down to ~1% (in the best cases) without using external standards. Additionally, RBS combined with the channelling effect (RBS/C), allows an evaluation of crystalline quality and determination of the strain state in epitaxial layered structures [4-10].

4.2 Basic physical principles of Rutherford backscattering

Two books give a detailed description of the relevant aspects of backscattering spectrometry. In Ref. [7] Chu *et al.* deal with Rutherford Backscattering and related techniques, whereas Feldman and Mayer discuss other analytical techniques as well in Refs [3,4].

The large angle scattering of MeV energy alpha particles by a gold foil, observed by Rutherford, established the atomic model of a positively charged heavy nucleus surrounded by a negatively charged electron cloud [1]. While in those experiments the alpha particles were obtained from the decay of radioactive nuclei, nowadays accelerators are used to obtain a monoenergetic beam of light particles, usually H^+ or He^+. The beam strikes a target, where a small[1] fraction the incident particles which collide directly with the nuclei of the target material are scattered backwards, and then detected.

During the event of backscattering of a charged particle, there are four fundamental physical principles that provide the basis of quantitative materials analysis. The phenomena describe different aspects of RBS that provide four *independent* pieces of information, summarized as follows:

Principle		***Information provided***
Kinematic cross section	$K \Rightarrow$	Mass identification
Scattering cross section	$\sigma \Rightarrow$	Concentration
Stopping cross section	$\varepsilon \Rightarrow$	Depth scale
Min. channelling yield	$\chi \Rightarrow$	Lattice defects (evaluation of strain and crystal quality)

The processes involved are classical, and easily quantifiable: from the energy of the backscattered particles (k) the target's elemental composition can be determined; from their intensity (σ), one determines the target's elemental concentration; and from the energy loss (ε) of the particles while penetrating and coming out of the target, the target's elemental depth distribution is determined. The wide use of the Rutherford backscattering technique, based on Rutherford's old experiment, provides answer to 3 questions: "*What* is the sample made of*?"*, "*How much* of each chemical element*?"*, and "*Where* is a given chemical element located in terms of depth*?"*.

In addition, for the case of crystalline targets, RBS combined with the channelling effect can also provide information about the crystalline quality. The degree of crystalline quality can be correlated with χ, which is defined as the ratio between RBS yield between a given

[1] The scattering probability is very low, only ~1/10 000 particles are backscattered in the RBS process.

crystallographic axis and a random direction in the crystal. The RBS/channelling effects are discussed in Section 4.8.

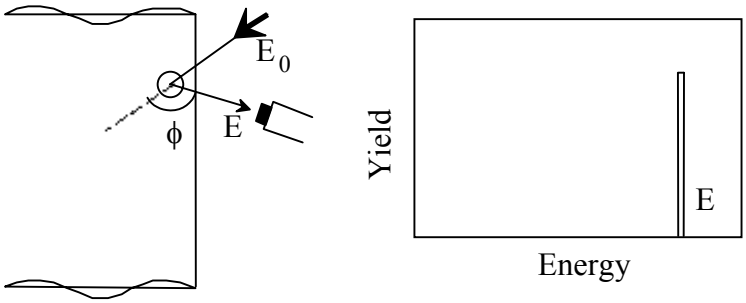

Figure 4.1: Schematic diagram illustrating how RBS can provide information on: "What is the sample made of?"

Consider an incident beam of particles with mass m and energy E_0 backscattered at the surface of a sample by atoms of mass M (Fig. 4.1). The energy, E, of the backscattered particles depends only on M and known quantities (E_0, m and the scattering angle ϕ), through the *kinematic factor (k)* [3],

$$k=E/E_0=\left[\frac{\left(M^2-m^2\sin^2\phi\right)^{1/2}+m\cos\phi}{M+m}\right]^2 . \qquad \text{(Eq. 4.1)}$$

Hence, measuring E allows to determine M, and the question: "*What* is the sample made of?" is answered.

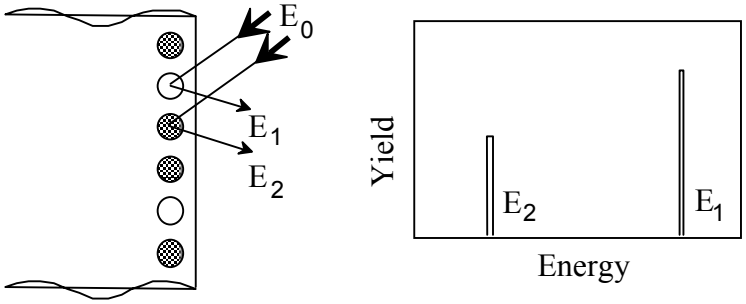

Figure 4.2: Schematic diagram illustrating how RBS can provide information on: *"How much* of each chemical element is present in the target *?"*

When more than one elemental species is present in the sample (Fig. 4.2), the relative intensity of the respective signals (E_1 corresponding to mass M_1 of the first species and E_2 to M_2 of the second) depends on their concentrations through the known cross-sections [4]

$$\sigma(\phi)=\left(\frac{Z\,m Z\,M e^2}{4E}\right)^2 \frac{4}{\sin^4\phi}\frac{\left[\left[1-(m/M)^2\sin^2\phi\right]^{1/2}+\cos\phi\right]^2}{\left[1-(m/M)^2\sin^2\phi\right]^{1/2}} \quad \text{(Eq. 4.2).}$$

So, the question: "*How much* of a given element does the sample contain?" is answered.

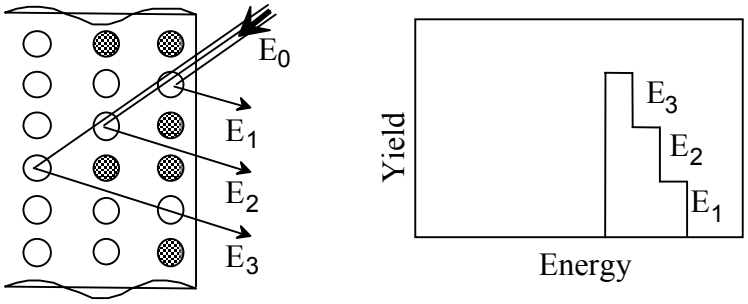

Figure 4.3: Schematic diagram illustrating how RBS can provide information on: "*Where* is a given chemical element located in terms of depth"*?*

The incident particles lose energy progressively when travelling through the material, mainly due to electronic scattering (Fig. 4.3). When a particle is scattered by an atom at a certain depth Δt, its energy will already be reduced compared with that of the incident beam. It further loses energy on the way back through the sample. For small thicknesses the reduction in detected energy amounts to

$$\Delta E/\Delta t = K \cdot \frac{\mathrm{dE}}{\mathrm{dt}}\bigg|_{E_0} + \frac{1}{|\cos\theta|}\cdot\frac{\mathrm{dE}}{\mathrm{dt}}\bigg|_{E'_0} \quad \text{(Eq. 4.3)}$$

at normal incidence, where E_0 is the energy of the incident particle immediately after scattering, and dE/dt is the stopping power of the incident particle in the given sample. As the stopping power is well known for most elements [11], the question "*Where* is a certain element located in a given sample?" is answered.

From the basic principles presented here it is clear that the collision process is insensitive to electronic configuration or chemical bounding. Therefore, contrary to other techniques such as XRD, the *composition values determined by RBS are independent of the state of strain in the samples*.

4.3 Shape of an RBS spectrum

With the concepts previously presented we can now easily recognize the shape of a random, i.e. measured out of a crystal axis direction, RBS spectrum. Therefore, one can begin to understand how the inverse RBS problem, to determine from the data the corresponding sample structure, can be solved.

In general, the backscattering spectra of a multi-elemental target can be viewed as a superposition of elemental backscattering spectra. In Fig. 4.4, a simplified schematic diagram representing an InGaN/GaN/Al_2O_3 heterostructure, where t_1 and t_2 are the InGaN and GaN thicknesses respectively together with simplified scheme of the expected RBS spectrum is presented.

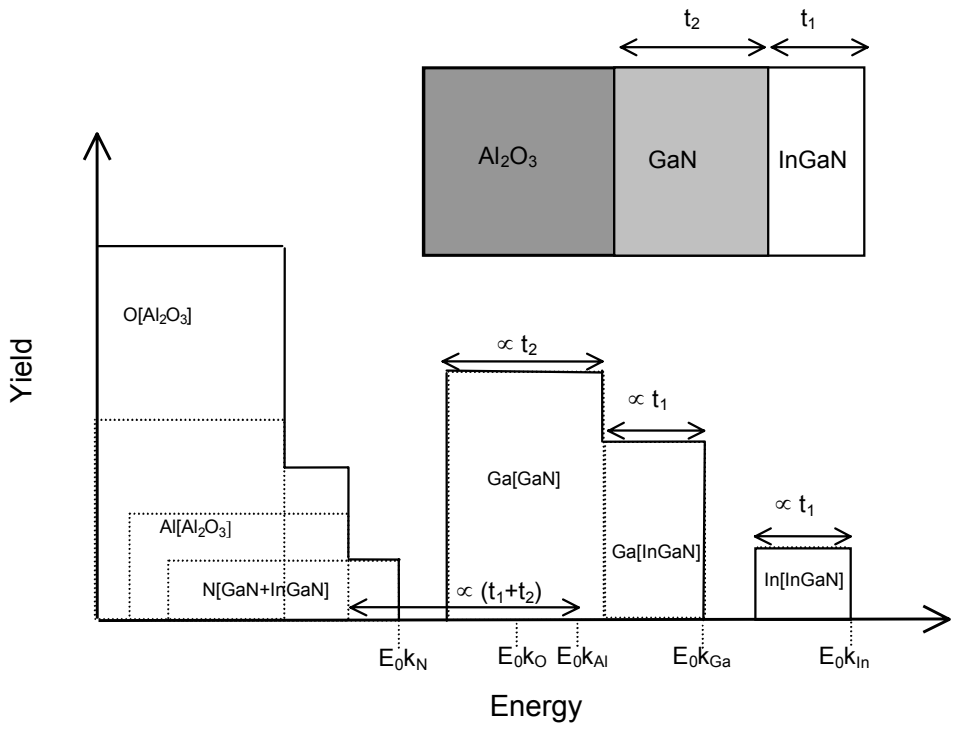

Figure 4.4: Schematic diagram representing an InGaN/GaN/Al_2O_3 heterostructure and its RBS spectrum.

The scattering energies of each chemical element present in the sample, In, Ga, Al, O and N, are indicated. Dashed lines represent the spectra of individual chemical elements and the full line is the resulting experimental spectrum, taking into account the signal overlap. Note that for elements that are not present at the surface layer (e.g. Al and O in sapphire) the corresponding signal appears at a lower energy, due to the energy loss of the beam as it crosses nitride layers.

While the scattering energy of chemical elements at the surface does not change with the sample tilt, the signal of a buried layer shifts to lower energies since the beam path, and thus the energy loss, increase with the incidence angle. This fact can be used to identify the presence of a specific chemical element at the surface.

An important aspect in Fig. 4.4 is the relation between the (height) intensities of the In and Ga related signals in the InGaN layer. This relation is the key to determine the InN molar fraction in the alloy. Note the complementary between the Ga and In intensity; as the In content decreases, the height of the Ga signal tends to approach that of the Ga in the GaN buffer layer. In practice, the intensities would not be rigorously equal since the RBS yield varies with the beam energy loss, but this small difference in yields can be neglected for illustration purposes, although it is fully taken into account in the simulation process, which will now be described.

4.4 Simulation of RBS spectra

For the general case, the shape of an RBS spectrum and the equations that relate the sample's structural parameters with the details of the experimental spectrum can be quite complicated. Fortunately, most of the data reductions are performed with the aid of computer programs capable of handling multilayer multi-elemental targets. For example the computer program RUMP, developed at Cornell University by Doolittle [12], can handle the basic physical aspects of the backscattering phenomenon.

The input parameters required to simulate a random RBS experimental spectrum are the (well defined) experimental conditions under which the spectrum was acquired: beam energy, incidence angle, detector geometry, detector energy resolution and a multi-layer model of the samples' structure. This model is interactively refined until simulated and experimental random RBS spectra match.

In this thesis, two computer programs were used to simulate the experimental results. RUMP [12] was used in most cases. It is a relatively simple code, appropriated for simple sample structures. The second fitting code IBA DataFurnance, also called NDF (*Nunos' Data Furnace*) [13,14], was used for more refined analysis, and is better for more complex samples such as samples with composition gradients, roughness and MQWs. NDF should be used in cases where the degradation of energy resolution as a function of depth (energy straggling) may be relevant for the analysis and when roughness or interdifusion may be present. NDF also presents the important advantage of being able to fit simultaneously different RBS spectra taken at different angles. This capability is fundamental for the analysis of InGaN/GaN MQWs.

4.5 Experimental setup

RBS/channelling measurements were performed at the Instituto Tecnológico e Nuclear (ITN) in Lisbon[2]. The typical experimental conditions used for the spectra discussed in the thesis consist of a 1 mm collimated beam of 2.0 MeV $^4He^+$ at currents of about 5 nA. The backscattered

[2]Visit the ITN webpage at: www.itn.pt.

particles were detected at 160º and close to 180º, with respect to the beam direction, using silicon surface barrier detectors located in the standard Cornell geometry with resolutions of ~12 and ~16 keV, respectively. Samples were mounted on a computer-controlled stepping motor driven two-axis goniometer with an accuracy of ±0.01º. A diagram illustrating the scattering and detection geometry in the Cornell setup is shown in Fig. 4.5.

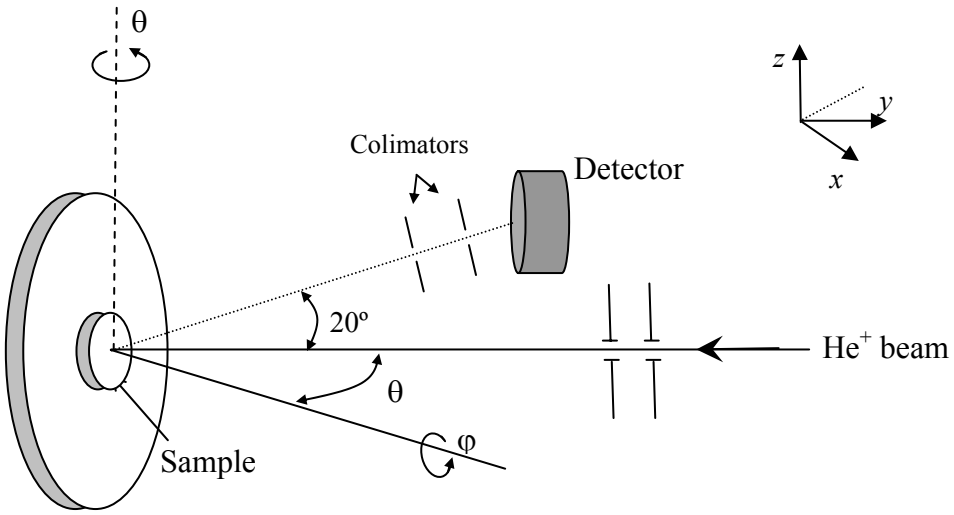

Figure 4.5: Diagram of the RBS experimental setup in the Cornell geometry.

As can be observed, in the Cornell geometry the detector is directly above (or below) the incident beam; the incident beam and the scattered beam are in the same (vertical,*y*-*z*) plane. The angle between the sample normal and the incident beam is controlled by the angle θ. Further details of the RBS setup used here, can be found elsewhere [15].

We should now turn our attention to RBS experimental results obtained in InGaN/GaN heterostructures of increasing complexity. This will illustrate the potential of the technique and at the same time will provide some results for discussion in next chapters.

4.6 Uniform single InGaN layers

Random and aligned RBS spectra from an $In_xGa_{1-x}N/GaN/Al_2O_3$ heterostructure are shown in Fig. 4.6. Note that in Fig. 4.6, there are two *x* scales, one in channel number and the other in energy. The energy axis of the spectrum is split into a number of discrete units called channels. There is a linear correspondence between the particle energy and the channel number; therefore, the energy-to-channel conversion can be given as:

$$E=\#_{ch}*\varepsilon+\Delta \qquad \text{(Eq. 4.4)}$$

where $\#_{ch}$, ε and Δ are the channel number, the channel energy width (keV/channel), and the energy corresponding to the zeroth channel, respectively.

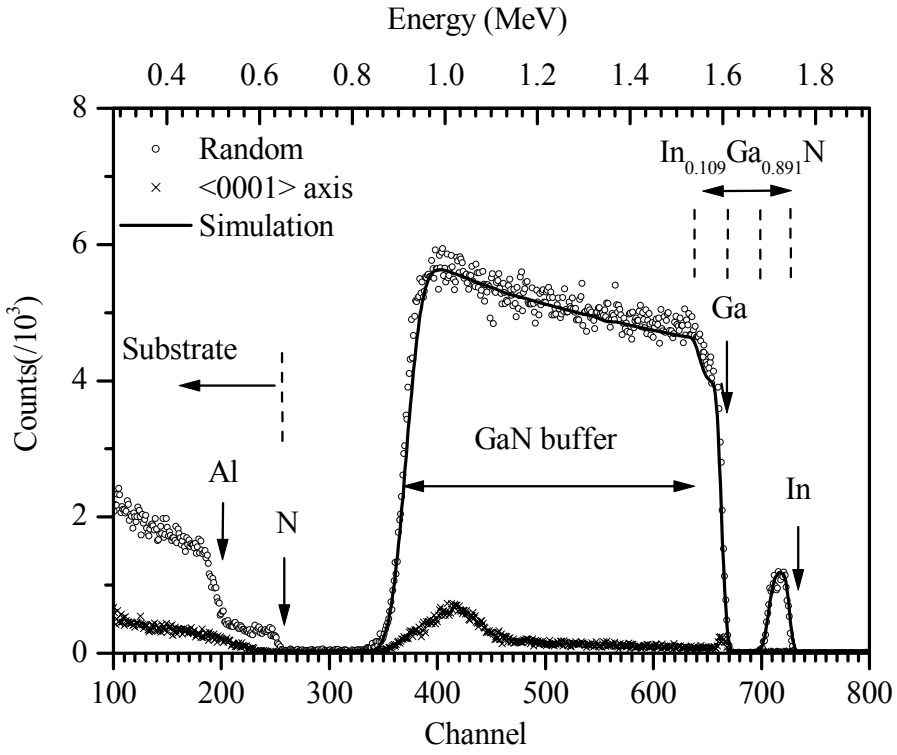

Figure 4.6: Random, aligned and simulated RBS spectra from an $In_{0.099}Ga_{0.891}N/GaN/Al_2O_3(0001)$ sample. Vertical arrows indicate the scattering energies of the different chemical elements. Horizontal arrows indicate the depth location in the sample.

In thin InGaN samples ($t_{InGaN} \leq 100$nm) the indium peak is clearly separated from the gallium related part of the spectra. The full curve is a computer simulation of the random spectra using RUMP [12]. Good statistics and a discerning simulation allows an accurate (<0.01 error) determination of the InN content, x, with a depth resolution of about 5-10 nm. For this sample, x=0.099±0.005 was obtained.

From the simulation one can also extract the InGaN (425×10^{15} atoms/cm^2) and GaN (5800×10^{15} atoms/cm^2) thickness. Note that n_t atoms/cm^2 are the natural units in RBS, used by the simulation programs. To get real physical thicknesses in the usual length units, the density, d, of the analysed film must be given. Thus, the thickness can be easily obtained from n_t:

$$t = \frac{n_t}{\frac{d \cdot N_a}{M}} \qquad \text{(Eq. 4.5)}$$

where, d is the *average* density, N_a Avogadro's number and M is the *average* atomic mass of the film. The average values are calculated using the RBS measured value of x.

Throughout this work the values used for GaN and InN density were: 6.11 g/cm^3 and 6.92 g/cm^3, respectively. The density used for an InGaN film of composition (x) was linearly

interpolated for *x*, since to the present date there are no measured values of density available for the alloy. This leads to a calculated InGaN film thickness of 50±5 nm and a GaN buffer layer thickness of 660±10 nm.

In this sample one can determine the thickness of the GaN buffer layer, since it is within the beam energy range. However, for these experimental conditions buffer layer thicknesses larger than ~1 micron are not possible to measure since the back edge of the Ga signal is not observed. The thickness of the substrate layer (Al_2O_3) cannot be assessed, as it is above the range of analysing beam. Thickness values determined by RBS simulation are in excellent agreement with direct measurements by cross section SEM, XRD, TEM [16,17] and by analysis of the interference fringes spacing extracted from the absorption spectra as shall be discussed in Chapter 5.

4.7 InGaN sample with composition profile

In the sample previously discussed (AEC51), a good fit to the experimental spectrum was attained using a model layer with an InGaN film of uniform composition over depth. However, this is not always the case. Let us consider the random (3º off axis) and aligned RBS spectra of sample AEC53, an InGaN/GaN/Al_2O_3 heterostructure shown in Fig. 4.7.

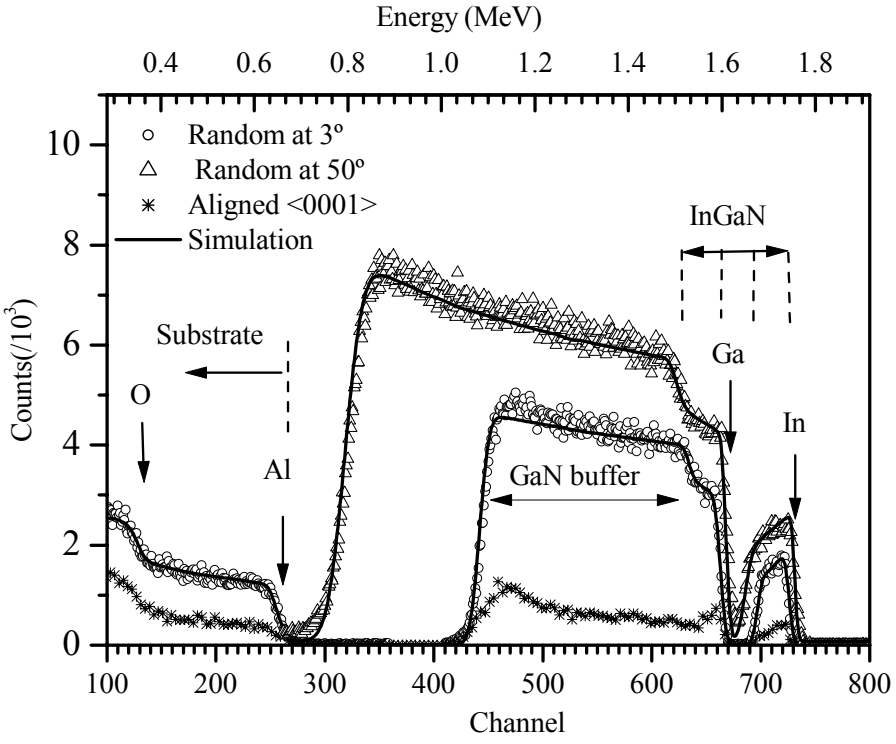

Figure 4.7: Random (3º and 50º) and aligned *<0001>* and simulated RBS spectra. Vertical arrows indicate the scattering energies of the different chemical elements. Horizontal arrows indicate the depth location in the sample.

A second random spectra acquired at a different point, with a sample tilt of 50º, was obtained in order to improve the depth profile. In principle, sample tilt could be further increased (nearly up to the natural limit of 90º) in order to fully maximise the path of the He^+ ions in the layer. However, this was not considered because the In and Ga related peaks would merge, reducing the certainty in the analysis since it is now impossible to collect In and Ga signals independently.

In a random RBS spectra performed on a target with a constant chemical composition, the backscattering yield form deeper sample regions is higher ($\propto 1/E^2$) due to the energy loss of the penetrating beam [4-6]. In the spectra of Fig. 4.7 this effect is clear in the energy window corresponding to random spectra of the GaN buffer layer. Regarding the $In_xGa_{1-x}N$ film this dependence is not verified, and it can be noticed that the In signal decreases as the beam penetrates deeper in the layer. Accordingly, the Ga signal increases at a faster rate than would be expected in a layer with uniform composition.

This is a clear qualitative indication that the In content is decreasing with depth. For a detailed quantitative analysis, simulation of the RBS spectra was performed with the computer programs RUMP [12] and NdF [13]. Using the experimental conditions as input parameters, a multilayer model is refined changing thickness and composition of the different layers until calculated and measured spectra closely match. A model layer consisting of a 75 nm thick $In_xGa_{1-x}N$ layer, with a composition profile:

$$x(d)=8\times10^{-3}(75-d)+0.14 \qquad \text{(Eq. 4.6)},$$

where *d* is InGaN layer depth in nm, followed by a 465 nm thick GaN buffer and the sapphire substrate provide an excellent fit for both angles, as shown in Fig 4.7.

In this simulation, instead of a single InGaN model layer, the way to simulate the composition gradient using RUMP was to subdivide the (initially) single layer into several (10) layers with differing InN mole fractions. Note that for this layer, and in general for thick layers, the composition results obtained using RUMP and NDF are rather similar. In addition, the results of the simulation suit both random spectra, at different angles, giving good confidence in the In mole fraction profile extracted and indicating that any lateral heterogeneity, which may exist, is below the sensitivity of the RBS measurements (≈0.005).

The lateral homogeneity, and the composition depth profile extracted, is entirely consistent with the results of optical characterization obtained by depth resolved cathodoluminescence [8]. The optical properties of composition graded InGaN layers are discussed in Chapter 7.

4.8 RBS/Channelling

In the discussion so far, we could have "viewed" the target material as amorphous, where atoms could be seen as randomly positioned in the three-dimensional space. In reality, the epitaxial layers studied in this thesis have a relatively high degree of crystallinity and this provides ground for a different type of RBS analysis.

When the incident ion beam is directed along a high symmetry crystal direction, ion channelling occurs [3-7]. The use of the channelling effect in conjunction with RBS (RBS/C) can provide an indication of the crystalline quality along a certain crystal direction, as a function of depth, and often also allows determination of the strain in epitaxial layered structures.

The channelling effect occurs because rows of atoms under certain geometrical conditions "steer" the incoming particles. These channelled particles do not approach the atomic nuclei closely enough to undergo Rutherford backscattering. This effect results in a strong reduction in scattering yield for channelling along major crystal axes [3-7].

4.8.1 Evaluating crystalline quality using RBS/C

Deviations from perfection in the crystal structure, for example misfit dislocations in strain-relieved structures or changes in the direction of crystal rows along inclined directions due to the strain induced distortions, will give rise to dechanneling and increased scattering of the ions. Therefore, comparison between random and aligned RBS spectra informs about the crystalline quality along the direction considered.

For an ideal crystal, with no topological disorder, the number of back-scattered ions would be close to zero: when aligned with a crystal axis the He^+ ion would basically find empty space, in consequence of the geometrical consideration that nuclear dimensions are much smaller than inter-atomic distances.

It can be easily imagined that lattice disorder (atoms displaced from the ideal positions) will increase the number of backscattered particles. In the limit of a polycrystalline or amorphous material no difference between "aligned" and random spectra exists. Crystal disorder can therefore be quantified by the parameter χ_{min} (ratio between back-scattering yields from aligned and random spectra in the near surface region). The value of χ_{min} may vary from few percent for good crystallinity up to 100% for amorphous or polycrystalline material.

In Figures 4.6 and 4.7 one can see how random and aligned RBS spectra compare. In both cases the aligned scan was performed along the *<0001>* (growth) direction. From this comparison one can see that in both cases the crystalline quality seems to worsen as we probe deeper in the GaN buffer layer. This trend is expected, since the first part of the GaN film to be grown is a highly

dislocated low temperature nucleation layer, which accommodates the lattice mismatch between GaN and the sapphire substrate, as described in Chapter 2.

Comparison between the χ_{min} values obtained for the InGaN film along *<0001>* in samples AEC51 (2.4%) and AEC 53 (17%) illustrates the general trend, also verified by XRD in Chapter 3 and TEM [19], of crystalline quality deterioration as the In content increases in InGaN. This degradation is easily understandable since the growth temperature has to be decreased to obtain greater incorporation of In and the lattice mismatch between GaN and InGaN increases with *x*. Nonetheless, measured values of χ_{min} are low compared to reported values for samples with similar InN content [10].

4.8.2 Measuring strain release as a function of depth

Although determination of composition by RBS is insensitive to the lattice strain, the channelling effect can be used to measure strain with depth resolution. Depth resolution is attained by energy selection of the backscattered particles. Lattice distortion was studied *over depth* in some selected $In_xGa_{1-x}N$ samples. Namely in samples that feature composition pulling effects such as AEC53, whose RBS spectra is discussed in Section 4.7.

In the hexagonal structure the angle between any tilted axis and the growth direction depends on both lattice constants. In Fig 4.8 the angular relation between the *<10-11>* and the *<0001>* growth axis is represented.

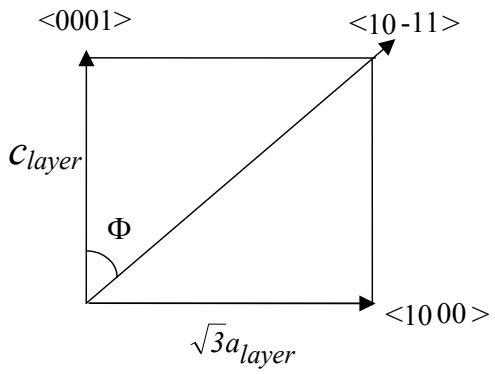

Figure 4.8: Diagram showing the angular dependence of the crystal axis on the wurtzite lattice constants.

As shown, the angle Φ between *<0001>* and *<10-11>* is given by: $\Phi = \arctan(\sqrt{3}a/c)$. The channelling effect along these axes was used to determine the strain release along the growth direction.

The tetragonal distortion, ε_T, as defined in Ref. [9] is given by:

$$\varepsilon_T \cong (\Phi_{epi}-\Phi_b)/(\cos\Phi_b \sin\Phi_b) \qquad \text{(Eq. 4.7)}$$

where Φ_{epi} is the measured angle, whereas Φ_b is the value expected for bulk (fully relaxed) $In_xGa_{1-x}N$. Using the InN mole fraction from RBS and Vegard's law [20], the lattice constants of bulk $In_xGa_{1-x}N$, for each sub-region considered, were interpolated from the GaN (c_{GaN}=*0.51850*, a_{GaN}=*0.31892 nm* [21]) and InN (c_{InN}=*0.57033,* a_{InN}=*0.35378 nm* [22]) relaxed values.
In Fig. 4.9 the results obtained for the angular RBS/C scans of sample AEC53 are presented.

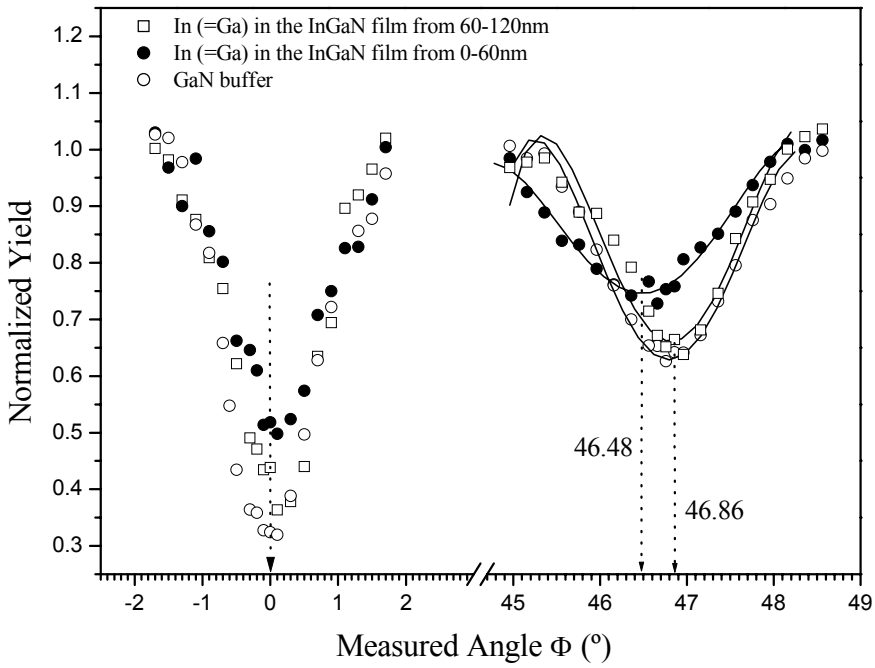

Figure 4.9: Angular RBS/channelling scans for sample AEC53, corresponding to the GaN buffer layer and the InGaN layer at the indicated depths, along the (*1-210*) plane from the *<0001>* to the *<10-11>* crystal axis.

The RBS spectra corresponding to the InGaN layer was divided into two integration regions (as indicated in Fig 4.7), corresponding to 0-35 and 35-70 nm depths, were considered and Φ_{epi} values of *46.11º* and *46.23º* were measured. The tetragonal distortions deduced from the RBS/channeling study were (*-2.63±0.1%)* for the film region closer to the GaN/ $In_xGa_{1-x}N$ interface and (*-2.17±0.1%)* for near the surface region, respectively. This difference in ε_T shows that the strain profile is also not uniform over depth, and slight release of the strain in the growth direction is noticed. Even though in this sample the region near the surface is still highly strained.
Sample AEC53 shows only one XRD peak, however the case of layers with double XRD peaks (for instance sample S101) was also investigated by RBS/C the results will be presented in Chapter 6.

4.9 Grazing incidence RBS: studying InGaN/GaN MQWs

So far we have shown how RBS provides rich structural information in single InGaN/GaN films. In this section, it will be shown how RBS can be extended to the study of ultrathin heterostructures, namely InGaN/GaN MQWs similar to those used in light emitting devices [25,26]. Typical depth resolution achieved with normal incidence RBS is around 5-10 nm [3-7]. This is not enough to study low dimensional InGaN/GaN heterostructures where the thickness of the active InGaN layer is around 2.5 nm. However, depth resolution can be improved markedly if the sample normal is tilted by a large angle, θ, relative to the incoming beam [27]. This tilt results in an increase of the path length ($\propto 1/\cos\theta$) required to reach a given depth in the sample. Consequently, the scattered particle energy loss increases, for a given depth difference. Therefore, optimisation of the scattering geometry offers a simple and powerful approach to reach the depth resolution necessary to study in detail InGaN/GaN MQWs. Angle-dependent RBS spectra of samples STR121 and STR94 are shown in Fig. 4.10 a) and 4.10 b), respectively.

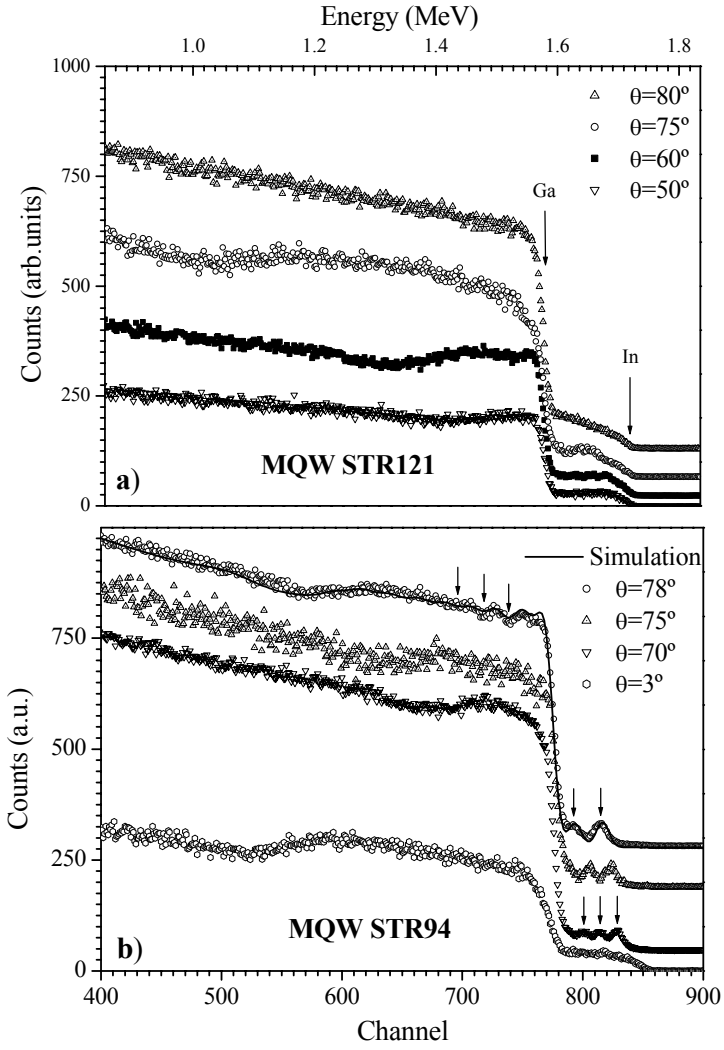

Figure 4.10: a) and b) are angle-dependent RBS spectra acquired for samples STR121 and STR94, respectively. The spectra are vertically shifted for clarity.

The two samples discussed here were grown in an Aixtron 200/4 RF-S MOCVD reactor. These MQWs were specifically grown to study the effects of the well composition on the structural and optical properties. Following deposition of a ~1.2 μm GaN buffer layers on c-sapphire substrates at 1140°C, growth was interrupted for cooling to the MQW growth temperature. The InGaN wells, GaN barriers and cap layers were grown at a constant temperature, without further interruption. More details on the InGaN growth conditions are given in Chapter 2 and in Ref. [17]. The 10-period MQW designated STR94 was grown at 832°C and the growth periods for wells and barriers were respectively 90 and 270 s, chosen to give nominal thicknesses of 2.5 and 7.5 nm. The other two structures discussed STR121 was grown at 760° C, and contained 18 wells. The barrier growth period was also 270 s, but for the well was 78 s.

Two main differences are evident between the spectra of the samples. For STR121, the MQW structure can not be resolved, even at the largest tilt angle. On the other hand, for sample STR94, despite its lower In/Ga ratio, which indicates lower In content in the wells, a clear signal modulation can be observed for $\theta > 70^{\circ}$. Moreover, while in the former case the rising edge of the In signal remains in the same channel independent of θ, in the latter it progressively shifts to lower energies with increasing tilt.

In RBS spectra acquired at different tilt angles, the high energy rising edge of peaks related to chemical elements present at the surface, is expected to maintain the same energy position. This is always the case for the Ga related signal since this element is invariably present at the surface in the samples studied here. However, buried layer related signals (In) should shift towards lower energies as the angle increases since the *effective* path of the He^{+} beam in the GaN cap increases with tilt angle. Therefore, since no shift is observed the RBS spectra of STR121, we deduce that there is In at the surface. Clearly, a strong In migration from the top well through the 17nm of the GaN cap layer must occur for this sample. This also suggests a pronounced well/barrier intermixing, resulting in a poor In/Ga interface contrast. The absence of signal modulation for this MQW is therefore explained.

Individual well compositions (and thickness) can not be accurately determined for sample STR121 since no complementary In/Ga signal modulation can be observed. In this case only a rough estimate of x in the wells, $x \sim 0.20 \pm 0.05$, can be obtained, if one assumes the layer thicknesses to be close to the target values. For sample STR94, simulation of the experimental spectra yields the GaN cap thickness (17.5±0.3 nm), the mole fraction in the wells (x=0.101±0.015), and the well (2.8±0.3 nm) and barrier (7.5±0.3 nm) thicknesses. The extent of In segregation to the GaN cap and well/barrier intermixing is small ($\sigma \leq 0.5$ nm). The intermixing parameter, σ, quantifies the deviation from ideal square wells through the standard deviation of

an error function distribution[3] [28]. However, it should be mentioned that a reliable analysis of this MQW could only be achieved for the first 3-4 wells. This is a consequence of depth resolution degradation with increasing depths due to the cap effective thickness and a low In content in the wells, giving rise to a small relative modulation in the Ga signal. Larger intermixing becomes impossible to analyse correctly with these methods. This is the case of sample STR121 where one can only estimate that $\sigma \geq 5$ nm. Clearly the MQW with higher well composition is of worse crystalline quality, confirming the degradation trend with *x* also verified in single layers.

Note that contrary to the case of relatively thick $In_xGa_{1-x}N/GaN$ layers previously discussed, where *x* could be measured with good precision using RBS simulation codes with simple energy straggling models, special care needs to be taken in data analysis of complex ultra-thin multilayer structures. There is a progressive broadening and distortion of the spectral contributions from deeper interfaces relative to what would be obtained if resolution were constant with depth. These effects are particularly relevant for grazing angles of incidence [29], and therefore energy straggling and multiple scattering should be taken into account as precisely as possible. The code used here to calculate energy straggling, DEPTH [30], includes energy straggling calculations with effective charge scaling and includes the effects of the geometrical dispersion effect caused by finite beam size and solid angle of the detector and multiple scattering.

4.10 Roughness determination by RBS

RBS can now also be used to extract information on the surface roughness of InGaN/GaN thin films. Within the framework of this thesis, an algorithm where the effect of roughness is considered as a broadening of the spectral features, approximating it as an extra contribution to the energy resolution at a given depth was tested and developed. This approach has the advantage of making the effect of roughness easy to incorporate in a standard spectrum simulator with only a minimal increase in calculation time. Quantitative analysis of the data, including the determination of the roughness parameters, was made through the application of models developed for specific idealised kinds of roughness. In a first step, the assumptions made in the development of the models were tested, and their limits of validity established [31]. In all cases, the models were found to be valid only under the following restrictions:

a) The beam area is considered large enough to probe a representative sampling of the inhomogeneity distribution. This condition is in practice always met when using

[3] A graphic representation of the effect of σ on the QW profile is illustrated in Section 6.9.2.

macroscopic beams of size typically 1×1 mm^2.

b) The roughness parameters are assumed to follow a Gaussian distribution. This means that other types of distributions (for instance, surfaces or interfaces with periodic structures) are not correctly modelled. This condition is probably never exactly met; nevertheless a Gaussian distribution can be used as a good approximation to model a large number of surface topographies.

c) The beam is considered not to re-enter the sample, which means that structures with large height to width aspect ratio cannot be correctly simulated with this method. This is the most stringent condition, since in cases where the beam does enter and leave the sample more than once (e.g. when structures with high aspect ratio are measured in grazing angles of incidence), the RBS spectrum obtained can be qualitatively different.

Within their limits of application and validity, the models used in the RBS data analysis are general, and can be used in the study of any given system. The roughness models, its approximations, and the details regarding the simulation procedures are published elsewhere [31]. Therefore, here we will limit the discussion to the fundamental results obtained for InGaN/GaN heterostructures.

The determination of the roughness in the InGaN/GaN bilayer samples depends fundamentally on the width of the Ga low energy edge. Let us consider a sample where the effect of roughness in the RBS data is quite pronounced. Sample AIX1025, with data shown in Fig. 4.12, is a good example.

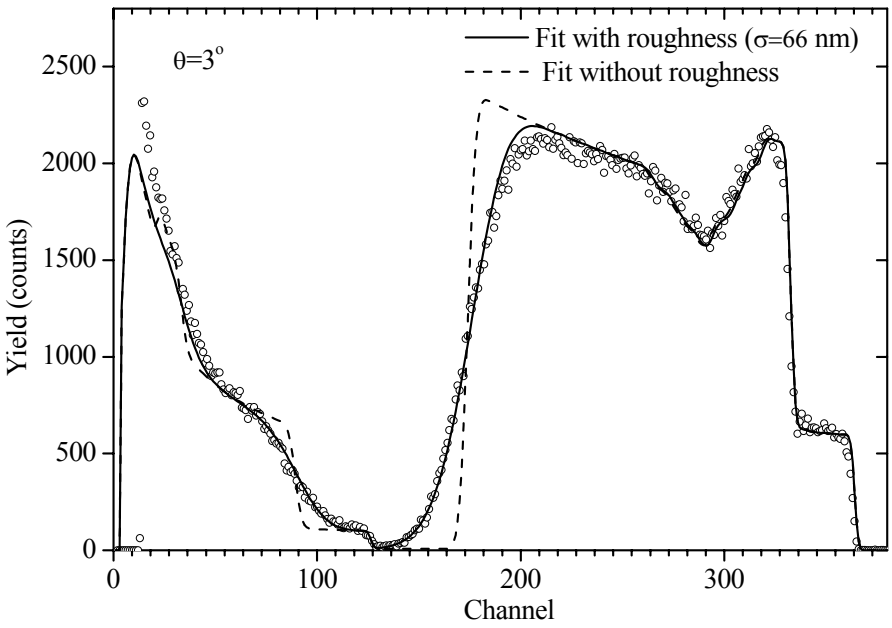

Figure 4.11: RBS random spectra (θ=3º) for sample AIX1025 together with the simulation considering a flat surface (dashed line) and considering surface roughness (full line).

One can notice that the fit done assuming sharp interfaces clearly does not describe the data correctly, particularly in the Ga back edge. However, when roughness is included, the fit is excellent. The roughness value derived was σ=66.0 nm, for a total GaN/InGaN thickness of 787 nm, that is $\sigma / t_{total} = 0.084$. Assigning all the roughness to the InGaN layer (fitted thickness 355 nm) would lead to $\sigma / t_{InGaN} = 0.186$, well within the domain of validity of the calculations. The fit assuming roughness used a model (model (1) in Ref. [28]), which considers that the thickness of the nitride bi-layer is inhomogeneous.

It is important to note that, in the samples studied in this thesis, we cannot conclude from the RBS data alone if the roughness is due to the InGaN top layer, or the GaN buffer. The reason is that the roughness is determined mostly from the Ga back edge, and Ga is present in both layers (50 at.% in the GaN, and above 40 at.% in the GaN layer in all samples analysed). Hence, the effect of the InGaN layer roughness in the Ga signal is propagated to the Ga signal of the GaN layer. In fact, equivalent fits can be made with any values of the roughness in the InGaN and GaN layers, respectively σ_{InGaN} and σ_{GaN}, as long as the total roughness given by: $\sigma_{tot} = \text{sqrt}(\sigma_{InGaN}^2 + \sigma_{GaN}^2)$ remains around the value determined. This uncertainty on the roughness origin, due to the similar chemical composition of the two adjacent layers, is easily overcome by an AFM analysis of GaN buffers grown under the same conditions. The contribution of the GaN roughness is indeed insignificant, with measured values of $\sigma_{GaN} < 1$ nm.

We compare the results obtained by our models with direct measurements of surface roughness by AFM. The results of RBS analysis and large area AFM scans[4] are summarised in Table 4.I.

Table 4.I: Comparison between the results obtained by RBS and AFM for surface roughness for samples with various thicknesses and compositions.

Sample	t_{InGaN} (nm)	t_{GaN} (nm)	x	roughness by RBS σ_{RBS} (nm)	surface roughness rms_{AFM} (nm)	rms_{AFM} / σ_{RBS}
AEC51	55	679	0.99	21.1	3.32	0.16
STR58	175	995	0.12	40.1	11.0	0.28
STR59	192	1010	0.24	42.0	37.2	0. 9
AEC53	76	477	0.17	13.5	15.6	1.1
AIX1025	355	432	0.14	66.0	59.9	0.91

The surface roughness determined with AFM agrees very well with the roughness derived from the RBS data for samples AEC53, STR59 and AIX1025. On the other hand, for samples AEC51 and STR58 the agreement is poor, with RBS leading to a roughness value much greater than

[4] It was ensured that the AFM scans were large enough to sample a macroscopic area so that the roughness obtained is representative of the sample surface. The typical scan sizes used was ~5 μm^2

that given by AFM. To understand the reasons why the method developed here to extract roughness from RBS data is quite precise on a certain group of samples (AEC59, STR59 and AIX1025) but appears to fail to give good results for others (AEC51 and STR58), one have to take into account the samples' surface characteristics.

Interestingly, when considering the surface morphology of these samples by SEM and AFM there is a trend. For the cases where the agreement between RBS and AFM results is good, the surface is found to be considerably rough with the surface featuring a 3D (islanding) growth mode. The SEM micrograph of sample AIX1025, Fig. 2.11 in Section 2.5.1, is representative of the surface of this group of samples. The surface structure is typical of InGaN/GaN relaxed layers, as shall be discussed in Chapter 6.

Alternatively, in samples where there is a discrepancy between AFM and RBS derived values, most of the surface is found to be essentially smooth, but interspersed with a large density of pits, as illustrated in Fig. 2.12 b) for sample AEC51. These pits, the so-called V-defects (hexagonal pinholes) [32] are characteristic of coherent InGaN/GaN layers. The surface morphology representative of these two groups of samples is shown in Fig. 4.12 a) and b) where the AFM (height) images of samples AIX1025 and AEC51, are shown, respectively.

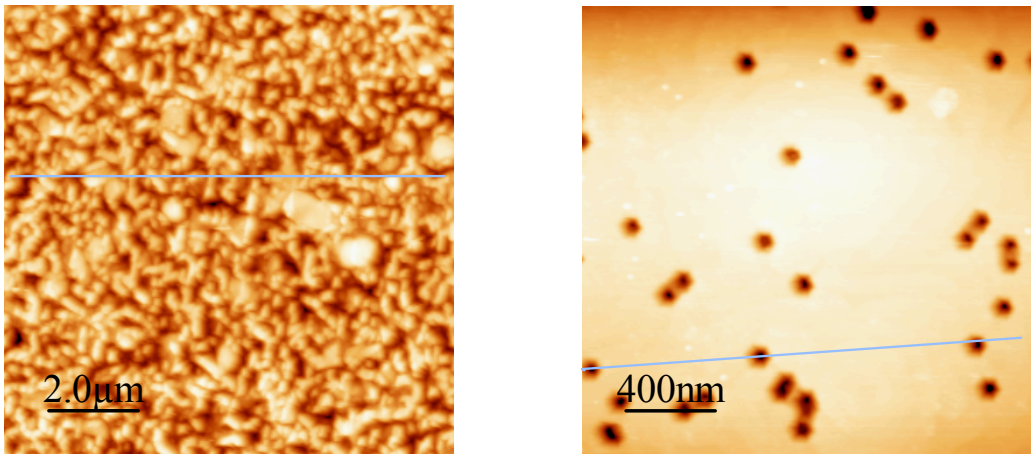

Figure 4.12: Atomic force microscopy micrograph of the samples AIX1025 a), and AEC 51 b), in the height mode. Note the line profiles along specific directions used to extract the surface profiles shown in Fig. 4.13.

In Fig. 4.13 a) and b), we represent the height profiles taken along the directions shown in Fig. 4.12. The profile crossing 3 of the pits, as shown in Fig. 4.13 b), evidences their large aspect ratio (~1:1) and the non-randomness of the roughness distribution. A small portion of the surface profile of sample AIX1025 along the line represented in Fig. 4.12 a) is also compared at the same length scale.

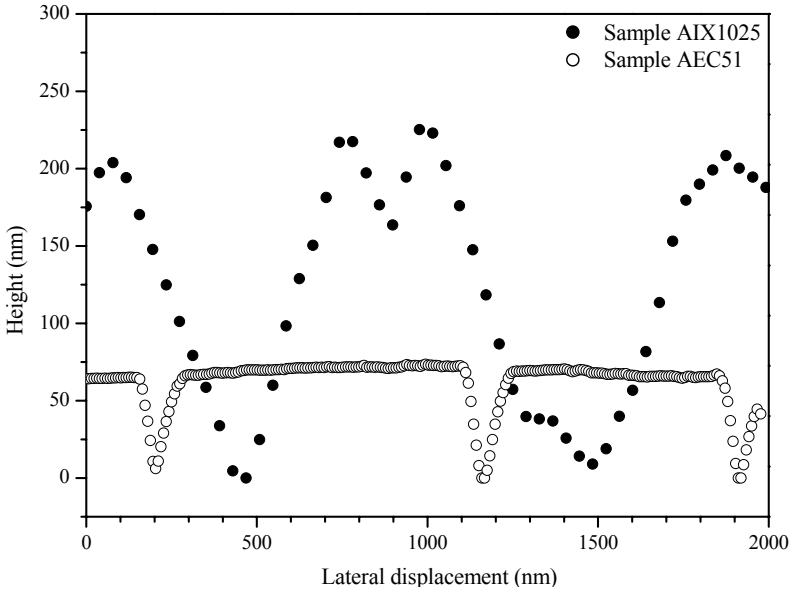

Figure 4.13: Line profiles extracted from the AFM image along the directions depicted in Fig. 4.12.

A convenient way to analyse the overall surface roughness features is to represent a histogram plot, as calculated from AFM data. These plots represent a map of the surface features height distribution, which provides quantitative information on the statistical nature of the sample roughness. The results of this analysis for the two representative samples under consideration are shown in Fig. 4.14 a) and b).

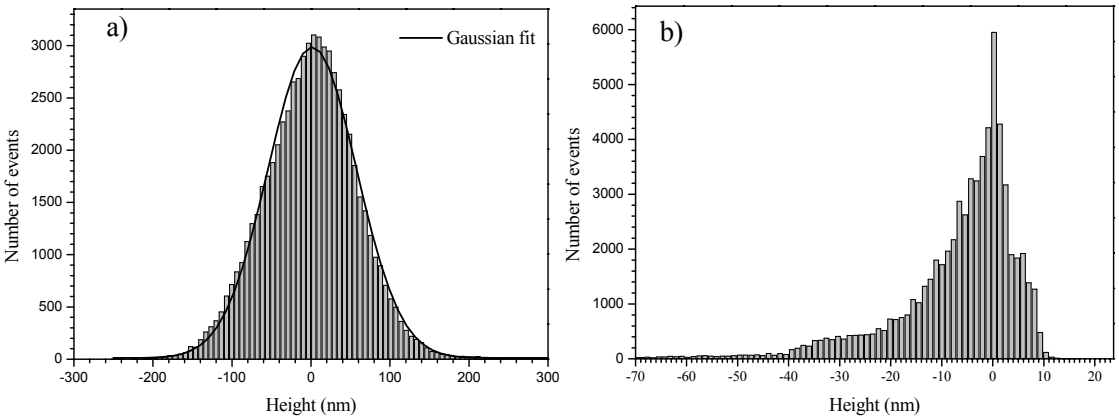

Figure 4.14: Histograms representing the sample's surface height distribution a) AIX1025 and b) AEC51. In a) a Gaussian fit to the height distribution is also shown.

The difference between the statistical surface analyses of the two samples is evident. Besides the expected difference in the height distribution widths, in sample AIX1025 the distribution almost perfectly follows a Gaussian function, whereas for sample AEC51 this is not the case. The asymmetry in the height distribution in AEC51 is, in large extent, originated from the pits

existing in the sample surface.

Considering the assumptions made in the roughness models developed, and the approximations introduced in their algorithmic implementation, it is clear that the type of roughness observed in samples like AEC51 cannot be correctly analysed with the code developed: Assumptions (b), and in particular (c), are not respected. The aspect ratio close to 1 of the pits observed with AFM means that an ion incident close to a pit has a high probability of re-entering the sample. On the other hand, the roughness of a sample characterised by a number of deep pits in an otherwise almost flat surface does not follow a Gaussian distribution. Furthermore, the effect of high aspect ratio structures on RBS energy spectra cannot be described solely by an increase of the apparent energy resolution, which was a condition assumed in the algorithm developed.

Therefore, it becomes clear why the roughness derived with RBS for these two samples is not correct. On the contrary, samples featuring 3D growth with a nearly "Gaussian" roughness consisting of islanding, with a low aspect ratio is well described by the models developed and their implementation. That the values derived by RBS for the samples with a random roughness agree very well with the AFM values shows that, within their limits of application and validity, the roughness models and algorithms developed work correctly. Therefore, it is demonstrated that from an RBS spectrum, quantitative information on the samples surface morphology can be extracted. This represents a novel and useful extension of the potential of the RBS analytical technique.

4.11 Summary

In this chapter the basic principles of the RBS technique were presented. The enormous potential of RBS for structural characterization of InGaN/GaN heterostructures was demonstrated through a series of examples. It was illustrated how thickness, composition and depth profile can be determined from simulation of a random RBS spectrum. Additionally, RBS results evidence rather interesting microscopic peculiarities of this material system.

Strong compositional pulling effects were discovered in InGaN layers whose growth was aimed to produce layers with $x>0.15$, the depth profile of x was extracted from RBS simulation. By exploring the channeling effect it was also shown how one could gain an insight on the crystalline quality and strain variations over depth. In samples showing composition gradients along the growth direction, a correlation between strain release and increasing In content was found.

It was also shown how thickness and composition of individual wells in InGaN/GaN MQWs could be measured directly for the first time. From detailed simulation of the RBS spectra, using a simulation code where the effects of energy resolution degradation over depth are included, we can also estimate the extent of intermixing between well and barrier. Similarly to the trend verified in single layers, it was shown that the overall MQW crystalline quality, and in particular the extent of intermixing, deteriorates with the increasing composition.

A novel algorithm that allows surface roughness to be extracted from an RBS spectrum was discussed and tested. The limits of application of the models were established, and the results obtained for several InGaN films regarding its surface roughness were compared to direct AFM measurements. In samples falling within the application range of the models, excellent agreement was found between the roughness determined by RBS and the surface roughness measured with AFM for thin films. In this way, we could extend further the potential of RBS analysis to characterise layer roughness.

4.12 References:

[1] E. Rutherford, Philos. Mag. **21**, 669 (1911).

[2] H. Geiger, E. Marsden, Proc. R. Soc. London, Ser. A **82**, 495 (1909).

[3] L.C. Feldman and J.W. Mayer, *"Fundamentals of surface and thin film analysis"*, North Holland, New York (1986).

[4] L.C. Feldman, J. W. Mayer and S. T. Picraux *"Materials Analysis by Ion Channelling. Submicron Cristalography"*, Academic Press, New York, (1982).

[5] J. R. Tesmer and M. Nastasi, "*Handbook of Modern Ion Beam Materials Analysis"* MRS, Pittsburgh (1995).

[6] B.G. Yacobi, D.B. Holt and L.L. Kazmerski *"Microanalysis of solids"*, Plenum Press, New York (1994).

[7] W. K. Chu, J. W. Mayer and M. A. Nicolet, *"Backscattering Spectrometry"* Academic Press, New York (1976).

[8] S. Pereira, M. R. Correia, E. Pereira, K. P. O'Donnell, C. Trager-Cowan, F. Sweeney and E. Alves, Phys. Rev. **B 64**, 205311 (2001).

[9] M. F. Wu, A. Vantomme, S. M. Hogg, G. Langouche, W. Van der Stricht, K. Jacobs and I. Moerman, Appl. Phys.Lett. **74**, 365 (1999).

[10] L. Nowicki, R. Ratajczak, A. Stonert, A. Turos, J.M. Baranowski, R. Banasik, K. Pakula Nucl. Instrum. Methods Phys. Res. B **161,** 539 (2000).

[11] J. F. Ziegler *"The stopping and ranges of ions in matter*" vol. 4, Pergamon Press, New York (1977).

[12] L. R. Doolittle, Nucl. Instrum. Methods B **9**, 344 (1985).

[13] N. P. Barradas, C. Jeynes, R.P. Webb, Appl. Phys. Lett. **71**, (1997) 291.

[14] C. Jeynes, N. P. Barradas, P. K. Marriott, G. Boudreault, M. Jenkin, E. Wendler and R. P. Webb *J. Phys. D: Appl. Phys.* **36**, R97-R126 (2003).

[15] E. Alves, PhD Thesis, *Faculdade de ciências da Universidade de Lisboa*, Lisboa, Portugal (1992).

[16] S. Pereira, M. R. Correia, T. Monteiro, E. Pereira, E. Alves, A. D. Sequeira, N. Franco Appl. Phys. Lett. **78**, 2137 (2001).

[17] C. J. Deatcher, C. Liu, S. Pereira, M. Lada, A. G. Cullis, O. Brandt and I. M.Watson, Semicond. Sci. Technol. **18**, 212 (2003).

[18] S. Pereira, M. R. Correia, E. Pereira, K. P. O'Donnell, E. Alves, A. D. Sequeira, N. Franco, I. M. Watson, and C. J. Deatcher Appl. Phys. Lett. **80**, 3913 (2002); S. Pereira, M. R. Correia, E. Pereira, K. P. O'Donnell, E. Alves, A. D. Sequeira, N. Franco, I. M. Watson, and C. J. Deatcher Appl. Phys. Lett. **81**, 3500 (2002).

[19] K. Hiramatsu *et al*, *MRS Internet J. Nitride Semicond. Res*., **2** 6 (1997).

[20] L. Vegard, Z. Phys. **5**, 17 (1921).

[21] T. Detchprohm, K. Hiramatsu, K. Itoh and I Akasaki, Jpn. J. Appl. Phys. **31**, L1454 (1992).

[22] W. Paszkowicz, Powder Diffraction **14**, 258 (1999).

[23] K. P. O'Donnell, S. Pereira R. W. Martin, P. R. Edwards, M. J. Tobin and J. F. W. Mosselmans Phys. Stat. Sol. (a) **195**, 532 (2003).

[24] K. P. O'Donnell, R.W. Martin S. Pereira, Appl. Phys. Lett. **81**, 1353 (2002)

[25] S. Nakamura and G. Fasol, "*The Blue Laser Diode"* Springer, Berlin (1997).

[26] B. Gil, Ed. *"Group III Nitride Semiconductor Compounds, Physics and Applications."* Series on Semiconductor Science and Technology 6 Oxford Science Publications, Oxford (1998).

[27] N. P. Barradas, J. C. Soares, M. F. da Silva, F. Pászti and E. Szilágyi, Nucl. Instrum. Methods Phys. Res. B **94** 266 (1994).

[28] N. P. Barradas, J. Phys. D: Appl. Phys. **34**, 2109 (2001).

[29] N. P. Barradas, A. P. Knights, C. Jeynes, O. A. Mironov, T. J. Grasby, E. H. C. Parker, Phys. Rev B, **59** 5097 (1999).

[30] E. Szilágyi, F. Pászti and G. Amsel, Nucl. Instrum. Methods Phys. Res. B **100**, 103 (1995).

[31] N. P. Barradas, E. Alves, S. Pereira, V. V. Shvartsman, A. L. Kholkin, E. Pereira, K. P. O'Donnell, C. Liu, C. J. Deatcher, I. M. Watson and M. Mayer, Nucl. Instr. and Meth. B **217**, 479 (2004).

[32] Y. Chen, T. Takeuchi, H. Amano, I. Akasaki, N. Yamada, Y. Kaneko, and S. Y. Wang, Appl. Phys. Lett. **72**, 710 (1998).

Chapter 5: Optical characterization of InGaN/GaN heterostructures

Overview

In this chapter, the basic optical properties of InGaN/GaN heterostructures are characterised. The fundamental physical principles and experimental setups of the analytical techniques used; optical absorption (OA) spectroscopy, photoluminescence (PL) spectroscopy, confocal microscopy/spectroscopy (CM) and cathodoluminescence (CL) spectroscopy with depth profiling, are briefly discussed.

The main characteristics of optical absorption spectra for InGaN layers with different composition are discussed. It is shown how to extract the nitride layer thickness from the interference fringes which appear on the OA spectra, and the values obtained are compared with the RBS thickness estimates. It is illustrated how to obtain a systematic measurement of the alloy bandgap energy (E_g) by fitting the absorption curves to a sigmoidal expression.

The PL spectra of $In_xGa_{1-x}N$ layers, with different values of x, are characterized. We also present the temperature dependent PL spectra of a layer featuring double peaks and briefly comment on the evolution of the two components with temperature. The CM technique is shown to be useful to study the light emitting properties, and correlate luminescence with surface morphology, at a μm length scale. The potential of CL spectroscopy with variable electron beam energy to depth profile luminescence properties in InGaN layers is illustrated.

Analysis of the results provided by these techniques allows some general trends regarding the material basic optical properties to be established.

5.1 Optical absorption spectroscopy

Optical absorption is the most direct, and perhaps the simplest, method to probe the band structure of semiconductors. By inserting a slab of semiconductor at the output of a monochromator, and measuring spectrum of the transmitted radiation as a function of wavelength, one can discover the possible transitions an electron can make, and learn much about the distribution of states. OA is a contactless, nondestructive method of ideally measuring, in a semiconductor, the joint density of states (JDOS) of the electron and hole states in the conduction and valence bands, respectively.

5.1.1 Basic principles

Optical absorption occurs when a photon of sufficient energy interacts with a semiconductor. The photon interaction process of greatest interest involves the highest energy valence electrons. In a collision of a photon with a valence electron of the semiconductor, the photon can be absorbed and hence "disappear". Thus, all of the energy from the photon can be transferred to the electron to elevate it into the conduction band, generating electron-hole pairs and creating excess carrier concentrations.

The absorption coefficient, $\alpha(E)$, for a given photon energy, is proportional to the probability P_{if} for the transition from the initial state to the final state and to the density of electrons in the initial state, n_i, and the density of available states n_f (joint density of states). This must be summed over all the possible transitions between states separated by an energy difference equal to $h\nu$:

$$\alpha(E)=A\Sigma P_{if}n_i n_f \text{ with } E_f-E_i=h\nu. \quad \text{(Eq. 5.1)}$$

The absorption coefficient can be easily measured experimentally. If light passes through a medium of infinitesimal thickness *dl* the loss of intensity due to absorption will be proportional to *dl*, so that

$$dI/I(E)=-\alpha(E)dl$$

hence

$$I(E)= I_0 e^{-(\alpha(E)l)}. \quad \text{(Eq. 5.2)}$$

I_0 is the incident light intesity, and $I(E)$ is the transmitted intensity. The absorption coefficient is frequency and polarisation dependent. Equation (5.2) can be written as:

$$\alpha(E)= ln[I_0(E)/I(E)]/l, \quad \text{(Eq. 5.3)}$$

where l is the layer thickness, and $I(E)/I_0(E)$ is the normalised transmission.

Fundamental absorption refers to band-to-band transitions. It manifests itself in a rapid rise of $\alpha(E)$ and can be used to determine the semiconductor bandgap. If transitions are "direct", we expect a rising parabolic absorption profile in a direct band gap semiconductor [28-30], as schematically represented in Fig. 5.1.

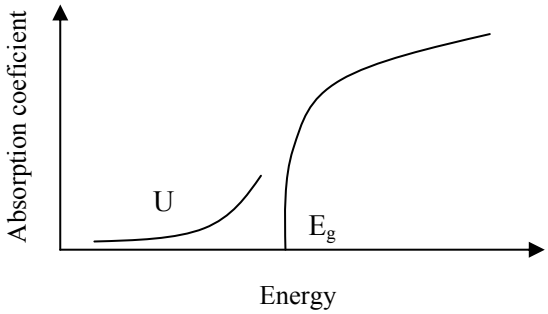

Figure 5.1: Schematic illustration of the optical absorption spectrum of a quasi ideal direct bandgap semiconductor. The absorption tail below the bandgap energy (U), equivalent to an Urbach tail, is also shown

As shown in Fig. 5.1, there is no optical absorption below the optical bandgap energy in ideal conditions. However, there are a number of processes related to static and thermal disorder that contribute to an exponential tail of absorption, (U in the figure), named the Urbach tail [4].

5.1.2 Experimental setup

The basic experimental setup of an OA experiment is schematically represented in Fig. 5.2.

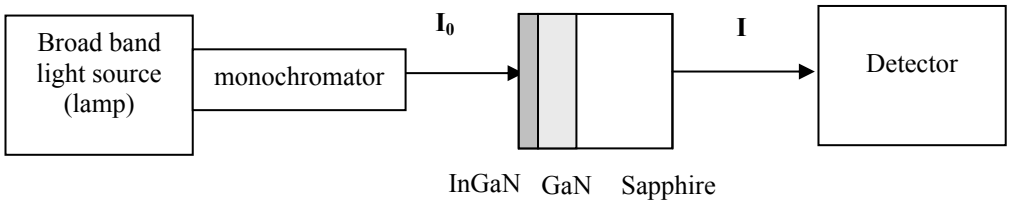

Figure 5.2: Illustration of the experimental setup used for optical absorption measurements. The relative thickness of the different layers in the InGaN/GaN/sapphire heterostructures is not to scale.

A high power tungsten filament lamp, supplied by a stabilised current source, was used as the broad band light source in the measurements described here. The monochromator was a 0.67m *McPherson 207* equipped with a grating blazed for 500nm, moved by a computer-controlled micro stepping motor. The sample was placed on a holder in a tube joining the output slits of the monochromator and the detector.

The detector consists of a photomultiplier tube (PMT). This device that transforms light into electrical current, as a result of the photoelectric effect, collects the light transmitted from the sample. Basically, a photomultiplier tube is a vacuum tube consisting of an input window, a

photocathode that emits electrons as it is struck by photons as a consequence of the photoelectric effect, and an electron multiplier sealed into an evacuated glass tube. The range of detected wavelengths is between 200 and ~800 nm. The PMT tube used was a GaAs R636. In the absorption measurements the reference signal, $I_0(E)$, is collected without the sample and $I(E)$ collected with the sample, so that the absorption can be calculated using Eq. 5.3.

5.1.3 The optical absorption spectra of InGaN/GaN layers

When considering the optical absorption spectra of InGaN/GaN/Al_2O_3 heterostructures it should be noted that light crosses the full heterostructure and the resulting absorption spectra sums the contributions of the various layers. The sapphire substrate is an insulator (with a very large band gap, E_g~9eV) and does not absorb light in the region of interest for these absorption experiments. GaN has a bandgap energy of ~3.4 eV at room temperature, and therefore it will strongly absorb any light with energy higher than E_g. The $In_xGa_{1-x}N$ bandgap is lower that 3.49 eV, and decreases with the InN fraction, down to the limit (for x=1) of the InN bandgap[1].
In Fig. 5.3 the RT absorption spectra of two InGaN/GaN samples with different compositions, STR58 (x=0.12) and STR59 (x=0.24), are shown.

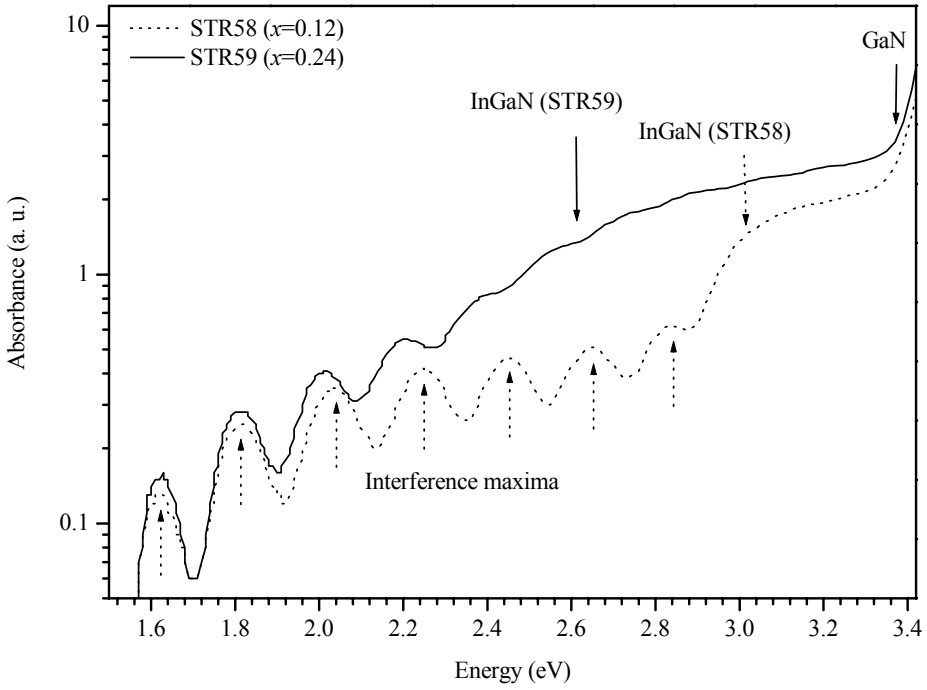

Figure 5.3: Optical absorption spectra of two $In_xGa_{1-x}N$/GaN samples, STR58 (x=0.12) and STR59 (x=0.24) at room temperature.

[1]As mentioned in Chapter 1, a bandgap energy of 1.9 eV has been widely accepted for many years, nevertheless there is presently an ongoing discussion about the bandgap of pure InN which, according to recent measurements [32], appears to fall in the range 0.6-1 eV.

The gallium nitride band edge can be clearly identified in the absorption spectra. The GaN band edge is at ~3.4eV, as expected, and below this energy one can identify the absorption related to the InGaN film. Note also that the onset of absorption shifts to lower energies for the higher *x* InGaN layer, as expected.

Absorption results for alloys, such as InGaN, are difficult to interpret and the bandgap energy determination by direct observation of the spectra is not unequivocal, since the onset of absorption is unclear. Furthermore, interference fringes are observed at the lower energy in each spectrum. These two issues are discussed in the next sections.

5.1.3.1 Fabry-Perot Interference fringes

The signal modulation that can be observed in the optical absorption spectra in Fig. 5.3, are Fabry-Perot interference fringes. These fringes are caused by interference of light occurring in the "cavity" formed by the nitride layer (n~2.5), sandwiched between air (n=1) on one side and sapphire (n~1.5) on the other. Fabry-Pérot interference fringes may also appear in the PL spectra and complicate the spectral features interpretation. However, these fringes can be removed using the mathematical procedure proposed by the authors of Ref. [35]. The fringe spacing in the absorption spectra can be used to estimate the nitride layer thickness.

Consider the basic equation for interference maxima:

$$2n(\lambda_i)t = m\lambda_i, \qquad \text{(Eq. 5.4)}$$

where t is the film thickness, n the refractive index, λ the wavelength and m is an integer. Eq. 5.4 can be rewritten as:

$$m = \frac{2tn(E)}{\lambda_i}, \qquad \text{(Eq. 5.5)}$$

which is in the form of a straight line if the fringe order $m(y)$ is plotted versus $[n(E)/\lambda](x)$, with a slope=2t.

In order to obtain a precise estimation of the total nitride layer thickness using the maxima, the GaN refractive index as a function of photon energy needs to be known[2]. The GaN refractive index has been determined by various techniques in the range of wavelengths used, and it varies from ~2.34 to ~2.65 for energies of 1eV to 3.4eV, respectively [33,34].

[2] A great part of the nitride stack is composed by the GaN buffer, typically about 10 times thicker than InGaN. Thus, the GaN refractive index is used for the calculations.

The energy variation of the GaN refractive index can be modelled by using the following equation [6]:

$$n(E) = \sqrt{\left(1 + \frac{A}{E_0^2 - E^2}\right)}, \qquad \text{(Eq. 5.6)}$$

where A=385 $(eV)^2$, E_0=9 eV and E is the photon energy.

If the consecutive orders $m(y)$ are plotted against the ratio between the refractive index at that specific wavelength, and the wavelength of the maxima position $[n(\lambda)/\lambda]$ (x), the graph shown in Fig 5.4 is obtained for sample STR58.

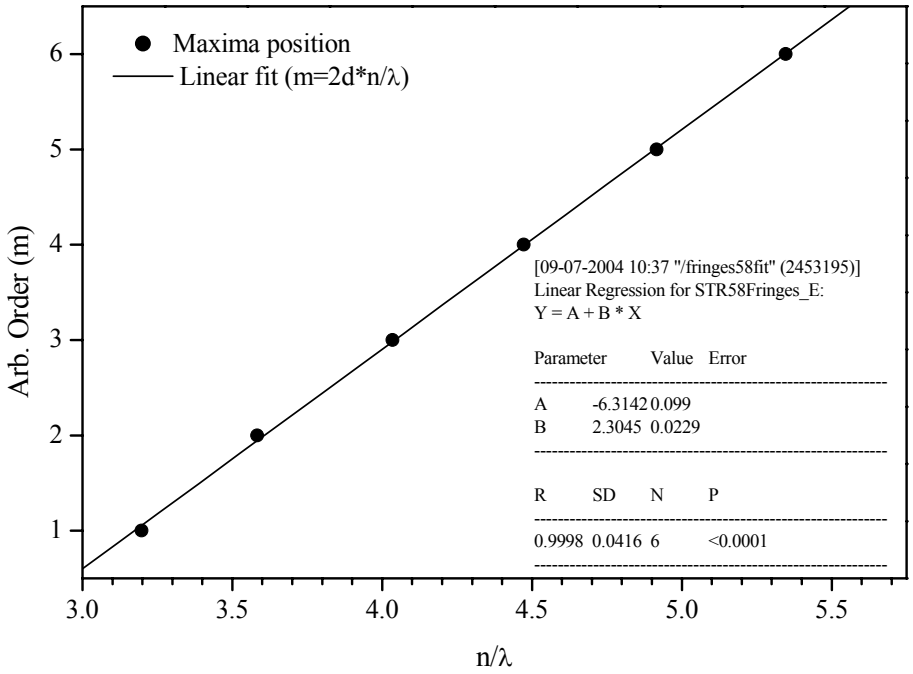

Figure 5.4: Plot of the order number $m(y)$ *versus* the ratio between the refractive index and the wavelength of the maxima position $[n(\lambda)/\lambda]$ (x) for sample STR58. A linear fit to data and the resulting fit parameters are also shown.

A linear least squares fit to the data yields t=1.152±0.001 μm. This result is in excellent agreement with the RBS measured thickness. Simulation of the RBS spectra yields an InGaN layer thickness of 180±5 nm and a GaN buffer layer thickness of 976±10 nm, i.e. a total nitride layer thickness of 1156±10 nm. The thickness determination process by RBS in InGaN/GaN layers is detailed in Chapter 4.

It is important to note that in smooth layers the interference fringes are better defined. If the thickness, t, is not uniform the fringes become damped or are destroyed. Therefore, considering

the better fringe definition in sample STR58 one may conclude that the roughness is lower. This conclusion is supported by RBS and AFM surface roughness analysis, as discussed in Section 4.10, where the values of σ_{AFM}=11.0 nm and σ_{AFM}=37.2 nm were obtained for samples STR58 and STR59, respectively.

It is important to note that for similar InGaN layer thickness (RBS measured thickness for STR59 is 190±5 nm) an increase of *x* appears to result in a surface roughness increase. The overall structural properties, and the morphological evolution, of InGaN layers as a function composition and layer thickness are discussed in Chapter 6.

5.1.3.2 A working definition of the bandgap in InGaN layers: the sigmoidal fit

The interpretation of the optical absorption spectra in InGaN layers presents additional complications compared to binary semiconductors. With increasing InN fraction the absorption broadens significantly as it shifts to lower energy, causing difficulties to obtain a reliable determination of the band gap energy.

A heterogeneous alloy can be depicted as a superposition of many different semiconductors, with a statistical distribution of composition/strain, and therefore bandgaps. It is not simple to calculate the expected absorption profile in the absence of microscopic statistical information about the distribution. In order to allow an accurate and reproducible description of the absorption edge the authors of reference [36] introduced an empirical description of alloy bandgaps, by fitting the experimental absorption spectrum (absorptance) to a sigmoidal function:

$$\alpha(E) = \frac{\alpha_0}{1 + \exp\left(\frac{E_g^{abs.} - E}{\Delta E}\right)} \qquad \text{(Eq. 5.7)}$$

where E_g^{abs} is the mean "effective band gap" energy of the alloy, and ΔE is the broadening parameter, equivalent to the Urbach tailing energy.

In Figure 5.5 we show the absorption curves for several InN concentrations fitted to the sigmoidal expression in Eq. 5.7. The values of E_g^{abs} obtained, as well as the broadening parameters ΔE, are shown in the graph of Fig. 5.5.

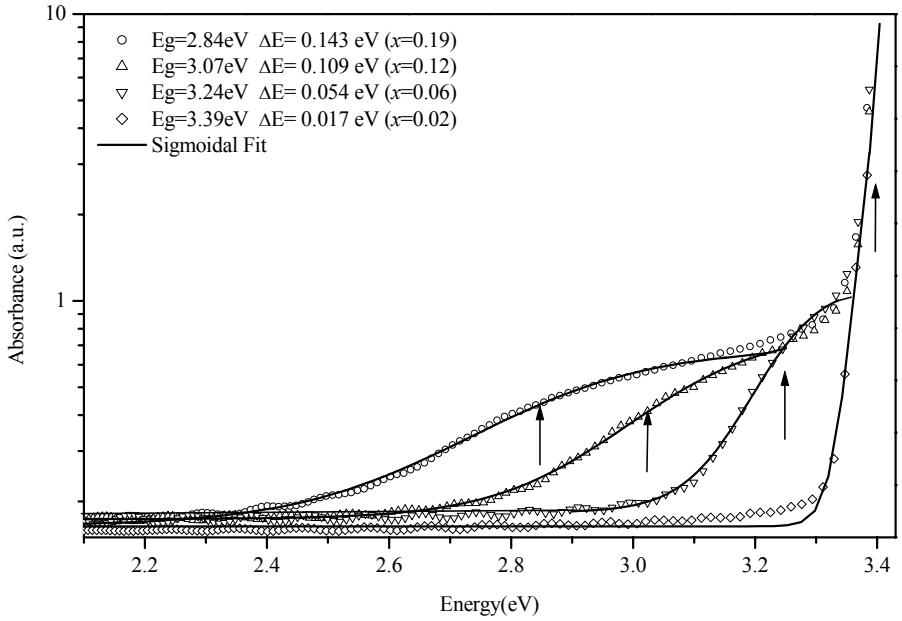

Figure 5.5: Room temperature absorption curves of InGaN/GaN layers with various compositions. The sigmoidal fit to data and the parameters obtained from the fit are also shown.

The OA results show a decrease of bandgap, and an increase of the broadening parameter, presumably related to an increased inhomogeneity, for InGaN layers with larger InN contents.
Now that we have described the optical absorption properties of $In_xGa_{1-x}N$ with various x, let us turn our attention to the emission properties, i.e. the inverse of the absorption process.

5.2 Photoluminescence spectroscopy

To excite luminescence in semiconductors, a high concentration of electron-hole pairs must be generated. This can be induced using different excitation mechanisms; If the excitation is due to a nearly monochromatic light beam with a photon energy above the material bandgap (*photoexcitation*) the resulting light emission is called *photoluminescence* (PL). When excitation accomplished by an accelerated electron beam the light emission is called *cathodoluminescence* (CL). On the other hand if the light emission is induced by current injection in a p-n junction the light emitted is called *electroluminescence*.
Because of its flexibility, PL is the classic, and one of the most useful optical methods for semiconductor science and industry. It has a recognisable ability to find impurities and defects in semiconductors, which affect materials quality and device performance. A given impurity produces a set of characteristic spectral features. This fingerprint identifies the impurity type, and often several different impurities can be seen in a single PL spectrum. Half widths of PL peaks are an indication of sample quality and crystallinity and the PL dependence on external

perturbations like temperature, pressure, stress, among others, also provides important information about the semiconductor physical properties.

5.2.1 Basic principles of PL

When electrons are excited across the band gap of a semiconductor by means of optical excitation, they move into allowed excited states in the conduction band. The photon energy has to be enough to excite the electrons across the bandgap, so that $h\nu \geq E_g$. Electrons excited from the *valence band* to the *conduction band* may move freely, or correlated with the holes via Coulomb interaction as pseudo-particles with hydrogen-like states called *excitons*, until they recombine.

When these electrons return to their equilibrium states, the excess energy is released, either as light (a radiative process) or by nonradiative processes, as conversion into lattice phonons. In spectroscopy, the spectral distribution of the emitted photons is referred to as the *emission spectrum*.

The emission spectrum is related to the energy difference between the two electron levels involved in the transition, that is, between the excited state and the ground state. The intensity of the emitted light is related to the quantum efficiency, the excitation power density and the absorption of exciting light. The quantum efficiency is the relative contribution of the radiative process to the total energy released (radiative and nonradiative). Increasing the excitation power density increases the number of photons, and therefore the number of photoexcited electrons.

Now, some specific applications of PL spectroscopy with relevance to this work are briefly discussed.

5.2.2 Some selected applications of photoluminescence spectroscopy

In favourable circumstances, photoluminescence can be used to *determine the semiconductor bandgap*. The most common radiative transition in very pure semiconductors is between correlated states in the base of the conduction band and the top of the valence band, for which the energy difference is primarily dependent on the bandgap. The bandgap can be determined from the PL peak energy as follows:

$$E_g = E_{PL} + E_{BE} + E_{SS}, \quad \text{(Eq. 5.8)}$$

where E_g is the bandgap energy, E_{PL} is the PL peak emission energy, E_{BE} is the free exciton binding energy and E_{SS} is the Stokes' shift (SS). The SS is related to the bandgap inhomogeneity and appears as a consequence of the relaxation processes of the excited carriers to lower energies or minima in the bandgap before they recombine [36,37]. Hence, the recombination from those local minima lowers the PL peak emission energy. Bandgap fluctuations can be related to material inhomogeneity. The Stokes' shift is a measure of the energy difference between the *emission peak energy* and the *band edge*, and can be obtained by comparing absorption and PL results. The magnitude of the SS provides a quantitative measure of exciton localisation [36,38]. We will get back to this issue, with reference to InGaN layers, in Section 5.5.

Local bandgap determination is important for InGaN, and other compound semiconductors, whose band gap varies with the composition. When the relation between gap energy and PL peak is precisely known, a PL measurement of the optical gap can be inverted to determine *x*. From this, a two dimensional map of the alloy composition can be obtained as the exiting beam is scanned across the surface of the sample. The spatial resolution attainable is higher than that reached with OA.

PL is also a useful technique to *detect impurity and defect levels*, which may produce localized states in the bandgap (donor-acceptor pairs, bound excitons, etc). The photoluminescence energy associated with these levels can be used to identify specific defects, and in some cases the intensity of photoluminescence can be used to estimate their concentration.

Information regarding the identification of the *recombination mechanisms* can also be obtained. As discussed above, the return to equilibrium, also known as "recombination", generally involves both *radiative* and *nonradiative* processes. The photoluminescence intensity, and its dependence on the level of photo-excitation and temperature, are directly related to the dominant recombination process. Dynamics of exciton formation-recombination can be studied by monitoring spectral shape, position and intensity variations as a function of time following photoexcitation (time resolved PL). Therefore, PL analysis helps to understand the underlying physics of the recombination mechanism.

Material quality evaluation. In general, nonradiative processes are associated with localised defect levels and extended defects, whose presence is generally detrimental to material quality and subsequent device performance. Such localized defect levels originate from material imperfections. Thus, material quality can be evaluated by the amount of radiative recombination, i.e. the PL intensity. The width, typically the *full width at half maximum* (FWHM), and the shape of luminescence peaks also provides information on strain or composition heterogeneity, in the case of single InGaN layers, and well/barrier interdiffusion in the case of quantum wells.

5.2.3 General description of PL experimental setup

In this section the photoluminescence setup used is described. Figure 5.6 is a schematic representation of the PL laboratory utilized for most measurements discussed in this thesis.

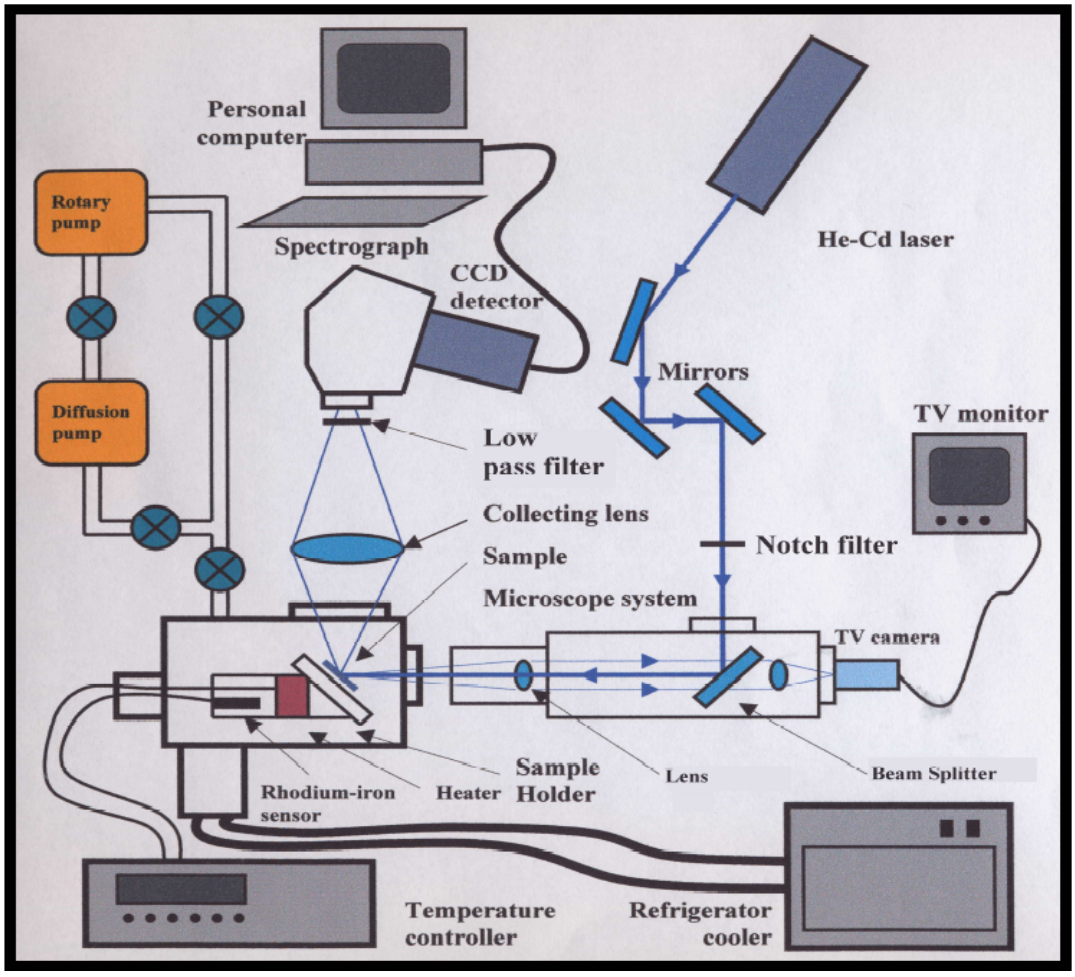

Figure 5.6: General view of the experimental set-up for PL spectroscopy measurements [39].

Let us briefly describe the main components of the experimental setup.

Exitation sources. The light provided by a laser is used to excite the sample. Figure 5.6 specifies a He-Cd laser, but both He-Cd and Ar+ ion laser were used in this work. The effective laser power reaching the sample is reduced by about a factor of 10, as it is reflected by mirrors and transmitted through a notch filter. He-Cd lasers are may produce output in the ultraviolet (325 nm) and the deep blue (442 nm). Here, only the ultraviolet output was available. The Ar^+ laser used here has an intercavity prism in order to select a particular output wavelength, ranging from the ultraviolet to green. Table 5.I shows some specifications of the He-Cd and Ar^+ ion lasers used.

Table 5.I: Relevant specifications of the He-Cd and Ar+ lasers used.

Laser	Model	Output wavelength (nm)	Output Power (mW)	Beam diameter (mm)	Beam divergence (mrad)
He-Cd	Melles Griot 3056-S-A2	325	~4.0	0.3	2.0
Ar^+	Coherent Innova 90-5	351.1-363.8 (used)	~30	1.5	0.5

Microscope system. The purpose of this component is to focus the beam on the sample using a focusing lens and a beam splitter. The beam splitter reflects the laser beam from the laser, and directs it to the sample. The luminescence is collected by the lens, transmitted through the dichroic beam splitter and focused on a camera, which sends the signal to a TV monitor. Reflected light is blocked by the dichroic element.

Vacuum chamber. The vacuum in the sample chamber is produced by a rotary and a diffusion pump disposed as shown in Fig. 5.6 which reach pressures down to ~ 10^{-2} mbar 10^{-5} mbar, respectively.

In the vacuum chamber the sample temperature is controlled using four elements:

1) *Film heater*. A non inductive heater set in Kapton film that delivers a power of 25 Watts and has a resistance of 25Ω.
2) *Refrigerator cooler*. It operates on the *Gifford-McMahon* principle, and consists of a piston that cyclically compresses a helium gas.
3) *Temperature sensor*. This component is installed in the lower part of the sample holder and is made of rhodium-iron metal alloy. It has 4 wires, through 2 of which an excitation current of 1 mA is passed. The remaining two are used to measure the temperature by measuring the change in the resistance (typically the resistance changes from 5Ω to 30Ω for the temperature change from 5 to 300 K). The resulting change in temperature due to self-heating is less than 1 mK over the range 1.4 to 300 K.
4) *Temperature controller*. This is an electronic device that both records the temperature and can be used to set it to specific values. Its calibration is important in order to read accurate temperatures. The temperature controllers usually contain a standard resistance versus temperature curve corresponding to the type of detector in use.

Detection system. This part of the setup is responsible for the light collection, and it consists of two basic elements.

1) *Spectrograph*. This device is used to disperse the light into the different wavelengths, so that it is possible to obtain the sample luminescence signal as a function of the wavelength. The spectrograph used is schematically pictured in Fig. 5.7.

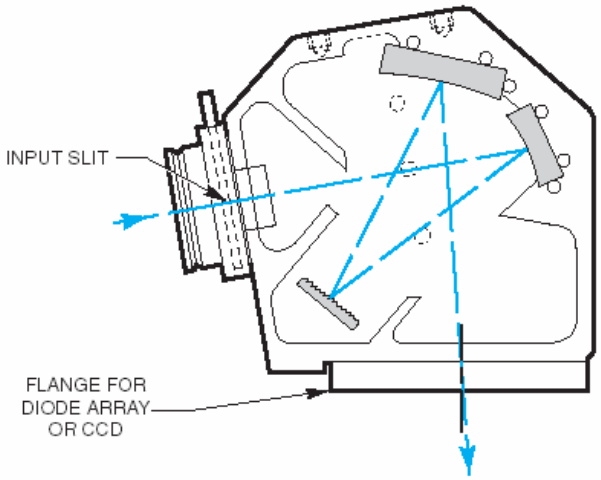

Figure 5.7: Optical configuration of the MS125™ spectrograph[3].

The incoming light passes through a 25 μm entrance slit, is reflected by the first mirror dispersed by the diffraction grating, reflected in the second mirror and then collected. Different gratings can be used in this setup. The grating choice depends on the spectral region to be measured, determined by the blaze wavelength, and the required spectral range/resolution. Note that gratings covering a wider range of wavelengths have less resolution. Typical values of resolution for a grating with 400 lines/mm blazed at 350 nm, covering the region from 200-800 nm, is about 1.0 nm. On the other hand, resolutions down to 0.2 nm can be obtained with a holographic grating with a line density of 2400 lines/mm, however the spectral range is reduced to 230-500 nm.

2) *CCD detector*. This device collects the light dispersed by the spectrograph. It contains a charged coupled device, or CCD, which is a silicon based semiconductor chip containing a two-dimensional matrix of photosensors, called pixels. Specifically, the ANDOR detector used in the PL experiments bears a CCD of 256 rows and 1024 columns. The CCD detector contains the CCD sensor and its pre-amplifier. It also contains a thermoelectric cooler based on the Peltier effect. This allows the CCD detector to be cooled to temperatures down to approximately –60 ^{0}C. Two connectors allow water to be passed through the head to assist cooling. The signal, once preamplified is sent to a PCI card connected to a computer, where the spectra are stored.

[3] See more details at http://www.spectra-physics.com/

The efficiency of the spectrograph – CCD detector system is determined by the width of the entrance slit and the type of grating installed in the spectrograph and the width of the diode array element used in the CCD detector system.

Optical filters. Filters are used to cover the desired range of the optical spectrum to reject unwanted radiation, such as second order diffractions of the laser. When the He-Cd laser setup was used, a 325 nm notch interference filter was placed in front of the sample. This filter allows the radiation with a wavelength of 325 nm, with a bandwidth of about 10 nm broad, so that unwanted plasma lines do not reach the sample. A low pass filter was placed in front of the detector. This filter is transparent to wavelengths longer than 345 nm and cuts out the 325 nm laser line to avoid detector damage. When the Ar+ ion setup was used, a 365 nm notch interference filter and a 450 nm low pass filter were placed in front of the sample and the detector respectively.

5.2.4 Experimental results

5.2.4.1 PL spectra of InGaN layers with increasing InN fraction

Typical PL spectra from several InGaN samples taken at 10K and normalised to unit are shown in Fig. 5.8.

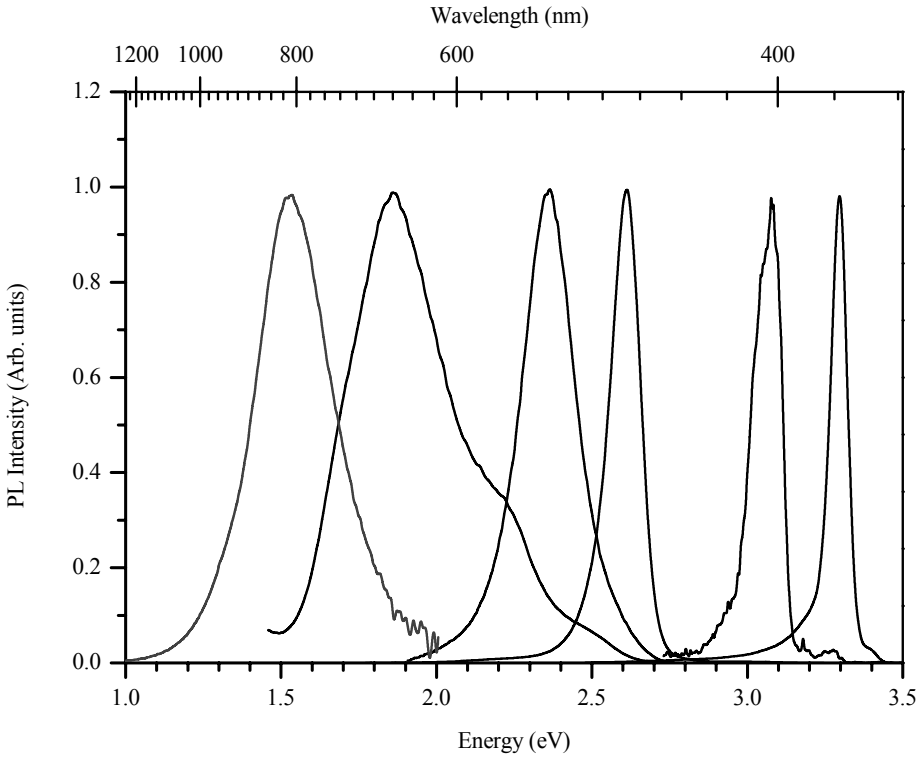

Figure 5.8: Low temperature photoluminescence spectra from InGaN/GaN layers with different compositions raging from infrared (higher *x*, low E) the ultraviolet spectral regions (lower *x*, higher E).

It is evident from Figure 5.8 that InGaN emission covers the entire range of the visible spectrum and beyond. This graph illustrates the most attractive physical property, from a commercial point of view, of InGaN alloys. Together with the high emission efficiency, it explains the enormous interest in using the alloy to produce optoelectronic devices.

The peak emission energies can be extracted directly from the graph to be ~3.30 eV, 3.07 eV, 2.61 eV, 2.36 eV and 1.53 eV for samples with increasing average InN fraction. A decrease in the peak emission energy is verified with an increase in the indium nitride content in InGaN, the same trend observed for the bandgap by OA. The relation between bandgap energy and PL peak energy is discussed in Section 5.5, and the PL peak energy composition dependence for InGaN will be discussed further in Chapter 7.

Note that PL spectra in Fig. 5.8 possess the same general shape: a single broadband feature with approximately exponential tails more pronounced on the low energy side. However, this is not always the case. Samples featuring asymmetric peaks, and even double PL peaks are found. The specific case of double PL peaks is illustrated in the next section.

Another feature evident from the spectra is a notable increase in the linewidth, from 0.06 eV to 0.29 eV, with decreasing peak emission energy. The broadening of the PL emission, which is accompanied by a decrease of PL luminescence intensity[4], further evidences a degradation of the optical properties with an increasing composition, as verified by OA. It is worth to mention that for high InN fraction (say, x>0.25) MOCVD-grown InGaN layers analysed by PL spectroscopy, one could observe extreme cases of optical inhomogeneity at a macroscopic scale. In these samples, the PL peak energy varies as the laser beam is scanned across the sample surface. An account of the results obtained in these samples is published in Ref. [40,41]. However, note that the results presented and discussed in this thesis concern only samples where a good lateral homogeneity (at least on a scale larger that the laser spot size) has been found by PL mapping.

5.2.4.2 Temperature dependence of PL: an example of double peaks

In Fig. 5.9 the evolution of the PL spectrum with temperature of an InGaN/GaN layer (STR99) is shown. The first notable spectra feature is that contrary to the PL spectra in Fig. 5.8, this InGaN layer features two luminescence peaks; a lower energy peak at ~ 2.77 eV and a higher energy component at about 2.96 eV. The observation of double PL peaks has been typically ascribed to phase separation effects or InN-rich quantum dot formation in the literature, see for instance Ref. [42,43]. This issue will be addressed in detail in Chapter 7, where an alternative explanation for this phenomenon is proposed.

[4] Although no absolute measurements of PL intensity were performed, it is clear that the PL intensity drops several orders of magnitude as the emission moves into the red.

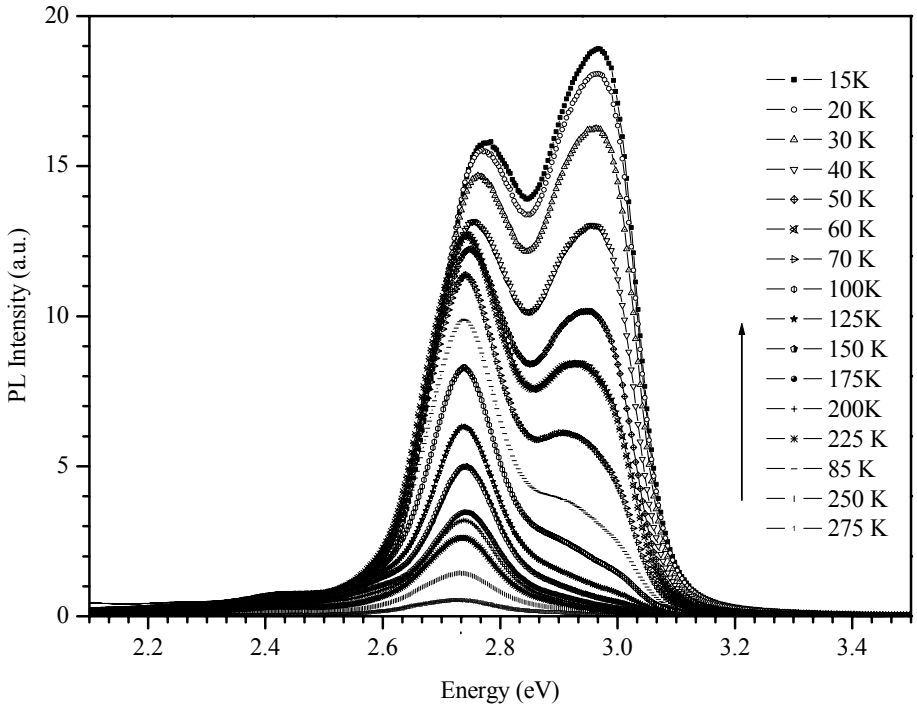

Figure 5.9: Temperature dependence of the PL spectra from an InGaN/GaN layer (STR99) featuring two luminescence peaks, centred at 2.77 and 2.96 eV respectively.

Also evident in the spectra of Fig. 5.9 is a strong decrease of the PL intensity with temperature. This trend can be explained by an increase of the nonradiative recombination probability for higher temperatures. With increasing T, trapping of carriers by the non-radiative sites in the material results in a quenching effect on the luminescence intensity.

Moreover, the temperature behaviour of the two peaks is quite distinct. As a result, the relative contribution to the overall sample luminescence of the two components changes strongly with T. Temperature quenching of the higher energy component is much more pronounced. At 15K this component dominates whereas at room temperature it almost disappears. From this behaviour it is suggested that the lower energy luminescence peak is more deeply localized thus suffering less quenching with T. Similar temperature behaviour in InGaN layers showing double luminescence peaks was reported by the authors of Ref. [42].

5.3 Confocal laser scanning microscopy and spectroscopy

Confocal microscopy (CM) is a planar imaging technique that uses spatial filtering by pinhole apertures to remove out-of-focus contributions to a microscopic image. CM was used in this work to study the light emission features of InGaN epilayers at a microscopic scale. Microscopic imaging and spectroscopy of selected InGaN layers provides simultaneously information on structural and luminescent properties down to a μm length scale.

5.3.1 Basic principles

Confocal microscopy was invented by Marvin Minsky 1955 and patented in 1957[5]. It is rather a successful technique in biology (since around 1985) because of the possibility to eliminate out-of-focus blur and thus obtaining a 3D fluorescence image from intact biological specimens by non-invasive optical sectioning. However, CM is not commonly applied in the study of semiconductors.

This optical technique can be used to study the luminescence from epilayers at a fairly high resolution (1-10 μm length scale). Confocal laser scanning microscopy uses a diffraction-limited laser spot to address the sample in a raster scan. In scan mode operation, the sample response is a function of beam position and this produces a image $Z(x,y)$ which contains spectroscopic information. This allows the collection of a series of single points to build up an image. The system allows the collection of fluorescence and reflection images concurrently and at a large range of temperature. Moreover, the lateral resolution can be improved by a factor of 1.4x compared to that obtained in a conventional optical microscope [45].

5.3.2 Experimental setup

Confocal microscopy was carried out using the Daresbury Laboratory Microscope SYCLOPS[6], at Warrington, UK [45]. This microscope has confocal illumination and detection optics arranged on an optical bench to allow more flexibility of application, and it features an attached scanning mirror head, objective lens mount and a sample stage. Both laser sources and synchrotron radiation can be used, the synchrotron radiation is used for fluorescence lifetime spectroscopy. The experimental set-up of the SYCLOPS scanning confocal microscope is shown in Figure 5.10.

The laser[7] beam is focused through the source pinhole (PH1) and collimated to a parallel beam. This passes through a short pass dichroic mirror (DM1, Tech Optics), with a reflecting cut on at 495 nm, to the scanning mirror head (SM). A Zeiss 10× objective lens (OL) gives a large field of view (~ 500 × 500 μm^2).

[5] See more details at: http://web.media.mit.edu/~minsky/papers/ConfocalMemoir.html
[6] SYnchrotron radiation for ConfocaL OPtical Scanning.
[7] A HeCd or argon ion laser was used to excite the InGaN samples with a diffraction limited laser spot focused down to approximately 1μm in diameter.

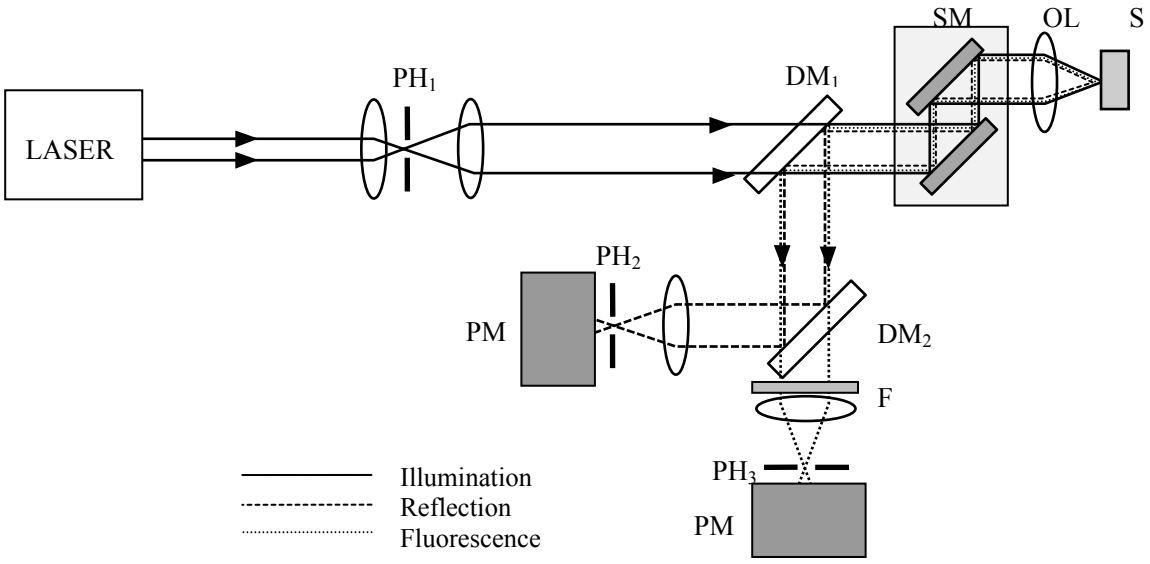

Figure 5.10: Schematic illustration of the SYCLOPS confocal microscope experimental setup [46].

Reflected and fluorescence light from the sample (S) is collected by the objective and passes back through the scan head. Fluorescence, plus a small portion of the reflected light is deflected by DM_1 into the detection beam path. Separation of reflected and fluorescent light is performed by a second dichroic mirror (DM_2, Nikon), reflecting below 510 nm (or 410 nm). Each portion of light is detected by one of the two detection channels, both containing a focusing lens, pinholes ($PH_{2,3}$) and cooled photomultiplier tube (PMT,Hamatsu R3896). This arrangement allows simultaneous collection of fluorescence and reflection images from the same focal plane within the sample. The area of the sample that the confocal image surveyed was dependent on the focal length of the objective lens used. The dimensions of the images were calibrated using a glass slide with a 50 μm by 50 μm grid pattern drawn onto it as a reference. On comparing the images obtained on the InGaN samples, high-resolution information on the spatial distribution of the sample luminescence was determined down to a length scale of ~1 μm.

To create an image of the sample, the focused beam was moved by the two scanning mirrors in a raster pattern over the sample surface and the time reference of the waveform generator, which drives the mirrors, used to trigger two slow-scan framegrabbers. The current signal from the two PMTs was then converted to voltage input to the framegrabbers to produce the reflected and fluorescence images simultaneously.

Spectral selection of the image, largely increasing the usefulness of CM for the study of InGaN layers, can be accomplished by inserting bandpass filters in the fluorescence light path at position **F**. This allows a rudimentary form of spectroscopy to be carried out. A more refined spectral analysis can be achieved by placing a spectrometer with a CCD detector array in the fluorescence channel instead of the PMT. The emission spectrum from the sample was recorded

and PL measurements could then be taken as either an average across the scanned sample surface or at selected points on the reflectance image by stopping the scanning at selected points, monitored using the reflectance image on the sample surface. Temperature dependence studies can also be done with this system. Sample temperature control, from near liquid nitrogen temperature (~80 K) to room temperature is achieved by using a Linkam HFS 91 liquid nitrogen cooled stage.

5.3.3 Confocal microscopy images

CM reflectance and fluorescence images of an InGaN epilayer sample taken at low temperature (~80 K) are shown in Figure 5.11. The surface is found to be heterogeneous with a number of large hexagonal structures observed. The images have been enhanced by computer generated false colours using the image processing software package PaintShopPro[8] 6. To distinguish fluorescence and reflectance images, the fluorescence image is coloured differently to the reflectance image, generally red or orange as opposed to green or blue. On forming a composite of the two images, regions of dominant fluorescence and reflectance can still be differentiated. Areas in which fluorescence and reflectance are equally prominent show as a 'mix' of the two colours. The effect of temperature on the fluorescence images is a notable increase of brightness, the intensity in the fluorescence image may increase up to ~50 x from RT to 77K.

In fluorescence and reflectance images of thick InGaN epilayers, the sample surface is generally found to be uneven and granular [40]. Comparing Figures 5.1 a) and b), the non-reflecting areas (i.e. absorbing) of the sample were found to fluoresce strongly and vice-versa; few regions on the sample are found to be bright in both. Combining the fluorescence and reflectance images may therefore form a complete image of the sample surface. Spatial variation in the luminescence from hexagonal structures has also been seen in cathodoluminescence studies of InGaN epilayers [47].

A granular contrast can be observed in these low-resolution images. By changing the magnification of the CM, the sample surface may be studied more closely, and regions of interested can be zoomed in. CM images at various magnifications are shown in Figure 5.12. A larger magnification lens was used in the CM to take these images, and glycerol placed between the lens and the sample surface to act as a refractive index matching fluid. The resolution of the system allows individual grains ~1μm in diameter to be distinguished. In Figure 5.12, we present a set of surface images with successively large magnifications of sample STR115.

[8] http://www.jascsoftware.com/

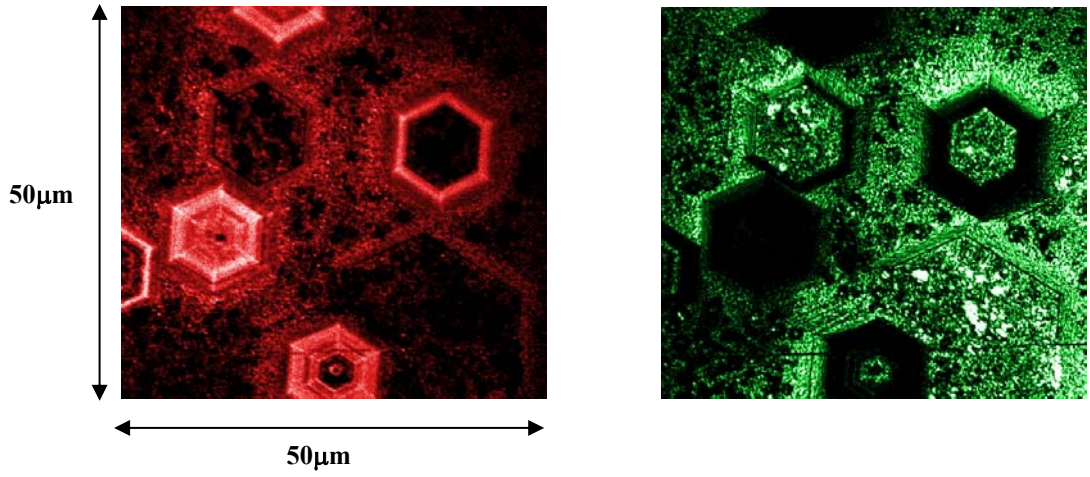

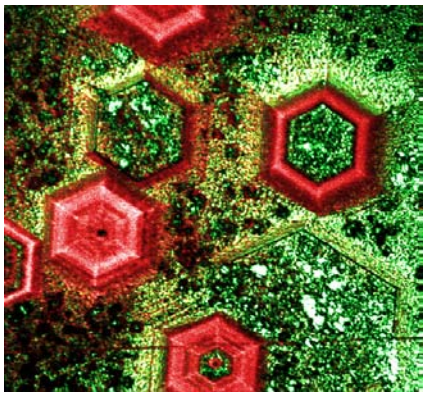

Figure 5.11: Combining fluorescence and reflectance confocal images from epilayer sample InGaN 331.

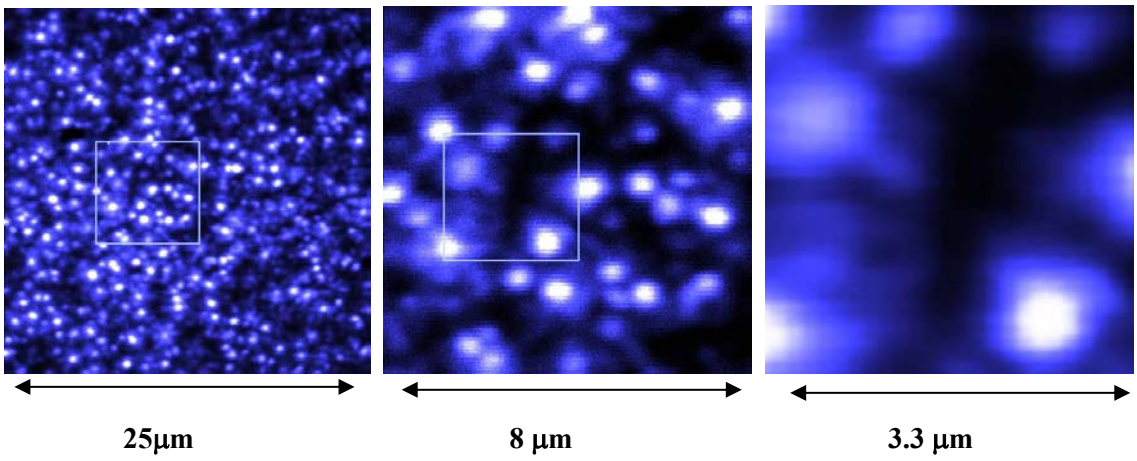

Figure 5.12: Reflectance image from InGaN Str115, the white box outlines the region of the sample selected for closer examination. PL can be performed.

5.3.4 Microspectroscopy at a μm scale associated to confocal microscopy

The main advantage of CM, with interest for the material under study here, is the ability to perform PL in selected regions of the sample surface. This capability is illustrated in Figure 5.13.

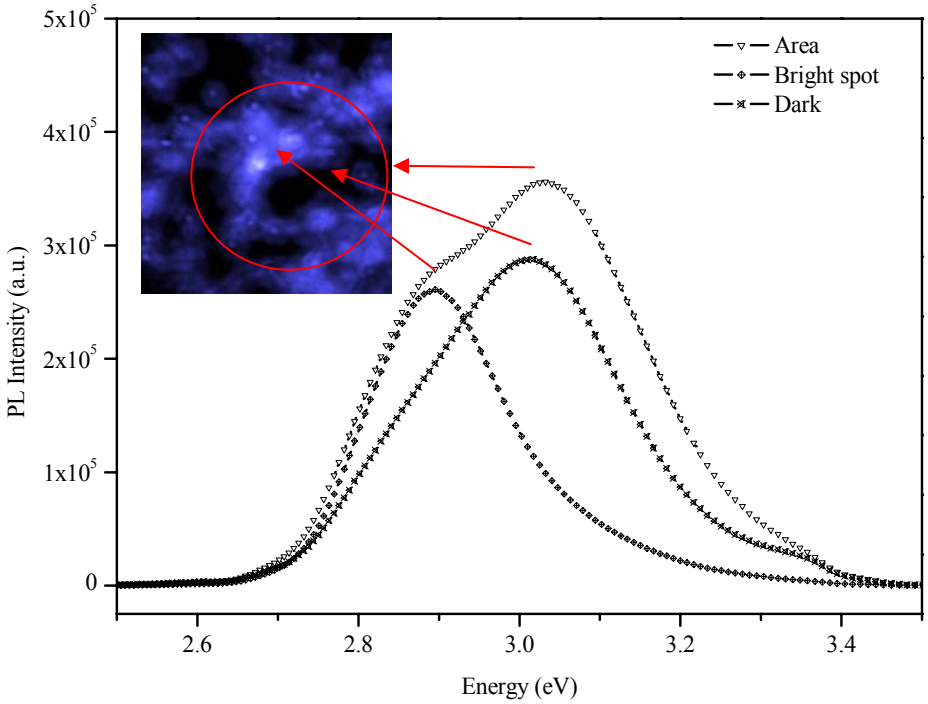

Figure 5.13: Spatial segregation of luminescence, as revealed by CM of an InGaN/GaN MQW sample on bulk GaN. The inset micrograph, 8 micron square, identifies the location of the spectra.

When the whole area is selected two components are noticed in the PL spectra. The PL signal originating from selected sample regions, characterised by brightness variations in the inset to Fig. 5.13 reveals two distinct luminescence components centred at around 2.88 eV and 3.02 eV, respectively. The relative intensity of the two PL components varies considerably when the position of the laser spot changes at a μm scale. The energy separation and the physical origin of the two PL components will be discussed in detail in Chapter 7.

5.4 Cathodoluminescence spectroscopy

Cathodoluminescence has been used for many years to spatially resolve the spectral emission of semiconductors [48]. The basic principles and the type of information that can be obtained from CL spectra are similar to the case of PL. Besides a better spatial resolution, that can in principle be attained, the fundamental advantage of CL is the possibility to control the excitation depth in the sample.

5.4.1 Basic principles

In-depth information about the optical properties of solids can be achieved by using an electron beam of variable energy to excite the luminescence [49]. This powerful technique to depth-profile semiconductor optical properties is based on the fact that the rate of energy loss of an electron beam in a solid depends on its incidence energy. The rate of energy loss by an electron beam transversing a solid depends on its energy at the surface and the specimen physical parameters. For example, a 5 keV electron beam will deposit most energy at a depth of order 50 nm in GaN, whereas a 30 keV electron beam will deposit its energy at a depth of ~1 μm.

5.4.2 Experimental setup

The electron beam excitation system used in this work is a locally built (Physics department, University of Strathclyde) system that provides an electron beam with variable energies up to 30 keV at current densities up to 20 A/cm^2. The electron beam excitation spot may be focused to a diameter of 200 μm, or defocused to illuminate the whole sample, up to a diameter of about 5 mm. In a common experimental set up, the electron beam is incident on the front face of the sample and the cathodoluminescence is detected from the edge of the sample, i.e. at right angle to the exciting beam. This excitation/detection geometry reduces potential distortions on the CL spectra due to sample depth heterogeneities.
The luminescence produced from the sample is focused on the entrance slit of a *Chromex* 0.5 m monochromator by a convex lens of focal length 17 cm. Spectral acquisition in the range of photon energies from 1.3-3.5eV utilises the *Oriel InstaSpec* cooled 2-dimensional CCD array mounted at the output focal plane of the monochromator. The *Chromex* monochromator has the option of three different diffraction gratings each blazed at different wavelengths and with different number of lines/mm allowing to choose the appropriate range/resolution to the experiment to be performed. The sample current is measured directly by a *Keithley* 428 current amplifier that is connected between the sample stage and the ground. The sample in this system can be cooled to a temperature of approximately 30K using a *Leybold* close cycle helium cryorefrigerator. Further details of the experimental apparatus are described in Ref. [50].

5.4.3 Monte-Carlo simulation of energy deposition as a function of depth

Monte-Carlo (MC) simulations of the electron beam energy dissipation in solids provide an invaluable tool in the interpretation of depth-resolved CL spectra [51]. In the MC method for electron trajectory calculations, it is assumed that each electron can undergo elastic and inelastic scattering, and can be backscattered out of the sample. The electron path is calculated in a

stepwise manner (as it travels a small distance in a straight line between random scattering events). At each step, random numbers determine the type of scattering event and the appropriate scattering angle.

The results for the MC simulations performed for sample AEC53 for various electron beam energies are represented in Fig. 5.14. In order to achieve statistical significance for each simulated electron beam energy, 10^5 trajectories were calculated.

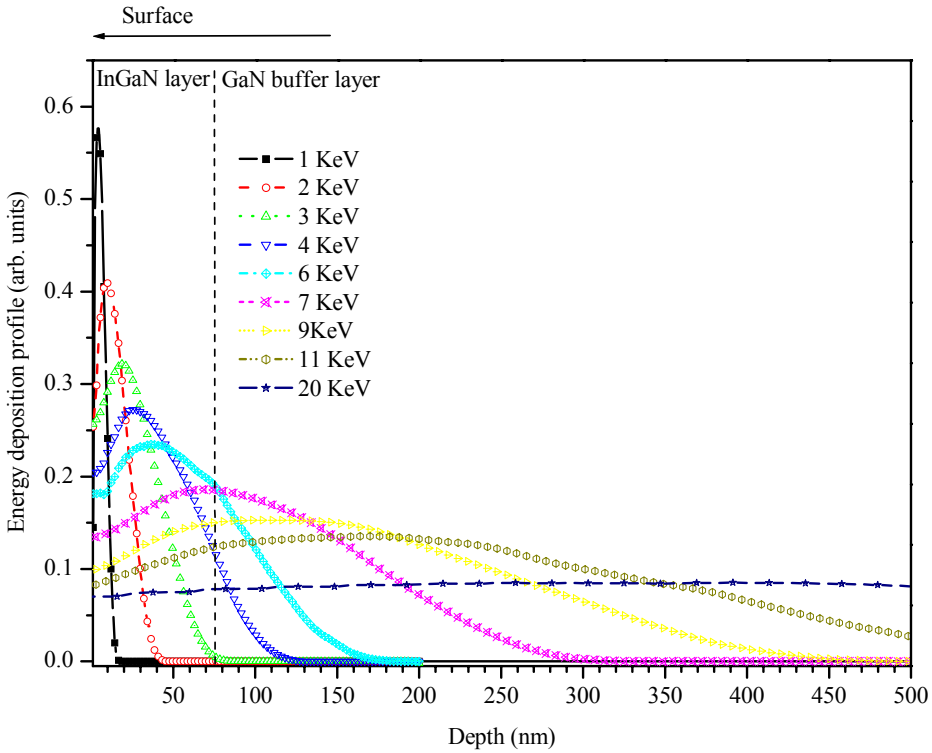

Figure 5.14: Electron beam energy deposition calculated using Monte-Carlo simulations of the electron trajectories for the 75 nm thick $In_{0.17}Ga_{0.73}N$ layer grown on top of a GaN buffer layer (AEC53).

To help the visualisation of the interaction volume for this sample the simulation results with only 10^2 trajectories, with energies of 3, 4 and 5keV, are shown in Fig. 5.15.

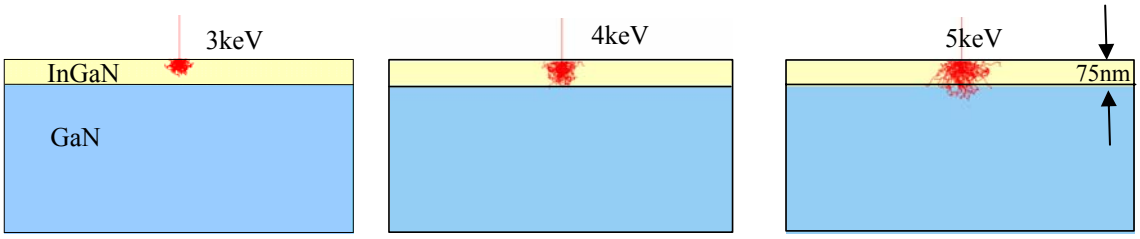

Figure 5.15: Diagram illustrating the electron trajectories when penetrating the nitride layer for increasing accelerating voltages, namely at electron beam energies of 3 keV, 4 keV and 5 keV.

From these simulations it would be expected that the electrons penetrate to the GaN buffer layer at energies in excess of 4-5 keV.

5.4.4 Experimental results

Low temperature (30K) CL spectra from the InGaN/GaN epilayer AEC53 at electron beam energies ranging from 1 to 7 keV are shown in Fig. 5.16. It can be observed that the InGaN related emission, that peaks at around 2.81 eV, is promptly excited even at the lowest accelerating voltages. This is the unique spectral feature for energies up to about 3 keV. However, for accelerating potentials higher than 4 keV, GaN related emissions start to be observed. Namely, the excitonic emission at ~3.47 eV, donor-acceptor pair related emission (~3.27 eV) and their respective longitudinal-optical (LO) phonon replicas.

These results are in excellent agreement with the MC calculations presented in Figures 5.14 and 5.15. This example, also illustrates very well the potential of CL spectroscopy using a variable energy electron beam to depth profile the optical properties of InGaN/GaN heterostructures. Further results on this sample, including a detailed analysis of the InGaN related peak as a function of the electron beam penetration, are presented and discussed in Section 7.3. This work is also published in the literature [52].

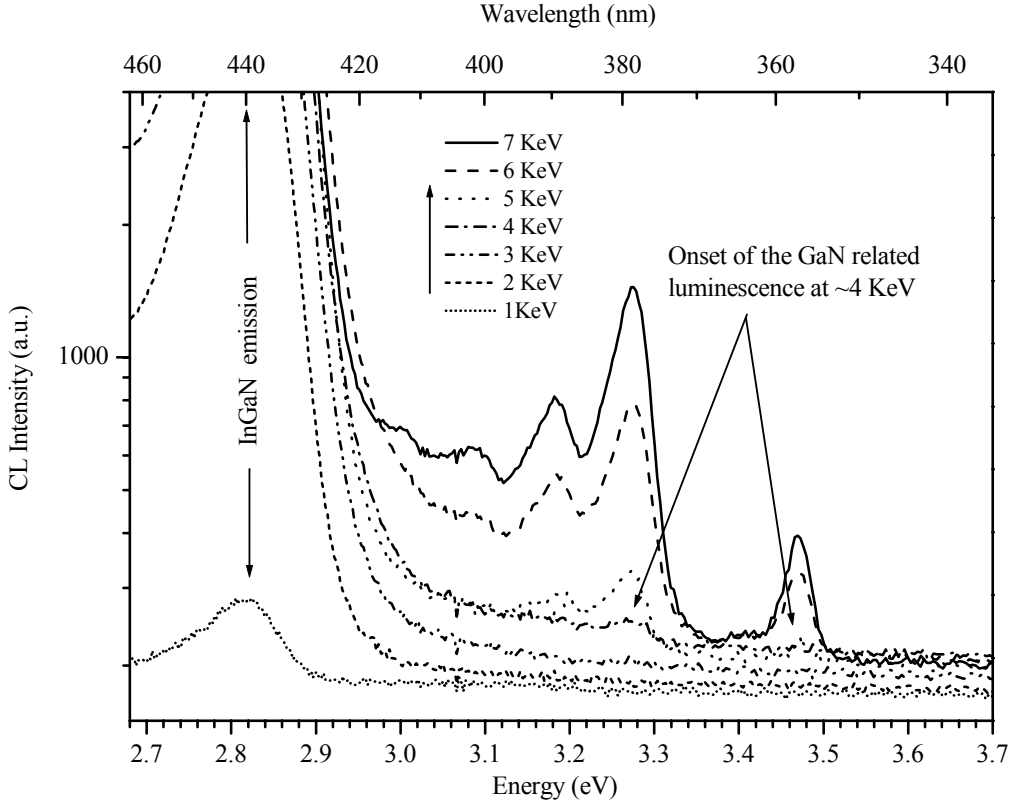

Figure 5.16: Low temperature cathodoluminescence spectra acquired at different electron beam energies (1-7 keV) from the InGaN/GaN/sapphire structure (AEC53). The InGaN related emission and the onset of GaN related luminescence are shown.

5.5 Some general remarks about InGaN spectral properties

In this section, we attempt to point out some general trends regarding InGaN optical properties, and establish correlations between some of the observed spectral features.

In general, optical characterization evidences a degradation of the optical properties when the In content and layer thickness increase. Starting form the OA results, it is found that the absorption curves broaden considerably as the absorption "edge" shifts to lower energies. This broadening indicates increased alloy inhomogeneity. Furthermore, a pronounced tailing of the absorption below the effective band gap indicates exciton localisation. When localised states are present they create a tail, typically described by an exponential function, in the density of states lower in energy than the semiconductor band gap [31,53]. Moreover, Fabry-Perot interference fringes (a surface quality indicator) tend to disappear for higher x and larger thickness of the InGaN films.

Concerning the PL results, it is found that the PL peaks also broaden as the peak emission energy decreases, also a sign of increased heterogeneity. The layers heterogeneity increases strongly with composition, reaching extreme cases of *macroscopic* variations of the PL peak energy, as revealed by PL mapping. It is also verified that the light emission efficiency drops sharply with increasing wavelength.

Beyond these direct observations, a systematic comparison of the band gap energy as measured by OA, E_g, and the PL emission peak, E_p, also reveals an increased mean energy loss in the excitation-emission cycle, as the PL peak energy decreases. A linear dependence of E_p on E_g was established by O'Donnell and co-workers:

$$E_p = 1.453(26)E_g - 1.54(8), \text{ with } 0<x<0.4. \qquad \text{(Eq. 5.9)}$$

This relation is found to cover a restricted range of indium incorporation [54]. The increased energy loss between absorption and emission, quantified by the Stokes' shift, $E_{SS} = E_g - E_p$[9], therefore increases as the PL emission shifts to the red, i.e. for higher x.

[9] Here we neglect the E_{BE} term given by Eq. 5.8. Despite the high exciton binding energy in III-nitrides, experimental absorption of InGaN fails to manifest peaks due to excitons. The main reason for this absence is a large inhomogeneous broadening, which increases with indium content. Hence, the term "effective band-gap" proposed in Ref. [36] and used here, acknowledges an excitonic contribution to the optical absorption.

The Stokes' shift shows a linear dependence on emission energy and, as expected, tends to a zero value near 3.4 eV, the GaN band gap at RT. These trends, which appear to be general for InGaN light emitting structures, indicate deeper exciton localization with decreasing emission energy. This enhanced localization is certainly related to the microscopic nature of InGaN alloys. Excitons in InGaN are localised within regions of lower band gap, since it is energetically favourable for the electrons and holes to move to these regions. The localisation process and the corresponding energy diagram are schematically represented in Fig. 5.17.

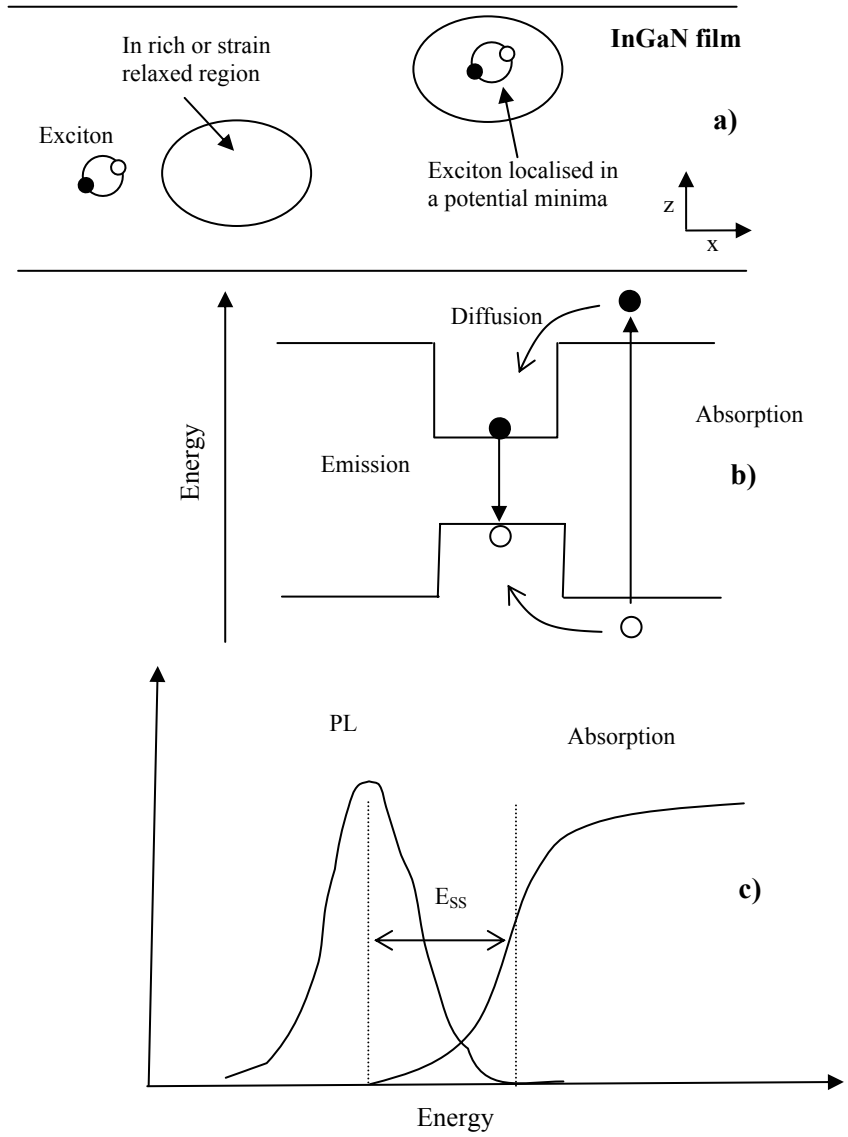

Figure 5.17: Exciton localisation in InGaN regions of lower band gap, due to strain or composition inhomogenieties. a) Spatial diagram b) Energy diagram c) schematic photoluminescence and absorption curves illustrating the origin of the Stokes's shift.

The localisation of excess carriers occurs on a more rapid time scale than radiative recombination, i.e. the luminescence from delocalized excitons is very weak, and the light emission is mainly from excitons after localization. An energy shift, the Stokes' shift, is therefore observed between the absorption edge and the luminescence peak of InGaN layers.

Now the question arises: what is the origin of the potential minima that localises the excitons in InGaN? It is hard to give a conclusive answer regarding the origin of localization in InGaN. Nonetheless, it is clear that a composition inhomogeniety, a small region of higher In content (lower E_g), would localize an excition. However, a small strain relaxed region[10] would lead to the same effect.

Additional information about the extent of localisation is provided by analysis of the temperature dependent PL spectra presented in Fig. 5.9. The temperature dependence measurements on an InGaN samples featuring double luminescence peaks (DLPs) systematically reveal that the lower energy component suffers less quenching with the temperature. This is also an indication of stronger localisation, since photoexcited carries captured in potential minima suffer less the influence of nonradiative recombination sites (for instance dislocations).

In Chapter 7, we try to correlate the puzzling optical properties of InGaN alloys with structural properties. In particular, the origin of DLPs is clarified with respect to the alloy structural properties. Therefore, the potential minima originating the localisation in this specific case can be understood.

[10] Strain relaxation in InGaN also lowers the band gap, the effect of strain on the band structure of InGaN will be studied in detail in Chapter 7.

5.6 Summary

In this chapter, the most relevant theoretical and experimental aspects of the optical characterization techniques used to investigate InGaN/GaN structures have been described. Some selected results from optical absorption spectroscopy, photoluminescence, confocal microscopy and cathodoluminescence spectroscopy measurements taken on a number of different InGaN epilayer samples, were used as illustrative examples.

It was shown how to obtain the effective bandgap energy in InGaN layers from OA measurements. The alloy bandgap was found to shift to lower energies for layers with larger In content. A broadening of the absorption curves, and less pronounced Fabry-Perot interference fringes, were found to scale with an increasing InN content. The period of the interference fringes could be used to estimate the nitride layer thickness.

Using PL spectroscopy the emission properties of InGaN samples were investigated. It is found that $In_xGa_{1-x}N$ luminescence covers the visible spectral region, and beyond. The luminescence peak energy was found to decrease with x, whereas a broadening of the PL linewidth with decreasing peak emission energy is verified. The luminescence intensity of the emission spectrum from the samples studied was found to decrease as the peak emission energy moves further into the red.

Temperature dependent PL measurements were taken on an InGaN sample that featured two luminescence peaks. It was found that the two components have different quenching rates with increasing temperature, and the higher energy component showed much more pronounced temperature dependence.

The usefulness of CM to study the surface morphology and light emission properties at a μm length scale was illustrated. Spectroscopic mapping by CM has revealed light emission inhomogenieties and resolved the location of two PL components originating at different surface location sites. The potential of CL spectroscopy with a variable energy electron beam, together with Monte-Carlo simulations of the electron beam penetration, to depth profile the optical properties of InGaN/GaN layers was also explored.

Analysis of the optical characterization results reveals a general trend of increasing inhomogeniety and an overall degradation of the optical properties as layer thickness and composition increase. The results also suggest a scaling of exciton localisation with the InN fraction.

5.7 References:

[1] B. Gil, ed. *"Group III nitride semiconductor compounds, physics and applications"* Series on Semiconductor Science and Technology 6, Oxford Science Publications, Oxford (1998).

[2] B. Gil, ed. "*Low-dimensional nitride semiconductors"* Oxford University Press, Oxford (2002).

[3] J. I. Pankove, "*Optical processes in semiconductors*" Dover. New York, USA. (1976).

[4] F. Urbach Phys Rev **92**, 1324 (1953).

[5] T. Matsuoka, H. Okamoto, M. Nakao, H. Harima, and E. Kurimoto, Appl. Phys. Lett. **81**, 1246 (2002).

[6] B. Monemar, "*Gallium Nitride I"* Semiconductors and semimetals, Vol. 50 pp. 305-368 (1998).

[7] Wim Van der Stricht, PhD thesis, University of Gent, Belgium (1999).

[8] L. Siozade, J. Leymarie, P. Disseix, A. Vasson, M. Mihailovic, N. Grandjean, M. Leroux, and J. Massies, Mater. Sci. Eng., B **82**, 71 (2001).

[9] R. W. Martin, P. G. Middleton, K. P. O'Donnell, and W. Van der Stricht, Appl. Phys. Lett., **74**, 263 (1999).

[10] F. Yang. M. Wilkinson, E. J. Austin and K.P. O'Donnell Phys. Rev. Lett. **70**, 323 (1993).

[11] K. P. O'Donnell, R. W. Martin, and P. G. Middleton, Phys. Rev. Lett. **82**, 237 (1999).

[12] R. Pecharromán-Gallego, PhD thesis, University of Strathclyde, UK (2004).

[13] K. P. O'Donnell, C. Trager-Cowan, S. Pereira, A. Bangura, C. Young, M.E. White and M.J. Tobin, Phys. Stat. Sol. (b) **216**, 157 (1999).

[14] M. E. White, PhD thesis, University of Strathclyde, UK (2004).

[15] Yong-Tae Moon, Dong-Joon Kim, Jin-Sub Park, Jeong-Tak Oh, Ji-Myon Lee, Young-Woo Ok, Hyunsoo Kim, and Seong-Ju Park, Appl. Phys. Lett. **79**, 599 (2001).

[16] S. Srinivasan, F. Bertram, A. Bell, F. A. Ponce, S. Tanaka, H. Omiya, and Y. Nakagawa, Appl. Phys. Lett. **80**, 550 (2002).

[17] M. J. Tobin, M. Martin-Fernandez and G. R. Jones, Synchrotron Radiation News, **11**, 24 (1998).

[18] C. J. R. Van der Oord, C. H. Gerritsen, Y. K. Levine, W. J. Myring, G. R. jones, I. H. Munro, Rev. Sci. Instrum. **63**, 1 (1992).

[19] K. P. O'Donnell, M. J. Tobin, S. C. Bayliss and W. Van der Stricht, J. of Microscopy, **193**, 1 (1998).

[20] P. G. Middleton, C. Trager-Cowan, A. Mohammed, K. P. O'Donnell, W. Van der Stricht, I. Moerman and P. Demeester, Mat. Res. Soc. Symp. Proc. **449**, 471 (1997).

[21] B. G. Yacobi and D. B. Holt, *"Cathodoluminescence microscopy of inorganic solids"*, Plenum Press. NY, 1990.

[22] C. Trager-Cowan, A. Kean, F. Yang, B. Henderson and K. P. O'Donnell, Physica B 185, 319 (1993).

[23] C. Trager-Cowan *et al*, J. Lumin. **48&49**, 773 (1991).

[24] E. Napchan and D. B. Holt, Inst. Phys. Conf. Ser., Eds A. G. Cullis et al., **8**7, 733 (1987).

[25] S. Pereira, M. R. Correia, E. Pereira E. Alves C. Trager-Cowan and K. P. O'Donnell Phys. Rev. B **64**, 205311 (2001).

[26] S. Permogorov and A. Reznitsky, J. Lumin. **52**, 201 (1992).

[27] K. P. O'Donnell, R. W. Martin, C. Trager-Cowan, M. E. White, K. Esona, C. Deatcher, P. G. Middleton, K. Jacobs, W. Van der Stricht, C. Merlet et al. Mat. Sci. Eng. B, **82**, 194 (2001).

5.7 References:

28 B. Gil, ed. *"Group III nitride semiconductor compounds, physics and applications"* Series on Semiconductor Science and Technology 6, Oxford Science Publications, Oxford (1998).

29 B. Gil, ed. "*Low-dimensional nitride semiconductors"* Oxford University Press, Oxford (2002).

30 J. I. Pankove, "*Optical processes in semiconductors*" Dover. New York, USA. (1976).

31 F. Urbach Phys Rev **92**, 1324 (1953).

32 T. Matsuoka, H. Okamoto, M. Nakao, H. Harima, and E. Kurimoto, Appl. Phys. Lett. **81**, 1246 (2002).

33 B. Monemar, "*Gallium Nitride I"* Semiconductors and semimetals, Vol. 50 pp. 305-368 (1998).

34 Wim Van der Stricht, PhD thesis, University of Gent, Belgium (1999).

35 L. Siozade, J. Leymarie, P. Disseix, A. Vasson, M. Mihailovic, N. Grandjean, M. Leroux, and J. Massies, Mater. Sci. Eng., B **82**, 71 (2001).

36 R. W. Martin, P. G. Middleton, K. P. O'Donnell, and W. Van der Stricht, Appl. Phys. Lett., **74**, 263 (1999).

37 F. Yang. M. Wilkinson, E. J. Austin and K.P. O'Donnell Phys. Rev. Lett. **70**, 323 (1993).

38 K. P. O'Donnell, R. W. Martin, and P. G. Middleton, Phys. Rev. Lett. **82**, 237 (1999).

39 R. Pecharromán-Gallego, PhD thesis, University of Strathclyde, UK (2004).

40 K. P. O'Donnell, C. Trager-Cowan, S. Pereira, A. Bangura, C. Young, M.E. White and M.J. Tobin, Phys. Stat. Sol. (b) **216**, 157 (1999).

41 M. E. White, PhD thesis, University of Strathclyde, UK (2004).

42 Yong-Tae Moon, Dong-Joon Kim, Jin-Sub Park, Jeong-Tak Oh, Ji-Myon Lee, Young-Woo Ok, Hyunsoo Kim, and Seong-Ju Park, Appl. Phys. Lett. **79**, 599 (2001).

43 S. Srinivasan, F. Bertram, A. Bell, F. A. Ponce, S. Tanaka, H. Omiya, and Y. Nakagawa, Appl. Phys. Lett. **80**, 550 (2002).

44 M. J. Tobin, M. Martin-Fernandez and G. R. Jones, Synchrotron Radiation News, **11**, 24 (1998).

45 C. J. R. Van der Oord, C. H. Gerritsen, Y. K. Levine, W. J. Myring, G. R. jones, I. H. Munro, Rev. Sci. Instrum. **63**, 1 (1992).

46 K. P. O'Donnell, M. J. Tobin, S. C. Bayliss and W. Van der Stricht, J. of Microscopy, **193**, 1 (1998).

47 P. G. Middleton, C. Trager-Cowan, A. Mohammed, K. P. O'Donnell, W. Van der Stricht, I. Moerman and P. Demeester, Mat. Res. Soc. Symp. Proc. **449**, 471 (1997).

48 B. G. Yacobi and D. B. Holt, *"Cathodoluminescence microscopy of inorganic solids"*, Plenum Press. NY, 1990.

49 C. Trager-Cowan, A. Kean, F. Yang, B. Henderson and K. P. O'Donnell, Physica B 185, 319 (1993).

50 C. Trager-Cowan *et al*, J. Lumin. **48&49**, 773 (1991).

51 E. Napchan and D. B. Holt, Inst. Phys. Conf. Ser., Eds A. G. Cullis et al., **8**7, 733 (1987).

52 S. Pereira, M. R. Correia, E. Pereira E. Alves C. Trager-Cowan and K. P. O'Donnell Phys. Rev. B **64**, 205311 (2001).

53 S. Permogorov and A. Reznitsky, J. Lumin. **52**, 201 (1992).

54 K. P. O'Donnell, R. W. Martin, C. Trager-Cowan, M. E. White, K. Esona, C. Deatcher, P. G. Middleton, K. Jacobs, W. Van der Stricht, C. Merlet et al. Mat. Sci. Eng. B, **82**, 194 (2001).

Chapter 6: Strain state and composition of InGaN epilayers

Overview

In this chapter, the issues of strain and chemical composition of InGaN/GaN heterostructures are discussed in detail. These two fundamental structural properties are experimentally characterized using X-ray diffraction (XRD) and Rutherford backscattering (RBS), introduced in previous chapters. Before introducing the components of the strain tensor, we show the interrelation between composition and strain, and critically address the methods to precisely determine these parameters in $In_xGa_{1-x}N$/GaN epilayers. We highlight the fact that the different levels of approximation regarding the interpretation of XRD data may critically affect the result obtained for x. The importance of characterizing the layer relaxation state, by measuring the in-plane lattice constant a, is evidenced.

A method based on the elastic theory of solids that takes into account the lattice distortion due to the effect of strain is presented. The results obtained for composition using XRD, under the various approaches usually considered, are compared with values of x measured by RBS. The issue of InGaN layers featuring double XRD components is discussed in detail. The important concept of critical layer thickness (CLT) is introduced and the CLT is calculated according to both the People and Bean (PB) and Matthews and Blakeslee's (MB) models of strain relaxation in epilayers. We also present a novel method to extract quantitatively and separate the strain and composition effects on the shape of asymmetric reciprocal lattice points (RLPs). The behaviour of InGaN layers near the CLT, regarding composition, strain and morphology is discussed. The influence of strain and composition on the overall structural quality of the single films and MQWs is also characterized using grazing incidence RBS measurements and asymmetric reciprocal space mapping (RSM).

6.1 Introduction

Accurate determination of the state of strain and the composition of thin epitaxial layers has been one of the most important issues for materials and device scientists in the last decades. In the case of InGaN/GaN heterostructures, a reliable determination of the composition in InGaN films is the key point regarding the understanding of the alloy's fundamental physical properties. The strain state and composition determination of group-III nitrides relies almost exclusively on X-ray diffraction, which is widely available, automated and non destructive (i.e.

easy to use). The fundamental problem regarding composition estimations using XRD is that too frequently, the presence of strain in the films is either neglected or incorrectly quantified. It is important to recognize that the two structural parameters are interrelated, and it is difficult to disentangle the two effects on the measured lattice constants. This may lead to errors in the composition and strain values derived from incomplete XRD characterization. Such errors, in the case of highly lattice mismatched material systems like that studied here, are likely to have severe consequences with respect to the quantitative understanding of the material's Physics. However, it is possible to separate strain and composition effects if a suitable XRD characterization is performed.

In the following, using RBS as a reference for the determination of x free from the effects of strain, we assess the validity of methods used to determine composition based exclusively on XRD. The ability to obtain reasonable estimates of composition by XRD is rather convenient, since this technique is widely available in most growth and characterization laboratories. Another fundamental parameter of InGaN layer growth is the so-called critical layer thickness (CLT), which is the greatest thickness that can support coherent growth. Sudden variations of the layers' properties near the CLT appear to have sow confusion in the literature regarding basic physical interpretation. In this chapter we intend to shed light on these issues, some of which are still under debate.

6.2 Basic concepts and definitions

In hetero-epitaxy, despite a difference in lattice parameter, a film may grow with an inter-atomic spacing constrained to the substrate value in the interface plane. We shall designate such structures as *coherent* or *pseudomorphic*. Within this type of growth we may have two distinct cases:

a) The layer in-plane relaxed lattice constant is smaller than that of the substrate. In this case ($a_L<a_S$) the film is subjected to a biaxial tensile strain.

b) The layer in-plane relaxed lattice constant is larger that that of the substrate. In this case ($a_L>a_S$) the film is compressively strained.

These situations are depicted in Fig. 6.1, where the behaviour of both the in-plane and out-of plane lattice constants is schematically illustrated.

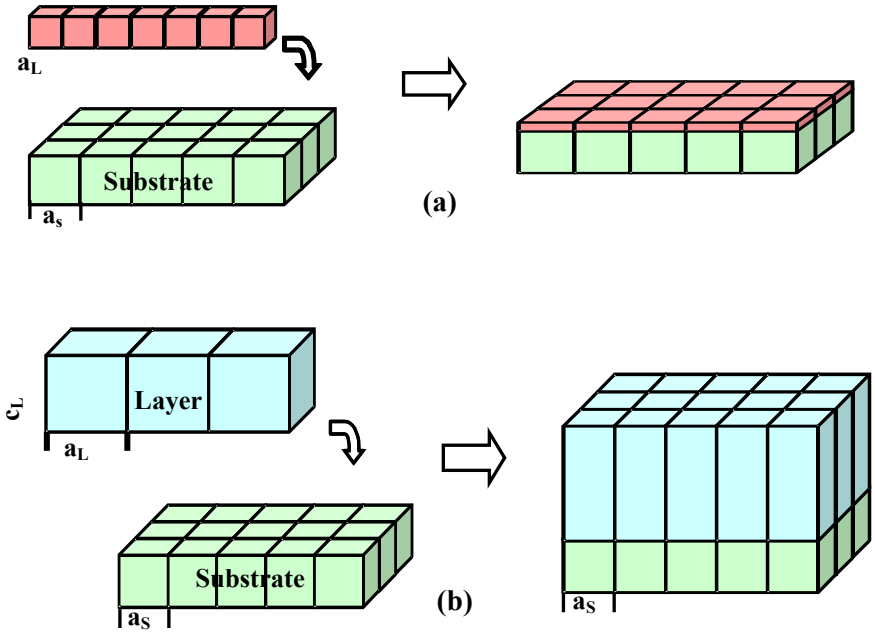

Figure 6.1: a) Schematic illustration of the origin of biaxial compressive ($a_L > a_S$) and **b)** biaxial tensile ($a_L < a_S$) strain. The out-of-plane lattice constants are either increased (compressive in plane strain) or decreased (tensile in-plane strain).

Note that in case a) the film out-of-plane lattice constants are *decreased* relative to the relaxed case whereas in case b) the coherent growth leads to a *higher* out-of-plane lattice constant relative to the case of a relaxed film. Since the lattice constants of relaxed InGaN are larger that those of an underlying GaN buffer, InGaN films on GaN pseudo-substrates, the most common growth mode, are represented by case b).

6.2.1 Critical thickness and relaxation coefficient

Up to this point, we have only discussed the case of perfect pseudomorphic growth. That is growth below the *critical layer thickness* (CLT) for strain relaxation. Note that for a given lattice mismatch, the elastic strain energy in the coherent deposit will increase with its thickness. When the strain energy is sufficiently large so that it can no longer be accommodated in the epilayer it will start to be relieved by deformation of the hitherto coherent structure. The magnitude of this CLT is decided by energy minimization considerations, and in the case of $In_xGa_{1-x}N/GaN$ is a strong function of x (via $l(x)$ which is the lattice mismatch defined in Eq. 2.4), as shall be described in Section 6.6.

Typically strain relaxation above the CLT occurs via the introduction of slipped regions within the crystal, bounded by line defects known as “misfit” dislocations. This process allows the epilayer to relax toward its bulk structure. We shall designate these structures as *partially*

relaxed (0<r<1) or *fully relaxed (r=1)*, according to the degree of relaxation. Let us define the degree of relaxation as:

$$r = \frac{a^L - a_0^S}{a_0^L - a_0^S} \qquad \text{(Eq. 6.1)}$$

where a^L and a_0^L are the measured and relaxed in plane lattice constants, respectively, of a layer of given composition and a_0^S is the *relaxed* lattice constant of the substrate (in this case the GaN under-layer).

Note that in nitride growth the substrate is a thick wafer of sapphire with well defined lattice constants. However, this is not the case for the GaN buffer layer which acts as the effective substrate for the InGaN film. During the growth process the lattice constants of GaN on sapphire change due to lattice mismatch and thermal incompatibility. In addition, in some cases the total thickness of the InGaN is not significantly smaller than that of the GaN; the lattice mismatch of the overlayer will also affect the GaN layer. Therefore, it is convenient to define the relaxation independently from the strain status of the substrate.

6.2.2 Vegard's law

The method to define the bulk, or fully relaxed, lattice constants in an alloy is based on Vegard's law [1]. According to Vegard's law, the relaxed lattice constants $c_0(x)$ and $a_0(x)$ of the binary mixture of compounds $In_xGa_{1-x}N$=xInN:(1-x)GaN, scale linearly with x:

$$c_0^{InGaN} = x c_0^{InN} + (1-x) c_0^{GaN} \qquad \text{(Eq. 6.2.a)}$$

$$a_0^{InGaN} = x a_0^{InN} + (1-x)\, c_0^{GaN} \qquad \text{(Eq. 6.2.b)}$$

Note that x *(0<x<1),* is the InN fraction on the $In_xGa_{1-x}N$≡InGaN alloy. However, for simplicity sake we also call it the In content or InN mole fraction, since for stoichiometric growth the number of atoms (In+Ga) is the same as the number of N atoms; (In/(In+Ga))≡InN/(InN+GaN). x is also called, loosely, the composition.

6.2.3 Strain components

In simple terms, the amount of strain present in a given sample is a quantitative measure of how much the lattice constants are changed relative to their fully relaxed value. Thus, it easily

follows that in an InGaN layer the perpendicular and parallel strain components, ε_{zz} and ε_{xx} can be defined as:

$$\varepsilon_{zz} = \left(\frac{c - c_0}{c_0}\right) \qquad \text{(Eq. 6.3.a)}$$

and

$$\varepsilon_{xx} = \left(\frac{a - a_0}{a_0}\right) \qquad \text{(Eq. 6.3.b)}$$

respectively, where c and a are the measured lattice parameters, while c_0 and a_0 are the relaxed parameters given by Eqs. 6.2 a) and b). Note that in order to know the amount of strain in any given $In_xGa_{1-x}N$ film, x needs to be known with good accuracy.

6.2.4 Stress-strain relations for wurtzite biaxially strained layers

In the case of biaxially strained hexagonal wurtzite structures, such as InGaN/GaN, distortion of the unit cell must be considered in order to separate strain and composition effects. The distortion of the hexagonal unit cell due to the effect of biaxial strain is illustrated in Fig. 6.2.

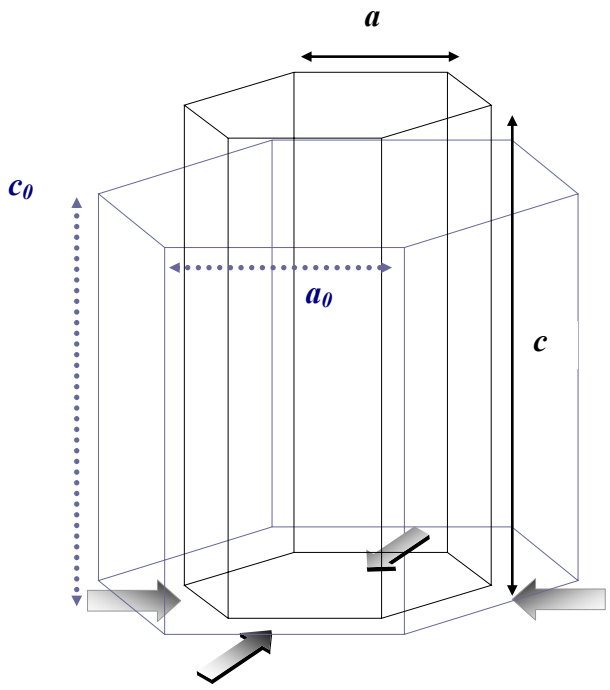

Figure 6.2: Illustration of the strain effect on epitaxial InGaN layers grown on top of GaN. Due to the fact that the in-plane InGaN lattice constant is larger than that of GaN the biaxial strain will compress the base of the hexagon and elongate the unit cell in the direction of growth.

The generalised Hooke's law can quantify this distortion [2-4]. The general stress-strain relationship for an hexagonal layer in the (*0001*) orientation for regular distortion is:

$$\begin{pmatrix}\sigma_{xx}\\ \sigma_{yy}\\ \sigma_{zz}\\ \sigma_{yz}\\ \sigma_{xz}\\ \sigma_{xy}\end{pmatrix}=\begin{pmatrix}c_{11} & c_{12} & c_{13} & 0 & 0 & 0\\ c_{12} & c_{11} & c_{13} & 0 & 0 & 0\\ c_{13} & c_{13} & c_{33} & 0 & 0 & 0\\ 0 & 0 & 0 & c_{44} & 0 & 0\\ 0 & 0 & 0 & 0 & c_{44} & 0\\ 0 & 0 & 0 & 0 & 0 & \frac{1}{2}(c_{11}-c_{12})\end{pmatrix}\begin{pmatrix}\varepsilon_{xx}\\ \varepsilon_{yy}\\ \varepsilon_{zz}\\ \varepsilon_{yz}\\ \varepsilon_{xz}\\ \varepsilon_{xy}\end{pmatrix} \qquad \text{(Eq. 6.4)}$$

where the c_{ij} are stiffness coefficients.

In the epitaxial system under consideration, the *c* axis of the unit cell is normal to the substrate surface allowing a simplification of the tensor of the elastic moduli. The stress normal to the film vanishes and the following ratio between strains in the growth direction and basal plane is obtained:

$$\sigma_{zz}=0=c_{13}\varepsilon_{xx}+c_{13}\varepsilon_{yy}+c_{33}\varepsilon_{zz} \qquad \text{(Eq. 6.5)}$$

which rearranges to give:

$$\varepsilon_{zz}=\frac{-c_{13}(\varepsilon_{xx}+\varepsilon_{yy})}{c_{33}} \qquad \text{(Eq. 6.6)}$$

if one considers that $\varepsilon_{xx}=\varepsilon_{yy}$, by symmetry, the expression

$$\varepsilon_{zz}=-\frac{2c_{13}}{c_{33}}\varepsilon_{xx} \qquad \text{(Eq. 6.7)}$$

is obtained. The ratio of out-of-plane to in-plane strain, equal to $-\frac{2c_{13}}{c_{33}}$, has been called both the "*two-dimensional Poisson ratio,*" [3], and the "*distortion coefficient, D*" [5], by various authors. Since the elastic constants are themselves a function of the composition, we call it $D(x)$, and the relation between ε_{zz} and ε_{xx} takes the general form:

$$\varepsilon_{zz}=-D(x)\varepsilon_{xx}\,. \qquad \text{(Eq. 6.8)}$$

6.3 Use of simple approximations to estimate composition

Before discussing the various approaches to obtain the accurate composition from XRD, it is important to understand that the *c* lattice constant of an InGaN film may be simultaneously

influenced by composition and strain. Since both structural parameters contribute to the value of *c* in the film it is *impossible* to determine *x* from a measured value of *c* unless some assumption is made regarding the relaxation state, defined by *r*.

In order to calculate the In content from XRD results, using *only* the lattice constant $c_{InGaN,}$ two extreme approximations (based on assumptions relative to the state of strain) are usually considered:

1) The layers may be fully relaxed. This assumption is likely to be justified when layers are relatively thick[1].

In this case, determination of chemical composition by X-ray diffraction is based on a unique relationship between the lattice parameters and the chemical composition, as given by Vegards' law [1]. Hence, from the measured lattice parameter c^{InGaN}, *x* can be obtained by rewriting equation 6.2a:

$$x_{relaxed} = \frac{c^{InGaN} - c^{GaN}}{c^{InN} - c^{GaN}}. \qquad \text{(Eq. 6.9)}$$

Approximation 1) is the one most frequently found in the InGaN literature.

2) Layers may be pseudomorphic: $a^{InGaN}=a^{GaN}$. In pseudomorphic growth a thin epilayer accommodates its in-plane lattice constant to that of the substrate (see Fig 6.1b), in this case a GaN pseudo substrate.

Basically, the second approach consists in using the measured value of c_{InGaN} and solving Eq. 6.8, setting $a^{InGaN}=a^{GaN}$. Eq. 6.8 can be rewritten in order to show explicitly the dependence on the c^{InGaN} and a^{InGaN} layer lattice constants:

$$\left(c^{InGaN} - c_0^{InGaN}\right) + D(x)\frac{c_0^{InGaN}}{a_0^{InGaN}}\left(a^{InGaN} - a_0^{InGaN}\right) = 0 \qquad \text{(Eq. 6.10)}$$

where c^{InGaN} and a^{InGaN} are the measured alloy lattice parameters, c_0^{InGaN} and a_0^{InGaN}, are the relaxed parameters given by Vegard's law and $C_{i,j}(x)$ are linearly interpolated values, based on elastic constants of the binary semiconductors. From the three possible solutions of the cubic equation, found by substituting c_0, a_0 and $c_{i,j}(x)$ by its interpolated quantities for the unknown value of *x* in Eq. 6.10), only one is physically acceptable *(0<x<1)* [6].

[1] The concept of "thick" layer is sometimes used with ambiguity in the literature; see for instance the comment in Ref. [7]. A thick layer is properly defined to be thicker than the critical layer thickness (CLT). In the same way, "thin" InGaN layers should refer to layers whose thickness is below the CLT. The CLT for InGaN/GaN layers is calculated in Section 6.6, and shown to be a very strong function of *x*.

The input parameters required for these calculations, in addition to the measured lattice parameters c_{InGaN} and a_{InGaN}, are the GaN and InN relaxed lattice and elastic constants. The parameters used in this work are summarised in Table 6.I.

Table 6.I: GaN and InN physical parameters required as input parameters to solve Eq. 6.10.

	c(Å)	a(Å)	C_{13}(GPa)	C_{33}[4](GPa)	D
GaN	5.1850[8]	3.1892[8]	103[9]	405[9]	0.509
InN	5.7033[10]	3.5378[10]	92[9]	224[9]	0.821

6.3.1 Comparison with RBS measurements of *x*

The variations of x, calculated under assumptions 1) and 2), are plotted as a function of the measured value of the lattice constant c_{InGaN} in Fig. 6.3.

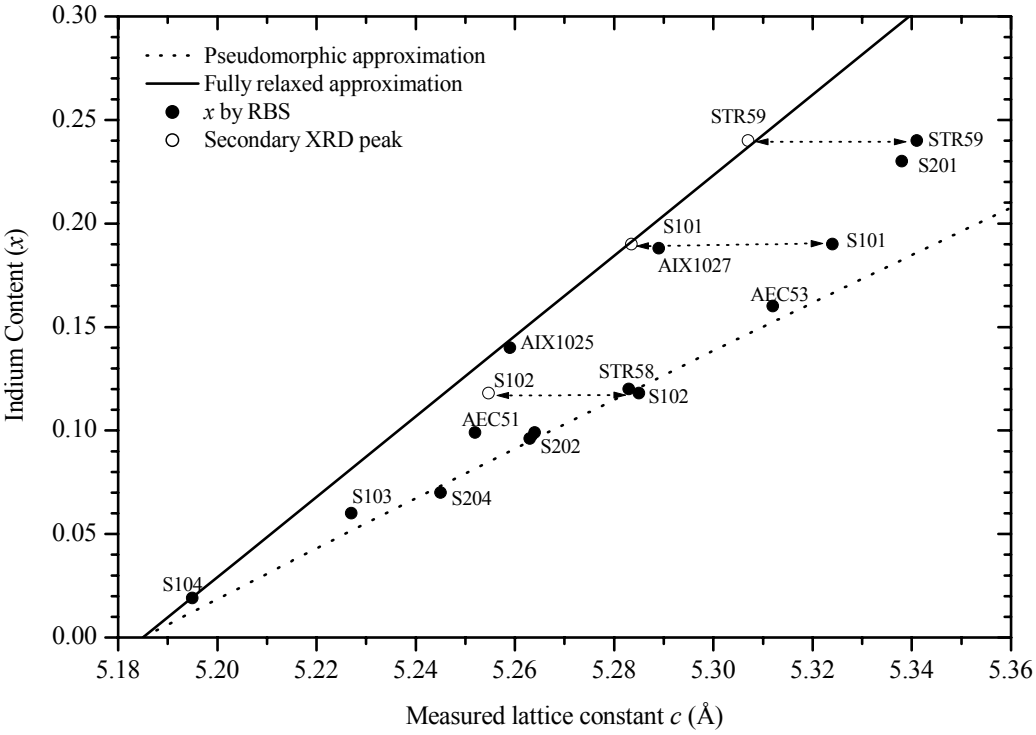

Figure 6.3: InN content of selected samples determined by RBS compared with the values of x predicted using the fully relaxed 1) and pseudomorphic 2) assumptions, and measured values of c_{InGaN} from XRD. Both values of c measured for InGaN layers featuring double peaks are shown.

The difference in estimated compositions x_1 and x_2, for the same value of measured c_{InGaN}, is quite significant at higher values of x. For instance, the fractional discrepancy $(x_1-x_2)/x_1$, increases from ~6% at x=0.1, to ~37% for x=0.25.

In the graph, are also included the results we obtained for a series of samples where x was determined by RBS, and the c lattice constants were measured from a symmetric XRD scan. Comparison of the different sample coordinates relative to the fully relaxed or pseudomorphic

lines indicates how strain may influence the determination of *x* if only the *c* lattice constant is used. This type of assessment highlights the misinterpretations that can be made if the samples' state of strain is "assumed", instead of measured [11-14]. Specifically, it is clear that a systematic *overestimation* of *x* is made under the *fully relaxed* assumption; see for instance [15-19], whereas an *underestimation* is made under the *pseudomorphic* assumption [20-23].

For samples featuring double XRD peaks both lattice constants are shown in Fig. 6.3. It is quite interesting to note that in these samples (e.g. S102) one of the components is generally close to the fully relaxed line, whereas the other corresponds to a *c* lattice constant close to that expected for pseudomorphic growth. Samples with intermediate (single) values, which we might call "partially relaxed" are relatively rare in InGaN.

6.4 A method to obtain estimates of *x* taking into account the strain effect

In order to conveniently separate the influence of strain and composition effects on c_{InGaN}, both lattice parameters, a_{InGaN} and c_{InGaN}, have to be measured. The experimental procedure to measure the in-plane and out-of-plane lattice constants is described in detail in Chapter 3. Using both measured lattice parameters and solving Eq. 6.10 for *x,* excellent agreement between XRD and RBS is obtained [6,14,24-28], as shown in Table 5.II.

Table 6.II: Values of *x* obtained using XRD measured lattice constants for several samples using; 1) the fully relaxed approximation, 2) taking into account the strain effect by solving Eq. 6.10, and 3) by direct RBS measurements.

sample	*thickness(nm)*	*c(Å)*	*a(Å)*	$x_{relaxed}$	$x_{Eq.10} \pm 0.01$	$x_{RBS} \pm 0.005$
AEC51	50	5.252	3.204	0.129	0.098	0.099
AEC53	75	5.312	3.193	0.246	0.159	0.160*
S103	157	5.227	3.199	0.082	0.062	0.061
S104	191	5.195	3.197	0.019	0.02	0.019
S201	325	5.338	3.200	0.295	0.197	0.23*
S202	225	5.264	3.188	0.153	0.096	0.099
S204	199	5.245	3.180	0.116	0.063	0.070
AIX1027	750	5.289	--	0.200	--	0.188*
AIX1025	355	5.259	--	0.142	--	0.140*
STR58	180	5.283	--	0.189	--	0.120
STR59	193	5.341	3.195	0.301	0.235	0.240
"	"	5.307	3.271	0.235	--	0.240
S101	120	5.324	3.215	0.263	0.194	0.190
"	"	5.284	3.256	0.190	0.191	0.190
S102	180	5.285	3.186	0.193	0.119	0.119
"	"	5.255	3.220	0.130	0.118	0.119

* Films featuring depth gradients of composition, the average value of *x* is given in these cases.

6.5 The case of layers with double XRD peaks: "evidence of phase separation"?

Samples which feature double XRD peaks raise an important question regarding the application of Vegard's law directly, i.e. without knowing if the film is fully relaxed. To estimate the composition of a layer of this type, a "blind" application of Vegards' law inevitably leads to two values of x. In the lower part of Table 6.II one can see that for those samples (S101 and S102) with two pairs of lattice constants [$c_{InGaN}(1)$, $a_{InGaN}(1)$], [$c_{InGaN}(2)$,$a_{InGaN}(2)$] the value obtained for composition when the strain effect is properly taken into account, is the same for the two components. This coincidence is probably not accidental.

Let us consider for example the case of sample S102, whose detailed XRD characterization was presented in Chapter 3. In this case, if we consider the two peaks as "belonging to" regions (1) and (2), under the fully relaxed assumption and each measured lattice parameter, $c_{InGaN}(1,2)$, is used to directly estimate the indium mole fractions $x(1)$ and $x(2)$. The two "regions" would have $x(1)$ = 0.193 and $x(2)$=0.130. This deficient application of Vegard's law to samples of unknown strain state has quite often been used as evidence of partial phase segregation [15-20], and attributed to the presence of "micro-regions" with different In content.

The magnitude of the correction due to strain depends on the relaxation degree of the layer, or more rigorously of the layer region, and can only be evaluated if the in-plane lattice constants are known. Solution of Eq. 6.10, taking into account the measured $a_{InGaN}(1)$ and $a_{InGaN}(2)$ lattice constants, yields values of $x(1)$=0.119 and $x(2)$= 0.118. Hence, if the state of strain of each sub-region is properly taken into account, the value of x obtained is actually the same, within the possible error limits of such an estimate (±0.01). It becomes clear that the two sub-regions co-existing in the InGaN layer (giving raise to distinct XRD peaks) are in fact under different states of strain; however, it is clearly demonstrated that both have the same, or at least very similar, InN content.

6.5.1 RBS/channelling analysis of samples with double InGaN related XRD peaks

RBS provides further complementary information regarding the structural properties of samples with double XRD peaks [25-28]. Random (3º off axis) and <*0001*>-aligned RBS spectra from the InGaN/GaN bilayer S102 are shown in Fig. 6.4 a). Simulation of the random spectrum using RUMP [31], reveals an InGaN layer thickness of 180±10 nm and a composition, x = 0.119±0.005. The simulation shows that the In content is, within the sensitivity of the technique, uniform over depth.

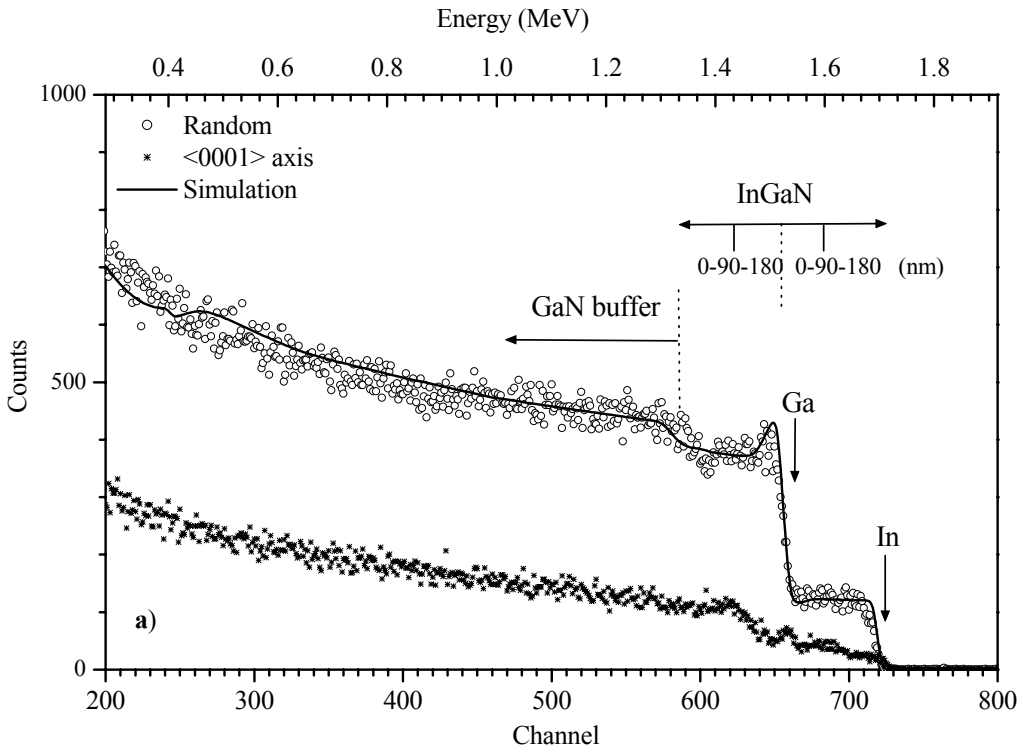

Figure 6.4: a) Random, aligned, and simulated RBS spectra of $In_{0.12}Ga_{0.88}N/GaN/Al_2O_3$(*0001*) sample, S102. Vertical arrows indicate the scattering energy of the different chemical elements. Horizontal arrows indicate the depth location in the sample

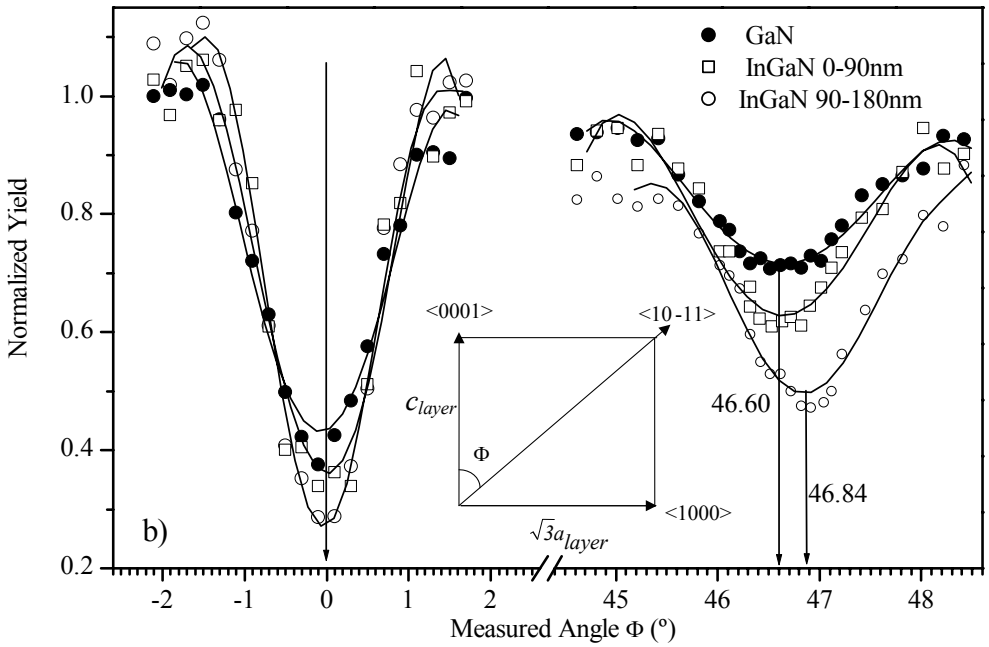

Figure 6.4: b) Angular RBS/channelling scans of S102, corresponding to the GaN buffer layer and the InGaN layer at the indicated depths, along the (*1-210*) plane from the *<0001>* to the *<10-11>* crystal axis. The inset shows the angular dependence of the crystal axis on the wurtzite lattice constants.

As indicated in Fig 6.4 a), in the RBS spectra corresponding to the InGaN layer, two integration regions, corresponding to In and Ga atoms at 0-90 and 90-180 nm depths, were used to monitor the number of backscattered ions as a function of the beam incidence angle. Angular scans were performed around the <*0001*> and <*10-11*> axis and the angle between these two directions measured along the (*1-210*) plane. Details of the RBS/channelling measurements can be found in Chapter 4, and Refs [24,26,42]. The results are shown in Fig 6.4 b).

The first point that should be noted about the angular scans is that, within the same depth scale, the channelling dips for the InGaN layer are found at the same position In and Ga. Therefore, for clarity only the In signal is represented in Fig. 6.4 b). This overlap shows that Ga and In occupy equivalent positions in the lattice, what would not happen if macroscopic phase separation occurred.

For the <*0001*> axis all three channelling dips have the same angular position. This shows that, within the angular resolution of the RBS angular scans, there are no tilts between the GaN buffer and the whole InGaN film. The same conclusion is obtained by XRD symmetrical reciprocal space mapping, as discussed in Chapter. 3.

It is rather interesting to note that the position of the InGaN <*10-11*> dip is a function of depth. As seen in Fig. 5.4 b), Φ_{epi} values of *46.60º±0.05º* and *46.9º±0.05º*, for the InGaN layer at the stated depths, were measured. Thus, according to the definition of tetragonal distortion given in Eq. 4.4 (Section 4.8.2) and in Ref. [32], the values for ε_T in the near-surface region: *–0.01±0.1%* and for the region closer to the GaN/InGaN interface: *–0.85±0.1%*, are deduced from the RBS/channelling study, respectively.

From this study, one can conclude that the part of the InGaN film closer to the surface can be considered fully relaxed, within the resolution of the RBS angular scans, whereas the near interface region is strained. The negative values for ε_T indicate that the InGaN layer is under tensile strain along the growth direction, as would be expected. This abrupt strain depth variation is the origin of the double XRD InGaN related peaks.

The unambiguous determination of the origin of double XRD peaks in thick InGaN films is a rather important result. Double XRD peaks have been systematically ascribed to the occurrence of phase separation in the alloy [15-20], as discussed in Ref. [28] The issue of InGaN layers with discontinuous strain relaxations over depth and its influence on the optical properties is a topic under discussion on the literature [28-30] and will be addressed in detail in Chapter 7.

6.6 Estimation of the critical thickness for InGaN/GaN bilayers

Now that we have understood that double XRD peaks in InGaN grown upon GaN may arise due to a strain relaxation along the growth direction, we shall try to predict the thickness-

composition range where this phenomenon is likely to occur for a given composition. It should be noted that in the case of InGaN grown on GaN the stored strain energy increases not only with thickness, but also with the lattice mismatch, *l(x)* (Eq. 2.4).

It might be expected that there will be a characteristic epilayer thickness, for a given composition, at which the coherent-relaxed transition occurs, or at least dramatically accelerates. The magnitude of this "critical layer thickness", CLT(x), is related to the balance between the relief of strain energy and the extra energy associated with the lattice distortions produced by the misfit dislocations. A number of equilibrium theories have been developed to attempt to describe the CLT as function of the elastic mismatch and the elastic constants of an epitaxial system. Here, we consider the two most commonly used models.

The CLT (x), at which strain relief is predicted to occur can be estimated as a function of the InN content, x, using the energy balance method proposed by People and Bean (PB) [34]. In brief, the PB model assumes that misfit dislocation generation is determined by energy balance. It is considered that interfacial misfit dislocations are generated when the areal strain energy density exceeds that required for the formation of screw dislocations. The equation for CLT(x) as a function of the lattice mismatch and the film structural properties is given by,

$$CLT(x) \sim \left(\frac{1-v(x)}{1+v(x)}\right)\cdot\left(\frac{1}{16\pi\sqrt{2}}\right)\cdot\left(\frac{b^2}{a(x)}\right)\cdot\left[\left(\frac{1}{f^2(x)}\right)\ln\left(\frac{CLT(x)}{b}\right)\right] \qquad \text{(Eq. 6.11)}$$

where $v(x)= c_{13}(x)/(c_{13}(x) + c_{33}(x))$ is Poisson's ratio, $a(x)$ the bulk (relaxed) lattice constant of the film, b is the slip distance (the magnitude of the Burger's vector) and $f(x)$ the lattice mismatch. The lattice and elastic parameters used in the CLT calculations described here are listed in Table 6.I. The value used for b was a_{GaN}, and Vegard's law was used to interpolate the relaxed $In_xGa_{1-x}N$ lattice constant $a(x)$ and $v(x)$. Calculated values for CLT for $In_xGa_{1-x}N$/GaN layers using the PB model are shown in Fig. 6.5.

The left side of the curves corresponds to the predicted region for the coherent regime, i.e. growth pseudomorphic to GaN, and the right side to the conditions for strain relief via misfit dislocation generation. The very strong dependency of CLT on x is striking.

The critical layer thickness just introduced is a key parameter to understand the overall physical properties of InGaN films. Now a criterion to define a "thick" or "thin" InGaN film can be suggested. The thickness, t, should be compared to the expected values of CLT(x) for a specific value of x. In general, thin layers feature distinct structural and optical properties from thick ones. Thus, it is convenient to compare the samples studied here with the calculated CLT(x) curve. This procedure is represented in Fig. 6.6.

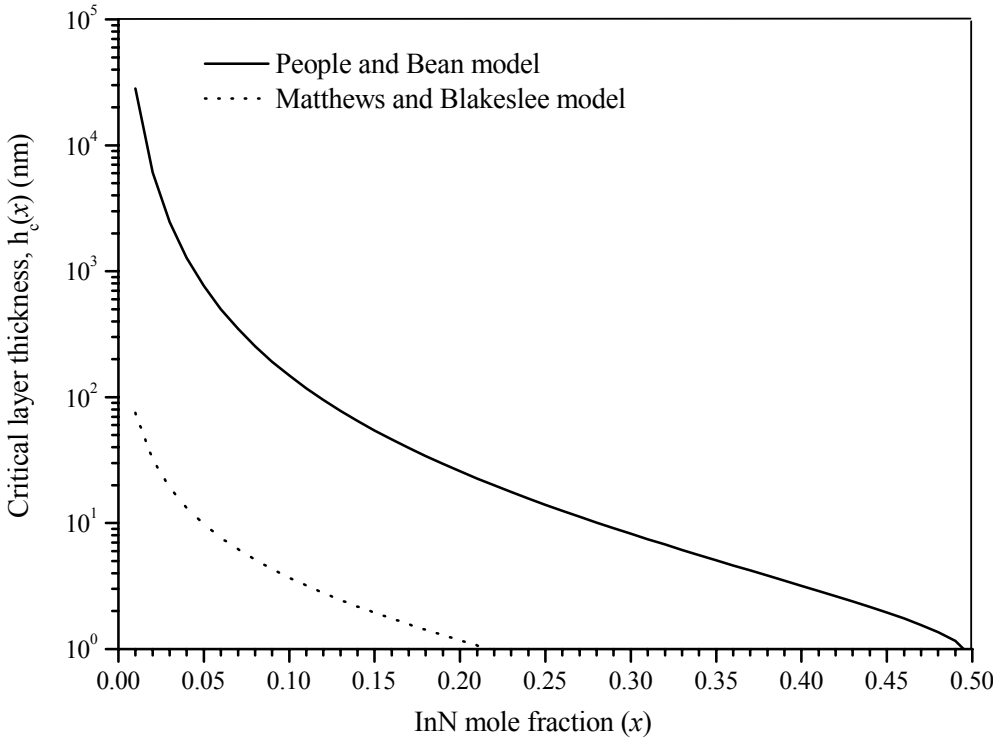

Figure 6.5: Calculated CLT for $In_xGa_{1-x}N$/GaN layers (with $0<x<0.50$) using the PB model. For comparison, the results obtained using the MB model are also included.

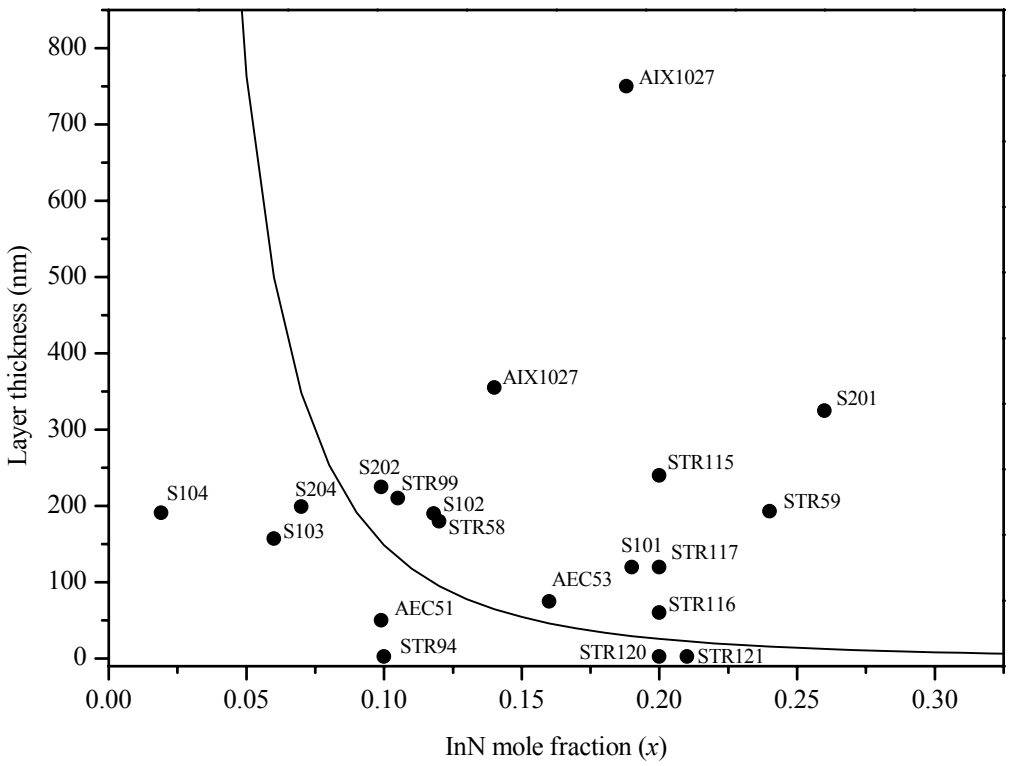

Figure 6.6: Location of the various samples studied, according to the (x,t) coordinates, relative to the calculated CLT(x).

Thick films (e.g. S201, AIX1025 and AIX1027) were found to be fully relaxed, whereas samples well below the CLT (e.g. STR120, STR121 and AEC51) are found to be coherent. Samples with thickness quite close to the transition thickness (e.g. S101 and S102) were found to have two regions of differing strain, as already demonstrated.

In addition, a great increase of the surface roughness as the films grow above the CLT(x) is observed, with thick layers featuring a pronounced 3D surface [28,43]. We will get back to the surface roughness issue in Section 6.8, where the structural and morphological evolution of films of increasing thickness is illustrated with reference to the samples STR11#. This set of 3 samples was specifically grown to understand the strain relaxation process and surface roughness evolution in InGaN. However, first let us introduce a general method to quantitatively interpret the XRD RSM of InGaN/GaN heterostructures.

6.7 Strain and composition distributions in wurtzite alloys by XRD reciprocal space mapping

So far, in order to obtain estimates of average composition and strain by XRD the layer average lattice constants were considered. In films with two XRD components, and therefore two pairs of InGaN lattice constants, we have shown that these may correspond to the same value of x.

The elastic theory approach used to separate the strain and composition effects described in previous sections, can be generalized and used to extract quantitatively additional information from RSM of InGaN/GaN layers.

It has already been recognized that in InGaN, or any other thin epitaxial alloy film, gradients of strain or chemical composition may lead to a variation of inter-planar separations. If such gradients occur within the scattering volume, they broaden the reciprocal lattice points (RLPs). For symmetric (h and k=0) Bragg reflections only variations in lattice constant perpendicular to the sample surface can be detected. The direction of RLP broadening along the surface normal does not distinguish its physical origin in this case. Uncertainties on the In content, and possible false-indications of partial phase decomposition may result when only symmetrical X-ray reflections are considered, as has already been discussed [24-28].

However, in the asymmetric case, the directions of elongation of the RLP due to strain and composition gradients differ significantly [39,40,41]. An opportunity to separate the two effects arises from the fact that an asymmetrical RSM contains combined information about the in-plane and out-of-plane lattice constants. When the measurements are on an absolute scale[2], any pair of coordinates (q_x,q_z) in the map, corresponds to a pair of lattice constants (a,c) of the wurtzite structure, and therefore to a certain value of x.

[2] The RSMs presented here are not referred to the GaN RLP position but placed on an absolute scale. The details on sample alignment procedure to obtain RSM in an absolute scale are discussed in detail in Ref. [38].

The ability to separate the effects of strain and composition from the distribution of the RLPs (its extent and orientation) can be best illustrated by considering hypothetical cases where only one of the parameters changes at a time. Let a film of *uniform* composition, *x,* progressively relax as it grows. The strain induced lengthening of the RLPs should be along the direction on the RS that preserves the relation between *a* and *c* for a particular value of *x*. Two such isocomposition lines along which relaxation varies from r=0 to r=1 are shown in Fig. 6.7, at the angles α_1 and α_2 with respect to the q_z axis (surface normal).

The angles $\alpha_i(x)$ shown in Fig. 6.7 can be calculated analytically. From the geometry in Fig. 6.7:

$$\tan\alpha(x) = \frac{q_x - q_x^0}{q_z^0 - q_z} \qquad \text{(Eq. 6.12)}$$

where $q_{x,z}$ and $q_{x,z}^0$ are the coordinates of the InGaN RLPs corresponding to the physical situations where r=0 and r=1, respectively.

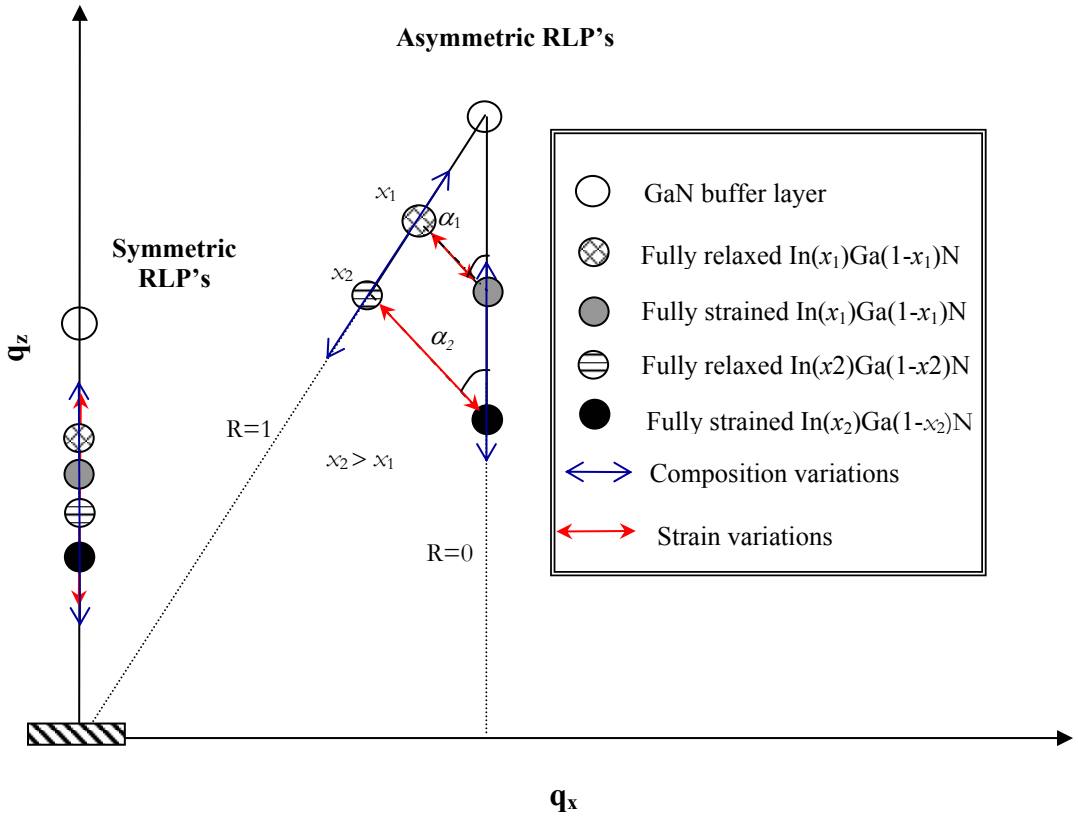

Figure 6.7: Reciprocal space diagram illustrating the effect of strain and composition gradients in the symmetric and asymmetric reciprocal lattice points of InGaN.

Substituting into Eq. 6.8, and taking into account the relations given by Eq.s. 6.2 and 6.3 , the relations between scattering vector components and the hexagonal lattice constants; $a=(8\pi/3)*(h^2+k^2)/q_x$ and $c=2\pi*l/q_z$, and using the expression for the angle φ between surface

normal and the (*hkl*) planes given by Eq. 3.3, $\alpha(x)$ can be expressed as a function of the elastic parameters, and the angle $\varphi(x)$ as:

$$\alpha(x) = \arctan\left(\frac{1}{D(x)} \cdot \tan\varphi(x)\right). \qquad \text{(Eq. 6. 13)}$$

The input physical parameters necessary to perform the calculations are listed in Table 6.I. Note that once x is defined, the relaxed lattice constants obtained from Vegard's law can be substituted in Eq. 3.3 to calculate $\varphi(x)$. $D(x)$ is calculated by interpolating the elastic constants for x, and hence $\alpha(x)$ can be computed.

Now consider the hypothetical case where the alloy has gradients of composition, but the relaxation is constant. The RLPs will elongate along the line characteristic of this relaxation state, also illustrated in Fig. 6.7. For simplicity only the cases of r=0 and r=1 are represented. In practice, a combination of both situations described may occur and will result in an extension of the RLP along some intermediate direction. Thus, comparison between the experimental RSM and the calculated directions in the RS allows the existence of strain gradients, composition gradients, or a combination of both, to be distinguished and investigated [40,41].

The method presented here is quite general. It can be used for any XRD reflection and applied to any hexagonal alloy with regular distortion, as far as Vegards law is valid. Let us use the concepts just outlined to examine the strain-composition features of InGaN/GaN films.

6.7.1 "Pure" strain relaxation near the CLT

The first practical application of this model is illustrated with reference to sample S101, representative of samples grown above the CLT(x), and which feature double XRD peaks. The asymmetric RSMs measured on the (*10.5*) and (*11.4*) reflections are shown in Fig. 6.8 a) and b), respectively.

Calculated isocomposition (for x=0.19), full relaxation and zero relaxation (pseudomorphic) lines are shown on the figure. Diffraction corresponding to the InGaN layer can be observed below (to larger c than) the much stronger GaN peak. In both RSMs, two main peaks, labelled $In_{0.19}Ga_{0.81}N$(R) and $In_{0.19}Ga_{0.81}N$ (S), compose the diffraction profile of the layer, corresponding to relaxed and strained $In_{0.19}Ga_{0.81}N$, respectively. The direction of "pure" strain relaxation in the RSM, i.e. the isocomposition line for x=0.19, was calculated according to the model proposed Eq. 6.13, see Ref. [40], for the two reflections considered: the values obtained are $\alpha_{10.5}(0.19)$=32.68º and $\alpha_{11.4}(0.19)$=54.26º, respectively.

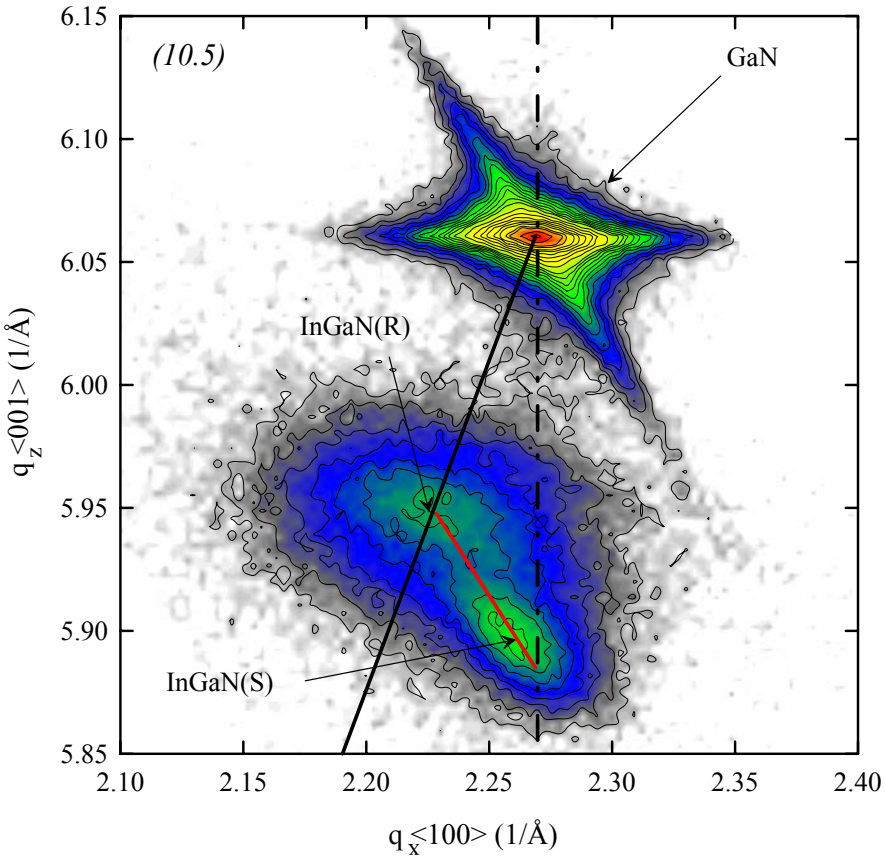

Figure 6.8 a) High resolution XRD reciprocal space map of the (*10.5*) reflection, on a $In_{0.19}Ga_{0.81}N$/GaN layer (S101). The vertical line indicates growth coherent to GaN, whereas the dashed line represents the relaxation line. The full line connecting the relaxed, InGaN(R), and strained, InGaN(S), regions, is the isocomposition line for x=0.19, calculated according to the model proposed.

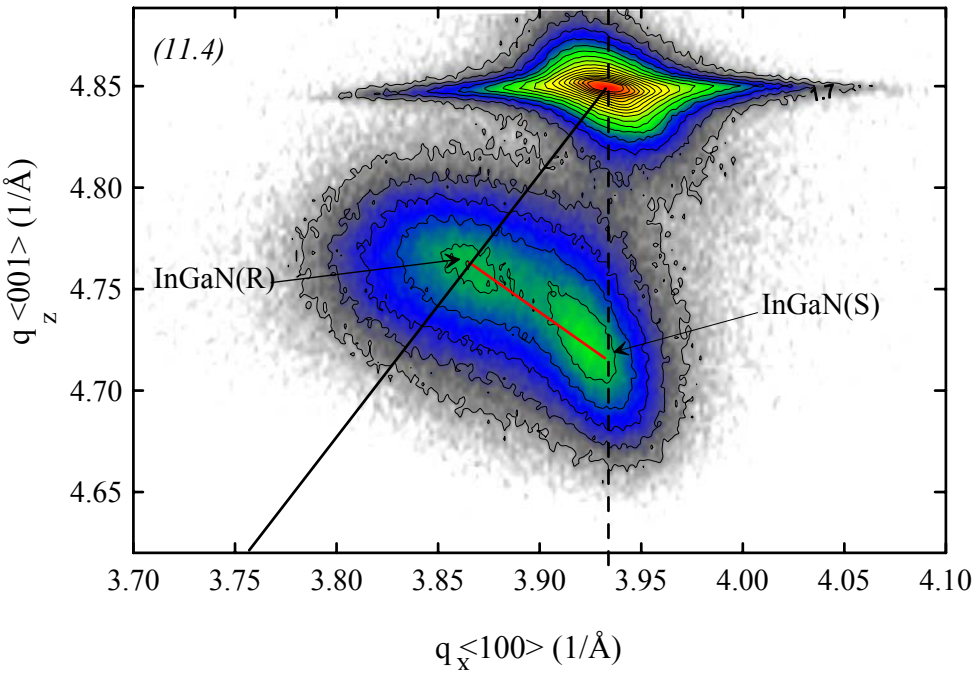

Figure 6.8 b): Same as 6.8a) but now the XRD reciprocal space map is on the (*11.4*) reflection.

For this layer, the relaxation process clearly follows the calculated lengthening direction for x=0.19, meaning that a "pure" strain relaxation has occurred, and no gradients of composition can be detected. The strong variation of strain from coherent to fully relaxed, over depth, conserves the relation between c and a, for x=0.19. It is also true that t(=120 nm) > h_c (0.19), in agreement with the theoretical prediction [28], as represented in Fig. 6.6.

A detailed Rutherford backscattering/channelling analysis in this layer, similar to that performed in Section 5.5.1, further confirms a uniform InN mole fraction (x=0.19±0.01) and the depth-location of strained (near InGaN/GaN interface) and relaxed (near surface) regions.

6.7.2 Strain relaxation and compositional gradients in InGaN layers

In this section a set of 3 samples, specifically grown to study the strain relaxation, the In incorporation process and the surface roughness evolution in InGaN layers, are analysed. The three layers (STR116, STR117, STR115) were prepared in consecutive runs, with successive growth periods of 25, 50 and 100 minutes corresponding to nominal thicknesses of 60, 120 and 240 nm, respectively. The target composition was x=0.25. The location of these samples relatively to the CLT(x) curve is shown in Fig. 6.6. The asymmetric RSM of the three structures under study, measured around the (*10.5*) reflection, are shown in Fig. 5.9 a) , b) and c).

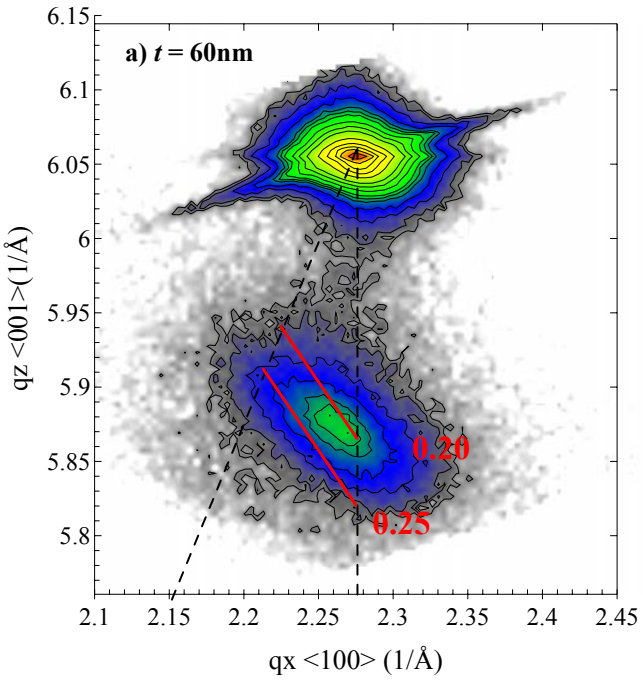

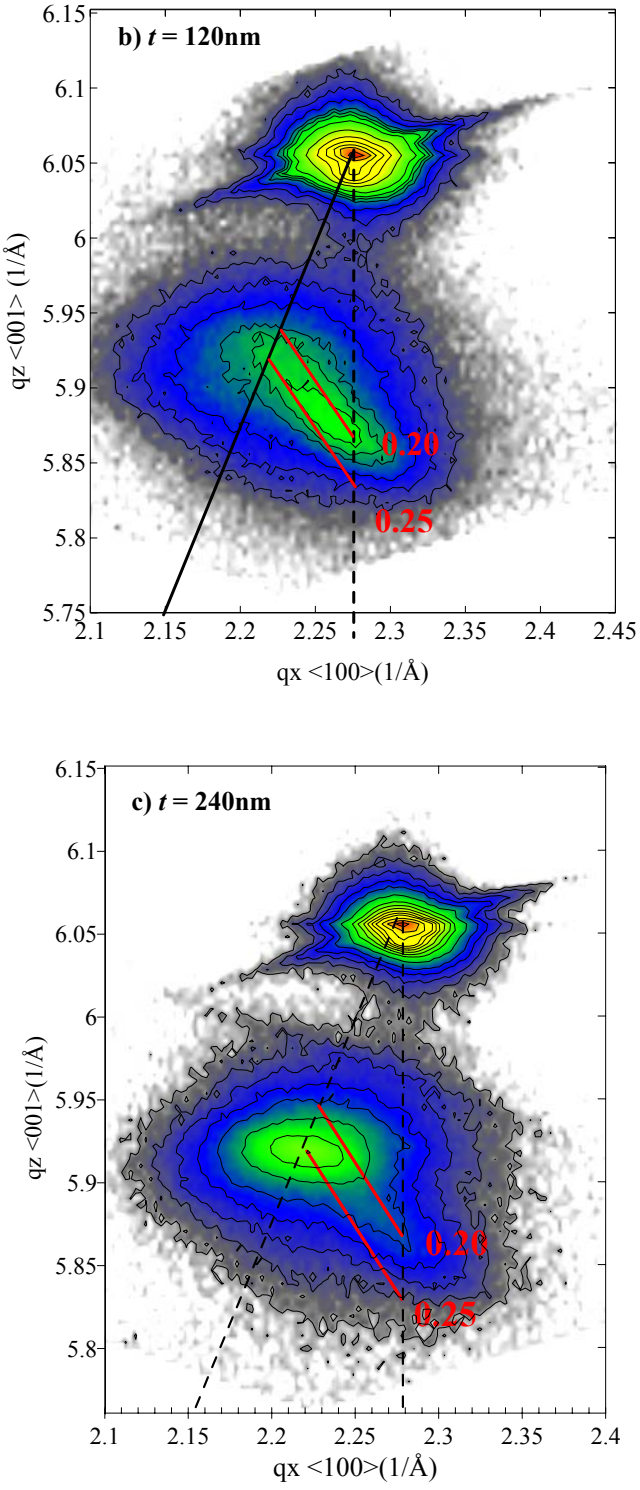

Figure 6.9: Reciprocal space maps for the (*10.5*) reflections of three InGaN/GaN layers with increasing thickness. The lines connecting the fully strained to the fully relaxed dashed lines indicate the calculated relaxation directions in the reciprocal space for various InN mole fractions.

Calculated isocomposition ($0.2<x<0.25$), full and zero relaxation lines are also shown on the various maps.

It can be noticed that with increasing layer thickness, the maximum of the InGaN RLPs progressively shifts from a fully strained (r=0) to a fully relaxed (r=1) position. It is clear that all layers start growing nearly pseudomorphic to GaN. However, not even the thinnest sample (60 nm) is *fully* coherent to GaN. Relaxation is progressive, and the layers do not relax uniformly along the growth direction. Even in sample STR115, which is *mostly* fully relaxed, it is observed that the first few monolayers remain coherent to the GaN buffer. In fact, by considering the increasing intensity in the region near the r=1 line, from sample STR117 to STR115 we may infer that further growth just leads to an increasing thickness of the relaxed part of the sample. This relaxation process is accompanied by an increase of mosaicity in the layer, as can be inferred from the width of the RLP. The dislocations induced during relaxation appear to induce tilts in the mosaic blocks, the maximum of which is verified for the fully relaxed part of the layer. In fact, the shape of the RLPs of sample STR115 indicates that the mosaic structure in InGaN has a larger tilt contribution (see Section 3.9.2.1).

Careful comparison between the lengthening of the InGaN RLPs with the calculated "pure" relaxation directions, for specific values of composition, reveals an interesting feature of InGaN growth. As the films relax (grow) the indium content increases towards the surface[3]. Note that in all samples the position of the RLPs in the coherent region, close to the GaN interface, indicates an In mole fraction of x~0.2. Thereafter, a progressive shift of the RLP maximun towards isocomposition lines for larger x follows the layer relaxation. In fact, for all the samples the fully relaxed regions intercept the isocomposition lines calculated for x~0.24-0.25. This was actually the nominal target composition in our films.

6.7.2.1 Composition depth profiling by RBS

In order to confirm the increase of In content along the growth direction, a detailed RBS analysis was performed. A random RBS spectrum from sample STR116 is shown in Fig. 5.10.

A relatively large sample tilt (θ=46.6º) was used to further improve depth resolution by maximising the path length of the $^4He^+$ ions in the film. The simulation line calculated with RUMP obtained using a layer model with x=0.24, only provides a good fit in the near surface region. For deeper InGaN regions the fit line clearly overestimates the In and underestimates the Ga related signals. Nevertheless, letting the InN content vary linearly from 0.20, near the GaN interface, to 0.24, close to the surface provides a good fit to the experiment as shown in Fig. 5.10.

[3] Note that in the case of InGaN layers, where the strain relaxation is progressive, the method to extract x from the XRD RSMs can obtain estimates of x with an extraordinary "virtual" depth resolution, not usual in conventional XRD measurements.

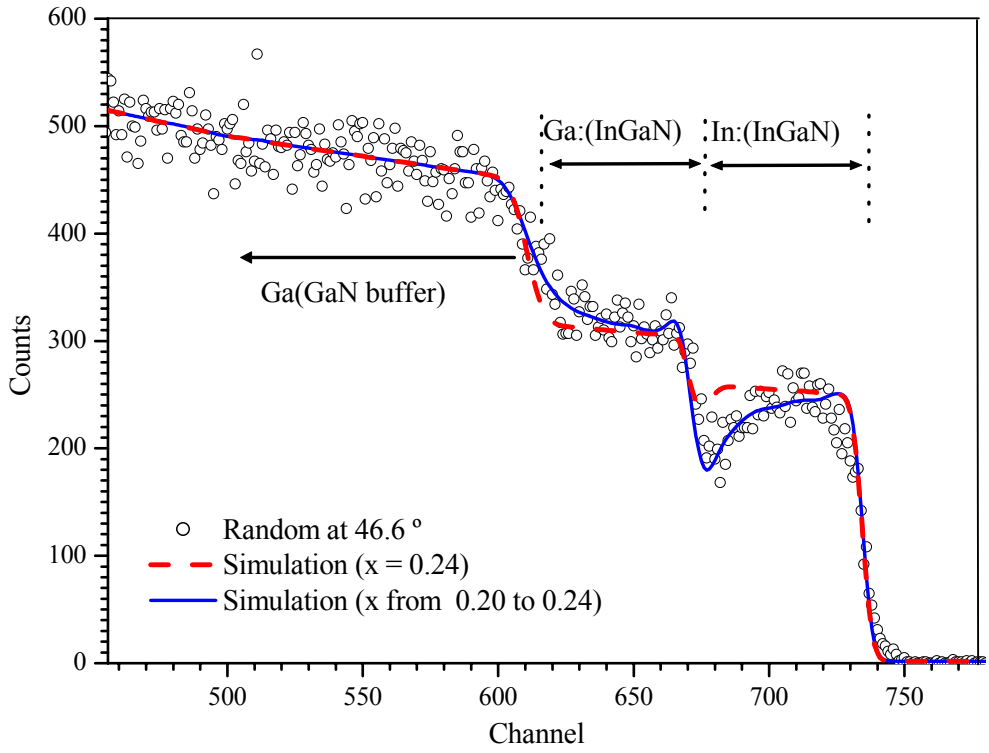

Figure 6.10: Random RBS spectrum of sample STR116. The dashed and solid lines represent the simulations obtained if we assume a uniform composition (x=0.24) over depth, and a varying composition (x from 0.20 to 0.24), respectively.

This is in excellent agreement with the results of the RSM analysis described earlier [40].

6.8 General remarks about strain state, morphology and composition of thick InGaN/GaN single layers

Let us briefly discuss some general trends observed in InGaN/GaN single films. From all experimental results discussed so far, it becomes apparent that there is an overall structural quality degradation with increasing thickness and composition in MOCVD-grown samples. It is also verified that the strain relaxation process accelerates noticeably when t_{InGaN} exceeds CLT(x). It is observed that the strain relaxation process is not continuous, and that the InGaN layers do not relax as a whole. Instead, it is found that further growth above the CLT just contributes to the increasing proportion of relaxed material, giving rise to strong strain gradients over depth. For some samples, those showing two well defined XRD peaks, a nearly discrete strain relaxation results in two extreme states of strain with depth. The peaks corresponding to the relaxed regions are usually broader. The general degradation of structural quality for thicker/higher-x samples is also verified by when comparing random and aligned RBS spectra. The values of χ_{min} (Section 4.8) obtained for the relaxed samples (sample regions) is much larger than in the coherent case.

A surface analysis by scanning electron microscopy (SEM) and atomic force microscopy (AFM) also evidences a strong correlation between surface morphology and strain state. The AFM results on the surface morphology of the STR11# samples are summarized in Fig. 6.11.

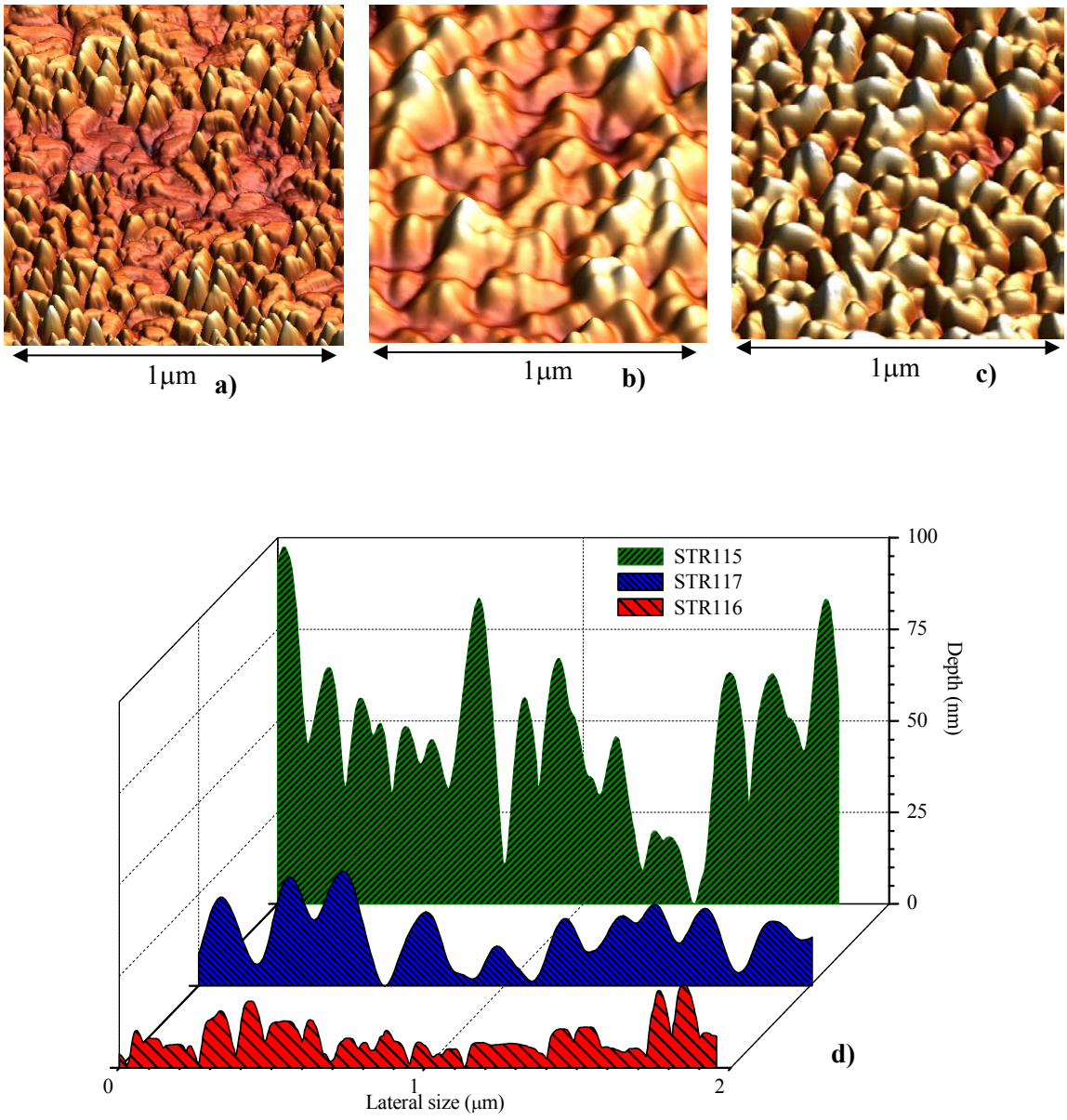

Figure 6.11: Atomic force micrographs illustrating the surface morphology of samples STR115 (a), STR116 (b) and STR117 (c), respectively. The surface profile (height variation *vs* lateral displacement) of the various samples is shown in (d).

With increasing layer thickness the surface becomes rougher, featuring gradually larger 3D islands, as the strain relaxes. This correlation suggests that a transition from 2D to mixed 2-3D

growth may be the most important mechanism in which allows the strain energy InGaN/GaN films to be minimized. The same kind of effect is found with increasing x.

In fact, neither composition nor thickness alone, but a combination of both physical parameters, seems to determine the structural properties. The importance of the CLT concept becomes evident in this context since a prediction of the strain state, the structural quality and surface morphology can be made based on the samples' (t,x) coordinates and its location relative to the CLT(x) curve.

Fig. 6.12 illustrates the structural model of a partially relaxed InGaN layer grown above the CLT(x). The depth variations of strain, at the critical point $CLT_c(x)$ and surface morphology are depicted. An SEM surface micrograph of sample STR115 is also shown in the Figure.

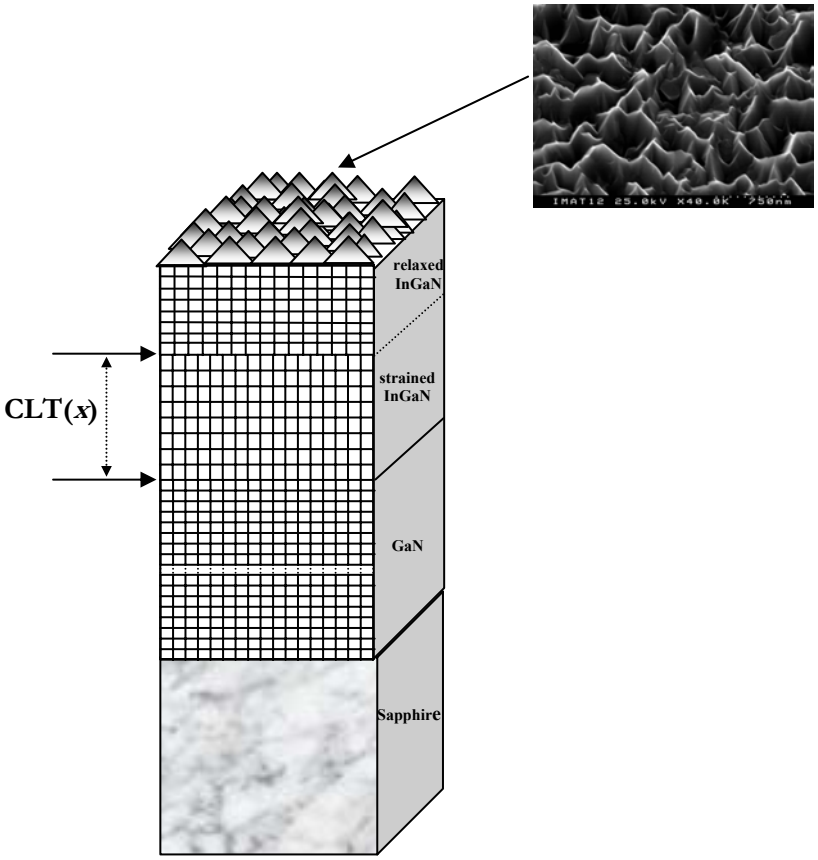

Figure 6.12: Schematic illustration of the strain relaxation process for a layer grown above the critical layer thickness, accompanied by a 3D growth mode. The top image is the SEM image of sample STR115, illustrative of the surface morphology of relaxed samples.

As supplementary work, a piece of sample STR115 was etched in a melt of NaOH/KOH, on the eutectic point at 230ºC for 30 sec. After etching, the InGaN layer thickness was reduced to about 10 nm. The XRD RSM of this part of the STR115 sample is identical to that of sample STR116, and the component of the RSM indicating relaxed 3D growth was eliminated. SEM

analysis confirms a smoother surface of the etched sample. These results were recently reported in Ref. [43]

The experimental results obtained also evidence a correlation between strain relaxation and In incorporation in InGaN samples that are intended to have relatively high, say over 0.20 InN content. Note that the results obtained by RSM analysis, regarding the relation of strain to composition, agree very well with the RBS/channelling results. The RBS/C results presented in Section 4.7 obtained for sample AEC53 also indicated strong composition pulling effects associated with a strain relaxation along the growth direction [42]. Hence, it is suggested that elastic strain has a major role in the In incorporation in the InGaN lattice. In atoms appear to have a tendency to be more easily incorporated (or actually move during growth) into the relaxed regions of the alloy, thus minimising the system strain energy.

Lowering the In content reduces the lattice misfit and associated strain at the interface. Therefore, exclusion of In atoms at the interface reduces the strain energy and allows the first monolayers to grow coherently with GaN. As the layer thickness increases the film partially relaxes allowing more In atoms to be incorporated in the lattice. It appears that there is an intrinsic limit for the amount of In that can be incorporated in a fully strained sample and, similarly, a limit to the layer thickness that can be grown coherently for a specific composition. These experimental findings can be interpreted with reference to the CLT(x) curve for the InGaN/GaN system.

6.9 Influence of the elastic strain on structural properties of InGaN/GaN MQWs

We have shown that the overall structural quality of InGaN single layers on GaN deteriorates both with x and with the increase of strain associated with larger layer thicknesses. In the case of MQWs, RBS characterization also shows that there is a degradation of the structural quality with an increase of x in the wells (Section 4.9)[44].

Nevertheless, it is not yet understood if such deterioration, and particularly the extent of intermixing, is intrinsically related to InN fraction alone, or is essentially a consequence of larger misfit energy. Note that the total strain energy accumulated in a MQW stack increases not only with x, via a larger InGaN/GaN lattice mismatch, but also with the number of QWs in the growth sequence.

In this section, by keeping x nominally constant in the well region and varying the amount of misfit strain energy by increasing the thickness (number of wells) for a set of samples, we attempt to isolate the effects of strain from those associated with composition. For that purpose two MQW structures, STR121 and STR120, were grown at 760° C, containing 18 and 8 wells respectively. The barrier layer period was 270 s, but the well growth period was 78 s. The

growth periods for the GaN cap layers were 540 s but growth of STR120 was terminated before the end of the pre-written recipe after ~15 s of cap growth after the 8th well [44].

6.9.1 RSM analysis by high resolution XRD

The symmetrical RSM for sample STR120 on the (*00.2*) reflection was shown in Fig. 3.23 (Section 3.9.5). A perfect alignment of the superlattice (SL) reciprocal lattice points (RLP) along q_x, demonstrates that the MQW grows aligned with the GaN buffer, i.e. no macroscopic tilts exist [45]. This is also verified in the (*00.2*) RSM for sample STR121 (not shown).
Now consider the (*10.5*) asymmetrical RSMs of the two MQW structures shown in Fig. 6.13 a)[4] and b).

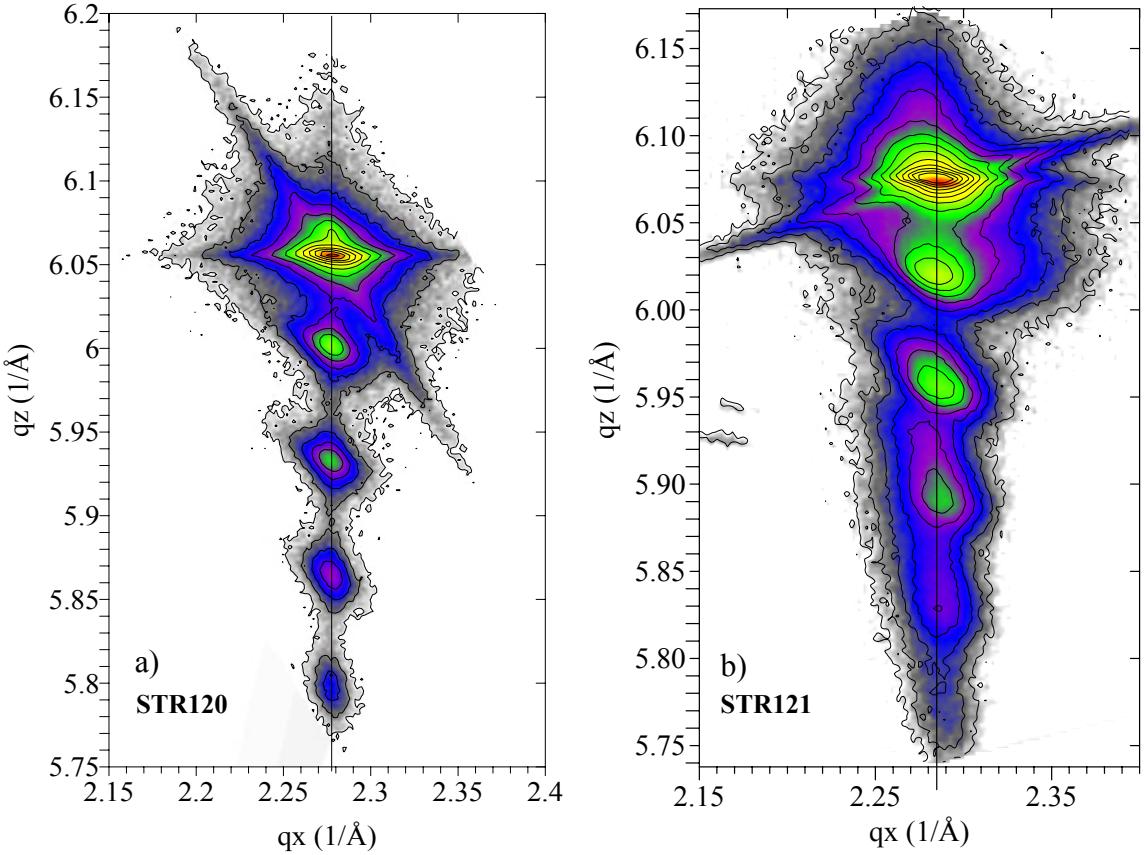

Figure 6.13: Asymmetrical (*10.5*) XRD RSMs of MQWs STR120 and STR121.

From these maps the state of relaxation, r, can be explicitly determined. As can be seen the MQW RLP are, in both cases, aligned along q_x. This shows that the MQWs grew coherent to the GaN buffer, and no strain relaxation (r=0) can be detected within the sensitivity limits of the measurement. Despite both MQWs evidencing pseudomorphic growth, the asymmetrical RSM of the two structures is different. Specifically, while sample STR120 shows well-defined and

[4] To facilitate comparison, the (*10.5*) RSM of STR120 shown as Fig 3.24 in Section 3.9.5 is repeated along side the (*10.5*) RSM of sample STR121.

relatively sharp SL RLPs, a pronounced smearing along the q_z direction is noticed in STR121. Note that diffraction theory predicts the opposite behaviour, i.e. the SL RLPs should become narrower as the number of periods increase. Therefore, the characteristic broadening of the (*10.5*) RLPs in STR121 evidences a poorer structural quality of the thicker sample, and provides a first indication of well/barrier intermixing [45]. A detailed grazing incidence RBS analysis was performed in these two structures to investigate this issue further.

6.9.2 Grazing incidence RBS analysis

A rather direct evidence of decreased chemical contrast in the 18-well sample is provided by RBS analysis. In Fig. 5.14 a) and b) the RBS spectra for the two samples are compared.

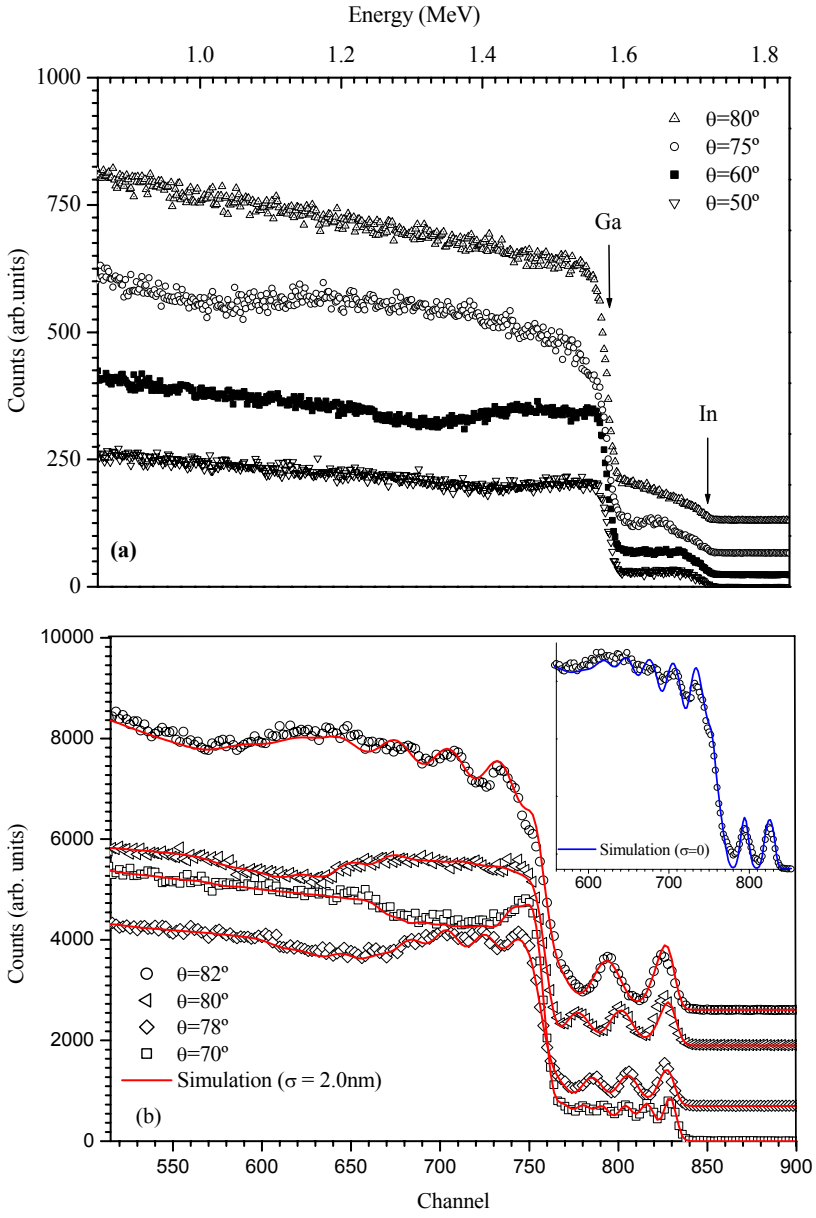

Figure 6.14: Angle-dependent RBS spectra acquired for samples STR121(a) and STR120 (b), respectively. The spectra are vertically shifted for clarity.

For sample STR121 the MQW structure can not be resolved, even at the largest tilt angles, indicating strong well-barrier intermixing. However, the striking modulations of the In and Ga related signals observed in the RBS spectra of sample STR120 indicate improved interface sharpness, in agreement with the XRD analysis. For STR121 only a rough estimate of x in the wells, x~0.20±0.03 can be obtained from RBS, whereas for STR120 individual well compositions and thicknesses can be determined by simulating the experimental RBS spectra.
The experimental spectra at various tilt angles were fitted with the same multilayer model (shown as Table 6.III).

Table 6.III. Multilayer model derived from the RBS simulations for sample STR120; from surface to deeper MQW regions.

Layer	***Areal density*** $(10^{15}$***at/cm2)***	***t*** ***(nm)***	***x*** $(In_xGa_{1-x}N)$
1	26.50	3.22 (2.83±0.15)	0.172 (0.196±0.025)
2	60.17	6.84±0.15	GaN (barrier)
3	21.90	2.71±0.15	0.220±0.025
4	58.59	6.66±0.15	GaN (barrier)
5	22.17	2.73±0.15	0.208±0.025
6	61.59	7.00±0.15	GaN (barrier)
7	17.66	2.20±0.50	0.245±0.040
8	53.89	6.12±0.50	GaN (barrier)
9	20.90	2.58±0.50	0.215±0.040
10	53.94	6.13±0.50	GaN (barrier)
11	23.25	2.86±0.75	0.210±0.05
12	61.59	7.00±0.75	GaN (barrier)
13	24.87	3.06±0.75	0.212±0.05
14	58.22	6.62±0.75	GaN (barrier)
15	21.51	2.62±0.75	0.175±0.05
16	>10042	>1141	GaN (buffer layer)

This simultaneous fit of all experimental RBS spectra greatly increases consistency and accuracy in the analysis. A good fit can only be obtained if moderate intermixing, with $\sigma = 2.0$ nm, is included. This roughness/intermixing parameter, σ, quantifies the deviation from an ideal square profile through the standard deviation of an error function distribution [46]. Fig. 6.15

presents a diagram illustrating the ideal MQW structure, and the effect of the intermixing parameter on the composition profile for different values of σ, relatively to the well thickness. For comparison, the simulation at θ=82º with no intermixing (σ=0) is shown in the inset of Fig. 6.14b). The intermixing value derived for STR120, σ=2.0±0.3 nm, is already a considerable fraction (~0.25) of the bilayer thickness, and close to the QW thickness, meaning that the limits of validity of the models in NDF are approached in this case. Larger intermixing becomes impossible to analyse correctly with these methods. This is the case for STR121 where one can only estimate that $\sigma \geq 5$ nm.

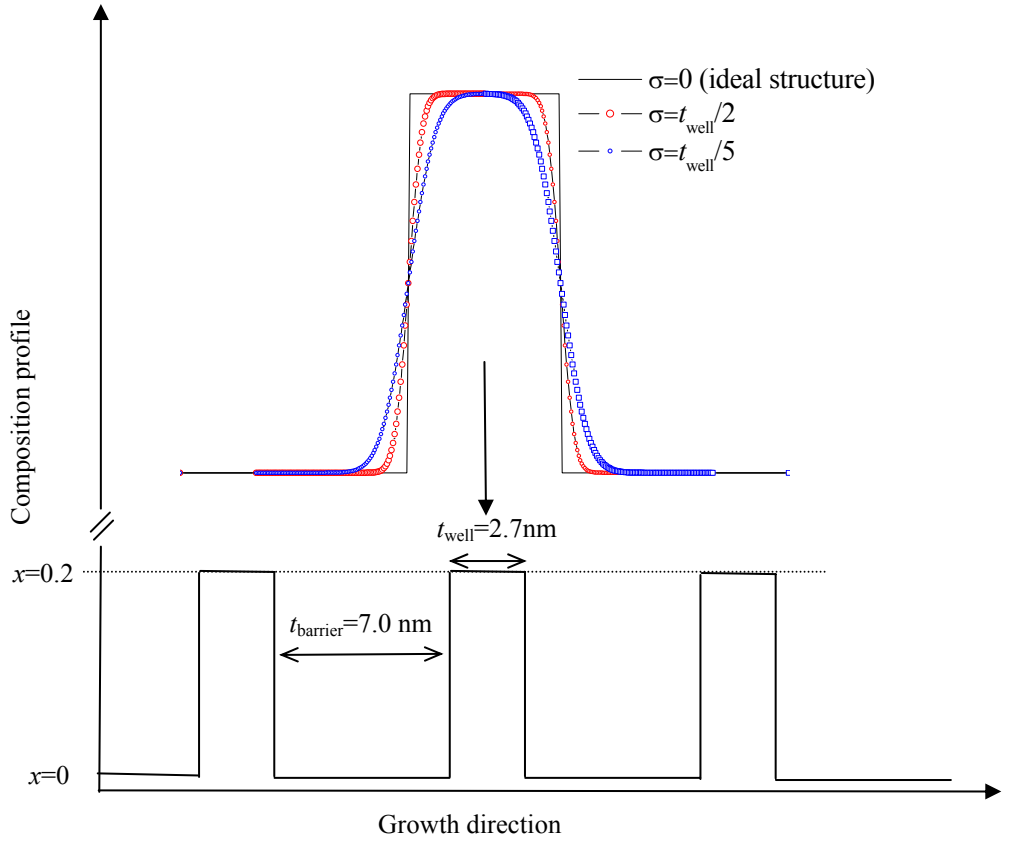

Figure. 6.15: Schematic illustration of the MQW structure and the effect of the intermixing parameter σ.

It is interesting to note in the model structure described in Table 6.III that the top well width is slightly larger than the average thickness of the deeper wells, whereas the calculated value of x is somewhat smaller. This is certainly related to the ~15s of GaN growth over the 8th well in this sample. Due to the intermixing verified in this sample, the first few monolayers of *nominal* GaN grown after the well region result in composition-graded $In_xGa_{1-x}N$ (with $x<x_{well}$). Hence, In is present at the surface, and RBS can not distinguish this ultra-thin cap from the last well. Therefore, this overgrowth just contributes to the *apparent* thickness of the near-surface well, as deduced from the simulations. Nevertheless, from the relative growth times, and considering that 275 s of growth leads to a GaN barrier thickness of ~7 nm, the average cap thickness can be

estimated as ~0.38 nm. Subtracting this value from the last well's estimated thickness gives t=2.84±0.15, in closer agreement with the other wells. The actual value of x for this well should also be recalculated. This can be easily performed by considering that the product of x and the well thickness, indicates the number of In atoms provided for the well growth, and should be constant. Hence, x~(3.22*0.172)/2.83=0.196±0.025, similar to the estimated values of the other wells and to the calculated average value for sample STR121.

The results presented here are the first to directly characterize InGaN/GaN MQWs by RBS. Note, however, that individual well compositions and a precise estimation of the extent of intermixing could only be obtained in the sample with a lower number of wells. It appears that the amount of strain in the stack critically affects the overall structural properties of InGaN MQWs, and therefore the amount of strain should be minimized to obtain high quality devices in this material system.

6.9.3 Strain-morphology-intermixing relation in InGaN MQWs

In this section we try to establish correlations between strain, surface morphology and intermixing in InGaN/GaN MQWs.

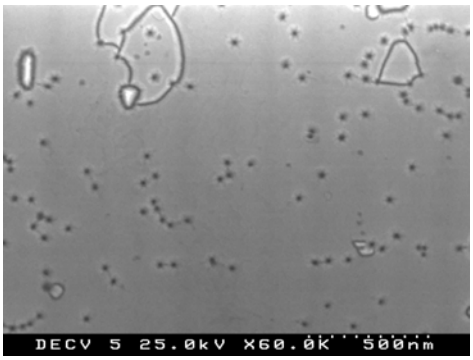

a) SEM of MQW STR120

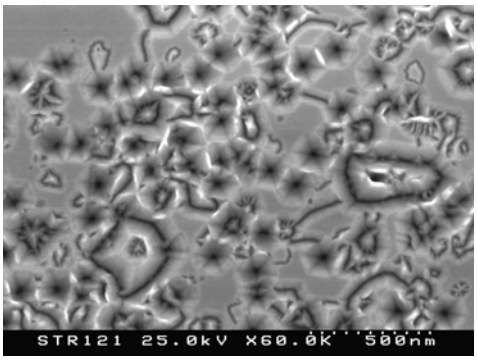

b) SEM of MQW STR121

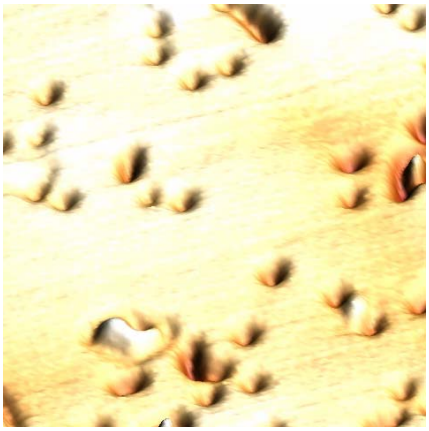

c) AFM of MQW STR120

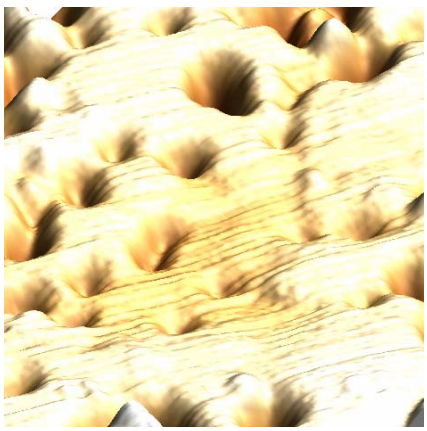

d) AFM of MQW STR121

Figure 6.16: (a, b) SEM (c, d) AFM surface micrographs of STR120 and STR121.

As we can see from the SEM and AFM micrographs, the surface of the sample with more wells is poorer, featuring larger/deeper pits and higher pit density.

For pseudomorphic InGaN grown on GaN, the termination of the threading dislocation gives rise to a specific type of pit known alternatively as an inverted hexagonal pyramid (IHP), a hexagonal pinhole, or a *V* defect. These defects are open hexagonal, inverted pyramids with {*10-11*} side walls, and thought to form as a result of reduced Ga incorporation which inhibits growth of the {*10-11*} planes [47-49].

The V-pit lateral size in STR120 is ~50 nm, whereas for sample STR121 sizes up to ~250 nm are found. The pit depth is also much greater in the 18-well sample. A detailed AFM surface profile analysis reveals that the average pit depth in STR120 sample is around 5-10 nm, but in STR121 depths of up to 50-60 nm can be found.

In order to reduce the system's strain energy the density, lateral size and depth of V-pits increases. As pointed out in Ref. [50], the energetic driving force of the V-pit formation is a reduction of strain energy achieved by avoiding the accumulation of strained material in the region near the dislocation core. This reduction in strain energy is accomplished at the expense of increased surface energy, and the size and shape of the pit is affected by the surface and dislocation energetics. As the V defect grows across the InGaN quantum well stack, it results in buried InGaN wells on its sidewalls.

Duxubury *et al* [51] have shown that dislocations promote the breakdown of the quantum well stack via increased In diffusion towards and along the dislocation core. Therefore, surface pitting and dislocations seem to play a fundamental role in the intermixing mechanism in InGaN/GaN MQWs. The intermixing effects observed here can not be related to the growth temperature, since the InGaN growth temperature is the same in both cases. Our results indicate that the amount of elastic strain energy accumulated in the MQW stack is the most relevant determinant of intermixing. We suggest that surface pitting and the associated dislocations assist the intermixing process. The correlation between these structural features and the MQWs optical properties is discussed in Chapter. 7.

6.10 Summary

Strain and composition in InGaN/GaN heterostructures was investigated in detail. The basic definitions regarding strain and composition of InGaN alloys were given, and the correlation between the two physical properties was highlighted. The two extreme approximations in common use regarding the strain state, fully relaxed or fully coherent growth, in order to determine x from the measured c lattice constant, were critically discussed. It was shown that considerable misjudgements can be made in the evaluation of the InN mole fraction if the strain effect on the lattice is not properly taken into account. Specifically, assuming full relaxation makes a systematic overestimation of x, whereas the pseudomorphic presumption yields the lower limit of x of a given sample. Strain insensitive RBS measurement of x provides a basis of comparison. Using the alloys in-plane and out-of-plane measured lattice constants, elastic theory was applied to account for the hexagonal lattice distortion due to biaxial strain, allowing strain and composition effects to be separated. If this is performed, excellent agreement between XRD and RBS estimates of x is obtained.

The peculiar case of InGaN layers showing double XRD components was treated in detail, in view of the fact that this observation has been mistakenly quoted as evidence of phase separation in InGaN. We have shown that the origin of this *misconception* is an inadequate application of Vegard's law to layer regions that are incompletely relaxed. It was found that when the strain effect is properly taken into account, the two XRD components correspond to the same value of x. An RBS/C analysis provided further evidence of uniform composition in such layers and allowed us to depth-locate the relaxed (near surface) and strained (near the GaN interface) regions. Thus, the presence of double XRD peaks was shown to be unrelated to phase separation, and is a consequence of a discontinuous strain relaxation over depth.

The important concept of *critical layer thickness* (CLT) for strain relaxation is introduced. The CLT(x) was calculated using the People and Bean model, demarcating the thickness-composition range where the strain relaxation is expected to dramatically accelerate in InGaN/GaN layers. The CLT(x) was found to be a very strong function of x.

We presented a model, based on elastic theory, which allows composition and strain gradients to be detected independently from an asymmetric high resolution XRD RSM. The directions of "pure" strain relaxation in the reciprocal space, for a given InN content (isocomposition lines), are calculated. The practical application of the model allows different situations regarding strain and composition gradients to be distinguished; first, the case of a pure strain relaxation in layers grown above the CLT, well represented by layers with 2 XRD peaks where the strain relaxation follows the calculated isocomposition line. On the other hand, analysis of a set of InGaN layers with thicknesses progressively increasing above the CLT allowed strain relaxation and In incorporation phenomena to be monitored as the alloy films grow. Comparison between

calculated directions and measured distributions of the RLP has shown that the relaxation process does not follow a specific isocomposition line for these samples. The In content increases as the films grow and relax. At the start of growth all the films have x~0.2 and are coherent to GaN. As they relax, x progressively increases towards the experimentally targeted value (0.25). Compositional gradients along the growth direction extracted from the RSM analysis were confirmed by complementary RBS depth profiling of x.

A general degradation of structural quality is verified with an increase of strain, i.e. larger thickness or x. Broader XRD profiles indicating increased mosaicity, composition and strain gradients and larger values of χ_{min} obtained by RBS, confirm the poorer crystalline quality of relaxed layers (or layer regions). In addition, it is found that the surface morphology becomes rougher for layers grown above the CLT, suggesting that 3D islanding is the main relaxation mechanism in InGaN.

Finally, by characterizing in detail two MQW samples with the same InN mole fraction and different thicknesses it was shown that the number of periods in the MQW sequence notably influences the structural properties. In particular, well/barrier intermixing was found to increase markedly with an increase in the number of wells from 8 to 18. A detailed surface analysis showed a correlation between an increased size and density of surface pits and the number of wells grown. In order to reduce the system's strain energy the density lateral size and depth of V-pits increases. This supported the suggestion that surface pitting and dislocations play a fundamental role in the intermixing mechanism in InGaN/GaN MQWs. Our results also indicated that the overall structural quality degradation is mainly determined by the total strain energy accumulated in the MQW stack, a similar situation to that observed in single layers.

6.11 References:

[1] L. Vegard, Z. Phys. 5, **17** (1921).

[2] J. F. Nye, *"Physical properties of crystals: their representation by tensors and matrices"* Clarendon Press, Oxford, U.K. (1995).

[3] D. J. Dunstan, J. Materials Science- Materials in Electronics **8**, 337 (1997).

[4] P. F. Fewster, "*X-Ray scattering from semiconductors* Imperial" College Press, London, U.K., (2001).

[5] C. G. Van de Walle, M. D. McCluskey, C. P. Master, L. T. Romano, and N. M. Johnson, Mat. Sci. and Eng. B **59**, 274 (1999).

[6] M. Schuster, P. O. Gervais, B. Jobst, W Hösler, R. Averbeck, H. Riechert, A. Iberl and R. Stömmer, J. Phys. D: Appl. Phys. **32**, A56 (1999).

[7] K. P. O'Donnell, R. W. Martin, and S. Pereira, Appl. Phys. Lett. **81**, 1353 (2002).

[8] T. Detchprohm, K. Hiramatsu, K. Itoh and I Akasaki, Jpn. J. Appl. Phys. **31**, L1454 (1992).

[9] A. F. Wright, J. Appl. Phys. **82**, 2833 (1997)

[10] W. Paszkowicz, Powder Diffraction **14**, 258 (1999).

[11] S. Pereira, M. R. Correia, T. Monteiro, E. Pereira, E. Alves, A. D. Sequeira, N. Franco, Appl. Phys. Lett. **78**, 2137 (2001).

[12] K. P. O'Donnell, J. F. Mosselmans, R. W. Martin, S. Pereira and M. E. White, J. Phys. Condens. Matter, **13**, 6977 (2001).

[13] S. Pereira, M. R. Correia, T. Monteiro, E. Pereira, M. R. Soares e E. Alves, J. Cryst. Growth **230**, 448 (2001).

[14] S. Pereira, M. R. Correia, E. Pereira E. Alves L. C. Alves C. Trager-Cowan and K. P. O'Donnell, Mat. Res. Soc. Proc. **639**, G3.52 (2001).

[15] N. A. El-Masry, E. L. Piner, S. X. Liu and S. M. Bedair, Appl. Phys. Lett. **72**, 40 (1998).

[16] Yong-Tae Moon, Dong-Joon Kim, Keun-Man Song, In-Hwan Lee, Min-Su Yi, Do-Young Noh, Chel-Jong Choi, Tae-Yeon Seong, and Seong-Ju Park , Phys. Stat. Sol. (b) **216**, 167 (1999).

[17] D. Rudolff, Phys. Stat. Sol. (b) **216**, 315 (1999).

[18] Z. Liliental-Weber, M. Benamara, J. Washburn, J. Z. Domagala, J. Bak-Misiuk, E. L. Piner, J. C. Roberts, S. M. Bedair, J. Electr. Mat, **30** (4), 439 (2001).

[19] E. Zielinska-Rohozinska, J. Gronkowski, M. Regulska, M. Majer, K. Pakula, Cryst. Res. Technol., **36** (8-10), 903 (2001).

[20] L. Görgens, O. Ambacher, M. Stutzmann, C. Miskys, F. Scholz, and J. Off Appl. Phys. Lett. **76**, 577 (2000).

[21] L. T. Romano, B. S. Krusor, M. D. McCluskey, and D. P. Bour, Appl. Phys. Lett. **73**, 1757 (1998).

[22] H. P. D. Schenk, P. de Mierry, M. Laügt, F. Ommès, M. Leroux, B. Beaumont and P. Gibart, Appl. Phys. Lett. **75**, 2587 (1999).

[23] M. D. McCluskey, C. G. Van de Walle, C. P. Master, L. T. Romano, and N. M. Johnson, Appl. Phys. Lett. **72**, 2725 (1998).

[24] E. Alves, S. Pereira, M. R. Correia, E. Pereira, A. D. Sequeira, N. Franco, K. P. O'Donnell, C. Trager-Cowan, Nucl. Instr. and Meth. B **l90**, 560 (2002).

[25] S. Pereira, M.R. Correia, E. Pereira, K.P. O'Donnell, R.W. Martin, M.E. White, E. Alves, A. D. Sequeira and N. Franco, Mat. Sci. Eng. B **93**, 163 (2002).

[26] S. Pereira M. R. Correia, E. Pereira K. P. O'Donnell E. Alves, A. D. Sequeira, and N. Franco, Appl. Phys. Lett. **79**, 1432 (2001).

[27] S. Pereira, M. R. Correia, E. Pereira, K. P. O'Donnell, E. Alves, A D. Sequeira, N. Franco, Appl. Phys. Lett. **80** (2), 337 (2002).

[28] S. Pereira M. R. Correia, E. Pereira C. Trager-Cowan, F. Sweeney and K. P. O'Donnell A. Sequeira, E. Alves, N. Franco, Appl. Phys. Lett. **81**, 1207 (2002).

[29] S. Srinavasan, F. Bertram, A. Bell, F. A. Ponce, S. Tanaka, H. Omiya, and Y. Nakagawa, Appl. Phys. Lett. **80**, 550 (2002).

[30] K. P. O'Donnell, R. W. Martin, and S. Pereira, Appl. Phys. Lett. **81**, 1353 (2002).

[31] L. R. Doolittle, Nucl. Instrum. Methods B **9**, 344 (1985).

[32] M. F. Wu, A. Vantomme, S. M. Hogg, G. Langouche, W. Van der Stricht, K. Jacobs and I. Moerman, Appl. Phys. Lett. **74**, 365 (1999).

[33] K. P. O'Donnell, S. Pereira R. W. Martin, P. R. Edwards, M. J. Tobin and J. F. W. Mosselmans, Phys. Stat. Sol. (a) **195**, 532 (2003).

[34] R. People and J. C. Bean, Appl. Phys. Lett. **47**, 322 (1985); **49**, 229 (1986).

[35] J. W. Matthews, A. E. Blakeslee. J. Cryst. Growth **32**, 265 (1974).

[36] H. Amano, T. Takeuchi, S. Sota, H. Sakai, and I. Akasaki, Mater. Res. Soc. Symp. Proc. **449**, 1143 (1997).

[37] C. A. Parker, J. C. Roberts, S. M. Bedair, M. J. Reed, S. X. Liu, N. A. El-Masry, and L. H. Robins, Appl. Phys. Lett. **75**, 2566 (1999).

[38] N. Franco, S. Pereira and A. D. Sequeira, Mater. Sci. Forum **455**,132 (2004).

[39] H. Heinke, S. Einfeldt, B. Kuhn-Heinrich, G. Plahl, M. O Möller and G. Landwehr J. Phys. D: Appl. Phys. **28** (4A), A104 (1995).

[40] S. Pereira, M. R. Correia, E. Pereira, K. P. O'Donnell, E. Alves, A. D. Sequeira, N. Franco, I. M. Watson and C. Deatcher, Appl. Phys. Lett. **80**, 3913, (2002).

[41] S. Pereira, M. R. Correia, E. Pereira, K. P. O'Donnell, E. Alves, A. D. Sequeira, N. Franco, I. M. Watson, C. J. Deatcher Appl. Phys. Lett. **81**, 3500 (2002).

[42] S. Pereira, M. R. Correia, E. Pereira E. Alves C. Trager-Cowan and K. P. O'Donnell Phys. Rev. B **64**, 205311 (2001).

[43] M. R. Correia, S. Pereira, E. Pereira, J. Frandon, I. M. Watson, E. Alves, A. D. Sequeira, N. Franco, Appl. Phys. Lett. **85** 2235 (2004).

[44] S. Pereira, E. Pereira, E. Alves, N. P. Barradas, K. P. O'Donnell, C. Liu, C. J. Deatcher and I. M. Watson, Appl. Phys. Lett. **81**, 2950 (2002).

[45] S. Pereira, M. R. Correia, E. Pereira, K. P. O'Donnell, E. Alves, N. P. Barradas, A. D. Sequeira, N. Franco, I. M. Watson, and C. Liu, Phys. Stat. Solidi (c) **0**, 302, (2002).

[46] N. P. Barradas, J. Phys. D: Appl. Phys. **34**, 2109 (2001).

[47] Z. Liliental-Weber Y. Chen, S. Ruvimov, and J. Washburn., Phys. Rev. Lett. **79**, 2835 (1997).

[48] Y. Chen, T. Takeuchi, H. Amano, I. Akasaki, N. Yamada, Y. Kaneko, and S. Y. Wang, Appl. Phys. Lett. **72**, 710 (1998).

[49] X. H. Wu, C. R. Elsass, A. Abare, M. Mack, S. Keller, P. M. Petroff, S. P. DenBaars, J. S. Speck, and S. J. Rosner, Appl. Phys. Lett. **72**, 692 (1998).

[50] J. E. Northrup and J. Neugebauer, Phys. Rev B **60**, R8473 (1999).

[51] N. Duxbury, U. Bangert, P. Dawson, E. J. Thrush, W. Van der Stricht, K. Jacobs, and I. Moerman, Appl. Phys. Lett. **76**, 1600 (2000).

Chapter 7: Correlation between optical and structural properties of InGaN/GaN heterostructures

Overview

The information about InGaN/GaN heterostructures provided by the structural and optical characterization techniques is integrated in this chapter. The optical properties are interpreted and discussed with reference to structural features, and the importance of knowing the samples' nanostructural details to understand the alloy optical properties is clearly evidenced.

By using Rutherford Backscattering (RBS) measured values of x, and bandgap energies extracted from optical absorption spectroscopy, the composition dependence of the alloy bandgap ($0<x<0.25$), free from the effects of strain, is established. The biaxial strain effects, quantified in all samples by X-ray diffraction (XRD), are taken into account to correct the bandgap of strained layers. The bandgap variation as a function of composition is discussed and compared with other results found in the literature.

The optical properties of samples with particular structural properties, namely: single layers with composition gradients along the growth direction, multiple quantum wells (MQWs) with different levels of intermixing and MQWs showing In segregation to the cap layer as well as, InGaN layers featuring depth variations of strain (i.e. double XRD peaks), are investigated.

Given the interest in the issue of InGaN samples showing double XRD peaks, the optical properties of these samples are analysed in detail. It is found that samples showing double XRD peaks also evidence double luminescence peaks (DLPs). Furthermore, by using cathodoluminescence (CL) spectroscopy with variable electron beam energy the two-luminescence components can be spatially resolved. This allows the origin of the photoluminescence (PL) peak splitting to be unambiguously identified. By using energy positions of DLPs found in this work and others from a literature survey, an interesting general trend is verified. Based on the structural knowledge about these samples, and using the energy splitting of the two PL components, a novel method to estimate the deformation potential in a semiconductor alloy is proposed.

7.1 Introduction

Nowadays (about 10 years after the introduction of commercial InGaN-based light emitting diodes), we may still consider that the semiconductor alloy at the core of these devices is, from a fundamental point of view, a poorly understood material [1,[2]. As already mentioned, the

physics involved in the light emission process is not yet fully understood, and various models have been proposed to explain its unique optical properties.

Attempts to model InGaN optical properties have not, so far, produced a sound physical description. In part, because nanostructure related effects in the optical spectra are not easy to quantify, and therefore most of the times are incorrectly taken into account or simply neglected. For instance, thickness effects, atomic ordering and biaxial strain effects concurrently tailor the optical response of InGaN [3-7], causing a major obstacle to obtain a consistent physical model based on optical measurements alone. On the other hand, due to the excitement around this material in the last years (with a remarkable growth of InGaN related publications) several results have not been carefully and systematically interpreted, leading to various misconceptions regarding InGaN. Research in this field has been mostly driven by technologists that look for solutions, which offer new functionality and commercial opportunities, to the detriment of understanding, see for instance Refs. [8-10]. Some of these misconceptions still have impact nowadays, through repeated citation in the literature, and providing an obstacle to further advances, as we have recently argued [4-6].

We have already discussed some examples of these misinterpretations. For instance, in Chapter 3 we have shown that diffraction due to metallic Indium droplets was confused with the InN phase. Additionally, the assertion that InGaN is a macroscopically phase-segregated mixture based on the observation of double XRD peaks was questioned in Chapter 6. Similar misconceptions are present in the interpretation of the optical properties [8,9].

Indeed, it is very difficult to interpret the optical properties without a detailed knowledge of the samples' structural properties. Therefore, the key to advance in the understanding of this semiconductor intriguing physical properties appears to be a suitable combination of structural and optical characterization techniques. On the other hand, it is not easy to integrate simultaneous expertise in structural and optical characterization to provide a systematic and multidisciplinary approach to the interpretation of the Physics of this semiconductor alloy.

In this chapter, we attempt to provide such an approach. By bringing together precise knowledge about the structural properties and the optical characterization results obtained in a set of InGaN heterostructures, we try to shed some light on some of the most pertinent open questions. In particular we analyze the effects of strain and composition, and issues ascribed to thickness dependence, on the optical properties.

7.1.1 The importance of considering the state of strain

It is crucial to reiterate the importance of taking into account the presence of strain when analyzing experimental results for InGaN layers. Strain directly affects enter in two major

structural and optical properties: the *c* lattice constant as measured by XRD, and the transition energies, measured by optical absorption (OA) or PL.

If the state of strain is not well characterised, and the measured *c* lattice constant is used directly to determine the composition, significant errors may occur. A systematic overestimation or underestimation of the In content are verified, according to the approximation considered, fully relaxed or coherent growth, respectively. The effect of strain on the composition values determined by XRD was discussed in detail in Sections 5.3 and 5.7, and in the literature [12-16], where methods based on elastic theory of solids are used to calculate the strain effect on the *c* lattice constant.

Moreover, strain has an important effect on the band structure: the hydrostatic component of the strain affects the band gap, and the biaxial component causes splitting of the valence-band states [17]. These effects need to be taken into consideration when interpreting measured transition energies. Let us try to understand how the strain may affect the band structure of wurtzite semiconductors.

7.1.2 Effect of strain on the band structure

Strain in an InGaN layer has an effect on both conduction and valence bands. The shift in the conduction band can be expressed as [17]:

$$\Delta E_c = a_{cxx} 2\varepsilon_{xx} + a_{czz}\varepsilon_{zz} \qquad \text{(Eq. 7.1)}$$
$$= 2a_c \left(1 - c_{13}/c_{33}\right) \varepsilon_{xx}$$

Where we have used Eq. 6.7, and assumed (in the absence of better information) that $a_{cxx}=a_{czz}$ i.e. the magnitude of the deformation potential, a_c, describing the response of the conduction band to strain does not depend on orientation.

For the valence bands, we focus on the heavy-hole band, which is the highest-energy band (i.e. the one participating in the lowest transition energy) under biaxial compressive strain:

$$\Delta E_{v,hh} = 2(D_2+D_4)\,\varepsilon_{xx} + (D_1+D_3)\,\varepsilon_{zz} \quad \text{(Eq. 7.2)}$$
$$= 2\left[-(D_2+D_4) - (D1+D3)\, c_{13}/c_{33}\right]\varepsilon_{xx}$$

where, D_i, are the strain deformation potentials [17]. The strain induced shift in the bandgap is given by:

$$\Delta E_g = \Delta E_c - \Delta E_{v,hh} \qquad \text{(Eq. 7.3)}$$

In general, the variation of the bandgap due to strain ΔE_g, can be parameterised as a function of either ε_{xx} or ε_{zz}. Assuming a linear variation of the bandgap with strain, Eq. 7.3 can be arranged to take the form of a product:

$$\Delta E_g = const_{xx} \cdot \varepsilon_{xx} \qquad \text{(Eq. 7.4)}$$

or alternatively,

$$\Delta E_g = const_{zz} \cdot \varepsilon_{zz} \qquad \text{(Eq. 7.5)}$$

where ε_{xx}, and ε_{zz} are the parallel and perpendicular strain components as defined in Chapter 6 by Eq. 6.3 a) and Eq. 6.3 b), and $const_{xx}$ and $const_{zz}$ are the strain coefficients, which quantify the strain effect on E_g due to ε_{xx} and ε_{zz}, respectively.

In the absence of better knowledge regarding deformation potentials, D_i, for InGaN it is considered appropriate[1], as a first approximation, to use experimental information about the band gap of GaN. Two excellent works deal with the strain effects on the excitonic transitions in GaN. In brief, the A-exciton[2] energy was measured as a function of biaxial strain using GaN samples grown on different substrates and with different thickness. Shikanai *et al.* obtained experimentally the relation between perpendicular strain and the GaN bandgap [18]:

$$\Delta E_g = -15.4\varepsilon_{zz}. \qquad \text{(Eq. 7.6)}$$

The variation of excitonic transition energies as a function of parallel strain was studied in GaN by Shan *et al.* [19]; Fig. 3 of Ref. [19] yields for the change in the lowest transition energy given by:

$$\Delta E_g = -9.3\varepsilon_{xx}. \qquad \text{(Eq. 7.7)}$$

7.2 Eg(*x*) for InGaN alloys free from the effects of strain

A good example of the lack of basic understanding regarding InGaN alloys is the fact that the bandgap dependence on composition, independent of the state of strain, is not well established.

[1] The justification for this procedure can be found in section 7.5.5

[2] Three exciton resonances associated with transitions referred to as A, B and C exciton transitions between the bottom of the conduction band (Γ_7^C) and the three upmost valence band edges (Γ_9^V+ Γ_7^V+Γ_7^V) are verified in GaN [20]. The A-exciton is the lowest energy transition.

A deviation from a linear dependence of the fundamental gap on x has been postulated, and the band gap of a relaxed unstrained alloy is usually expressed as:

$$E_g(In_xGa_{1-x}N)=xE_g^{InN}+(1-x)E_g^{GaN}-bx(1-x) \qquad \text{(Eq. 7.8)}$$

where b is the bowing parameter. A wide range of bowing parameters can be found in the literature for InGaN [21-27].

Note that in order to establish the relation between strain free bandgap and x, a suitable combination of structural and optical characterization results viz, precise knowledge of composition, the bandgap energy and the state of strain are required. Thus, one can identify several sources of error in the establishment of a consensual relation, explaining the variety of bowing parameters found in the literature. In some studies what is measured is the luminescence peak energy, instead of the bandgap, ignoring the large Stokes' shift of emission with respect to the band edge, verified in InGaN [28,29]. When the bandgap is derived from optical absorption or photoluminescence excitation experiments, a difficulty arises from the spectral broadening, which hinders a clear identification of the band edge energy.

At the same time, accurate determination of In content is difficult in InGaN layers. Frequently, the composition is derived from XRD, using Vegard's law directly, without properly considering the state of strain in the samples, with the implications previously discussed.

An additional source of error is the assumption regarding the state of strain typically made (coherent growth) to correct the band gap due to strain, leading to an over correction in relaxed or partially relaxed samples.

7.2.1 A programmatic approach to establish Eg(x)

In this work, optical bandgaps were determined exclusively by OA spectroscopy. The absorption curves for samples of several concentrations were fitted to a sigmoidal expression [28], providing a reproducible criterion to determine the bandgap of InGaN layers. This procedure, rather than using an unclear threshold, was used to determine, $E_g^{abs.}$, the "effective bandgap" and the broadening parameter, ΔE, equivalent to the width of an Urbach tail. The method to extract E_g from OABS was explained and illustrated in Section 5.1.3.2.

RBS was used to accurately determine the alloy composition *independently* from the effects of strain. Subsequent XRD measurements permit the evaluation of strain in all samples. A precise knowledge of the InN mole fraction, combined with X-ray diffraction measurements of c, allows perpendicular strain, ε_{zz}, to be evaluated. Hence, the magnitude of the bandgap correction due to strain can be calculated for each sample.

The alloy's relaxed energy gap can be given as:

$$E_g^{rel.}(InGaN) \cong E_g^{abs.} - \varepsilon_{zz}^{InGaN}.const_{zz}^{GaN}. \qquad \text{(Eq. 7.9)}$$

where, $E_g^{rel.}$, is the bandgap corresponding to relaxed material, E_g^{abs}, is the bandgap energy measured directly from OABS. The last term[3] in Eq. 7.9 is the magnitude of strain correction in the band gap, and corresponds to $const_{zz}$ in Eq. 7.5. It is assumed that for the composition range studied x<0.25, the strain coefficient of $In_xGa_{1-x}N$ is identical to that of GaN:

$$const_{zz}^{InGaN} \cong const_{zz}^{GaN} = -15.4eV \quad \text{(Eq. 7.10)}$$

7.2.2 Results and comparison with literature

In Fig. 7.1, the strain corrected optical bandgap as a function of composition is plotted for a range of samples with 0<x<0.24.

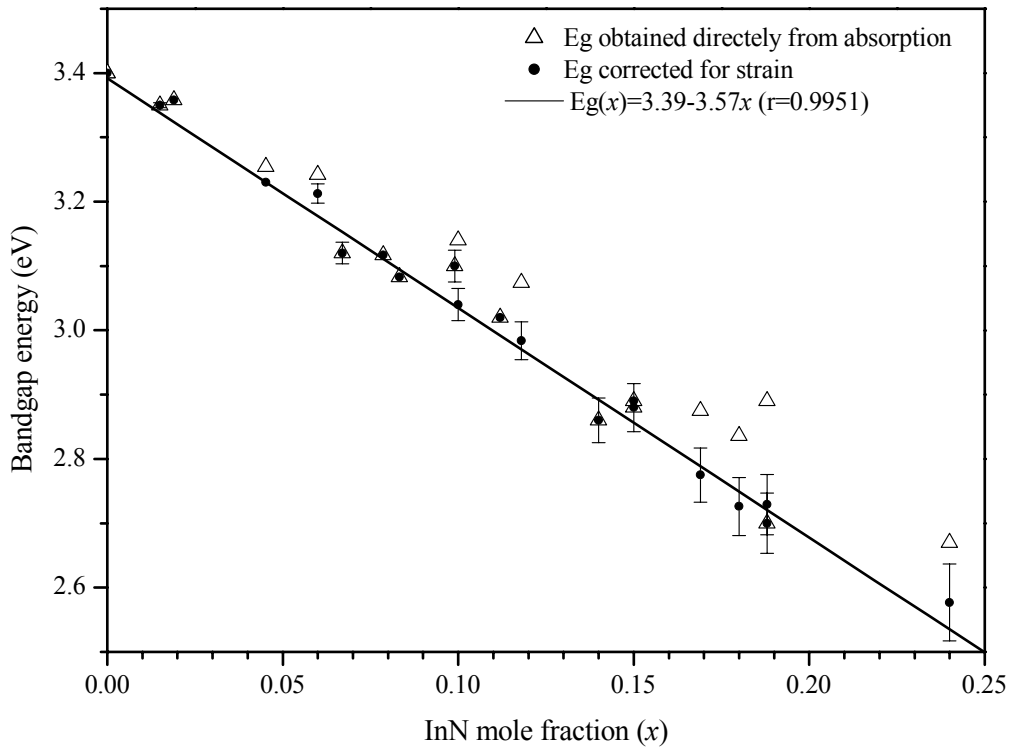

Figure 7.1: Bandgap energies obtained from optical absorption spectroscopy measurements and corrected for the strain, plotted as a function of x obtained from RBS for $In_xGa_{1-x}N$ in the range 0<x<0.25.

[3] Note that positive strain increases the bandgap, and therefore the correction due to strain is a negative term.

The $E_g(x)$ dependence is found to be linear in the x range measured. A least squares fit to the data yields: $E_g(x)=3.39-3.57x$ ($r=0.995$). Comparing this to Eq. 7.8, would yield the unphysical result: b=0, E_g(InN)=-0.18 eV.

An additional problem arises when using Eq. 7.8 due to the fact that the bandgap of InN is not yet well established. When a band gap of ~1.9 eV for InN is assumed as the end point value[4], very large bowing parameters are required to fit the composition dependence of the fundamental bandgap energy in InGaN. The bowing parameter required to fit same $E_g(x)$ data, will decrease for lower values of E_g^{InN}.

Figure 7.2 compares our measurements with a set of experimental results obtained in other publications [30-33] in similar composition ranges.

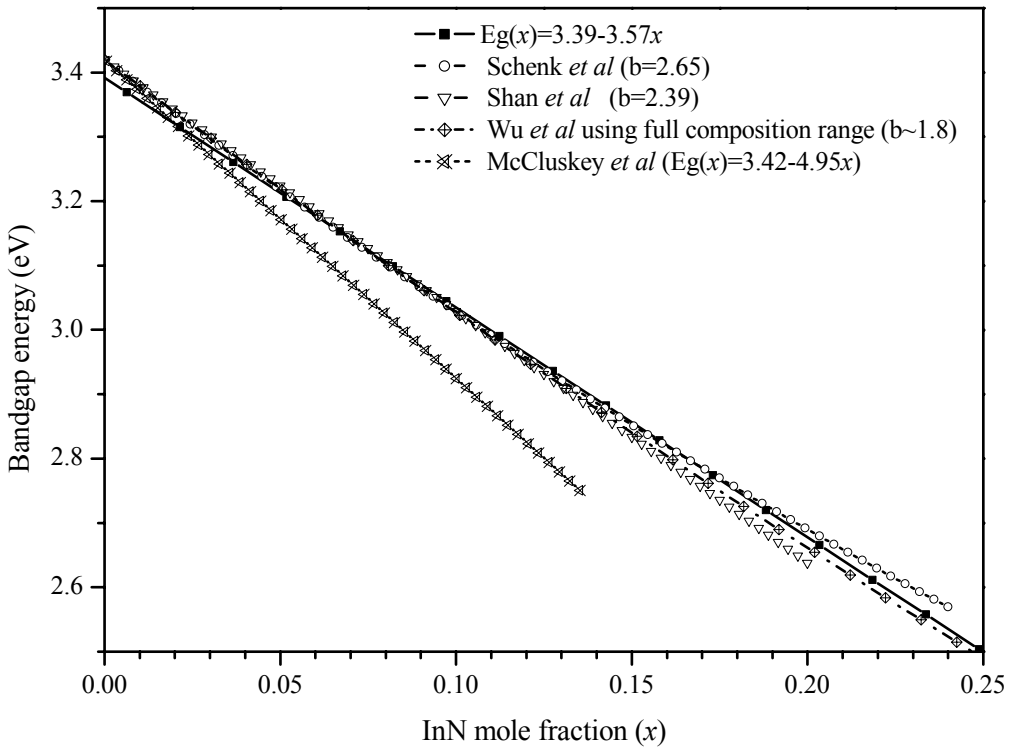

Figure 7.2: Comparison between various $E_g(x)$ curves obtained for InGaN.

Our data is in good agreement with the results obtained by Shan *et al.* [31] and Schenk *et al.* [30], where InN content was measured by RBS and XRD (Schenk *et al.* have considered the strain relaxation in the determination of x by XRD) and bandgap determined at RT by photoreflectance and photothermal deflection spectroscopy, respectively.

However, for instance, the $E_g(x)$ trend obtained by McCluskey *et al.* [32] differs significantly from our results. The disagreement, in this specific case, can be explained by several factors; the different criteria used to define the bandgap. In Ref. [32], McCluskey *et al.* used the threshold

[4] This was the value commonly accepted at the time of publication of these works, as discussed in Section 1.6.1.

for the increase of the InGaN absorption which, as discussed in Section 5.1.3, is rather unclear. The reduced composition range ($0.05<x<0.11$) and the low number of data points (5) used. The major error is probably an over-correction for strain, for layers assumed to be pseudomorphic, when a partial relaxation occurred. This last factor lowers the estimated band gap in layers that are not coherent to GaN.

The pseudolinear behaviour of $E_g(x)$ that we have obtained here for InGaN is "anomalous", and quite distinct from a simple interpolation between the gap energies of the binary compounds [7]. It is clear that the decrease of the bandgap occurs at a faster rate with x than would be expected in that case. This work only considers $x \leq 0.25$, however if this trend is maintained, a value of ~1.9eV the previously accepted bandgap energy of pure InN, would be reached at $x\sim 0.42$. The interest of this extrapolation arises from the fact that an absorption edge below 1.89 eV was measured for thick $In_xGa_{1-x}N$ layers with $x \geq 0.4$ [34]. Moreover, intrinsic infrared emission from InGaN epilayers has also been observed (see Fig. 5.8), and reported in the literature [35].

These results provide an indication that the InN gap may be smaller than the widely accepted value. The explanation for this anomalous trend, and further observations of IR luminescence, came along with recent measurements in InGaN layers in the high InN content ($x>0.5$) range. In a recent work, Wu *et al*. [33] reported a systematic study on the optical properties of In-rich $In_xGa_{1-x}N$ (referred to as $In_{1-x}Ga_xN$) alloys. The investigation further reveals that the narrow fundamental band gap for InN is near 0.8 eV. Thus, the emission spectrum of the $In_{1-x}Ga_xN$ system extends to near-infrared. The $E_g(x)$ curve in the entire composition range could be fitted with a small bowing parameter of ~1.4 eV. This value of b is much smaller than previously reported bowing coefficients for which a band gap of ~1.9 eV for InN was used as the lower-energy end point, and is similar to that observed (1.3 eV) in the $Al_xGa_{1-x}N$ alloy system [36]. The $E_g(x)$ dependence obtained by Wu *et al*. is compared with our results in Fig. 7.2. A very good agreement is obtained.

The artificially large bowing parameters have been discussed in terms of a so-called "*large and composition dependent bowing parameter", b(x),* by the authors of Refs [17,32]. As we have pointed out, the experimental band gaps on the Ga-rich side can be better fit with a pseudolinear composition dependence (a direct consequence of a low bowing parameter), and the argument for introducing the concept of a $b(x)$ disappears when the InN band gap of ~0.8 eV is used. The results of Wu *et al*., obtained after the publication of our pseudolinear composition dependence on the Ga-rich side [**7**], provided conclusive evidence of small bowing in the InGaN system.

An additional significance of these results is that they also confirm the possibility of IR emission from InGaN alloys, as we previously reported [35]. The fundamental band gap of this ternary alloy system alone covers a wide spectral region ranging from near-infrared at ~1.6 μm to near-ultraviolet at ~0.36 μm. These findings are of extraordinary technological significance,

since it is demonstrated that it is possible to cover the visible IR spectral regions with the same material system.

Let us now turn our attention to another problem that arises when studying InGaN alloys, complicating the establishment of unambiguous relations between structural and optical properties; the possibility of a depth variation in the structural and optical properties. Therefore, the length-scale at which structural and optical characterization results are obtained is quite relevant. In the following sections, the issue of depth variation of structural and optical properties is tackled. The first case to be considered is the effect of a depth variation of composition on the luminescence of InGaN.

7.3 Samples with depth variations of composition

Structural characterization by RBS and XRD shows that in some samples composition varies strongly over depth, with x increasing towards the surface (Sections 4.7 and 6.7.2). The observation of this composition pulling effect was first reported by Hiramatsu *et al*. [37], in studies of the effect of lattice mismatch on In incorporation in MOVPE-grown InGaN. In that work, the growth of a series of samples with different thickness, under the same nominal growth conditions, has shown that the *average* In mole fraction increases for thicker (more relaxed) samples. This effect, resulting into a shift of the luminescence peak energy to the red, was found to be stronger with an increasing lattice mismatch with the underlying epitaxial layer used. However, no information about the luminescence features and indium distribution over depth *within* the InGaN layers was obtained in these studies.

In this section, we try to gain insight into these phenomena, and the effects of a composition depth variation on the optical properties are investigated. For this purpose, we probe the optical properties directly over depth, by using cathodoluminescence (CL) spectra acquired at different electron energies in a single InGaN layer. The basic principles of this technique were described in Section 5.4.

7.3.2 Results

The illustrative sample studied here (AEC53) was characterized in detail by RBS in Section 4.7. The thickness of the InGaN layer was determined to be 75±5 nm, and a strong compositional pulling effect with x varying from 0.14 near the GaN interface up to x~0.20 at the surface, was deduced from the RBS simulation. The best fit profile, $x(d)$, was given by: $x(d)=8\times10^{-3}(75-d)+0.14$, where d ($0<d<75$) is InGaN depth in nm.

It is important to note that for InGaN samples whose composition may change over depth, the CL collection geometry is important. If for instance a 45º (electron beam incidence-light

detection) setup had been used, self-absorption of emitted light would become an issue. In that case luminescence originating from regions of lower *x* would have to pass regions with higher *x,* being strongly attenuated before detection. This would favour the detection of the lower energy emission and would distort the sample emission spectra. In the geometry used here (right-angle), although self-absorption may also exist, no distortion of the CL signal is verified. Photons created at a certain depth of the sample do not travel through regions of different band gap before being collected [38].

Figure 7.3 shows the dependence on the electron beam energy of the InGaN luminescence. The whole CL spectra in the visible range containing the GaN related emission, and the MC simulations of energy deposition as a function of depth, were discussed in Section 5.4.3. In order to interpret the CL results it is important to know the electron energy deposition profile as a function of depth for different accelerating voltages. To perform an accurate simulation of the electron trajectories, the relevant geometrical (thickness) and physical parameters (composition and densities) of the different layers need to be known. All the required parameters are provided by previous XRD and RBS analysis. The results of MC simulations, presented in Section 5.4.3, are also shown in the inset to Figure 7.3.

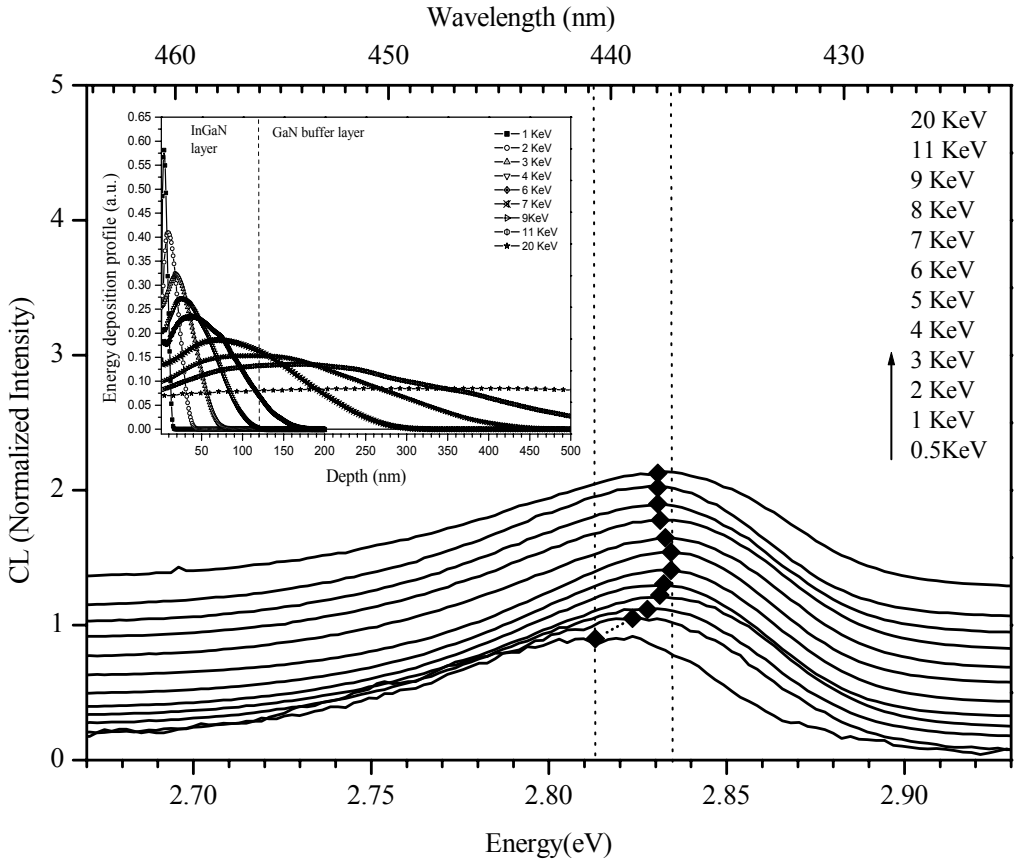

Figure 7.3: Low temperature cathodoluminescence spectra acquired at different electron beam energies (0.5-7 keV) from the InGaN/GaN/sapphire structure (AEC53) showing the InGaN related emission. The inset shows the electron beam energy deposition profile calculated using Monte-Carlo simulations of the electron trajectories for this layer.

As can be observed, in Fig. 7.3 the CL emission peak shifts to higher energies with increasing electron kinetic energy. However, this only occurs up to energies of ~7 keV. It can be noticed that the shift progressively decreases in magnitude until about 7 keV, and thereafter a small shift to lower energies is verified from ~7 to 9 keV. The CL spectral peak position remains practically unchanged for higher voltages.

7.3.3 Discussion

The shift of the CL peak position can be explained by the substantial compositional variation over depth, as measured by RBS. In principle, it could also be due to a continuous strain relaxation along the growth direction, since strain also affects the emission energy. However, this hypothesis is excluded by the analysis of the XRD reciprocal space map on the *(105)* reflection of this bilayer. The RSM shows only a minimal misalignment between GaN and InGaN diffraction peaks, indicating that the InGaN strain relaxation is very small.

Let us interpret the CL results in terms of the energy deposition profile. As it can be observed in the inset to Fig. 7.3, for electron energies from below 1 keV to about 7 keV, the region of maximal energy deposition (where most electron-hole pairs are created) progressively moves from the near surface region towards the InGaN/GaN interface. The point of optimum excitation produces the peak maximum in the set of CL spectra. Further electron energy increase tends to broaden the excitation profile within the InGaN layer. Therefore, at this stage the situation changes from one that favours the near interface region, to one where a more uniform excitation over depth is attained. As a result, a more evenly averaged contribution of the different depth regions to the CL spectrum is achieved, corresponding to a reversal of the shift around 8-9 keV. Once a uniform excitation over depth is reached for voltages over about 10 keV, an increase in the electron beam energy is not expected to result in any further shifts, as experimentally observed up to electron energies of 20 keV.

A simple calculation can be performed in order to interpret the results in a more quantitative way. If the electron energy deposition curves as a function of depth are multiplied by the compositional depth profile *x(d)* as given by RBS, the relative variation of the CL peak energy with the electron beam energy, can be reproduced, as shown in Figure 7.4.

Following this approach, the overall trend of the CL, and in particular the “turning point”, verified on the CL peak position at electron energies of about 7 keV, can be well reproduced. Note that this simple calculation is only valid due to the fact the PL emission energy depends linearly on the composition within the *x* range considered. Thus, the relative shift for different electron beam energies is linear with the In content. This simple calculation does not include a possible variation of the luminescence recombination efficiency with depth.

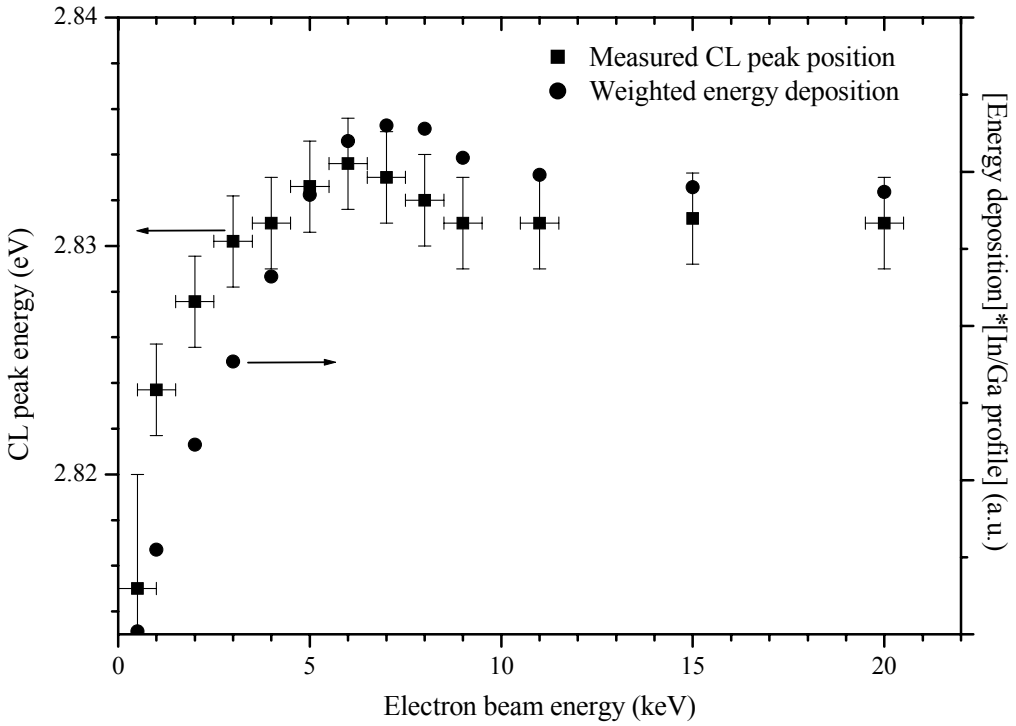

Figure 7.4: Shift of the CL peak energy compared to the product of energy deposition profile and the composition profile, plotted as a function of electron beam energy, for sample (AEC53).

The good agreement between calculated and experimentally measured CL behaviour confirms the consistency between the RBS and CL analysis and establishes directly the influence of a composition pulling in InGaN light emitting properties for the first time [38]. Let us now address the issue of In surface segregation and well/barrier intermixing effects in the case of MQWs.

7.4 MQWs with indium segregation to the surface and well/ barrier intermixing effects

In this section, the effects of well composition and the number of periods (total thickness) of the MQW structure on the optical properties are investigated. Three illustrative MQWs are considered: The 10-period MQW designated (STR94) was grown at 832°C and the growth periods for wells and barriers were respectively 90 and 270 s, chosen to give nominal thicknesses of 2.5 and 7.5 nm. The other two structures discussed STR121 and STR120, are grown at 760° C, and contained 18 and 8 wells, respectively. The barrier growth period was also 270 s, but for the well was 78 s. Growth periods for the GaN cap layers of STR94 and STR121 last 540 s. However, growth of STR120 cap was interrupted ~15 s after the 8th well, as described previously.

7.4.1 Results and discussion

Figure 7.5 compares the low temperature PL spectra of three MQW: STR94, STR120 and STR121. The inset to Fig. 7.5 shows the PL spectra of samples STR120 and STR121 on a logarithmic scale, to emphasise the large energy spread into the "tails" of the emission.

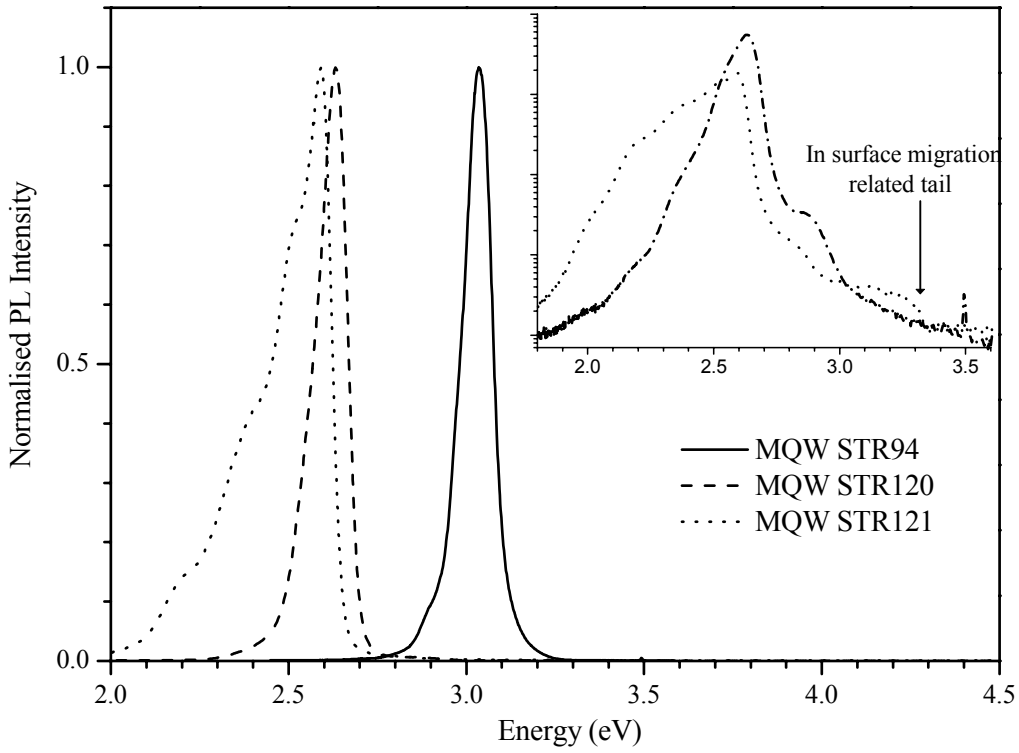

Figure 7.5: Normalised low temperature (14K) PL spectra for samples STR94, STR121 and STR120. The inset shows the unnormalised PL of samples STR121 and STR120 on a logarithmic scale.

The PL spectrum of sample STR94 is centred at ~3.05eV, blue shifted relative to the PL peak energy of samples STR120 and STR121 at around 2.6 eV. Despite the similar peak energies of MQWs STR120 and STR121, there is a clear degradation of the PL properties for the sample with a larger number of wells. While STR120 features a symmetric and narrow PL peak (FWHM~100 meV) STR121 has a broader (FWHM~170 meV) and lower intensity main peak, with a distinct high-energy tail.

The differences in the PL between the various samples can be promptly explained with reference to the structural analysis obtained by XRD, RBS and atomic force microscopy (AFM) results, discussed in Sections 4.9 and 6.9 and published in the literature [39-41].

In first place, the blue shift of the PL peak emission of sample STR94 is a consequence of a lower value of x in the well region (x~0.10) compared to an average mole fraction of (~0.20) in

samples STR120 and STR121. The *x* values are derived from RBS analysis in Sections 4.9 and 6.9.

Regarding samples STR120 and STR121 the similar PL peak energy confirms identical *average* composition in the well region for the two MQWs. However, despite a similar PL peak energy, it can be noted that the PL spectrum of STR121 is slightly shifted to the red (ΔE~50meV). We interpret this red shift as indication of a progressively higher average composition in the last wells closer to the surface. Despite similar growth conditions we suggest that there is also a compositional pulling effect in MQWs. Unfortunately, due to the absence of well/barrier modulation RBS spectra of sample STR121, no individual well composition can be extracted. Thus, in this work no direct evidence of this pulling effect in MQWs could be obtained.

Nevertheless, a recent study by Hao *et al.* [42] has extended our work on the composition pulling effects in InGaN/GaN single layers, which has discussed in the previous section, to InGaN/GaN MQWs. In Ref. [42], high-resolution X-ray diffraction studies reveal that the InN composition generally increases along the growth direction from the bottom to the top well.

Another difference noticed between PL spectra of STR121 and STR120, is the larger width of the emission from sample STR121 relative to STR120, which indicates a degradation of the MQWs optical quality with the number of wells. Note that, as discussed in detail in Section 6.9 and Refs [40,41], XRD, RBS and surface analysis, also indicate deterioration on the structural properties of the MQW with larger number of wells. In brief, detailed analysis of the last two samples shows that surface pitting and well/barrier intermixing is much more pronounced for sample STR121, where σ>5 nm. The sharper interfaces (σ~2.0 nm) and smother surface in sample STR120, result into a narrower emission, compared to STR121.

The distinctive high energy PL tail in STR121, observed in the inset to Fig. 7.5 starting at around 3.35eV, can also be explained with reference to the structural analysis results previously obtained. In Section 4.9, ultra-high depth resolution RBS measurements have show that in MQW STR121 In migration from the top well through the 17nm of the GaN cap layer occurs. This diffusion of In into the cap results into a compositionally graded InGaN alloy layer at the surface[5], instead of the nominally preset GaN cap. The tail noticed in STR121, reflects the progressive band gap $E_g(x)$ variation over depth, which results from the *x* depth variation.

The PL results in InGaN MQWs discussed here indicate a close relation between the PL properties and structural quality. They also confirm that the overall structural quality degradation is mainly determined by the total strain energy accumulated in the MQW stack, reinforcing the conclusions drawn in Section 6.9.

[5] In this particular case, the composition grading is from near surface to deeper regions of the cap layer. The source of In atoms is the well region, and therefore the InN content decreases as we approach the surface in the cap layer.

These results are an outstanding example of the potential of complementary structural and optical characterization. The optical properties of these MQWs could hardly be consistently interpreted without detailed knowledge on their structural properties.

7.5 Interpretation of the optical properties of InGaN layers with double PL peaks

Present day light emitting devices rely on InGaN/GaN quantum wells, where the active InGaN layers are under compressive stress due to the lattice mismatch to GaN. It is well known that the best structural, electric and optical properties of epitaxial films are achieved when the layers are thinner than the critical layer thickness (CLT) for strain relaxation. However, most research on InGaN entails unwarranted comparisons of ultrathin layers, as used in devices, with thick (say over 50 nm) layers that provide sufficient material for accurate compositional and structural analyses.

In fact, we may consider that perhaps the major obstacle to understanding optical properties of InGaN can be ascribed to issues of thickness dependence. For instance, strong segregation of In towards the surface of thick layers has been verified, and its effects on the optical properties investigated [38]. On the other hand, structural studies of thick layers frequently reveal double XRD peaks. The observation of multiple X-ray diffraction and photoluminescence peaks in an InGaN epilayer is widely regarded as an indicator of phase segregation, as already discussed [12-16].

In previous chapters, based on detailed characterisation results using RBS/channelling (Chapter 3), grazing incidence XRD (Chapter 4), and XRD reciprocal space mapping (Chapters 5 and 6) associated to interpretation models based on elastic theory, we have questioned this direct interpretation. Instead it has been demonstrated that layers grown above the CLT(x) feature a nearly discrete strain variation over depth explaining the occurrence of a double XRD peak [6]. This allowed a simple structural model of an InGaN layer grown above the CLT(x) to be proposed. As discussed in Section 5.8, essentially such films consist in two regions, a coherent planar layer region followed by a relaxed 3D region near the surface, as schematically depicted in Fig. 6.12 of Section 6.8.

The effects of this strain variation over depth on the optical properties of InGaN are still uncertain. As discussed in Section 7.1.2, it is expected that strain will influence the optical bandgap, and therefore the luminescence spectrum. Indeed, this effect was used qualitatively to estimate CLT of $In_xGa_{1-x}N$/GaN heterostructures by Parker *et al*. [43] A change in PL was used as the criterion to detect a strain relaxation as the $In_xGa_{1-x}N$ film thickness increased. Parker and co-workers could not measure the strain state of the samples by XRD, but noticed that the sample surface of thicker samples became 3D. This was interpreted as a secondary indication of strain relaxation.

In more recent work, Srinivasan *et al.* [10] and Moon *et al.* [9], have reported the appearance of double luminescence peaks under certain conditions, relating to layer composition or thickness, respectively. The appearance of a second lower energy peak in "thick" $In_xGa_{1-x}N$ layers has been invariably attributed to the presence of the "quantum dot-like In-rich" or "phase separated" regions. The reasoning behind these conclusions is quite similar to that used in the interpretation of double XRD peaks; a PL spectrum with two components implies the coexistence of two regions with different (well defined) compositions resembling spinodal phase decomposition in the alloy. The effects of strain are, within this analysis, once again neglected.

Therefore, it is important to investigate the effects that a strain relaxation in layers close to the CLT may have on the optical properties of $In_xGa_{1-x}N$. It is of fundamental importance to clarify under what conditions double luminescence peaks (DLPs) can be regarded as a signature of "quantum dot-like In-rich regions", or may just indicate strain relaxation of layers grown above the CLT. In the following sections, we critically address this issue.

We attempt to answer directly the following questions: Is there a clear relation between double XRD peaks and DLPs? Are double PL peaks in an InGaN an indicator of phase segregation? Under what conditions do DLPs appear? Is it possible to explain the energy separation between the two PL components?

7.5.1 Results: depth profiling of samples with double PL components

We have seen earlier that such samples show characteristic depth variations. It should be noted that samples which showed 2 XRD peaks also show 2 PL components. The representative sample examined to illustrate the optical properties is S101, a 120±10 nm thick wurtzite $In_{0.19}Ga_{0.81}N$/GaN bilayer, already well characterised structurally. The variation of strain with depth and the composition uniformity of this layer have been verified in Section 6.7.1 by XRD RSM using the elastic theory model proposed in Section 6.7, and by RBS.

Figure 7.6 presents the depth resolved CL spectra of this sample. The inset to Fig. 7.6 shows the depth scale of the electron beam penetration. The series of CL spectra show that an $In_{0.19}Ga_{0.81}N$ related emission peaked at ≈2.50 eV, is excited, even at the lowest electron energies. This spectral feature is unique for beam energies up to about 3 keV. However, at higher accelerating potentials, a second emission peak, centred at ≈2.67 eV, emerges. It is clear that this peak labelled as $In_{0.19}Ga_{0.81}N$(R), originates from near the surface region, while $In_{0.19}Ga_{0.81}N$(S) from a region closer to the GaN buffer. Note also that the luminescence peak $In_{0.19}Ga_{0.81}N$ (R) is broader and its intensity is lower compared to $In_{0.19}Ga_{0.81}N$(S) when the whole layer is almost uniformly excited over depth at the highest beam energy.

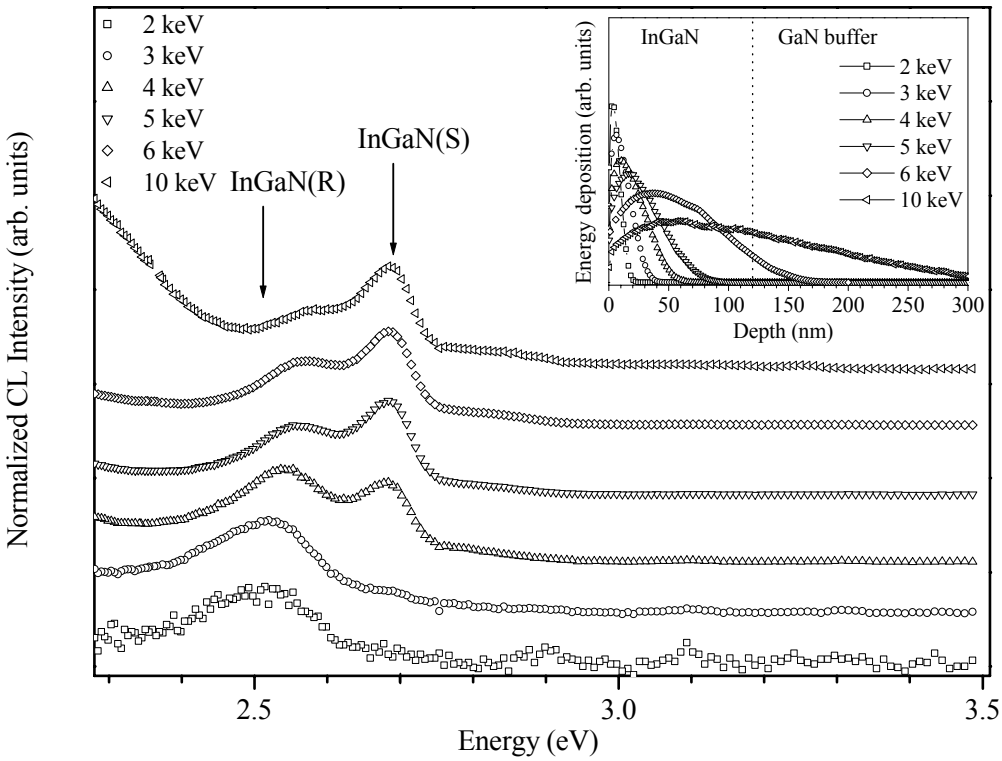

Figure 7.6: CL spectra acquired at different electron beam energies (2-10 keV) from the $In_{0.19}Ga_{0.81}N$/GaN structure (S101) at 25 K. The spectra were normalised and vertically displaced for clarity. The inset shows the Monte-Carlo simulations for electron beam energy deposition in this structure.

7.5.2 Discussion and literature overview

The explanation proposed for these observations is that the relaxed region, grown above the CLT, is the origin of the lower energy component, whereas the coherent region near the GaN interface contributes the higher energy peak.

This interpretation, based on structural knowledge of these samples, is entirety consistent with the relative energy position of the two peaks. Compressive strain shifts the band gap to higher energies, and therefore the relaxed region near the surface originates the lower energy peak, whereas the PL component at higher energy arises from the strained region deeper in the layer.

In addition, the relaxed region near the surface is found to be of worse crystalline quality. In fact, a broader diffraction profile in the XRD RSM (see Fig. 6.8) and higher values of χ_{min} in RBS/channelling analysis confirm the expected anti-correlation between crystalline quality and relaxation in an epitaxial film. This accounts for the lower luminescence efficiency of the relaxed region and the broader PL peak of $In_{0.19}Ga_{0.81}N$(R).

The surface morphology of InGaN films featuring double PL peaks was also investigated by SEM and AFM. As discussed in Section 6.8, films thicker than CLT(x), show a mixture of 2D and 3D growth, characterised by a large surface roughness and a microcrystalline texture, in good agreement with the results of Parker *et al*. [43]. A correlation between the 3D surface, with its pronounced islanding, and the spotty appearance of the confocal microscopy/spectroscopy images, is also suggested. As shown in Fig. 5.13, bright areas in the confocal reflectance image, seem to originate in the lower energy component of the micro PL. It can be speculated that these brighter regions may correspond to the tips of the 3D islands clearly observed by SEM and AFM surface micrographs of relaxed samples, as shown in Section 6.8. There is, at least so far, no *direct* evidence of such association. But it does seem rather likely via comparison of AFM and confocal images of the same region.

We should now use our analysis to discuss some results recently published in the literature. Moon *et al.* [9] studied the optical properties of a 100 nm and a 30 nm thick $In_{0.12}Ga_{0.88}N$/GaN layers and found that;

1) The 30nm thick layer had a single PL component, whereas the 100nm thick film showed an additional second lower energy component.

2) The second lower energy luminescence, in the thicker sample, was found to disappear when a thickness of ~70 nm was etched from the surface, reducing the 10 nm layer to ~30 nm close to the GaN interface.

3) The authors observed the so-called S-shaped temperature dependence of the PL peak energy, with the higher energy component showing stronger temperature dependence.

These findings were interpreted as indicating an origin of the lower luminescence in In-rich regions QD-like regions near the surface. The weaker temperature dependence of the lower energy peak was explained by increased carrier localization in such In-rich regions.

In another recent work, published by Srinivasan *et al.* [10], the CL spectra of ~100 nm thick $In_xGa_{1-x}N$ ($0.03<x<0.17$) layers was studied. Here, the parameter varied was the composition. A second emission band, at lower energies, was also observed to appear for $x \geq 0.08$. The energy separation between the two components was found to increase with increasing x. Again, the explanation advanced was the presence of In-rich regions, near defects.

Clearly, our results suggest a different explanation for both sets of observations. Most of the results can be accounted for with reference to the CLT(x) curve calculated in Section 6.6. Thus, the disposition of the samples discussed here, relative to the CLT(x) curve is shown in Figure 7.7.

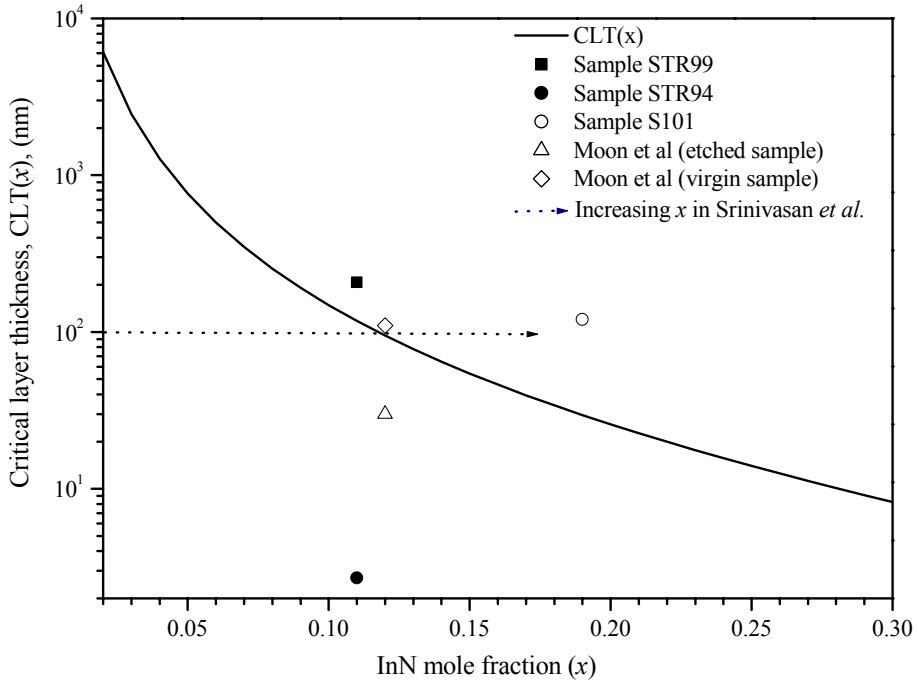

Figure 7.7: Plot of the critical layer thickness, CLT(x), for strain relaxation as a function of InN mole fraction, and the location of selected samples relative to this curve. The arrows indicate the physical parameter which is changing in the works of Moon *et al*. [11] and Srinivasan *et al*. [10] and explain the transition from the case where only one PL peak is observed, to that where DLP are observed.

The results in Ref. 11 can be directly accounted for by a strain relaxation above the CLT. Films thicker than the CLT (~90 nm for x=0.12) are expected to feature a double PL peak. If the top part of the sample is etched, the relaxed part is removed, and only the peak originating from the coherent region near the interface remains. Moon *et al*. also remark that the surface roughens is much larger for the 100 nm (also a sign of strain relaxation) film compared to the 30 nm thick layer. In addition, the same authors also reported the occurrence of double XRD peaks for thick $In_xGa_{1-x}N$ layers in a previous work [11].

For the samples of Ref. [10] the CLT is varying rapidly via the different compositions in the ~100nm thick films. While 100nm is below the CLT(x) for layers with x<0.08, it is more than the CLT(x) estimated for compositions larger than x=0.12, as illustrated in Fig. 7.7. Therefore, it is also strongly suggested that the second lower energy luminescence peak appears at higher x due to strain relaxation. The observation that the energy separation between the two components increases with the InN content supports our proposed explanation. The magnitude of the strain variation between coherent and relaxed components increases systematically with x, as will be discussed in the next section.

In order to further confirm the model proposed to interpret the results, two samples were grown under identical nominal conditions; one below (STR94) and another above (STR99) the CLT(x)

for the targeted composition, x=0.105. The (x,t) coordinates of the two samples, relative to CLT(x), is also shown in Fig. 7.7.

The low temperature PL spectra of the two samples are shown in Fig. 7.8.

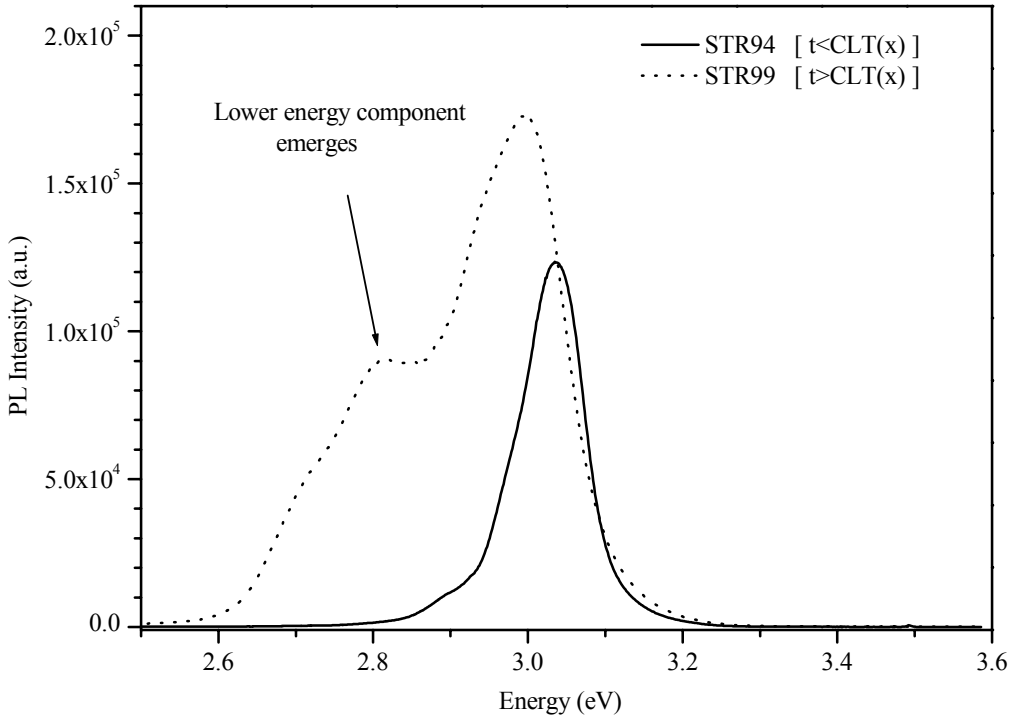

Figure 7.8: Low temperature (14K) PL spectra of samples STR99 and STR94.

The interpretation of Fig 7.8 follows from what has been previously discussed, with the support of Fig 7.7.

7.5.3 Temperature dependences of PL spectra of samples with DLPs

Let us briefly comment on the PL temperature dependence of samples with DLPs. The PL spectra at various temperatures ranging from 14 to 275K of sample STR99 is shown in Fig. 5.9. The behaviour is quite typical of samples featuring DLPs: the low energy component suffers less quenching with T and dominates the PL at RT, whereas the higher energy peak dominates at low T but rapidly disappears with increasing temperature.

This relative trend of the two components agrees with the behaviour observed by Moon *et al*. However, taking into account the different explanation for origin of the second PL component advanced in this work, a different physical explanation for the weaker T behaviour is also suggested.

It is proposed that the origin of the potential minima, responsible for stronger exciton localisation, are not In-rich QD-like regions, but strain relaxed regions, possibly strain relaxed

3D islands at the surface. These strain relaxed regions near the surface explain the increase of surface roughness verified in all samples studied here, and in the works by Moon *et al*. and Srinivasan *et al*., and the granular appearance of the TEM micrographs in Ref. [9]
The unusual S-shape behaviour reported in the literature [44-50] can also be explained within the terms of this conjecture. We suggest that the relative intensity variation of two (usually unresolved) components gives raise to this anomalous behaviour. The peak energy is determined by the maximum of the sum of the two PL components, rather than reflecting the semiconductor bandgap. A systematic analysis of the temperature dependence of each of the resolved PL components to study the anomalous temperature behaviour in InGaN alloys is still missing.

Considering that the questions "*are double PL peaks in an InGaN an indicator of phase segregation?*" and "*under which conditions do DLPs occur?*" have been answered, let us now turn our attention to the energy separation between the two PL components. In the next section a simple theoretical model to account for the magnitude of the energy separation is proposed

7.5.4 Effect of strain in the PL peak energies

Given the importance of this issue, and the confusion caused by a misinterpretation of DLPs in the literature, it is convenient to provide an integrated view of the several results obtained by different authors [10,11,23,51,52].
An additional and decisive argument that this is a *general behaviour* of InGaN/GaN heterostructures, and that DLPs in such films are indeed due to a discontinuous strain relaxation, is provided by the existence of a characteristic energy correlation between the two PL components. In Fig. 7.9 we plot the peak energies of DLPs, some observed in this work and some obtained from the literature, against that of the higher energy component.
The trend of the data is striking. As expected from a strain-induced origin for the peak separation, the energy difference between the two components appears to vanish at an emission energy close to that of GaN. Obviously, the magnitude of strain variation between coherent and relaxed components decreases with x, and any strain-induced shift should therefore disappear as x (i.e, the lattice mismatch between $In_xGa_{1-x}N$ and GaN) tends to zero.
The absence of experimental points above a certain energy (E ~3.1 eV) in Fig. 7.9 is also explained by our interpretation model. As indicated by Fig. 7.7 the layer thickness required to observe strain relaxation would have to be very large (~1μm)[6] for a composition of ~0.05,

[6] InGaN films studied here, and in the literature, are typically from 2 to about 500 nm thick. Therefore, we can not observe strain relaxation in the low composition range, say for x<0.05 since the CLT is much larger than the thickness of the layers typically available.

corresponding to a PL peak energy of about 3.2eV. Such samples are very scarce. In addition, with decreasing separation of components, in obviously becomes more difficult to spectrally resolve them.

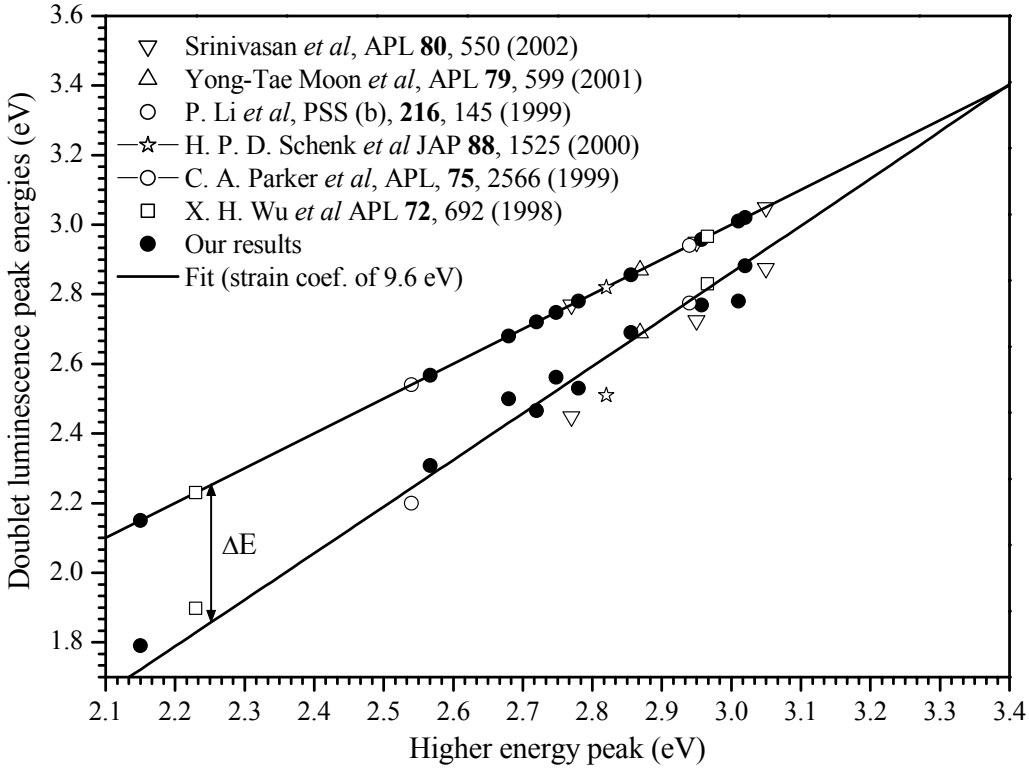

Figure 7.9: Energy positions of the DLP as a function of the higher energy "main" peak.

In fact, it is possible to model the energy separation between the two components and estimate the bandgap strain coefficient for $In_xGa_{1-x}N$ (x<0.25). In the following, we propose a novel route to estimate the strain coefficient in InGaN by modelling the strain related splitting in the PL peak energy. The method is quite general and could be used in any semiconductor alloy.

7.5.5 A method to extract the InGaN bandgap strain coefficient from DLPs

In the following, a procedure to estimate the bandgap strain deformation potential in InGaN is presented and a set of simple relations between key physical parameters in InGaN is given.
The method to calculate the bandgap strain coefficient from Fig. 7.9 takes the following sequence of steps:

$$E_{PL} \rightarrow x \rightarrow \Delta\varepsilon_{xx} \text{ and } \Delta E_{PL} \rightarrow \Delta E_g \rightarrow coef._{xx} * \Delta\varepsilon_{xx}$$

First, to make it possible to compare different data points from literature, we rely on the relation between PL peak energy and x for relaxed InGaN, which is now fairly well established [53]. Following this approach, one can avoid miss-estimations due to different methods and

approximations used to obtain x in the reported values, and can use results even if the composition is not reported in the cited works.

Hence, from the PL peak energy position of the lowest energy component, the composition is obtained using the relation established by Martin *et al.* in Ref. [53]:

$$E_{PL} = 3.398 - 3.91 \cdot x \text{ eV} \qquad \text{(Eq. 7.11)}$$
$$E_{PL} \rightarrow x$$

Knowing x, one can estimate the variation between extreme states of strain corresponding to fully coherent and fully relaxed layer regions. The maximum strain variation, $\Delta\varepsilon_{xx}$, is therefore given by:

$$\Delta\varepsilon_{xx} \cong (a_0^{InGaN} - a^{GaN}) / a_0^{InGaN} \qquad \text{(Eq. 7.12)}$$
$$x \rightarrow \Delta\varepsilon_{xx}$$

where a_0^{InGaN} is the relaxed InGaN lattice constant as given by Vegard's law.

The fact that the origin of the DLPs is an extreme variation of strain states, from fully coherent to fully relaxed, is supported by the detailed structural information extracted from HRXRD RSM, discussed in Chapter 6. As shown in sections 6.7.1 and 6.8, the XRD analysis evidences that these samples basically comprise a fully relaxed region near the surface (3D growth) and a fully coherent region close to the InGaN/GaN interface. This approximation represents the upper limit of strain variation, for a given x.

Note that in Fig. 7.9 we are considering the PL peak energies, E_{PL}, and not the bandgap energies E_g. Therefore the PL measured values should be corrected taking into account the magnitude of the Stokes' shift. As discussed in Chapter 5 the Stokes' shift is also a function of E_{PL}, and the relation between PL peak energy and E_g was established by O'Donnell *et al.* [54], and is given by:

$$E_p = 1.453(26) E_g - 1.54(8) \qquad \text{(Eq. 7.13)}$$
$$\Delta E_{PL} \rightarrow \Delta Eg$$

The difference in strain between the two regions coexisting in the layer causes a variation on the bandgap which, as discussed in Section 7.1.2, is proportional to $\Delta\varepsilon_{xx}$, so that:

$$\Delta E_g = coef._{xx} * \Delta\varepsilon_{xx} \qquad \text{(Eq. 7.14)}$$
$$\Delta E_g \rightarrow coef._{xx} * \Delta\varepsilon_{xx}$$

we may set the $coef_{xx}$. in Eq. 7.14 as the only fitting parameter, and let it vary so that it describes the experimental data of Fig. 7.8. Note that Eq. 7.14 is of the same form as Eq. 7.4. Thus, the fitting parameter $coef._{xx}$, is the bandgap strain coefficient as defined in Section 7.1.2, i.e. $coef_{xx}$= $const_{xx}$. Finally, from the best fit to data in Fig. 7.8 a value of $coef._{xx}$=-9.6±0.4 eV is obtained. This estimation is only possible by assuming that the strain coefficient is constant within the composition range considered.

To our knowledge this is the first experimental determination of the deformation potential of a semiconductor alloy. Presently there are no theoretical estimations of deformation potentials for InGaN because of the complexity of its electronic structure. Therefore, at the present stage of knowledge, no direct comparison with theory is possible.

Nevertheless, as discussed in Section 7.1.2, in the case of GaN the variation of excitonic transition energies was measured as a function of in-plane strain (ε_{xx}) by Shan *et al.* [19]. From the data in Ref. [19] a $const._{xx}^{GaN} = -9.3\ eV$ can be determined from a linear least square fitting to the GaN A-exciton dependence on ε_{xx}. Taking into account the fact that we are limiting our analysis to the small x range (x<0.3), it would be expected that the strain coefficient of $In_xGa_{1-x}N$ is not much different from that of GaN, as it is verified. Given the similarity of GaN and InGaN strain coefficients, the procedure taken in section 7.2 to correct the bandgap for strain, using the GaN strain coefficient, seems to be justified.

In conclusion, regarding the somewhat contentious issue of InGaN films showing DLPs, our results show clearly that this feature can be interpreted with reference to a DSR over depth. However, it is important to underline that this does not imply that *all* double luminescence peaks can be assumed to be due to strain relaxation. Certainly, in principle, many other physical reasons can lead to a multi-peak luminescence structure. However, the results presented here help to demarcate the thickness-composition range where the strain relaxation effects can not be neglected. Together with considerations of the energy separation between peaks, it should be easy to ascertain whether the observed spectral features can (or can not) be explained by a strain relaxation above the CLT.

These results are another instructive example of how the advances in the understanding of InGaN basic physical properties require a combined approach, using structural and optical characterization results for their solution.

7.6 Summary

In summary, in this chapter we have attempted to establish correlations between optical and structural properties of InGaN/GaN heterostructures. The importance of knowing the samples structural properties in order to correctly interpret the optical features was emphasized.

The method used in this work to establish $E_g(x)$, was presented; RBS is used to obtain x, independently from the state of strain in the samples. The optical bandgaps in InGaN are measured by OA spectroscopy using the sigmoidal fit to extract the bandgap from the absorption curves. Subsequently, using the perpendicular lattice constant measured by XRD, the measure bandgap of InGaN is corrected, that is, used to calculate the relaxed bandgap.

Following this approach, a linear relation between bandgap energy and InN content, was experimentally established: $E_g(x)=3.39-3.57x$ ($x\leq 0.25$). Our results were compared with other works from the literature, and the various possible reasons for the cases where disagreement is observed, are discussed. We commented on the dispersion of bandgap bowing parameters reported in the literature. In particular, our results were found to be entirely consistent with the trend observed for InGaN alloys in the high InN composition range, which were not previously available due to the difficulties to grow high InN content films.

The $E_g(x)$ relation established showing a fast decrease of E_g with composition, and the observation of IR luminescence, could be understood by considering the results presented by Wu *et al.* in Ref. [33] regarding the InN band gap. Wu *et al.* determined a band gap energy of ~0.7eV, whereas the previously accepted value was ~1.9eV. These findings explained the unusually large bowing parameters required to describe the bandgap behaviour with composition, and left behind the idea of "composition dependent" bowing parameter proposed by some theorists.

In single layers that show a composition pulling effect, one could depth profile the optical properties by using CL spectroscopy with variable electron beam energy. The CL spectra has shown a red shift as the electron beam penetrated deeper into the layer, showing the influence of In surface segregation on the optical properties. The trend observed could be well reproduced by combining the RBS profile of x, and the Monte–Carlo simulations of the electron beam depth profile.

A set of three InGaN/GaN MQW samples, well characterised by XRD, AFM and RBS analyses, were examined by PL spectroscopy. The MQW with lower x is found to have a PL emission blue shifted (~3.05eV) relatively to the other two MQWs (~2.5-2.6eV). In addition, when comparing two MQWs grown under the same nominal conditions, but with a different number of wells, it is found that the PL emission of the thicker MQW is slightly red-shifted and broader. These observations were interpreted as result of a compositional pulling effect that leads to

higher In incorporation in the later wells, and an overall deterioration of the MQW quality with an increasing strain energy for thicker MQW stacks.

The case of InGaN epilayers with double PL components was also studied in detail. The two components of the sample's luminescence could be discriminated for the first time by depth-resolving cathodoluminescence spectroscopy. The lower energy peak was shown to originate from the near surface region, whereas the high energy component is found to emerge from the deeper sample regions closer to the InGaN/GaN interface.

The physical conditions for the appearance of DLPs are directly connected to the concept of critical layer thickness (CLT). Both composition and layer thickness must be considered to locate the samples in the (x,t) phase space. If t>CLT(x), is likely that DLP will appear. The appearance of a DLP in InGaN layer can be either reached by keeping the thickness constant and increasing the composition as in Ref. [10], or for the same x in the films, by increasing the thickness as reported in Ref. [9]. The PL of two samples specifically grown under the same nominal conditions, above and below the CLT, features two and one luminescence components, respectively. This reinforced the validity of the simple interpretation model proposed.

Based on the overall trend of the energy position of high and low energy components of the DLPs, found in this work, it was shown that high and low energy components converge to the GaN bandgap at around 3.4eV, as x tends to zero. By modelling the energy separation of the two components, we have establish a method to estimate the strain deformation potential in semiconductor alloys. It is found that for the low composition range (x<0.3) the bandgap parallel strain coefficient for InGaN ($const._{xx}$= -9.6±0.4 eV) is quite similar to that obtained for GaN ($const._{xx}^{GaN}$ = -9.3 eV), as might be expected.

The solution for the issue of InGaN/GaN samples featuring double luminescence peaks, is perhaps the most impressive example where the correlation between structural and optical characterization is shown to be crucial to understand the Physics of this fascinating semiconductor alloy.

7.7 References:

[1] S. Nakamura and G. Fasol, *The blue laser diode*, Springer, Berlin (1997).

[2] B. Gil, ed. *"Group III nitride semiconductor compounds, physics and applications".* Series on Semiconductor Science and Technology 6*,* Oxford Science Publications, Oxford (1998).

[3] A. F. Wright, K. Leung, and M. van Schilfgaarde, Appl. Phys. Lett. **78**, 189 (2001)

[4] K. P. O'Donnell, S. Pereira R. W. Martin, P. R. Edwards, M. J. Tobin and J. F. W. Mosselmans Phys. Stat. Sol. (a) **195**, 532 (2003).

[5] K. P. O'Donnell, R. W. Martin, and S. Pereira, Appl. Phys. Lett. **81**, 1353 (2002).

[6] S. Pereira M. R. Correia, E. Pereira C. Trager-Cowan, F. Sweeney and K. P. O'Donnell A. Sequeira, E. Alves, N. Franco, Appl. Phys. Lett. **81**, 1207 (2002).

[7] S. Pereira, M. R. Correia, T. Monteiro, E. Pereira, E. Alves, A. D. Sequeira, N. Franco,Appl. Phys. Lett. **78**, 2137 (2001).

[8] N. A. El-Masry, E. L. Piner, S. X. Liu and S. M. Bedair, Appl. Phys. Lett. **72**, 40 (1998).

[9] Yong-Tae Moon, Dong-Joon Kim, Jin-Sub Park, Jeong-Tak Oh, Ji-Myon Lee, Young-Woo Ok, Hyunsoo Kim, and Seong-Ju Park, Appl. Phys. Lett. **79**, 599 (2001).

[10] S. Srinavasan, F. Bertram, A. Bell, F. A. Ponce, S. Tanaka, H. Omiya, and Y. Nakagawa, Appl. Phys. Lett. **80**, 550 (2002).

[11] Yong-Tae Moon, Dong-Joon Kim, Keun-Man Song, In-Hwan Lee, Min-Su Yi, Do-Young Noh, Chel-Jong Choi, Tae-Yeon Seong, and Seong-Ju Park*,* Phys. Stat. Sol. (b) **216**, 167 (1999).

[12] S. Pereira, M.R. Correia, E. Pereira, K.P. O'Donnell, R.W. Martin, M.E. White, E. Alves, A. D. Sequeira and N. Franco, Mat. Sci. Eng. B **93**, 163 (2002).

[13] S. Pereira M. R. Correia, E. Pereira K. P. O'Donnell E. Alves, A. D. Sequeira, and N. Franco, Appl. Phys. Lett. **79**, 1432 (2001).

[14] S. Pereira, M. R. Correia, E. Pereira, K. P. O'Donnell, E. Alves, A. D. Sequeira, N. Franco, I. M. Watson and C. Deatcher, Appl. Phys. Lett. **80**, 3913, (2002).

[15] S. Pereira, M. R. Correia, E. Pereira, K. P. O'Donnell, E. Alves, A D. Sequeira, N. Franco, Appl. Phys. Lett. **80** (2), 337 (2002).

[16] S. Pereira, M. R. Correia, E. Pereira, K. P. O'Donnell, E. Alves, A. D. Sequeira, N. Franco, I. M. Watson, C. J. Deatcher **81**, 3500 (2002).

[17] C. G. Van de Walle, M. D. McCluskey, C. P. Master, L. T. Romano and N. M. Johnson, Mater. Sci. Eng. B **59** 274 (1999).

[18] A. Shikanai, T. Azuhata, T. Sota, S. Chichibu, A. Kuramata, K. Horino and S. Nakamura, J. Appl. Phys. **81**, 417 (1997).

[19] W. Shan, R. J. Hauenstein, A. J. Fischer, J. J. Song, W. G. Perry, M. D. Bremser, and R. F. Davis, and B. Goldenberg, Phys. Rev. B **54** 13460 (1996).

[20] R. Dingle and M. Ilegeme, Solid state commun. **9**, 175 (1971)

[21] L. T. Romano, B. S. Krusor, M. D. McCluskey and D. P. Bour, K. Nauka, Appl. Phys. Lett. 73, 1757 (1998).

[22] C. Wetzel, T. Takeuchi, S. Yamaguchi, H. Katoh, H. Amano and I. Akasaki, Appl. Phys. Lett. **73**, 1994 (1998).

[23] C. A. Parker, J. C. Roberts S. M. Bedair, M. J. Reed, S. X. Liu, N. A. El-Masry and L. H. Robins, Appl. Phys. Lett. **75**, 2566 (1999).

[24] F. B. Naranjo, M. A. Sanchez-Garcia, F. Calle, E. Calleja, B. Jenichen, and K. H. Ploog, Appl. Phys. Lett. **80**, 231 (2002)

[25] S. F. Chichibu, M. Sugiyama, T. Kuroda, A. Tackeuchi, T. Kitamura, H. Nakanishi, T. Sota, S. P. DenBaars, S. Nakamura, Y. Ishida, and H. Okumura, Appl. Phys. Lett. **79**, 3600 (2001)

[26] L. Bellaiche, T. Mattila, L.-W. Wang, S.-H. Wei, and A. Zunger, Appl. Phys. Lett. **74**, 1842 (1999)

[27] M. Ferhat, J. Furthmuller, and F. Bechstedt, Appl. Phys. Lett. **80**, 1394 (2002

[28] R. W. Martin, P. G. Middleton, K. P. O'Donnell, and W. Van der Stricht, Appl. Phys. Lett., **74**, 263 (1999).

[29] K. P. O'Donnell, R. W. Martin, and P. G. Middleton, Phys. Rev. Lett. **82**, 237 (1999).

[30] H. P. D. Schenk, P. de Mierry, M. Laugt, F. Omnes, M. Leroux, B. Beaumont, and P. Gibart, Appl. Phys. Lett. **75**, 2587 (1999).

[31] W. Shan, W. Walukiewicz, E. E. Haller, B. D. Little, J. J. Song, M. D. McCluskey, N. M. Johnson, Z. C. Feng, M. Schurman and R. A. Stall, J. Appl. Phys. **84**, 4452 (1998).

[32] M. D. McCluskey, C. G. Van de Wall, C. P. Master, L. T. Romano and N. M. Jonhson, Appl. Phys. Lett. **72**, 2725 (1998).

[33] J. Wu, W. Walukiewicz, K. M. Yu, J. W. Ager III, E. E. Hailer, H. Lu, and W. J. Schaff, Appl. Phys. Lett. **80**, 4741 (2002).

[34] L. H. Robins, A. J. Paul, C. A. Parker, J. C. Roberts, S. M. Bedair, E. L. Piner, N. A. El-Masry, MRS Internet. J. Nitride Semicond. Res. **4S1**, G3.22 (1999).

[35]K. P. O'Donnell, R. W. Martin, S. Pereira, A. Bangura, M. E. White, W. Van der Stricht and K. Jacobs, Phys. Stat. Sol. B **216**, 141 (1999).

[36] W. Shan, J. W. Ager III, K. M. Yu, W. Walukiewicz, E. E. Haller, M. C. Martin, W. R. McKinney, and W. Yang, J. Appl. Phys. **85**, 8505 (1999).

[37] K. Hiramatsu *et al*, MRS Internet J. Nitride Semicond. Res., **2** 6 (1997).

[38] S. Pereira, M. R. Correia, E. Pereira E. Alves C. Trager-Cowan and K. P. O'Donnell Phys. Rev. B **64**, 205311 (2001).

[39] Ian C. J. Deatcher, C. Liu, S. Pereira, M. Lada, A. G. Cullis, O. Brandt and I. M.Watson, Semicond. Sci. Technol. **18**, 212 (2003).

[40] S. Pereira, E. Pereira, E. Alves, N. P. Barradas, K. P. O'Donnell, C. Liu, C. J. Deatcher and I. M. Watson, Appl. Phys. Lett. **81**, 2950 (2002*)*.

[41] S. Pereira, M. R. Correia, E. Pereira, K. P. O'Donnell, E. Alves, N. P. Barradas, A. D. Sequeira, N. Franco, I. M. Watson, and C. Liu, Phys. Stat. Solidi (c) **0**, 302, (2002).

[42] M. Hao, H. Ishikawa, T. Egawa, C. L. Shao, and T. Jimbo, Appl. Phys. Lett. **82**, 4702 (2003).

[43 C. A. Parker, J. C. Bedair, S. M. Bedair, M. J. Reed, S. X. Liu, and N. A. El-Masry, Appl. Phys. Lett. **75**, 2776 (1999).

[44] K. L. Teo, J. S. Colton, P. Y. Yu, E. R. Weber, M. F. Li, W. Liu, K. Uchida, H. Tokunaga, N. Akutsu, and K. Matsumoto, Appl. Phys. Lett. **73**, 1697 (1998)

[45] Petr G. Eliseev, Piotr Perlin, Jinhyun Lee, and Marek Osinski, Appl. Phys. Lett. **71**, 569 (1997)

[46] Yong-Hoon Cho, G. H. Gainer, A. J. Fischer, J. J. Song, S. Keller, U. K. Mishra, and S. P. DenBaars, Appl. Phys. Lett. **73**, 1370 (1998)

[47] K. S. Ramaiah, Y. K. Su, S. J. Chang, C. H. Chen, F. S. Juang, H. P. Liu, and I. G. Chen, Appl. Phys. Lett. **85**, 401 (2004)

[48] K. S. Ramaiah, Y. K. Su, S. J. Chang, B. Kerr, H. P. Liu, and I. G. Chen, Appl. Phys. Lett. **84**, 3307 (2004)

[49] F. B. Naranjo, M. A. Sanchez-Garcia, F. Calle, E. Calleja, B. Jenichen, and K. H. Ploog, Appl. Phys. Lett. **80**, 231 (2002)

[50] Yong-Hoon Cho, G. H. Gainer, A. J. Fischer, J. J. Song, S. Keller, U. K. Mishra, and S. P. DenBaars, Appl. Phys. Lett. **73**, 1370 (1998)

[51] P. Li, S.J. Chua, G. Li, W. Wang, X.C. Wang, Y.P. Guo, Phys. Stat. Sol. (b), **216**, 145 (1999).

[52] X. H. Wu, C. R. Elsass, A. Abare, M. Mack, S. Keller, P. M. Petroff, S. P. DenBaars, J. S. Speck, and S. J. Rosner, Appl. Phys. Lett. **72**, 692 (1998).

[53] R. W. Martin P. R. Edwards, K. P.O'Donnell, E.G. Mackay, and I.M. Watson, Phys. Stat. Sol. (a) **192**, 117 (2002).

[54] K. P. O'Donnell, R. W. Martin, C. Trager-Cowan, M. E. White, K. Esona, C. Deatcher, P. G. Middleton, K. Jacobs, W. Van der Stricht, C. Merlet et al. Mat. Sci. Eng. B, **82**, 194 (2001).

Chapter 8: Conclusions and suggestions for future work

Overview

In this chapter we review the work carried out and highlight the main conclusions of this thesis. Some suggestions concerning the direction of possible future work on InGaN, and extension of analysis methods developed under the context of this thesis for other material systems are given.

8.1 General review and conclusions

The spectacular breakthroughs obtained in the last years in InGaN research have allowed the compactness, high efficiency and reliability of solid-state-based light emitting technology to be extended to shorter wavelengths. InGaN-based high brightness visible LED's emitting in the three primary colours are now commercially available, a development which has transformed the market of LED-based full colour displays and opened the way to applications such as in traffic lights, car brake lights, efficient low voltage flat panel white light sources and general lightning systems amongst others. In addition, UV and blue LDs with lifetimes over 10000 hours have been demonstrated and commercialized. This has originated a great interest for high density optical storage systems, high resolution printing systems, UV lithography and projection displays.

However, these fast technologic developments were, in great extent, achieved through a semi-empirical approach. InGaN was, from a fundamental point of view, a poorly understood material. The advances in this rather peculiar semiconductor material system have been limited by approaches where the correlation between nanostructure and optical properties were not duly taken into account. This situation represented an obstacle for fundamental understanding and further technological improvements.

In this thesis we have tried to provide an alternative approach and attempted to overcome this situation. The aim of this work was to obtain an insight on the structural and optical properties of InGaN heterostructures through a systematic and multidisciplinary characterization. In this way our purpose was to help to fill the gap between basic scientific knowledge and technological applications in this area. The approach taken in this contribution was to combine several complementary structural and optical characterization techniques and bring together detailed information on InGaN nanostructure and optical properties.

Specifically we have combined:

1) Controlled growth with specific features in an attempt to isolate the influence of structural parameters, such as thickness and composition.

2) Detailed nano-structural characterization by a suitable selection of techniques including; SEM, AFM, XRD and RBS.

3) Optical characterisation at complementary length scales by: OA, PL, and CL spectroscopy and confocal microscopy/spectroscopy in selected samples based on the structural characterization results.

Finally, we have proposed interpretation models to describe the structural and optical features and, whenever possible, established the correlation between both. Following this methodology, we have addressed the key open questions regarding InGaN basic material science presented in Chapter 1, whose clarification was the remit of this work.

The material presented in this thesis was divided into eight chapters. The first five chapters provided the necessary background and presented the results obtained by the various experimental techniques, while in Chapters 6 and 7 we brought together, integrated and developed interpretation models to account for the results obtained.
In Chapter 1 the context, motivation and the scope of this PhD work were presented. The technological importance of the development of efficient solid state light emitting devices covering the visible spectral region was pointed out as the strongest driving force to investigate InGaN. The fundamental physical properties that make it an ideal semiconductor for light emitting devices in the visible region, and some of the open questions regarding basic material science, were highlighted. Finally, the objectives and the general layout of this thesis were specified.
In Chapter 2, the basic principles of the techniques used to grow InGaN/GaN heterostructures, with particular emphasis on MOVCD growth, were presented. Some of the difficulties in growing high quality InGaN/GaN heterostructures were discussed. Namely, the issues of lattice mismatch between the sapphire substrate and the GaN layer and the consequent 3D growth, were described. Furthermore, it was shown that difficulties in the growth process may lead to an undesired rough surface morphology, In droplet formation, and heterogeneous growth rates and In incorporation. The usefulness of the *in situ* optical reflectivity technique to monitor the films growth process was demonstrated.

In Chapter 3 it was shown how XRD could provide rich microstructural information about InGaN/GaN heterostructures. It was also shown how XRD allows the different phases that might exist in the film to be identified. In particular, XRD readily confirmed the existence of metallic In droplets in a poor quality InGaN film. We discussed the misinterpretations of the XRD-related diffraction peak as sign of phase separation in InGaN.

It was also shown how the modulation of the XRD spectra due to interference can determine the layer thickness for layers with good surface and interface quality. We have also learned how a reciprocal space map can yield further information about microstructural details of the InGaN/GaN films. In particular, it was shown how macroscopic tilts between the different layers can be immediately detected by interpretation of a symmetrical RSM. The methodology for simultaneous measurement of c and a lattice constants via asymmetric RSM was introduced. It was shown how direct comparison of the InGaN and GaN RLP positions in a asymmetric RSM allows to infer the InGaN film coherency relative to the GaN pseudo substrate.

The particular case of InGaN/GaN films showing two InGaN related diffraction peaks was treated. A detailed asymmetrical RSM shows that the component with larger c is almost perfectly aligned along q_x indicating that this InGaN component has the same lattice constant as the GaN substrate. By using in-plane diffraction, it was shown that the relaxed part of the InGaN layer originates from the surface region.

Finally, we have shown how MQWs feature a rather complex XRD structure and illustrated how simulation of the XRD profiles allows fundamental structural parameters such well and barrier thickness and composition to be extracted.

In Chapter 4 the basic principles of the RBS technique were presented. It was illustrated how thickness, composition and depth profile can be determined from simulation of a random RBS spectrum. Strong compositional pulling effects were discovered in InGaN layers whose growth was aimed to produce layers with x>0.15 and the depth profile of x was extracted from RBS simulation. By exploring the channeling effect, it was also found that in samples showing composition gradients along the growth direction there is a direct correlation between strain release and increasing In content.

It was also shown how thickness and composition of individual wells in InGaN/GaN MQWs can be measured directly. From detailed simulation of the RBS spectra we could also estimate the extent of intermixing between well and barrier. Similarly to the trend verified in single layers, it was shown that the overall MQW crystalline quality, and in particular the extent of intermixing, deteriorates with the increasing composition.

A novel algorithm that allows surface roughness to be extracted from an RBS spectrum was discussed and tested allowing the potential of RBS analysis to characterise layer roughness to be further extended.

In Chapter 5, the optical characterization techniques used to investigate InGaN/GaN structures have been described.

It was shown how to obtain the effective bandgap energy in InGaN layers from OA measurements, the bandgap was found to shift to lower energies for layers with larger In content. A broadening of the absorption curves, and less pronounced Fabry-Perot interference fringes, was verified with increasing InN content. Both sets of observations were found to be in good agreement with the AFM, XRD and RBS evaluations of surface and overall structural quality, respectively. The period of the OA interference fringes was also used to estimate the nitride layer thickness, in good agreement with RBS and XRD measured thickness.

Using PL spectroscopy emission properties of the samples were investigated; the PL peak energy was found to decrease with *x,* while a broadening of the PL linewidth with decreasing peak emission energy is also verified. The luminescence intensity was found to decrease as the peak emission energy moves further into the red. Temperature dependent PL measurements were taken on an InGaN sample that featured two luminescence peaks and showed that the two components have different quenching rates with temperature.

The usefulness of CM to study the surface morphology and light emission properties at a μm length scale was illustrated. Spectroscopic mapping by CM revealed light emission inhomogenieties and could spatially resolve the location of two PL components originating at different surface location sites. The potential of CL spectroscopy with a variable energy electron beam, together with Monte-Carlo simulations of the electron beam penetration, to depth profile the optical properties of InGaN/GaN layers was explored.

Analysis of the optical characterization results reveals a general trend of increasing inhomogeniety and an overall degradation of the optical properties as layer thickness and composition increase. These trends were found to be consistent with the results presented in the previous chapters regarding structural characterization.

Chapter 6 was dedicated to investigate in detail the important issue of strain and composition in InGaN/GaN heterostructures. The two extreme approximations in common use regarding the strain state, fully relaxed or fully coherent growth, in order to determine x from the measured c lattice constant, were critically discussed. It was shown that considerable misjudgements can be made in the evaluation of the InN mole fraction if the strain effect on the lattice is not properly taken into account. Specifically, it was found that assuming full relaxation makes a systematic overestimation of x, whereas the pseudomorphic presumption yields the lower limit of x of a given sample. Strain insensitive RBS measurement of x provided a basis of comparison.

Using the alloys in-plane and out-of-plane measured lattice constants, elastic theory was applied to account for the hexagonal lattice distortion due to biaxial strain, allowing strain and composition effects to be separated. If this is performed, good agreement between XRD and RBS estimates of x is obtained.

The peculiar case of InGaN layers showing double XRD components was treated, and it was shown that the origin of the wide-spread misconception of assuming phase separation is an inadequate application of Vegard's law to layer regions that are incompletely relaxed. It was found that when the strain effect is properly taken into account, the two XRD components correspond to the same value of x. An RBS/channelling analysis provided further evidence of uniform composition in such layers and allowed us to depth-locate the relaxed (near surface) and strained (near the GaN interface) regions. Thus, the presence of double XRD peaks was shown to be unrelated to phase separation, and is a consequence of a DSR over depth.

The important concept of critical layer thickness (CLT) for strain relaxation was introduced. The CLT(x) was calculated using the PB model, demarcating the thickness-composition range where the strain relaxation is expected to dramatically accelerate in InGaN/GaN layers. The CLT was found to be a very strong function of x.

We have also proposed a model, based on elastic theory, which allows composition and strain gradients to be detected independently from an asymmetric high resolution XRD RSM. The directions of "pure" strain relaxation in the reciprocal space, for a given InN content (isocomposition lines), were calculated. The practical application of the model allowed different situations regarding strain and composition gradients to be distinguished; first, the case of a pure strain relaxation in layers grown above the CLT, well represented by layers with 2 XRD peaks, where the strain relaxation follows the calculated isocomposition line. On the other hand, analysis of a set of InGaN layers with thicknesses progressively increasing above the CLT allowed strain relaxation and In incorporation phenomena to be monitored as the alloy films grow. Comparison between calculated directions and measured distributions of the RLP has shown that the relaxation process does not follow a specific isocomposition line for these samples.

A general degradation of structural quality is verified with an increase of strain. Broader XRD profiles indicating increased mosaicity, composition and strain gradients and larger values of χ_{min} obtained by RBS, confirm the poorer crystalline quality of relaxed layers (or layer regions). In addition, it was found that the surface morphology becomes rougher for layers grown above the CLT, suggesting that 3D islanding is the main relaxation mechanism in InGaN.

This chapter also addressed the case of two MQW samples with the same InN mole fraction and different thicknesses. It was shown that the number of periods in the MQW sequence notably influences the structural properties. In particular, well/barrier intermixing was found to increase markedly with an increase in the number of wells from 8 to 18. An AFM and SEM surface analysis showed a correlation between an increased size and density of surface pits and the number of wells grown. This observation supported the suggestion that surface pitting and dislocations play a fundamental role in the intermixing mechanism in InGaN/GaN MQWs. Our results indicated that the overall structural quality degradation is mainly determined by the total

strain energy accumulated in the MQW stack, a similar situation to that observed in single layers.

Finally, in Chapter 7 we have attempted to establish correlations between optical and structural properties of InGaN/GaN heterostructures. It was shown that strain effect must be taken into account to establish the strain free bandgap dependence on composition, $E_g(x)$. The method used in this work to establish $E_g(x)$, was presented; RBS was used to obtain x, independently from the state of strain in the samples as shown in Chapter 4. The optical bandgaps in InGaN were measured by OA spectroscopy using the sigmoidal fit to extract the bandgap from the absorption curves, as detailed in Chapter 5. Subsequently, using the perpendicular lattice constant measured by XRD in Chapter 3, the measure bandgap of InGaN is corrected, that is, used to calculate the relaxed bandgap.

Following this approach, a linear relation between bandgap energy and InN content, was experimentally established: $E_g(x)=3.39-3.57x$ ($x\leq 0.25$). The $E_g(x)$ relation established, showing a fast decrease of E_g with composition, and the observation of IR luminescence, could be understood by considering recent results regarding the InN band gap.

In single InGaN layers that showed a composition pulling effect, one could depth profile the optical properties by using CL spectroscopy with variable electron beam energy. The CL spectra showed a red shift as the electron beam penetrated deeper into the layer, evidencing the influence of In surface segregation on the optical properties. The trend observed could be well reproduced by combining the RBS profile of x determined in Chapter 4, and the Monte–Carlo simulations of the electron beam depth profile.

A set of three InGaN/GaN MQW samples, well characterised by XRD, AFM and RBS in Chapter 6, were examined by PL spectroscopy. The MQW with lower x is found to have a PL emission blue shifted relatively to the other two MQWs. In addition, when comparing two MQWs grown under the same nominal conditions, but with a different number of wells, it is found that the PL emission of the thicker MQW is slightly red-shifted and broader. These observations were interpreted as result of a compositional pulling effect that leads to higher In incorporation in the later wells, and an overall deterioration of the MQW quality with an increasing strain energy for thicker MQW stacks.

The case of InGaN epilayers with double PL components was also studied. The two components of the sample's luminescence could be discriminated for the first time by depth-resolving CL. The lower energy peak was shown to originate from the near surface region, whereas the high energy component is found to emerge from the deeper sample regions closer to the InGaN/GaN interface.

Taking into account what has been learned about the structural properties of these samples in previous chapters, and the energy location of the two CL components, it was unambiguously demonstrated that the origin of the DLPs is a DSR along the growth direction. Based on this

experimental evidence, it was argued that the appearance of luminescence doublets in InGaN layers is not evidence of "quantum dot-like In-rich" or "phase separated" regions, as previously proposed.

The physical conditions for the appearance of DLPs were directly connected to the CLT calculated in Chapter 6. We have shown that both composition and layer thickness must be considered to locate the samples in the (*x,t*) phase space. If the thickness exceeds the CLT(*x*), is likely that DLP will appear. It was found that the appearance of a DLP in InGaN layer can be either reached by keeping the thickness constant and increasing the composition, or for the same *x* in the films, by increasing the thickness. The PL of two samples specifically grown under the same nominal conditions, above and below the CLT, featured two and one luminescence components, respectively, reinforcing the validity of the simple interpretation model proposed.

Based on the overall trend of the energy position of high and low energy components of the DLPs, found in this work, it was shown that high and low energy components converge to the GaN bandgap at around 3.4eV, as *x* tends to zero. By modelling the energy separation of the two components, we established a method to estimate the strain deformation potential in semiconductor alloys. It is found that for the low composition range ($x<0.3$) the bandgap in-plane strain coefficient for $In_xGa_{1-x}N$ is quite similar to that obtained for GaN, as might be expected.

Looking back, we see that most open questions described in the Introduction, namely the issues of accurate measurement of InN fraction, the influence of *x* in the structural and optical properties and the strain phenomena in InGaN, were directly addressed and clarified in the course of this thesis.

An elucidation on the topic of phase separation in InGaN was also a concern of this work. Putting in perspective all the observations quoted as evidence for phase separation found in the literature, and the results discussed along this thesis, we propose an explanation for the common belief among the research community that InGaN alloys frequently feature phase segregation above a certain value of *x*.

The reasoning to the reach the conclusion of phase separation is generally based on a systematic observation of peculiar changes on the structural and optical properties above a certain composition; these include appearance of double XRD or luminescence peaks, surface roughening or changes in the TEM image contrast, typically observed for $In_xGa_{1-x}N$ samples with $x>0.1$. Considering that the majority of InGaN films investigated in the literature have thickness of the order of ~100 nm, we argue that what most researchers are in fact observing are effects of strain relaxation. According to what has been discussed regarding the CLT in Chapters 6 and 7, for a 100 nm thick $In_xGa_{1-x}N$/GaN film the maximum InN content (what we may call a critical value of *x*) that a coherent film can incorporate without relaxing is about 0.1.

The differences between coherent and relaxed InGaN layers are well described in this thesis, and the phenomena quoted as evidence for phase separation are remarkably similar to what is observed in relaxed or partially relaxed layers. This is not likely an accidental coincidence.
It clearly seems that strain-related phenomena have been somehow overlooked in InGaN research. That explains, at least in part, the great controversy on the interpretation of InGaN structural and optical properties.

8.2 Some suggestions for future work

The extension of this work to higher InN content samples, ideally covering the full alloy range up to *x* approaching 1, would certainly be an interesting point. Now it is possible to obtain such samples through collaboration with Professor Y. Nanishi of *Ritsumeikan University* (Japan) that can grow InGaN samples in the very high InN content range by MBE. This will allow the validity of some models proposed to be tested for to the full composition range. In addition, it will open the way to verify the linearity of some physical parameters, and to compare MOCVD and MBE grown InGaN.
The second point of interest would be to explore further the possibility to study samples grown with specific parameters to conveniently isolate the influence of the various structural parameters. Now with the MOVCD reactor working at the *Institute of Photonics* at the *University of Strathclyde*, we may take the opportunity to study tailor made samples to address specific problems, this is a key advantage which was unfortunately not available at the beginning of this work.
Following the work undertaken in this thesis and particularly exploring the benefit of samples whose detailed structural and optical characterization has been performed, there is much space for further fundamental characterization. For instance the study of lattice dynamics and free carrier properties by Raman spectroscopy and IR ellipsometry are areas that have shown interesting potential for further developments [1-3].
Another interesting subject will be the comparison of XRD results with extended X-ray absorption fine structure (EXAFS) analysis. In addition resonant XRD RSM analysis using synchrotron radiation at the In and Ga edge (possible at the ESRF in Grenoble) will be rather interesting, since the diffraction can favour In and Ga rich sample regions respectively.
It will be useful to extend the methods developed here to characterize InGaN/GaN heterostructures to other material systems. In particular, RBS roughness models developed to derive the layer roughness can be applied to other thin films and the methodology proposed to separate strain from composition effects by RSM can be extended to other alloy systems and different crystal structures. Work in this line is also in progress.

From a more applied point of view, it will also be attractive to investigate the possibility to obtain a white emitting InGaN heterostructures, by tuning various emissions energies at different wells in a MQW structure or using a composition profile. Finally, there is also great interest to explore the potential of rare earth doping in InGaN [4-5].

8.3 References:

[1] M. R. Correia, S. Pereira, E. Pereira, J. Frandon, M. A. Renucci and E. Alves Appl. Phys. Lett. **83**, 4761 (2003).

[2] M. R. Correia, S. Pereira, E. Pereira, J. Frandon, I. M. Watson, C. Liu, E. Alves, A. D. Sequeira, and N. Franco, Appl. Phys. Lett. 85, 2235 (2004)

[3] A. Kasic, M. Schubert , J. Off, B. Kuhn, F. Scholz, S. Einfeldt, T. Böttcher, D. Hommel, D. J. As, U. Köhler, A. Dadgar, A. Krost, Y. Saito, Y. Nanishi, M. R. Correia, S. Pereira, V. Darakchieva, B. Monemar, H. Amano, I. Akasaki, G. Wagner Phys. Stat. Sol. **0**, 1750 (2003).

[4] M. R. Correia, S. Pereira, A. Cavaco, E. Pereira, and E. Alves Appl. Phys. Lett. **80**, 4504 (2002).

[5] E. Alves, U. Wahl, M.R. Correia, S. Pereira, B. De Vries, A. Vantomme Nucl. Instr. and Meth. B, **206**, 1042 (2003).